On the Design of Fly's Eye Lenses at Sub-THz Frequencies for Wideband Communications

Arias Campo, M.

DOI
10.4233/uuid:a9bb41e0-3d2a-4028-a218-bd85f2053545

Publication date
2021

Document Version
Final published version

Citation (APA)
Arias Campo, M. (2021). *On the Design of Fly's Eye Lenses at Sub-THz Frequencies for Wideband Communications*. [Dissertation (TU Delft), Delft University of Technology].
https://doi.org/10.4233/uuid:a9bb41e0-3d2a-4028-a218-bd85f2053545

On the Design of Fly's Eye Lenses at Sub-THz Frequencies for Wideband Communications

Ph.D. Thesis

Marta Arias Campo

On the Design of Fly's Eye Lenses at Sub-THz Frequencies for Wideband Communications

DISSERTATION

for the purpose of obtaining the degree of doctor
at Delft University of Technology
by the authority of the Rector Magnificus Prof. dr. ir. T. H. J. J. van der Hagen,
chair of the Board of Doctorates,
to be defended publicly on
Monday 11th January 2021 at 12:30 o'clock

by

Marta ARIAS CAMPO

Ingeniera de Telecomunicación,
Universidad Politécnica de Madrid, Spain

born in León, Spain.

This dissertation has been approved by the promotors.

Composition of the doctoral committee:

Rector Magnificus,	Chairman
Prof. dr. ir. N. Llombart Juan,	Delft University of Technology, promotor
Prof. dr. ing. A. Neto,	Delft University of Technology, promotor
Independent members:	
Prof. Dr.-Ing. T. Kürner,	Technische Universität Braunschweig, Germany
Prof. dr. L. Jofre Roca,	Universitat Politècnica de Catalunya, Spain
Prof. dr. R. Sauleau,	Université de Rennes 1, France
Prof. dr. ir. L.C.N. de Vreede,	Delft University of Technology, Netherlands
Reserve member:	
Prof. dr. ir. J.J.A. Baselmans,	Delft University of Technology, Netherlands
Other members:	
Dr. ing. S. Bruni,	IMST GmbH, Germany, daily supervisor

The work presented in this thesis has been performed in the frame of a collaboration between TU Delft and IMST GmbH. In TU Delft, the work has been financed by the European Research Council starting Grant LAA-THz-CC Grant 639749. In IMST GmbH, the work has been partly financed by the German Ministry of Education and Research.

Keywords: Lens antennas, leaky-wave antennas, multi-beam antennas, dielectric gratings, polarizer, Green's function method, wideband communications.
Cover design by: Marta Arias Campo
Printed by: Ipskamp Printing B.V., Enschede, Netherlands.

ISBN 978-94-6421-183-2

To my parents and Sebastian

Preface

This dissertation describes the research work carried out over a period of four years (from July 2016 to July 2020) in the frame of a close collaboration between the THz Sensing group, Delft University of Technology, the Netherlands, and the department of Antennas and Electromagnetic Modelling, IMST GmbH, Kamp-Lintfort, Germany. In Delft University, the project was embedded in the ERC Starting Grant ERC-2014-StG LAA-THz-CC No. 639749, with emphasis in lens arrays for sub-terahertz bands, leaky-wave lens feeds and FO analysis techniques. Besides, the thesis was co-financed in part by IMST GmbH, and in part by the German Ministry of Education and Research (BMBF) through the project HYPATIA, under grant ES2TECH019.

The three G-band prototypes, presented in Chapters 4, 5 and 6 were fabricated at DEMO, in Delft University of Technology, financed by the ERC grant. The H-band prototype, introduced in Chapter 7, was fabricated by Fraunhofer Institute for Applied Solid State Physics (IAF), Freiburg, Germany, financed by HYPATIA project. All prototypes have been characterized at Delft University of Technology.

Contents

Chapter 1

Introduction

1.1 Beyond 5G Communications

Wireless communication systems are experiencing a revolution driven by new, data demanding applications and the rapid growth in the number of users and devices. Future use cases will need wireless links with capacities orders of magnitude larger than currently achieved in back-haul, front-haul, and access networks. The booming demand for high-speed wireless communications calls for a revolution in the way the networks and systems are conceived. Exploiting small RF bandwidths with advanced signal processing techniques has reached a saturation point, and the availability of spectrum in the lower frequency bands is becoming scarce [1, 2]. The newly emerging 5G generation already relies on the use of higher frequency bands (K-, Ka-, Q-bands), which provide larger RF bandwidth and therefore lead to higher link capacities [3]. The way towards the use of higher frequencies (D-, G- or H-bands) will continue in the next Beyond 5G and 6G generations [1, 2, 4, 5, 6, 7, 8, 9, 10, 11]. The standardization of wireless communications at carrier frequencies in the H-band (300 GHz) has already started, regulating the use of more than 60 GHz bandwidth [12] for point to point applications. However, significant development of system architectures, active and passive devices enabling efficient use of the mm- and sub-mm wave spectrum is still required.

Beyond 5G and 6G networks will come with new connectivity strategies. *Fixed Wireless Access* (FWA) will provide homes, offices and industries with fixed broadband connections via high-speed wireless point-to-multipoint links, being an alternative to xDSL, cable and fibre optic technologies. Implementing wireless links instead of cable and fibre connections results in reduced costs for network deployment and maintenance. Additionally, FWA will be one of the pillars to enable fast network deployment and acceptable data service in remote areas, which is one of the objectives marked in the 6G path [5, 9]. For these reasons, FWA demand is forecasted to experience a strong growth in the upcoming years [13]. In order to strengthen worldwide connectivity, the new 6G generation will revolutionize the network layer. To this end *3D network architectures* are proposed incorporating non-terrestrial nodes, such as drones, satellites and underwater vehicles, expanding the network and adding flexibility [1, 5]. The new *front-haul small cell* networks [7] will provide users with data rates unthinkable with current systems. Specifically access networks in crowded scenarios, such as football stadiums, concert halls or auditoriums, will profit from the new small cell strategies. In order to cope with the huge amount of aggregated data, the use of the sub-THz spectrum will become essential as well in the network *backhaul* [1, 4, 10, 11].

Innovations in communication technologies and infrastructure come hand in hand with the development of *data demanding applications*. Beyond 5G and 6G networks and communication systems will meet the needs of emergent applications, such as augmented reality, telepresence [1, 11], holographic, tactile and human-bond communications [5, 9]. The automotive industry will apply 6G technology for vehicle-to-vehicle communications, vehicle-to-infrastructure and in-car communications [7, 9]. Additionally, the field of Industry 4.0 will benefit from the new communication generations, which will be used in applications like connected robotics and autonomous systems [1, 14]. Due to their lower complexity, kiosk downloading and data center connections [11, 15] are foreseen to become some of the first applications making use of sub-THz frequencies.

1.2 Challenges of sub-THz Communications

While allowing for larger bandwidths, the use of sub-THz frequencies raises many technical challenges. Those should be overcome by means of high-performance solutions suitable for mass-production processes, in order to achieve competitive systems. Among others, some of the hurdles which come along with the use of higher frequencies are:

- **Propagation spreading and loss:** the wave propagation spreading factor increases proportionally to the square of the frequency. At 300 GHz, the signal is attenuated 122 dB at 100 m range due to energy spreading. In order to fulfil the link budget, the use of high gain antennas ($> 30\,\mathrm{dB}$) is required at these high frequencies. On top of that, the atmospheric attenuation increases as well for shorter wavelengths, as shown in Fig. 1.1. This contribution is not dominant for short link distances but becomes relevant for link distances of several 100 m. Special attention should be paid in the resonance regions, where strong attenuation can appear [2, 10].

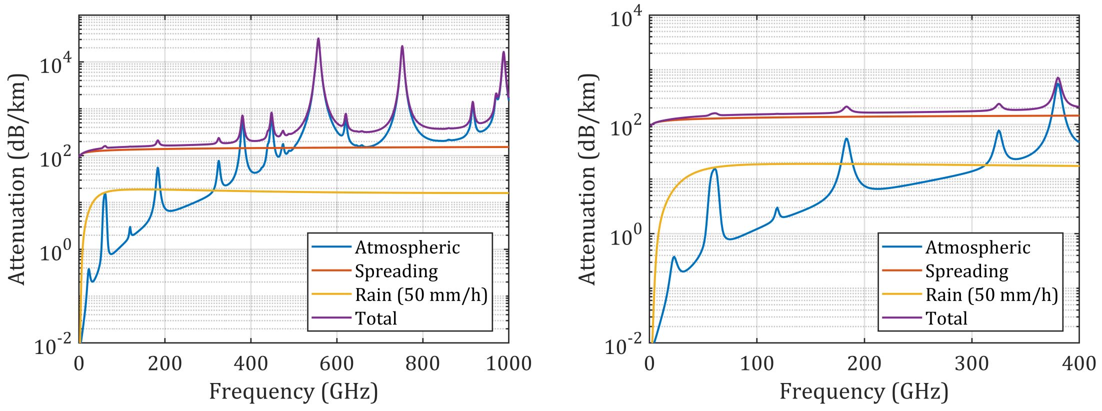

(a)

(b)

Figure 1.1: Path attenuation considering water vapor density of 7.5 gr/m^3, 15°C ambient temperature and dry air pressure of one standard atmosphere at sea level. a) Frequency range from 0 to 1 THz. b) Frequency range from 0 to 400 GHz.

- **Output power available:** the generation of power at high frequency is much less efficient than at low frequency, due to the cost of up-converting signals generated at lower frequency. The limited $f_t/f_{\max}$ in the active technology limits the maximum achievable output power per device [16]. The larger impact of parasitic components at high frequency limits as well the output power. This fact magnifies the importance of maximizing the efficiency in the last system stages, and especially in the antennas and their transition to the active front-end. Fig. 1.2 shows the output power achieved for different technologies over frequency. A decrement of $1/f^3$ is reported for frequencies higher than 100 GHz [17].

- **Implementation of wideband, multi-beam system architectures:** in order to profit from the use of high frequencies, new antenna and system architectures are required. Large bandwidths should be supported in all system layers, for which strategies such as frequency aggregation may be introduced in baseband and intermediate frequency sub-systems. The new high-frequency systems will need high gain antennas with multiple beams, static or steerable, to provide connectivity to several nodes or users. Narrow beams and large bandwidth availability enable FDMA/SMDA architectures to reduce interference between cells or links. As will be later explained, phased array concepts suffer from integration problems at these high frequencies. Focal plane arrays [18, 19] or lens array concepts [20] are proposed as more promising

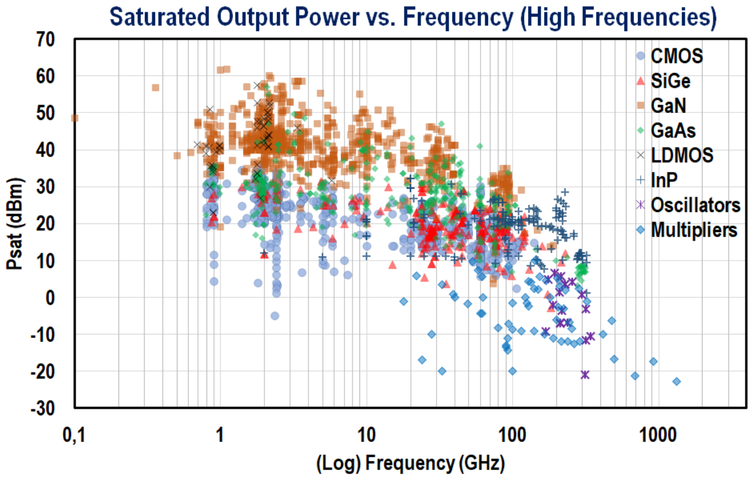

Figure 1.2: Amplifier output power for different technologies, from [16].

solutions to provide multi-beam and steering capability in the new communication generations.

- **Front-end integration:** Passive RF structures scale down with increasing frequency. On the contrary, the chip area scales up, due to decreasing efficiency of the electronics at higher frequencies. At frequencies up to Ka-band, beamforming with half-wavelength phased arrays is a very convenient strategy, due to their flexibility and scalability [21]. However, the classical integration concepts for the front-end and antennas at lower frequencies cannot be simply scaled. The high integration density and decreasing efficiency in the active circuitry for higher frequencies causes thermal problems. Beam-forming with focal plane arrays has been the traditional approach in THz systems, as this architecture facilitates the front-end integration [22, 23].

In the frame of this thesis, some of these challenges are addressed, proposing efficient, wideband, high-gain lens antenna concepts that bring low-cost implementation of sub-THz communications a step closer. Nevertheless, innumerable advances are needed in all system layers (transceivers, channel modelling, modulation and coding, medium access control protocols, network... [1, 8, 10, 14]) in order to enable future Beyond 5G and 6G communications.

1.3 Fly's Eye Lens Arrays

In the frame of the ERC Starting Grant ERC-2014-StG LAA-THz-CC, No. 639749, the use of lens arrays combined with leaky wave (LW) feeds [24] was proposed for communications and sensing applications at high frequencies. In particular, a Fly's eye lens architecture consists of an array of integrated lenses, enabling the generation of multiple, simultaneous, fixed high-gain beams.

This thesis focuses in the design of passive fixed beam lens antenna solutions to be integrated in the proposed Fly's eye lens arrays. In this section, the application scenarios suitable for this kind of fixed multi-beam architectures are discussed, and the requirements for the lens designs within this dissertation (bandwidth, gain, steering range) are derived by means of preliminary system dimensioning and link budgets.

The use of lens antennas allows achieving the required high gain efficiently, over larger bandwidths ($> 20\,\%$) in comparison to other more resonant antenna solutions, such as Fabry-Pérot [25], metasurfaces [26] or transmitarrays [27], or classical phased array solutions with lossy feeding networks [28, 29]. A high gain beam with stable pointing angle over the whole bandwidth is achieved in contrast to other frequency dispersive leaky-wave concepts, e.g. [30, 31].

Moreover, the lens steering capability enables the generation of simultaneous multiple beams pointing in different directions with planar Fly's eye lens array panels, as displayed in Fig. 1.3a. This facilitates the integration with high frequency front-ends, which can be in this way mounted on a single Printed Circuit Board (PCB) per panel. Other antenna solutions such as horn antennas [32], reflectors [33], transmitarrays [27] or reflectarrays [34, 35] illuminated by focal plane arrays of horns, would not allow for such a planar configuration, resulting in a more bulky and expensive solution. Thanks to the larger periodicity introduced in the lens array concepts, integration and thermal issues arising in classical array approaches [28, 29] are significantly reduced.

In order to arrive to a more compact antenna array, each lens can host several transceivers or beams. The number of beams per lens will be mainly limited by the size of the active circuitry in terms of wavelength. The integration of different beams under one aperture is not possible with other solutions, such as horn antennas [32], which therefore would not allow optimizing for compactness.

Maximizing the lens aperture efficiency allows reducing further the lens array size. Lens antennas enable very high aperture efficiencies over a wide band, in contrast to other multi-beam solutions such as transmitarrays [27], reflectarrays [34, 35] or metasurfaces [36]. Apart from reducing the required aperture size, proper lens illumination, with low spill-

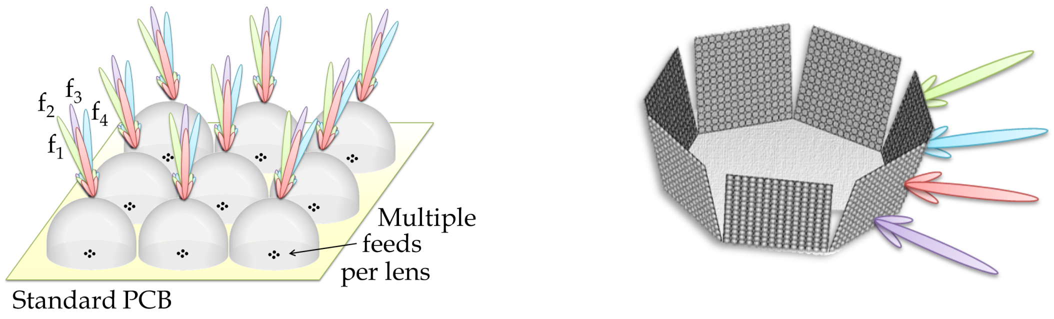

(a) (b)

Figure 1.3: a) Fly's eye antenna structure on a standard PCB with multiple feeds per lens indicated by black dots. b) Fly's eye antenna with 7 panels covering ±25 deg in elevation and 360 deg in azimuth.

over, reduces the coupling between lenses in the Fly's eye array (and hence interferences between links).

1.3.1 Fly's Eye Use Cases

Among all named Beyond 5G and 6G possible use cases, Fly's eye architectures are suitable for scenarios where multiple, fixed high-gain beams are required. Multi-beam systems with a single transceiver per beam have been contemplated. Each of the beams corresponds to a link, intended to provide coverage to single nodes or multiple users.

Possible application examples for systems with multiple, fixed beams are future point-to-multipoint front-haul connections, such as the already mentioned Fixed Wireless Access (FWA), or access networks in dense small cells, e.g. football stadiums, auditoriums, etc. (Fig. 1.4). In Fixed Wireless Access, different beams in the base station point simultaneously at multiple static receivers situated in different buildings. In the dense small cell use case, overlapping beams should simultaneously cover the whole field of view where the users are distributed [20].

The small cell use case has been evaluated specifically for a football stadium in the frame of the *XG Communications* research team of the in TU Delft Micro-electronics Department [20], where a Fly's eye antenna architecture in D-band, tailored for this scenario, is proposed. This use case may be one of the most demanding scenarios for network providers nowadays. The initial scenario considered, reported in [20], is a stadium with a capacity of 80000 people. A data rate target of 150 Mbps per user (100 Mbps download plus 50 Mbps

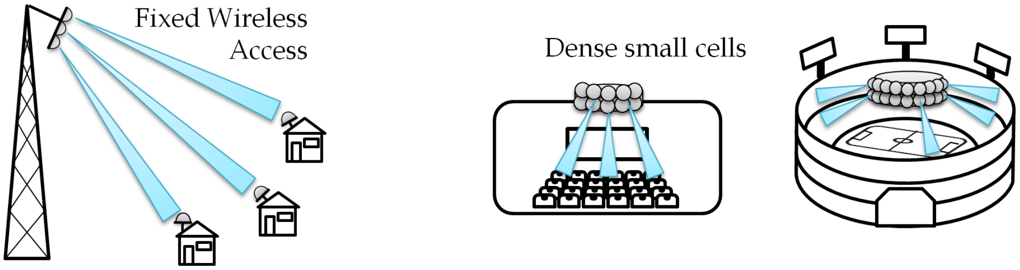

Figure 1.4: Fixed Wireless access and small-cell use cases, in which multiple, fixed beams cover simultaneously several nodes or cells with groups of users.

upload) was set as a challenging requirement to be covered in Beyond 5G communications. In this case, a total data rate requirement of 12 Tbps would be reached, which is 300 times higher than the currenty provided in stadium solutions at lower frequencies provide [37, 38]. The proposed system is based on a central, compact base station which generates multiple-directive beams, dividing the stadium tribune into a number of cells, using a FDMA/SDMA scheme in order to reduce interferences between cells. The cell distribution should provide full coverage over the whole tribune area. The base station, suspended above the center of the stadium, should cover a Field of View (FoV) of 360 deg in azimuth and 50 deg in elevation, where the tribune is found (Fig. 1.5).

In the following, we present an example of the system dimensioning at G-band, based on a RF bandwidth of 42 GHz centered at 150 GHz. A SDMA/FDMA scheme with seven 6 GHz channels is chosen, assigned to alternating cells. This channel bandwidth could be shared among 54 users using time modulation, reaching an equivalent bandwidth per user of 112 MHz. A beam-width $\Delta\theta_{-3\,\mathrm{dB}}$ of 3.6 deg in azimuth and elevation (34 dB directivity) would cover an angular spatial cell of 54 users, considering 0.5 deg beam-width needed per user at 100 m distance.

For the link-budget calculations we have considered a line-of-sight link of 100 m. The chosen modulation scheme is QPSK, for which 150 Mbps could be reached per user[1], shared between up-and down-link. This modulation is very convenient when moving to higher frequencies, as no amplitude information is needed and therefore the power amplifiers can be operated in saturation, maximizing the output power. As already mentioned, the single antenna gain in the base station is set to 34 dB, while the antenna at the user terminals should reach 10 dB gain. In both directions, we suppose that the transmitted power reaches 18 dBm which could be accomplished with state-of-the-art InP amplifiers (Fig. 1.2). The low transmitted power fulfils the link budget thanks to the high antenna directivity and

---

[1] $R_s = BW/(1 + \mathrm{roll-off})$, where R_s is the data rate, BW is the channel bandwidth and the roll-off refers to the steepness of the filter preventing cross-talk between channels

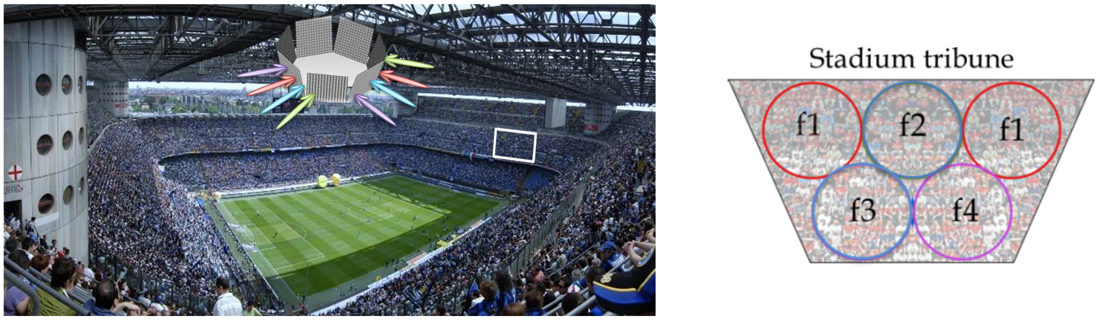

(a) (b)

Figure 1.5: a) Football stadium with central base station, generating multiple, fixed beams to cover the full tribune. b) View of part of the stadium tribune with different cells, with an FDMA/SDMA scheme using 4 frequencies.

the limitation of the cell or beam bandwidth. This leads to a total RF transmitted power of ∼ 90 W for the full base station (18 dBm on each of the 14×100 cells). A noise figure of 10 dB is considered in the receivers. Using time division multiplexing, 100 Mbps in downlink and 50 Mbps in uplink can be reached per user, assuming a BER of 10^{-6}. Table 1.1 shows the simplified link budget analysis that was realised for this case at 150 GHz.

In the FWA use case, in contrast with the small cell coverage, the considerations in the system dimensioning are less restrictive, as every link is in principle intended to take place exclusively between two nodes, for example, between a base station and an access point situated in a building. Therefore, in this case it is not needed to consider full area coverage, but single connections. A SDMA/FDMA scheme could still be useful here to reduce interferences between adjacent links. However, in this case the beams are more separated angularly and therefore less frequency channels are needed, each of them reaching more capacity. As example, FDMA schemes of 2 channels are considered. Transmission and reception channels are located as well in different bandwidths, to enable a full-duplex link.

As we are not dealing with moving users in this case, the antennas in both ends can be highly directive, elongating the reachable link distance. In Table 1.2, two examples are presented for systems centered at 150 GHz and 270 GHz, considering different link

---

[2] C/N [dB] $= P_t + G_t - 20\log_{10}(4\pi d/\lambda) - L_{\text{at}} - L_{\text{rain}} + G_r - 10\log_{10}(kT/BW)$ being $T = T_{\text{LNA}} + T_{\text{ant}}$ with $T_{\text{LNA}} = [10^{NF/10} - 1]T_0$, $T_{\text{ant}} = 300\,\text{K}$ and $T_0 = 290\text{k}$

[3] Including ohmic loss between antenna and LNA

[4] Rain 50 mm/h: 19 dB/km. Atmospheric loss: 3 dB/km (water vapor density of 7.5gr/m^3, 15°C ambient temperature and dry air pressure of one standard atmosphere at sea level.)

Scenario	**Small Cell**
Modulation	QPSK
C/N[2]	~ 10 dB
Frequency	150 GHz
RF channel bandwidth (BW)	6 GHz
FDMA scheme	7
Scenario RF bandwidth	42 GHz
Link data rate	8 Gbps
Antenna gain Tx (G_t)	34 dBi
Antenna gain Rx (G_r)	10 dBi
PA output power (P_t)	18 dBm
NF of receiver[3]	10 dB
Atmospheric and rain loss[4] ($L_{\rm at} + L_{\rm rain}$)	2.2 dB
Maximum link distance (d)	100 m
Cell angular size	3.6 deg
Number of cells	14 × 100
Total angular coverage	50 × 360 deg
Data rate per user	150 Mbps
Aggregated capacity	11.2 Tbps
Cell connection density	193 Mbps/m^2

Table 1.1: Link budget for the small cell scenario in a football stadium.

ranges and channel bandwidths. In the same way as in the small cell use case, QPSK modulation is chosen here to allow the amplifiers operate close to the saturation point. In the 270 GHz link, lower output power has been considered, as well as higher noise figure, as a consequence of the higher frequency. It is shown that for the 270 GHz example more than 20 Gbps per link for a range of 158 m could be reached, when considering 34 dBi antenna gains.

---

[5] C/N [dB] $= P_t + G_t - 20\log_{10}(4\pi d/\lambda) - L_{\rm at} - L_{\rm rain} + G_r - 10\log_{10}(kT/BW)$ being $T = T_{\rm LNA} + T_{\rm ant}$ with $T_{\rm LNA} = [10^{NF/10} - 1]T_0$, $T_{\rm ant} = 300$ K and $T_0 = 290$k

[6] Including ohmic loss between antenna and LNA

[7] Rain 50 mm/h: 19 dB/km. Atmospheric loss: 3 dB/km (water vapor density of 7.5gr/m^3, 15°C ambient temperature and dry air pressure of one standard atmosphere at sea level.)

[8] Rain 50 mm/h: 18.2 dB/km. Atmospheric loss: 10 dB/km (water vapor density of 7.5gr/m^3, 15°C ambient temperature and dry air pressure of one standard atmosphere at sea level.)

Scenario	**Fixed Wireless Access**	
Modulation	QPSK	
C/N[5]	∼ 10 dB	
Frequency	150 GHz	270 GHz
RF channel bandwidth (BW)	12 GHz	17.5 GHz
FDMA scheme	2	
Scenario RF bandwidth	48 GHz	70 GHz
Link data rate	16 Gbps	23.3 Gbps
Antenna gain Tx (G_t)	34 dBi	
Antenna gain Rx (G_r)	34 dBi	
PA output power (P_t)	18 dBm	12 dBm
NF of receiver[6]	10 dB	12 dB
Atmospheric and rain loss ($L_{\text{at}} + L_{\text{rain}}$)	10 dB[7]	4.4 dB[8]
Maximum link distance (d)	455 m	158 m

Table 1.2: Link budgets for the Fixed Wireless Access scenario.

1.3.2 Fly's Eye Array Requirements

Wideband Fly's eye lens array architectures with integrated elliptical lenses enable the generation of multiple, simultaneous, fixed high-gain beams for the previously mentioned scenarios. From the link budget analyses presented previously, antenna gain requirements higher than 30 dB per link have been derived, as well as relative bandwidths higher than 30 %. Fig. 1.3b shows a conceptual representation of a possible cost-effective implementation of a base station antenna, composed by seven planar Fly's eye panels, covering fields of view of 50 deg.

With the aim of enhancing the wireless link efficiency, especially in scenarios with moving terminals, circularly polarized lens antennas are even better candidates to be used as single elements in the Fly's Eye lens arrays, as they minimize the loss due to polarization misalignment. However, wideband, low loss and cost-effective concepts are needed to generate circular polarization (CP), in order not to compromise the performance reached with the linearly polarized (LP) lenses.

The use of lens antennas is proposed as an efficient solution to provide high gain. However, the implementation of wide-band, low loss transitions from the antenna to the active front-end remains a challenge. As already mentioned, this is of great importance in sub-THz systems, due to the low output power available in the transmitters, and also to avoid degrading significantly the noise figure in the receptor.

Summarizing, the main antenna specifications required to implement compact, efficient Fly's Eye lens arrays, which are addressed in this thesis, are:

- High gain: $> 30\,\mathrm{dB}$
- Wideband characteristic: $> 30\,\%$
- Multi-beam capability, large steering range with low scan loss: ± 25 deg
- High aperture efficiency: $> 70\,\%$
- Circular polarization: axial ratio $< 3\,\mathrm{dB}$
- Low loss (antenna and transition to front-end): $\sim 1\,\mathrm{dB}$

1.4 State-of-the-Art in Sub-THz Antennas

The advantages of lens antennas have been already pointed out w.r.t. other antenna solutions. In this section, the state-of-the-art is reviewed for integrated lens antennas (bandwidth and steering capability), integration approaches for the lens feed (bandwidth and efficiency), and circularly polarized antennas at sub-THz frequencies (bandwidth, high-gain), being those the main topics on which we have concentrated along this dissertation.

1.4.1 Lens Antennas

When looking at integrated lens antenna designs in the literature, materials with high dielectric permittivity, ε_r, such as silicon ($\varepsilon_r = 11.9$) or alumina ($\varepsilon_r = 9$) are chosen in many cases, presenting very low dielectric losses. The main disadvantage of these designs lays on the high reflection in the lens-air interface. There are several designs reported reaching high lens aperture efficiencies over a relative bandwidth of $15 - 20\%$ [39, 40]. Double-slot antennas [39], or waveguide apertures [40] are usually used as lens feeds. Larger bandwidth designs are presented using double bow-tie antennas, in [41], and non-resonant leaky-wave antennas, in [42]. However, in both cases the feed pattern which illuminates the lens surface does not allow for reaching high aperture efficiencies and higher side- lobe levels are reported. In [24, 43], a resonant Leaky-Wave Antenna (LWA) or Fabry-Pérot antenna was proposed as a promising solution to act as a silicon lens feed, due to its high directivity, symmetric pattern, compactness, low profile and compatibility with silicon fabrication processes, but presented narrow bandwidth. The use of lenses with higher dielectric permittivities enables larger scan angles.

Designs using lenses in quartz ($\varepsilon_r = 3.8$) and MACOR$^{\mathrm{TM}}$ material ($\varepsilon_r = 5.6$) have been reported respectively in [18, 44, 45]. In [18], the beam shape is degraded due to the effects of multiple reflections. In [44], the feed pattern asymmetry results in lower lens aperture efficiency, presenting high reflection losses. In [45], the use of a shell with lower ε_r improves the reflection efficiency and optimizes the lens steering capabilities. Unfortunately in both cases the dielectric loss is very high, which leads to a considerable power loss ($3.7 - 5.6\,\mathrm{dB}$ reported in [45]).

Low ε_r plastic materials ($\varepsilon_r \leq 2.5$) represent a good candidate to fabricate lens antenna arrays, due to the availability of moderate loss materials (HDPE, Rexolite, Topas, ...), presenting light weight and enabling cost-effective manufacturing through processes such as injection moulding or 3D printing. Nevertheless, the efficient illumination of these lenses is more challenging. The larger lens eccentricity, e, needed for low ε_r lenses implies that directive feeds are needed to avoid the lens critical angle. Most of the reported designs for lenses with $\varepsilon_r \leq 2.5$ present reflection issues which decrease the antenna efficiency and degrade the radiation pattern [19, 46, 47]. However, the achievable scanning angular range is relatively small with low permittivity lenses.

There are several concepts in the literature aiming to enlarge the field of view of integrated lenses [45, 48, 49, 50, 51, 52]. In [45] and [48], the design effort is focused on the lens or lens system shape, achieving very stable gain over the scan angle. However, neither of them achieves high η_{ap} at broadside ($\sim 50\,\%$). In [48], the relative positioning between the objective and immersion lenses causes tolerance problems. In [49], the feed geometry is optimized to perform a beam-tilting in the radiation pattern inside the lens, improving the off-axis performance over a narrow band. References [50], [51] propose the combination of shaped lenses with an array of feeds in order to achieve maximum directivity at broadside and off-axis beams. However, the complexity of the array feeding network would be difficult to realize at high frequencies and would introduce high losses. Moreover, the design in [51] does not reach high η_{ap} at broadside ($52\,\%$). In [18], the lens extension length is optimized in order to reduce the reflection loss, with the cost of losing 2.7 dB in broadside directivity and increasing the side-lobe level. Other examples are based on 2D lenses, with enhanced scanning and high aperture efficiency in one plane [52].

1.4.2 Lens Feed Integration Approaches

The majority of systems present in these frequencies make use of wave-guide technology to interface between the front-end and antenna. Several chip to wave-guide transitions have been proposed in the literature at H-band, presenting mostly losses higher than 1 dB [53, 54, 55, 56]. In [57], a transition integrated in a GaAs chip with 0.5 dB loss was presented, reaching however only 40 GHz bandwidth. In any case, the manufacturing of mm-wave-guide split blocks is very costly, and therefore they become unattractive for future commercial applications.

On-chip antennas have been already proposed as a more cost-effective and integrated approach. Solutions based on grounded patches with front-side radiation show increasing radiation efficiency for higher frequencies, but cover only a small bandwidth [58, 59]. Dielectric loaded on-chip antennas with front-side radiation [60, 61, 62] and end-fire radiation [63] have been proposed at 300 GHz, reaching high efficiencies but bandwidths lower than 13 %. Antenna concepts based on radiation through the chip with silicon lenses have been proposed for imaging, radar or communication applications [41, 64, 65, 66, 67, 68], achieving large impedance bandwidths. In these back-radiating concepts, 1–1.5 dB losses occur due to the propagation through the lossy chip substrate. Antenna concepts such as double slots or dipoles are usually proposed, which do not reach high lens aperture efficiency over large bandwidths. In order to enable wideband, compact lens array concepts as discussed in Section 1.3.2, and coherent lens arrays as proposed in [69], high lens aperture efficiency is required over a large bandwidth, and therefore more complex lens feed designs are needed, such as leaky-wave feeds [24]. However, those are difficult to implement in on-chip approaches [64].

Off-chip antennas have been as well proposed at frequencies higher than 100 GHz for antenna-in-package approaches, using e.g. Alumina [70], LTCC [71], Silicon membranes [72] or quartz carriers [73], achieving narrow bandwidths ($< 10\,\%$). In these concepts, MMIC area is spared and more degrees of freedom for the antenna design are introduced. Most of the concepts make use of bond-wires to connect the antenna with the active front-end MMIC, introducing loss and inductive effects which can be compensated with narrow-band matching networks. In [72], beam-leading technology is used at 150 GHz as an alternative to bond-wire transitions, enhancing the transition performance. A state-of-the-art compilation concerning 300 GHz on- and off-chip antenna solutions with front radiation was published in the recent work [73], reporting relative bandwidths lower than 15 %.

1.4.3 Circularly Polarized Antennas

Many linear to circular polarization conversion concepts can be found in the literature up to 60 GHz [74, 75, 76, 77, 78, 79, 80, 81, 82, 83, 84, 85, 86]. However, this is not the case for mm-wave frequencies higher than 100 GHz, where only few examples have been published to our knowledge [32, 46, 87, 88, 89, 90, 91, 92, 93]. Waveguide polarizers are widely used as horn feeds, achieving large 3 dB AR relative bandwidths ($> 20\,\%$) by means of grooves [74], dielectric [75], [76] or metallic septa [77]. However, the tolerances in the fabrication of such structures as well as in the mounting of the septum inside the waveguide are critical in frequencies higher than 100 GHz. CP horn antennas have been as well proposed, based on Antipodal Tapered Slot Antennas (ATSA) [78], [87] or hexagonal waveguides [32], reaching excellent 3 dB AR relative bandwidths ($> 35\,\%$) but gains lower than 18 dB. Higher gain could be reached when using them as reflector feeds, resulting however in a more bulky solution, not suitable for a planar configuration (Fig. 1.3a). Horn arrays have as well been proposed in [79] at 30 GHz or [88] at 140 GHz, reaching gains higher than 30 dB but compromising the 3 dB AR bandwidth ($< 16\,\%$).

Several approaches in the literature make use of LP feeds illuminating linear-to-circular add-on polarization converters. Many of those are based on single- or multi-layer designs with metallic sub-wavelength structures, which present different susceptances for orthogonal linear polarizations [80]–[82], [89]. When the LP field from the source impinges the polarizer with a polarization rotated 45 deg with respect to the polarizing axis, the two incident orthogonal in-phase field components propagate along the polarizer experimenting ideally negligible modifications in the amplitude, but different phase delays, reaching 90 deg and so originating circular polarization in the transmitted wave. Although they achieve large 3 dB AR relative bandwidths ($> 25\,\%$), the use of very thin metal printed structures makes their fabrication impossible in standard PCB technology for frequency bands higher than 100 GHz. The design presented in [89] at 325 GHz is fabricated with complex wafer based silicon micromachining techniques, not suitable for low-cost mass-production. The mentioned fabrication issues are as well present in circularly polarized transmitarrays [83] and reflectarrays [84].

Polarization converters based on dielectric gratings present higher potential to become a cost-effective and, at the same time, high-performing solution at mm- and sub-mm wave frequencies. We have therefore taken this concept as starting point in our work. Their working principle is based on the effective dielectric permittivity anisotropy originated by the asymmetric dielectric gratings, which results in different propagations constants for orthogonal LP field components. The examples proposed in the literature are mostly based on rectangular gratings, either in low relative permittivity for mm-wave applications [85], [86] or in high relative permittivity in optics [90], [91]. Whereas high relative permittivity gratings present lower profile and smaller bandwidth, the opposite properties appear for low relative permittivity polarizers, leading to high aspect ratios which encumber their manufacturing at frequencies higher than 100 GHz. Metal grating polarizers, based on the reflection of orthogonal polarizations with 90 deg of phase delay, are as well used in terahertz bands [92]. However, they present a narrow bandwidth and cannot be integrated into a lens antenna, resulting in a more bulky solution. In [93], a 130 GHz tunable liquid crystal polarizer concept working in reflection was presented, with high insertion loss due to the lossy material (> 4 dB), and with narrowband AR ($< 3\,\%$).

Regarding CP antenna designs with multi-beam capability, not many examples are present in the literature. The mentioned transmitarrays and reflectarrays, apart from the named fabrication issues, present very low aperture efficiencies, hindering a compact solution. In [46], a concept based on CP patches feeding an integrated elliptical Rexolite lens, exhibits a very small 3 dB AR bandwidth (2.6 %). In [76], a homogeneous spherical Teflon lens fed with CP horns is presented, with good AR properties but low aperture efficiency ($< 37\,\%$). In [86], the rectangular dielectric gratings are integrated in an extended hemispherical lens, achieving 29 % 3 dB AR bandwidth and 21 dB of gain at 60 GHz. The side-lobe level is however high (-12 dB) due to the poor illumination of the lens. Besides, despite the low directivity achieved, high dielectric losses are present (> 3 dB) due to the material used in the 3D printing fabrication.

1.5 Research Goals and Methodology

The scope of this work is the development of sub-THz antennas, specifically at G-band ($140 - 220$ GHz) and H-band ($220 - 320$ GHz), meeting the requirements of Beyond 5G and 6G communication scenarios. In particular, this dissertation concentrates in the design of wideband, efficient single integrated lenses, targeting to meet the listed specifications to be embedded in Fly's eye lens arrays. These requirements are to our knowledge not fulfilled in the state-of-the-art.

New wideband, highly-efficient antenna concepts at G-band and H-band, based on lenses with resonant leaky-wave feeds, are presented. The use of low-cost plastic lenses combined with leaky-wave feeds is explored within this dissertation, seeking to enable wideband operation. The limited scanning range in plastic lenses is addressed as well in this thesis, aiming to reach wide steering angles, in order to maximize the number of beams in the proposed planar Fly's eye panels. The efficient and wideband generation of circular polarization is pursued, investigating strategies and geometries compatible with standard fabrication techniques at these high frequencies. Besides, integration strategies for leaky-wave fed lenses are explored, targeting state-of-the-art wideband and efficient transitions to the active front-end.

In order to allow a fast optimization of large lenses in terms of wavelength (up to $18\lambda_0$), new quasi-analytic design methodologies need to be developed. Those are applied in all designs to maximize the lens aperture efficiency over a wideband. New measurement and calibration strategies to characterize lenses at high frequencies are introduced as well in this thesis, enabling the validation of the developed prototypes. The characterization of circular polarized fields, which is specially challenging at these high frequencies, is addressed in this work by developing new measurement approaches.

1.6 Scientific Contribution in this Thesis

In this dissertation, new design methodologies for large lenses are introduced, based on an analysis of the lens in reception combined with spectral techniques, enabling a fast aperture efficiency optimization. Applying these analyses, four lens prototypes in G- and H-band have been developed, making use of leaky-wave feeds. In all those designs, bandwidths larger than 35 % are reached, with aperture efficiencies higher than 70 %, including taper, spill-over and reflection loss. This large bandwidth and high efficiency were reached for the first time using leaky-wave resonant feeds. In order to characterize the developed high-frequency lenses, new measurement and calibration methods are proposed.

The novel designs, theoretical contributions, and new measurement methods developed within this thesis are summarized in the following:

Design contributions

D1 The properties of the resonant LWA as an integrated elliptical lens feed are derived, depending on the contrast between the cavity and lens permittivities, applying the analysis in reception (T1). Design rules are derived for the geometrical parameters of lenses with different ε_r, fed by LWAs. The steering properties of truncated lenses are as well studied, depending on the lens truncation angle and lens permittivity[9].

D2 A wideband plastic lens prototype is designed in the $140 - 220\,\text{GHz}$ bandwidth. The lens aperture efficiency is optimized applying the analysis in reception (T1). For the broadside beam, 80 % aperture efficiency and good impedance matching are achieved over 44 % bandwidth. The maximum dielectric loss is 0.5 dB. In this design, the steering range is limited due to the low permittivity, reaching 4 dB scan loss for the beam steering at 15 deg[10].

D3 A wideband circularly-polarized lens prototype in the $140 - 220\,\text{GHz}$ bandwidth is designed, integrating a wide-band polarizer, based on pyramidal dielectric gratings, inside the elliptical lens. The polarizer is built in several layers, lowering each layer's aspect ratio and enabling its fabrication with standard milling technology at these

---

[9] This contribution is published in [J1] (see List of Publications in page 173).

[10] This contribution is published in [J1].

high frequencies. The antenna is optimized combining the analysis in reception (T1) with the Green's Functions in multilayer stratified and anisotropic media (T2). An AR lower than 3 dB and aperture efficiency higher than 75 % is achieved over 35 % bandwidth, preserving the wideband characteristic and steering range of the linearly-polarized lens design. Thanks to integrating the polarizer inside the lens, the AR bandwidth is preserved as well for steered beams[11].

D4 In order to improve the steering range in low ε_r lenses, we propose to integrate a wedge of dielectric gratings inside the lens, introducing a beam steering in the feed radiation pattern. A prototype reaching ±25 deg beam steering with 3.6 dB scan loss is designed. The scan loss for the lens with integrated grating wedge is optimized applying the analysis in reception (T1) combined with the procedure in T3. FW simulation results show a scan loss reduction of 2 dB with respect to a lens without gratings, providing better radiation pattern symmetry. This improvement is visible over a wide band[12].

D5 An integrated LW feed in the $220 - 320$ GHz bandwidth is implemented on a quartz chip, and excited by a dipole antenna. A truncated elliptical silicon lens is placed on top of the quartz chip. The antenna is connected with the active GaAs MMIC with a new wideband, low-loss air-bride technology. This architecture allows mounting the chips and lens on the top side of the PCB, facilitating the integration. Thanks to the silicon lens, 25 deg of steering can be potentially achieved with this prototype. The performance of the integrated prototype, validated via measurements, shows more than 70 % aperture efficiency over 37 % bandwidth and more than 68 % radiation efficiency, including the interconnect and feeding line loss[13].

Theoretical contributions

T1 An analysis in reception combined with spectral Green's functions for multilayer stratified media is proposed to optimize a LW feed and elliptical lens geometry for the first time. This method enables a fast optimization of the antenna aperture efficiency over a wideband. Besides, this analysis can be applied to calculate the near-field coupling between two lenses, or the energy received back in a lens with a metallic reflector on top. This near-field coupling is relevant to estimate the antenna gain, as proposed later in the measurement contributions (M1 and M2)[14].

---

[11] This contribution is published in [J2].

[12] This contribution is submitted for publication [J4].

[13] This contribution is accepted for publication [J3].

[14] This contribution is published in [J1].

T2 In order to optimize a circularly polarized lens, spectral Green's functions for stratified anisotropic media are combined with the polarizer S-parameters estimated by FW Floquet mode simulations for a single unit cell. Applying this method with the analysis in reception (T1), the lens axial ratio and aperture efficiencies can be efficiently co-optimized[15].

T3 An iterative synthesis procedure for a dielectric gratings wedge is developed, taking into account the wave impinging angle on each coordinate, as well as the lateral wave propagation through the wedge. The gratings are discretized and represented as stacked media with homogenized anisotropic effective permittivity, applying Effective Medium Theory, and enabling a fast synthesis of the wedge geometry[16].

T4 The intrinsic differences between the LW excitation with a dipole and a slot have been studied, for the case where the LW is applied to feed integrated lenses. The radiation patterns are evaluated with spectral Green's functions for stratified media, and the contributions related to each mode are separated by approximating the potential solution in the surrounding of the LW poles[17].

Measurement contributions

M1 A method to estimate the dielectric loss in dielectric lenses, and hence the gain, is proposed by measuring the coupling in the near-field between two identical lenses. An equivalent setup is proposed by measuring the reflection coefficient of the lens under test with a flat metallic reflector on top, at near-field distance. This coupling can be calculated with the analysis in reception mentioned in T1. This method has been applied in the measurements of the prototypes described in D2 and D5[18].

M2 On a similar approach as described in M1, the gain and AR of a circularly polarized lens is estimated by measuring the coupling in the near-field to a linearly-polarized lens, in two orthogonal polarizations (phase-amplitude method). This can be as well calculated applying spectral Green's functions for anisotropic stratified media and the analysis in reception, as proposed in T2. A measurement setup for the fast estimation of the antenna polarization purity is as well introduced by measuring the reflection coefficient of the circularly polarized antenna with a flat metallic reflector on top. These measurement approaches are applied in the characterization of the prototype described in D3. An accurate phase calibration method is proposed to be applied

---

[15] This contribution is published in [J2].

[16] This contribution is submitted for publication [J4].

[17] This contribution is accepted for publication [J3].

[18] This contribution is published in [J1].

for circularly-polarized amplitude-phase near-field characterization at G-band. This calibration approach is applied in the near-field and coupling characterization (M2) of the prototype described in D3, enabling an accurate AR characterization[19].

1.7 Outline of the Thesis

A detailed description of the chapters of this dissertation is given in the following:

Chapter 2 describes the analysis in reception applied for the calculation of the lens aperture efficiency, as well as the coupling in the near-field used for the gain and axial ratio estimation.

Chapter 3 describes the resonant LW feed, which has been used in the designs developed within this thesis. The fundamental differences between the slot and dipole LW excitation are discussed. Design rules are derived for elliptical lenses with LW feeds, which serve as a framework for the lens designs presented in the following chapters. The bandwidth properties of elliptical lenses with different ε_r fed by the resonant LW lens are derived applying the analysis in reception explained in Chapter 2. The steering properties of truncated lenses are as well studied, depending on the lens truncation angle and lens permittivity.

Chapter 4 introduces a wideband linearly polarized plastic lens design at $140-180\,$GHz. A resonant leaky-wave feed based on an air cavity is used, excited by a double-slot. This design has been optimized in terms of aperture efficiency applying the analysis in reception explained in Chapter 2, achieving more than $80\,\%$ aperture efficiency over $44\,\%$ bandwidth.

Chapter 5 presents a wideband circularly polarized plastic lens design at $140-180\,$GHz. A dielectric-gratings polarizer with wide-band transmission coefficients is proposed, which do not degrade the reached bandwidth with respect to the design in Chapter 4. The polarizer geometry enables its fabrication in plastic material at frequencies higher than $100\,$GHz. Appendix A describes the spectral Green's functions for anisotropic media which have been applied together with the analysis in reception in Chapter 2, to optimize the feed-polarizer-lens system.

Chapter 6 introduces a strategy to enhance the field-of-view in lenses with low ε_r (Chapter 4 and Chapter 5) over a wide band, by means of integrated dielectric gratings with modulated height (gratings wedge) inside the elliptical lens. The iterative wedge synthesis procedure is explained in this chapter. Appendix B describes the analysis of the pyramidal gratings as stacked media with homogenized anisotropic effective permittivity, applying

---

[19] This contribution is published in [J2].

Effective Medium Theory and deriving a transmission line model. A design of a plastic elliptical lens with an integrated wedge is presented at $140 - 180\,\mathrm{GHz}$, reaching 25 deg steering.

Chapter 7 presents a wideband linearly-polarized silicon lens with an integrated LW quartz feed at $220 - 320\,\mathrm{GHz}$. A new low-loss, wideband air-bridge technology is used to connect the quartz feed to the GaAs active front-end chip. A dipole is used in this design to excite the LW feed, enabling a differential transition with no need of ground connection. The contrast between the quartz cavity and silicon lens allows for comparable bandwidths than the ones achieved with the designs based on plastic lenses (Chapter 4, Chapter 5 and Chapter 6).

Chapter 8 concludes the dissertation with an overview of the achieved results, and provides an outlook for possible future research paths.

Chapter 2

Analysis in Reception Applied to Lens Antennas

2.1 Introduction

In [94], an analysis in reception for the optimization of reflector feeds was proposed. The power received by the feed can then be estimated using a Thévenin equivalent circuit when the reflector is illuminated with a plane wave. The open circuit voltage at the defined terminals can be expressed as a reaction field integral between the considered problem in reception and an equivalent problem in transmission. The generalization of this procedure to any geometry via the use of the equivalence theorem was described in [95].

In this chapter, a similar methodology is applied to analyse the the truncated elliptical lens geometry, used in the designs in this dissertation. The proposed lens geometry is shown in Fig. 2.1a. The lens consists of an elliptical surface characterized by an eccentricity $e = 1/\sqrt{\varepsilon_r}$, being ε_r the lens dielectric permittivity, and truncated at an angle θ_{edge} defined from the bottom lens focus. The lens truncation helps to achieve high aperture efficiency when compared to more classical full hemispherical lens designs [39]. It is assumed that the ground plane is placed at a distance Δz above the lens focal plane, as it is the case in the resonant LWA feeds used in the lenses developed in this thesis [96].

In this dissertation we propose to apply the analysis in reception to evaluate the lens antenna aperture efficiency, η_{ap}. The aperture efficiency can be in this way expressed as a field reaction between a frequency independent analytical field and the field radiated by the feed in an infinite dielectric medium. This approach in reception allows us to maximize the lens aperture efficiency by optimizing the lens feed geometry, its phase centre position, Δz,

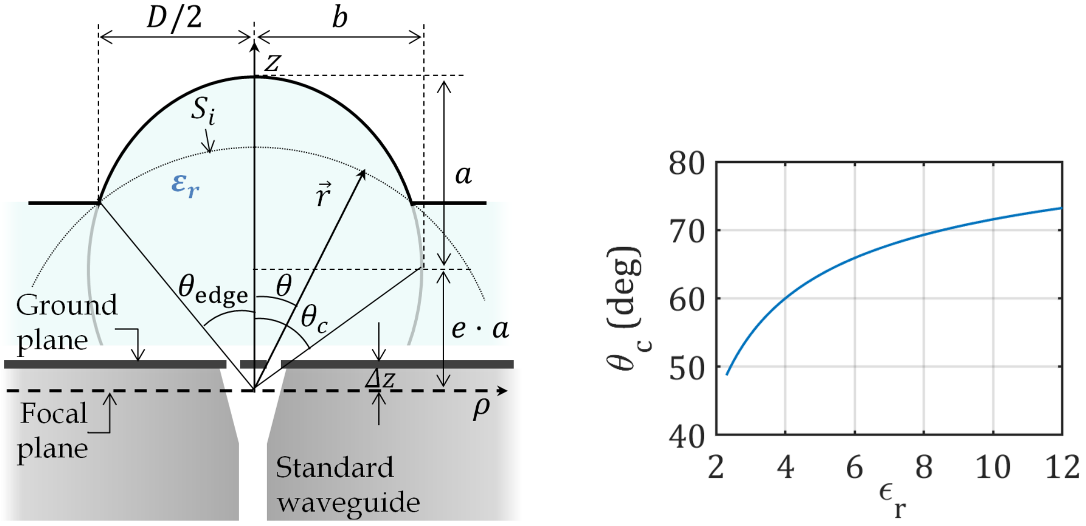

(a) (b)

Figure 2.1: a) The elliptical lens parameters are related as $a^2 = b^2 + (e \cdot a)^2$, and the focal distance is defined as $F = a + e \cdot a$. b) Lens critical angle, θ_c, as shown in (a).

and the lens θ_{edge}, without performing the secondary pattern computation, which would be more time-consuming, as in more standard Physical Optics (PO) approaches [39].

Besides, this methodology is used to calculate the coupling between two lenses in the near-field, or the coupling in reflection of a lens with a flat metallic reflector on top, also at near-field distance. These parameters will be applied in the gain and axial ratio characterization of the prototypes designed within this thesis.

This chapter explains the derivation of the equivalent Thévenin circuit, introduced in [97], as well as the definition of the reaction integrals to calculate the power received in the antenna. Finally, the calculation of the lens aperture efficiency and near-field coupling are discussed.

2.2 Thévenin Equivalent Circuit

An equivalent Thévenin circuit for the problem in Fig. 2.1a can be derived by evaluating the open circuit induced by the incident field onto the antenna terminals, AA′, inside the waveguide, the antenna input impedance Z_a and the load impedance Z_L (Fig. 2.2b). The open circuit field inside a single mode waveguide can be expressed as $\vec{E}_{\text{oc}} = V_{\text{oc}}\vec{e}_0$, where

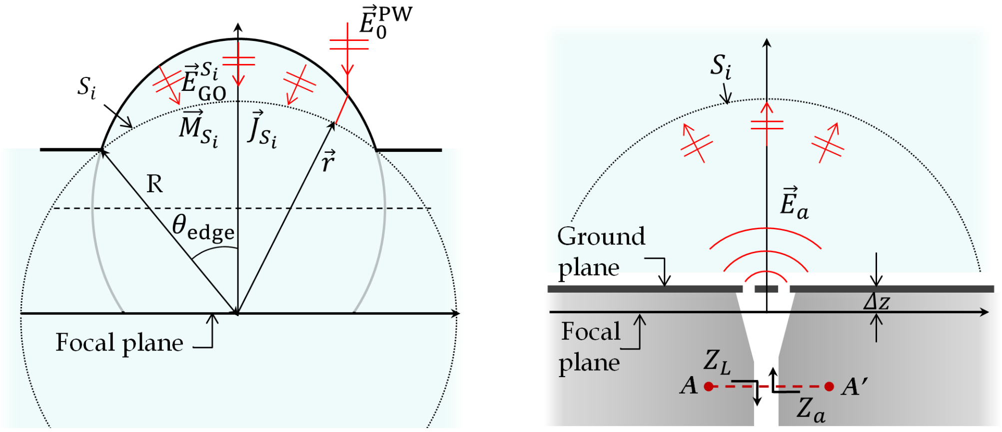

(a) (b)

Figure 2.2: a) Boundary conditions to calculate the incident field, $\vec{E}_{\mathrm{GO}}^{S_i}$, from the ideal plane wave impinging the lens, $\vec{E}_0^{\mathrm{PW}}$, and associated induction currents in S_i, $\vec{M}_{S_i}$ and $\vec{J}_{S_i}$. b) Boundary conditions to calculate the fields radiated in transmission mode, $\vec{E}_a$.

$\vec{e}_0$ is the electric-field associated eigen-vector of the considered wave-guide mode (TE_{10} in this case). The open circuit voltage, V_{oc}, can be evaluated as

$$V_{\mathrm{oc}} = \iint_{S_{\mathrm{AA'}}} \vec{E}_{\mathrm{oc}} \cdot \vec{e}_0 dS \tag{2.1}$$

The power dissipated in a matched load ($Z_a^* = Z_L$) can be calculated as $P_L = |V_{\mathrm{oc}}|^2/(8R_a)$, being $R_a = \mathfrak{Re}(Z_a)$ the antenna radiation resistance.

2.3 Reaction Integral

The value of the open-circuit voltage, V_{oc} in Eq. (2.1), necessary to evaluate the received power, P_L, can be expressed as a reaction integral between the open-circuit field in the antenna in reception and the equivalent currents characterizing the same antenna in transmission. Let us consider the antenna in transmission fed by an electric current, $\vec{J}_{\mathrm{tx}}$, with arbitrary amplitude, I_{tx}. This current is related to the magnetic field by $\vec{J}_{\mathrm{tx}} = -\hat{z} \times \vec{H} = -\hat{z} \times I_{\mathrm{tx}}\vec{h}_0$, where $\vec{H}$ is the magnetic field and $\vec{h}_0$ is the magnetic field associated eigen-vector of the considered wave-guide mode. Since $\vec{e}_0 = \hat{z} \times \vec{h}_0$, the integral in Eq. (2.1) can be then expressed as

$$V_{\mathrm{oc}} I_{\mathrm{tx}} = -\iint_{S_{\mathrm{AA}'}} \vec{E}_{\mathrm{oc}} \cdot \vec{J}_{\mathrm{tx}} dS \tag{2.2}$$

The antenna radiation resistance, R_a, can at the same time be related to the power radiated by the antenna, P_{rad}, excited by the same current amplitude, I_{tx}, as $P_{\mathrm{rad}} = |I_{\mathrm{tx}}|^2 R_a/2$. Thus, P_L can be expressed using the reaction integral in Eq. (2.2) as

$$P_L = \frac{|V_{\mathrm{oc}} I_{\mathrm{tx}}|^2}{16 P_{\mathrm{rad}}} \tag{2.3}$$

Eq. (2.3) was reported in [97]. Note that the actual amplitude of the equivalent current in transmission, I_{tx}, cancels out in this expression. Once we have expressed the received power as a reaction integral between two different problems (currents in transmission and open circuit field in reception) we can use the reciprocity theorem to change this reaction integral to any surface, by interchanging fields and currents between both problems.

2.4 Lens Aperture Efficiency

2.4.1 Coupling to a Plane-Wave

The aperture efficiency for this focusing system can be evaluated dividing the power P_L received by a matched load by the power captured by the lens aperture from the incident plane wave, $P_{\mathrm{in}} = 1/(2\zeta_0)|E_0^{PW}|^2 A_{\mathrm{lens}}$, being ζ_0 the wave impedance in free space, $A_{\mathrm{lens}} = \pi D^2/4$ the projected area for a lens with diameter D (Fig. 2.1a), and E_0^{PW} the plane wave amplitude, as follows

$$\eta_{\mathrm{ap}} = \frac{P_L}{P_{\mathrm{in}}} = \eta_{\mathrm{il}} \eta_{\mathrm{ref}} \tag{2.4}$$

η_{ap} accounts for the illumination efficiency and the reflection efficiency, and is equivalent to the ratio between the lens directivity and that of a uniform circular aperture. The efficiency η_{il} represents the antenna efficiency assuming the use of a perfect matching layer in the whole frequency band. It accounts for taper and spill over efficiencies (power reaching the focal plane but not intercepted by the feed). η_{ref} is the power reflected in the air-lens interface.

The power received by the load, P_L can be expressed as a reaction integral between two terms: 1) the inward incident field inside the lens, $\vec{E}_{\mathrm{GO}}^{S_i}$, caused by the broadside plane wave impinging on the lens, which is frequency independent, and 2) the field radiated in an infinite dielectric medium by the feed antenna considered in transmission, $\vec{E}_a^{\mathrm{GP}}$. The steps to derive the reaction integral are explained in the following.

2.4.2 Reaction Integral

In order to carry out the lens optimization, a convenient surface to perform the reaction integral is the spherical surface S_i, shown in Fig. 2.1a and Fig. 2.2, defined as close as possible to the lens surface, since here all fields involved in the reaction integral can be evaluated analytically. S_i, with radius R, is centred at the lens focus and limited by the lens truncation angle, θ_{edge}.

In the equivalent problem in reception, the field induced by the incident plane wave at the open-circuited antenna terminals, $\vec{E}_{\mathrm{oc}}$, can be evaluated by means of a set of surface equivalent currents $\vec{M}_{S_i}$ and $\vec{J}_{S_i}$ at S_i. In the equivalent problem in transmission, the fields radiated by the feed antenna excited by $\vec{J}_{\mathrm{tx}}$, $[\vec{E}_a, \vec{H}_a]$, should be evaluated at S_i in presence of the lens. We can therefore apply the reciprocity theorem, and reformulate Eq. (2.2) as

$$V_{\mathrm{oc}} I_{\mathrm{tx}} = \iint_{S_i} \left(\vec{H}_a \cdot \vec{M}_{S_i} - \vec{E}_a \cdot \vec{J}_{S_i} \right) dS \tag{2.5}$$

This expression can be further simplified. On one side, the equivalent currents $\vec{M}_{S_i}$ and $\vec{J}_{S_i}$ used in Eq. (2.5) can be approximated using a GO field propagation $[\vec{E}_{\mathrm{GO}}^{S_i}, \vec{H}_{\mathrm{GO}}^{S_i}]$ evaluated in absence of the antenna feed (Fig. 2.2a), as $\vec{M}_{S_i} = \vec{E}_{\mathrm{GO}}^{S_i} \times \hat{n}$ and $\vec{J}_{S_i} = \hat{n} \times \vec{H}_{\mathrm{GO}}^{S_i}$ being $\hat{n} = -\hat{r}$. These fields can be approximated in S_i as a superposition of local plane waves, whose amplitude can be analytically derived applying geometrical optics (GO) [98]. The diffracted fields are neglected, since S_i is taken very close to the lens surface. On the other side, neglecting the impact of the multiple reflections at the lens-air interface, the radiated fields $[\vec{E}_a, \vec{H}_a]$ used in Eq. (2.5) can be approximated as the ones radiated into an infinite dielectric medium (Fig. 2.2b). If the reaction surface S_i is chosen to be in the far-field of the feed antenna, a small displacement in z direction of the feeding antenna with respect to the lens focal plane, Δz, (Fig. 2.2b) can be accounted with a variable phase term intrinsic in $\vec{E}_a$, as follows

$$\vec{E}_a(\theta, \phi) = \vec{E}_a^{\mathrm{GP}}(\theta, \phi) e^{j k_d \Delta z \cos\theta} \tag{2.6}$$

where $\vec{E}_a^{\mathrm{GP}}(\theta, \phi)$ is the far-field of the antenna calculated with phase reference placed at ground plane, and $k_d = \sqrt{\varepsilon_r} k_0$, being k_0 the propagation constant in free space and

ε_r the lens dielectric permittivity. This field can be evaluated resorting to an asymptotic evaluation of the spectral Green's function for stratified media [99].

Since both the GO incident field, $\vec{E}_{\text{GO}}^{S_i}$, and the far-field radiated by the antenna, $\vec{E}_a$, are spherical waves, Eq. (2.5) can be simplified into

$$V_{\text{oc}} I_{\text{tx}} \approx \frac{2}{\zeta_d} \int_0^{2\pi} \int_0^{\theta_{\text{edge}}} \vec{E}_{\text{GO}}^{S_i}(\theta,\phi) \cdot \vec{E}_a^{\text{GP}}(\theta,\phi) e^{jk_d \Delta z \cos\theta} dS \tag{2.7}$$

where ζ_d is the wave impedance in the lens medium. Using Eq. (2.7), Eq. (2.3) and Eq. (2.4), η_{ap} results in

$$\eta_{\text{ap}} \approx \frac{\left| \int\limits_0^{2\pi} \int\limits_0^{\theta_{\text{edge}}} \vec{E}_{\text{GO}}^{S_i}(\theta,\phi) \cdot \vec{E}_a^{\text{GP}}(\theta,\phi) e^{jk\Delta z \cos\theta} R^2 \sin\theta d\theta d\phi \right|^2}{4\zeta_d^2 P_{\text{rad}} P_{\text{in}}} \tag{2.8}$$

where P_{rad}, is the total power radiated by the feed antenna in the infinite dielectric medium, and ζ_d the wave impedance in the lens medium.

2.4.3 Inward Incident Field

The aperture efficiency is maximized when the inward incident field, $\vec{E}_{\text{GO}}^{S_i}$, is a conjugate match (in terms of amplitude, phase and polarization) with the field radiated by the feed antenna, $\vec{E}_a^{\text{GP}}$ Eq. (2.8). Moreover, in order to achieve high reflection efficiency, η_{ref}, only the lens region above the lens critical angle, θ_c, should be illuminated (top half of the ellipse, see Fig. 2.1). θ_c depends exclusively on the dielectric ε_r, and increases for higher values of ε_r as $\theta_c = \tan^{-1}\sqrt{\varepsilon_r - 1}$ (see Fig. 2.1). Thus lenses with lower ε_r need to be illuminated with more directive beams than denser lenses.

Fig. 2.3 shows the amplitude of the incident field, $\vec{E}_{\text{GO}}^{S_i}$, for non-truncated elliptical lenses in materials with $\varepsilon_r = 2.3$ and $\varepsilon_r = 12$, plotted until θ_c. The phase of this field is constant over the chosen sphere S_i, where the integral in Eq. (2.8) is evaluated. The amplitude taper is mainly caused by the Fresnel transmission coefficients in the air-lens interface [100], which decay when approaching θ_c. Here, lenses without matching layer have been considered. If a matching layer was introduced, the corresponding transmission coefficients would result in a more symmetric incident field, $\vec{E}_{\text{GO}}^{S_i}$, w.r.t. the azimuth angle ϕ. A smaller contribution to this taper is originated by the power spreading factor in the refracted rays inside the lens. The lens eccentricity, e, increases for lower ε_r, resulting in a $\vec{E}_{\text{GO}}^{S_i}$ which approaches the cosine pattern. Instead, for high ε_r, where the lens approaches

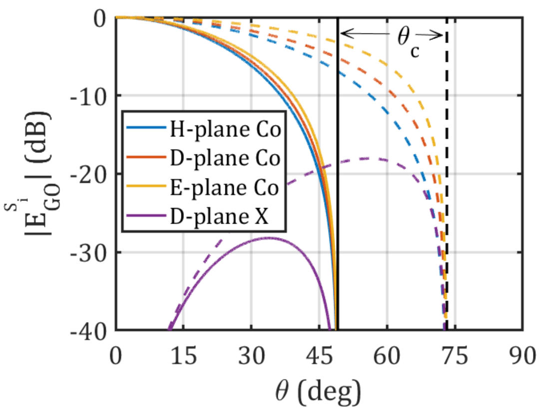

Figure 2.3: Normalized $|\vec{E}_{\text{GO}}^{S_i}|$ vs. lens elevation angle θ over S_i, until lens critical angle. Solid line: $\varepsilon_r = 2.3$, dashed: $\varepsilon_r = 12$. The lens critical angles, θ_c, are marked with black lines. Results shown with no matching layer.

a spherical form, $\vec{E}_{\text{GO}}^{S_i}$ is closer to a squared pattern. In any case, both fields present a very low taper at the edges, differing very much to those corresponding to a parabolic reflector, where $\vec{E}_{\text{GO}}^{S_i}$ presents a secant shape [101].

2.5 Lens Near-field Coupling Efficiency

A good estimation of the lens aperture and radiation efficiency can be obtained by calculating the power coupled between two lenses, or the power coupled back to the lens feed when placing a metallic reflector on top of the lens, in the near-field (Fig. 2.4). Measurements based on these coupling configurations can be as well useful to calculate the axial ratio in a circularly polarized lens, as will be discussed in detail in Chapter 5. In the following, the quasi-analytic calculation of this coupling with the analysis in reception is explained.

2.5.1 Coupling Between Lenses

In order to determine the near-field coupling efficiency η_c between two lenses (Fig. 2.4a), one of them is considered in transmission mode, whereas the other is analysed in reception. In this way, the field impinging the receiving lens corresponds to the field radiated by the lens considered in transmission. η_c is then calculated as the ratio between the power dissipated at the receiving lens load, P_L, and the power radiated by the transmitting lens feed, P_{rad}. Following similar steps than in the previous sections, the term $V_{\text{oc}}I_{\text{tx}}$ can be determined as the reaction integral between the fields transmitted by both lenses, $[\vec{E}^{S_c}_{\mathrm{GO}}, \vec{H}^{S_c}_{\mathrm{GO}}]$, in the plane between the two lenses (S_c in Fig. 2.4a). This analysis neglects the impact of multiple reflections, inside and between both lenses. The fields transmitted at S_c can be approximated using a GO approach, where the rays are assumed to be propagating in z direction with a uniform phase front (valid only when the feed's phase centre is at the ellipse's focus). For such case:

$$\vec{E}^{S_c}_{\mathrm{GO}}(\rho,\phi) = [\tau_{\|}(\rho)(\vec{E}_a(\vec{r})\cdot\hat{\theta})\hat{\rho} + \tau_{\perp}(\rho)(\vec{E}_a(\vec{r})\cdot\hat{\phi})\hat{\phi}]e^{-jk_0 z'} \tag{2.9}$$

being $\vec{r}$ the vector defining the lens surface, z' the distance between the lens surface and the integration plane (Fig. 2.4a), and $\tau_{\|}$ and $\tau_{\perp}$ the parallel and perpendicular Fresnel transmission coefficients as defined in [39], respectively. Since the propagation of the transmitted field from the lens surface up to S_c assumes all transmitted rays to be propagating perpendicularly to S_c, the near-field coupling efficiency, η_c, can be expressed only as a function of the electric fields as

$$\eta_c \approx \frac{P_L}{P_{\mathrm{rad}}} = \frac{\left|\frac{2}{\zeta_0}\int_0^{2\pi}\int_0^{D/2} \vec{E}^{S_c,1}_{\mathrm{GO}}(\rho,\phi)\cdot\vec{E}^{S_c,2}_{\mathrm{GO}}(\rho,\phi)\rho d\rho d\phi\right|^2}{16P_{\mathrm{rad},1}P_{\mathrm{rad},2}} \tag{2.10}$$

being D the lens diameter, and $P_{\mathrm{rad},i}$ with $i = 1, 2$ the power radiated by each lens. If the lenses can be considered to be identical and rotated 180 deg, $\vec{E}^{S_c,2}_{\mathrm{GO}}\cdot\hat{x} = \vec{E}^{S_c,1}_{\mathrm{GO}}\cdot\hat{x}$, $\vec{E}^{S_c,2}_{\mathrm{GO}}\cdot\hat{y} = -\vec{E}^{S_c,1}_{\mathrm{GO}}\cdot\hat{y}$ and $P_{\mathrm{rad},1} = P_{\mathrm{rad},2}$.

Note that in case of evaluating the coupling between identical lenses, the efficiencies contributing to η_c are the spill-over η_{so}, reflection η_{ref}, phase η_{ph}, and radiation efficiency η_{rad}, as

$$\eta_c = (\eta_{\mathrm{so}}\eta_{\mathrm{ref}}\eta_{\mathrm{ph}}\eta_{\mathrm{rad}})^2 = \left(\frac{\eta_{\mathrm{ap}}}{\eta^{\mathrm{amp}}_{\mathrm{tap}}}\eta_{\mathrm{rad}}\right)^2 \tag{2.11}$$

where $\eta^{\mathrm{amp}}_{\mathrm{tap}}$ is the taper efficiency term related only to the field amplitude, which can be calculated as $\eta^{\mathrm{amp}}_{\mathrm{tap}} = \eta_{\mathrm{tap}}/\eta_{\mathrm{ph}}$, being η_{tap} the taper efficiency. $\eta^{\mathrm{amp}}_{\mathrm{tap}}$ is the only term in η_{ap} which does not come in to play in the coupling because, assuming that the lenses are symmetric and equal, the amplitude of their electric fields is also equal.

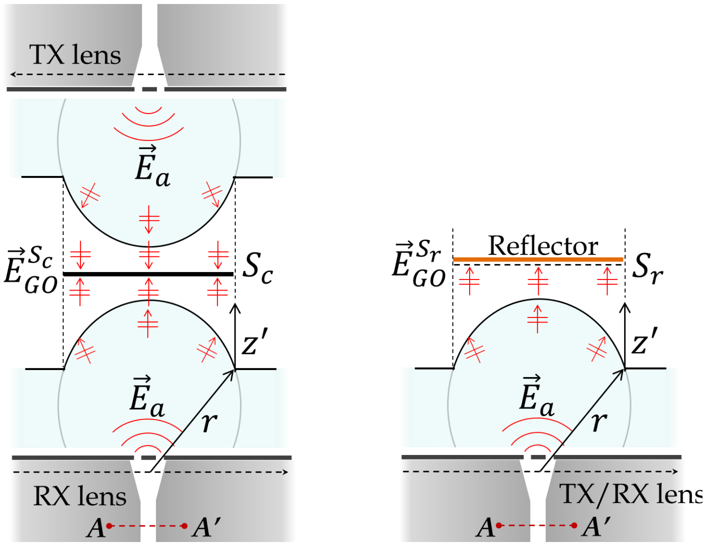

(a) (b)

Figure 2.4: a) Analysis in reception of lens-to-lens near-field coupling. b) Analysis in reception of lens self-coupling.

2.5.2 Coupling in Reflection or Self-Coupling

The analysis in reception has been as well applied in this dissertation to estimate the power coupled back to a lens from a flat metallic reflector placed on top, at near-field distance. This is equivalent to computing the power coupled between mirrored lenses (image theory), as performed in Section 2.5.1. The lens self-coupling can be calculated quasi-analytically using a first order GO ray approach combined with the analysis of the antenna in reception. In order to perform the analysis in reception in this case, the incident field on the lens evaluated in reception is the field radiated by the same lens, reflected back at the metallic plate. The reaction integral to estimate V_{oc} is here calculated on the plane where the reflector is placed, S_r, as shown in Fig. 2.4b. The field radiated by the lens in transmission mode, $\vec{E}_{\mathrm{GO}}^{S_r,\mathrm{Tx}}$, is calculated on S_r using a GO approach, as explained in Section 2.5.1, assuming that the rays are propagating out of the lens only in z-direction. Under this assumption, only field components tangent to the metallic plate are present in $\vec{E}_{\mathrm{GO}}^{S_r,\mathrm{Tx}}$, and therefore the reflected field, used as incident field in the analysis of the antenna in reception, can be approximated as $\vec{E}_{\mathrm{GO}}^{S_r,\mathrm{Rx}} = -\vec{E}_{\mathrm{GO}}^{S_r,\mathrm{Tx}}$. η_c becomes in this case

$$\eta_c \approx \frac{P_L}{P_{\text{rad}}} = \frac{\left| \frac{2}{\zeta_0} \int_0^{2\pi} \int_0^{D/2} \vec{E}_{\text{GO}}^{S_r,\text{Tx}}(\rho,\phi) \cdot \vec{E}_{\text{GO}}^{S_r,\text{Tx}}(\rho,\phi) \rho d\rho d\phi \right|^2}{16 P_{\text{rad}}^2} \tag{2.12}$$

2.6 Conclusion

An analytical design methodology based on an analysis in reception is proposed to optimize truncated elliptical lenses fed with resonant LWAs. With this aim, the aperture efficiency is expressed as a reaction integral between the lens inward spherical GO field and the field radiated by the LW feed inside the lens. Both fields can be evaluated analytically, simplifying the optimization of the lens antenna w.r.t. other full wave or PO techniques. The analysis in reception is as well applied to calculate the near-field coupling in lenses, useful to characterize their radiation efficiency.

Chapter 3

Elliptical Lenses with Resonant Leaky-Wave Feeds

3.1 Introduction

In the lens designs developed within this dissertation, resonant LW feeds have been used, achieving high aperture efficiency over large bandwidths. In this section, the resonant LW and its application as lens feed is explained. The fundamental differences in the radiation pattern inside the lens when exciting the LW with a dipole or a slot are discussed. Finally, the bandwidth properties for lenses with different ε_r excited by LW feeds are analysed.

3.2 Resonant Leaky-Wave Feed

The physical phenomenon exploited in standard resonant LWAs or Fabry-Pérot antennas is the excitation of a pair of nearly degenerated $\mathrm{TM}_1/\mathrm{TE}_1$ LW modes inside a resonant dielectric cavity [24, 102], such as air, placed between a ground plane and a quarter wavelength dielectric substrate with higher ε_r. These modes propagate radially by means of multiple reflections along the cavity, leaking at the same time energy into the infinite air medium. This effect increases the antenna effective area and thus its directivity but at the cost of bandwidth [99]. In [24] it was shown that an enhancement in the bandwidth × directivity performance of a resonant LWA can be achieved by using a resonant cavity with $\varepsilon_r = \varepsilon_r^c$ below a semi-infinite dense medium (the lens), with $\varepsilon_r = \varepsilon_r^l > \varepsilon_r^c$, as displayed in Fig. 3.1. In this configuration, the LW modes present propagation phase constants $\beta_{\mathrm{LW}} = k_0\sqrt{\varepsilon_r^l}\sin\theta_{\mathrm{LW}} < k_0\sqrt{\varepsilon_r^c}$, which implies that LW modes radiate always in

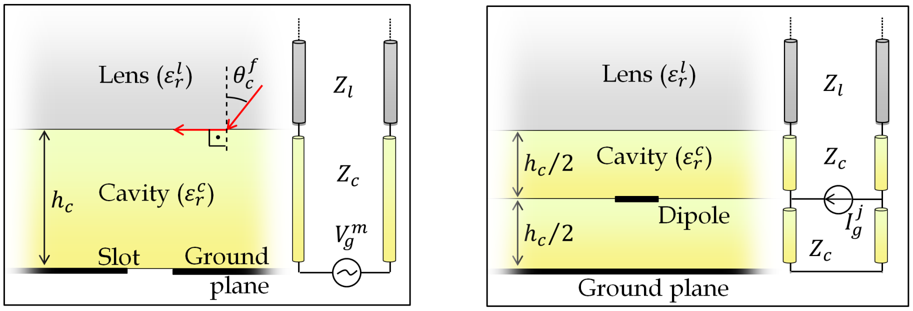

(a) (b)

Figure 3.1: Stratification geometry and equivalent transmission line models for the resonant LW radiating in a semi-infinite medium, fed by a) slot and b) dipole. The red arrows represent incident and transmitted rays in the lens-cavity interface in reception. The lens medium is considered semi-infinite. Metal is drawn in black.

elevation angles smaller than the feed critical angle (θ_c^f in Fig. 3.1a), and very low power is radiated at $\theta > \sin^{-1}(\sqrt{\varepsilon_r^c/\varepsilon_r^l})$. Furthermore, in order to achieve a broadband design, it is convenient to choose a low permittivity contrast between the cavity and lens media, $\sqrt{\varepsilon_r^l/\varepsilon_r^c} \sim 1.5 - 1.8$ to reduce the frequency dispersion of the $\mathrm{TM}_1/\mathrm{TE}_1$ LW modes [100].

The cavity allows also the propagation of a TM_0 LW mode [99], conceptually associated with the TEM mode of the parallel plate waveguide, which radiates close to the critical angle. Moreover, the TM_0 presents less frequency dispersion than the main $\mathrm{TM}_1/\mathrm{TE}_1$ LW modes.

Fig. 3.2 shows the dispersion diagrams for the TM_1, TE_1 and TM_0 modes, for different cavity and lens materials (designated as [cavity material]-[lens material]), derived from the equivalent transmission line models shown in Fig. 3.1. Note that the dispersion equations are defined by the stratification, regardless of which type of source is used to excite the LW (dipole or slot). The curves are displayed within 40 % relative bandwidth. In all cases, a cavity with $h_c = \lambda_d/2$ has been considered, where λ_d is the wavelength in the cavity. The real part of the propagation constant k_d corresponds to β_{LW}, which is related to the LW mode radiation angle as explained before. The imaginary part of the propagation constant corresponds to the attenuation constant, α_{LW}, which defines the LW effective area, as the LW modes power attenuates inside the cavity as $e^{-2\alpha\rho}$ [103, 104]. The dispersion diagrams corresponding to air-HDPE (High Density Polyethylene) and to quartz-silicon stratifications (Fig. 3.2a and Fig. 3.2b) present very similar and low dispersive characteristics, as their contrast ratios $\sqrt{\varepsilon_r^l/\varepsilon_r^c}$ are low and comparable (1.52 and 1.77 respectively). This results in wideband LW feeds, with stable radiation patterns over frequency. The air-

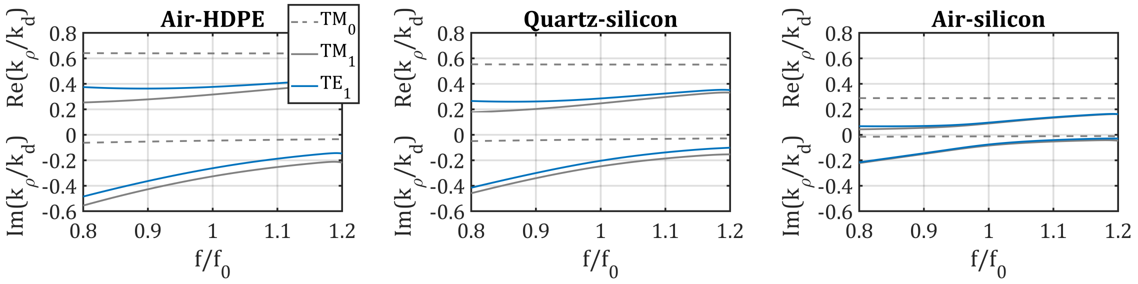

(a) (b) (c)

Figure 3.2: Solutions of the TE and TM dispersion equations for the stratification in Fig. 3.1. a) Air cavity and HDPE lens ($\varepsilon_r^l = 2.3$). b) Quartz cavity ($\varepsilon_r^c = 3.8$) and silicon lens ($\varepsilon_r^l = 11.9$). c) Air cavity and silicon lens.

HDPE stratification has been used in the designs presented in Chapter 4, Chapter 5 and Chapter 6; the quartz-silicon stratification is applied in the design presented in Chapter 7. In Fig. 3.2c, the dispersion diagram of an air-silicon stratification is displayed [24], where a higher dispersion in both real and imaginary part of the propagation constant can be appreciated. This leads therefore to more narrow band feed radiation patterns inside the lens.

3.3 Leaky-Wave Source: Dipole vs. Slot

As previously discussed, resonant LW stratifications with a cavity between a ground plane and a denser semi-infinite media support the propagation of three LW modes: TM_0, TM_1 and TE_1 [102]. TM_1 and TE_1 modes radiate near broadside, and contribute therefore to increase the feed antenna directivity, enhancing the lens illumination efficiency, as explained in Section 3.2. The TM_0 mode, on the contrary, radiates at larger angles, being likely to degrade the lens aperture efficiency, η_{ap}. However, depending of the type of excitation used in the LW cavity, even though the dispersion diagram remains unchanged, these modes are excited with different intensity, impacting in the radiation pattern in different magnitude. Slot excitations have been usually applied in the literature to excite LW lens feeds (Fig. 3.1a), fed by squared wave-guides [24]. This is also the case in the designs presented in Chapter 4, Chapter 5 and Chapter 6. For a slot excitation, the effect of the TM_0 mode is very visible in the radiation pattern, and it is either cancelled [24, 105] or attenuated (Chapter 4, Chapter 5 and Chapter 6) by means of a double-slot, in order to keep high lens η_{ap}, as it will be discussed in Section 3.4. The suppression of the TM_0

LW mode has been as well discussed in the literature for Fabry-Pérot antennas radiating in free-space. In [106], the use of an inductive grid was proposed to reduce the spurious lobes caused by the TM_0 leaky-mode, which is transformed into a surface-wave mode. In the antenna presented in Chapter 7, a dipole is instead proposed to excite the LW lens feed, enabling the use of a simple quartz chip stratification, without ground connections between layers and not supporting the propagation of surface waves. It will be shown that, in contrast with the slot source, the dipole does not excite the TM_0 LW mode, which effect is therefore not visible in the radiation pattern.

The electric field radiated in the far-field by the quartz-silicon stratification (Fig. 3.2b), excited by an elementary magnetic source (infinitesimal slot, Fig. 3.1a), or by an elementary electric source (infinitesimal dipole, Fig. 3.1b), are compared in Fig. 3.3 for the E- and H-planes. The radiation patterns are calculated with multi-layer Spectral Green's Functions (SGF) at the center frequency for $h_c = \lambda_d/2$ where λ_d is the wavelength in the cavity. As the radiation in the H-plane for both sources is comparable (Fig. 3.3b), we will focus in the differences present in the E-plane. The contribution of both TM_0 and TM_1 leaky modes in the far-field E-plane has been separated for both excitations with the approach described in [99], which approximates the voltages and currents in the surrounding of the LW poles ($E^{\text{app}}_{\text{TM}_0}$, $E^{\text{app}}_{\text{TM}_1}$ in Fig. 3.3a). The sum of the calculated contributions results in an approximated shape of the far-field, which has been as well plotted in Fig. 3.3a ($E^{\text{app}}_{\text{TM}_0+\text{TM}_1}$ has been normalized to broadside for the sake of comparison).

The contribution of the TM_1 and TE_1 modes is similar for both excitations, and represents well the fields in the surrounding of these poles. However, as it is clear in Fig. 3.3a, the contribution of the TM_0 mode, which is strong and well represented by the approximation in case of the slot, is completely cancelled in case of the dipole. The dipole introduces a zero in the E-plane, inherent to the electric elementary source. In the case where the LW is radiating into a lens, $\varepsilon_r^{\text{FF}} = \varepsilon_r^l > \varepsilon_r^c$, being $\varepsilon_r^{\text{FF}}$ the permittivity of the medium where the far-field is calculated, the dipole zero is found in the critical angle between the cavity and lens, $\theta_{zero} = \sin^{-1}\sqrt{\varepsilon_r^c/\varepsilon_r^l}$, [107]. Both the zero and TM_0 radiation angles are constant and almost coincident over a wide band, in which the contribution of the TM_0 to the far-field is consequently cancelled, as shown in Fig. 3.3a on the left. As the approximation in [99] only represents the poles and not the zeros, the contribution of the TM_0 to the far-field is not that well represented in case of the dipole. This property has been used to improve the radiation pattern symmetry in Fabry-Pérot antennas radiating in free-space [108]. In this case, the zero is located at $\theta_{\text{zero}} = 90$ deg, as the dipole is embedded in a cavity with $\varepsilon_r^c > \varepsilon_r^{\text{FF}}$.

Being the TM_0 mode contribution intrinsically cancelled by the dipole excitation, the geometry of this source does not need to be specifically optimized to shape the radiation

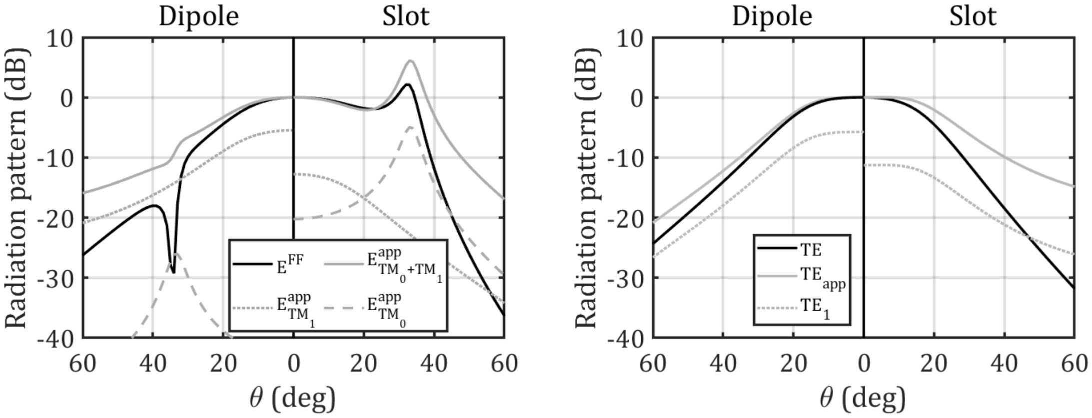

(a) (b)

Figure 3.3: a) E-plane radiation patterns normalized to broadside at the center frequency for the stratification shown in Fig. 3.1, considering a quartz cavity and silicon lens. Left: elementary electric source. Right: elementary magnetic source. Black: asymthotic calculation of the far-field with multi-layer Green's Funtion. Grey: far-field calculated with the potentials and currents approximated in the surrounding of the LW pole. b) Same for H-plane.

pattern. In this way, in contrast to the double slot, a single dipole may be used to excite the LW, and the dipole geometry may be optimized by only aiming for a wideband impedance matching. However, it is worth mentioning that the dipole feeding line may introduce undesired cross-polar radiation, which is very low in case of a double-slot excited by a waveguide.

3.4 Design Rules and Bandwidth Properties of the Resonant Leaky-Wave Lens

The analysis in reception described in Section 2.4 has been applied to quantify the LWA bandwidth in terms of pattern stability, or equivalently illumination efficiency, η_{il}, when acting as an integrated elliptical lens feed. The analysis has been applied to LW feeds excited by a double-slot, considering an air cavity. ε_r refers therefore in this section to the lens permittivity. The LWA radiation patterns have been calculated with an asymptotic evaluation of the SGF in stratified media [99], convoluted with the following approximation of the double slot iris current:

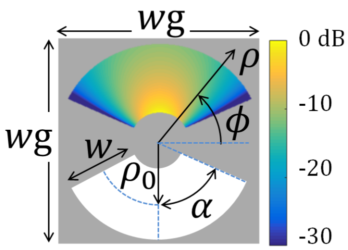

Figure 3.4: Main parameters of the double-slot iris and approximated magnetic current distribution from Eq. (3.1).

$$\vec{m}_s(\rho,\phi) \approx \frac{1}{\rho}\cos\left[\frac{\pi}{2\alpha}\left(\phi \pm \frac{\pi}{2}\right)\right] \mathrm{rect}\left(\phi \pm \frac{\pi}{2}, 2\alpha\right) \mathrm{rect}\left(\rho - \frac{\rho_0}{2}, w\right)\hat{x} \tag{3.1}$$

which is displayed in Fig. 3.4. This approach allows us to optimize the feed-lens system aperture efficiency exclusively applying analytical tools. The first step to estimate the bandwidth properties for different ε_r is to calculate the optimum lens, LW cavity, and double-slot parameters which give the maximum η_{il}. Next, the relative bandwidth for these optima cases is determined in terms of the lens η_{il} over frequency.

When evaluating the resonant LWA as lens feed, the main effect on the bandwidth is associated to the dispersion of the main LW modes [100]. However the maximum η_{il} depends highly on the spurious TM_0 contribution [106] (see slot radiation pattern in Fig. 3.3a). The TM_0 radiation angle, θ_{TM_0}, can be located inside or outside the truncated lens rim, θ_{edge} (Fig. 2.1a). The distance ρ_0 in the double slot (Fig. 3.4) becomes a key parameter to optimize this maximum efficiency, as it is directly related to the position of a null in the Fourier Transform (FT) of the double slot equivalent currents, which can be used to further shape the pattern. The double slot, circular to achieve rotationally symmetric patterns, has been considered for this analysis with an angle α of 60 deg and width w of $0.15\lambda_0$, being those realistic values to achieve a good matching to the waveguide.

In order to clarify the impact of the TM_0 radiation and double slot distance in η_{il}, we analyse more deeply two extreme cases: $\varepsilon_r = 2.3$ and $\varepsilon_r = 12$. This ε_r-range is representative for most common lens materials found in the literature. Fig. 3.5 shows the far-field patterns of the resonant LWA, $\vec{E}_a$, for these two cases with maximum η_{il}, with an elementary excitation (left) and with the double slot iris (right). For $\varepsilon_r = 12$, the feed critical angle (Fig. 2.1a) arrives at 16.7 deg, and so the radiation is confined in smaller angles. The lens should be therefore intuitively truncated at $\theta_{\mathrm{edge}} \leq 17$ deg, in order to obtain high η_{tap}. $\vec{E}^{S_i}_{\mathrm{GO}}$ presents an almost constant amplitude distribution at $\mathrm{S_i}$ for $\theta < 17$ deg (Fig. 2.3 and Fig. 3.5a), and therefore a squared primary pattern is required

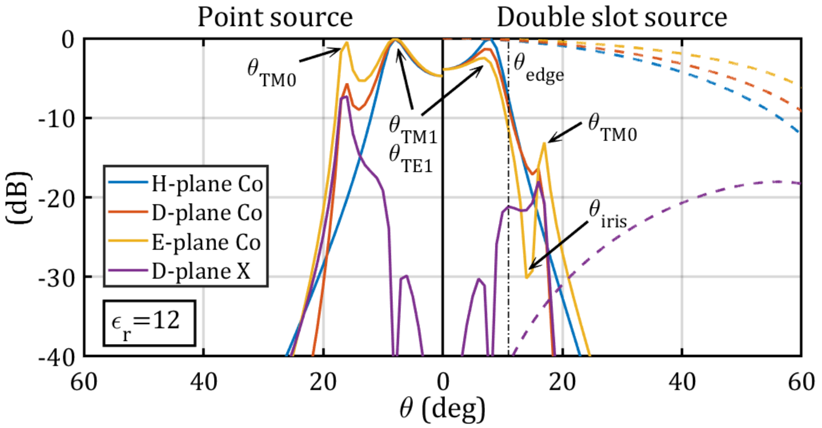

(a)

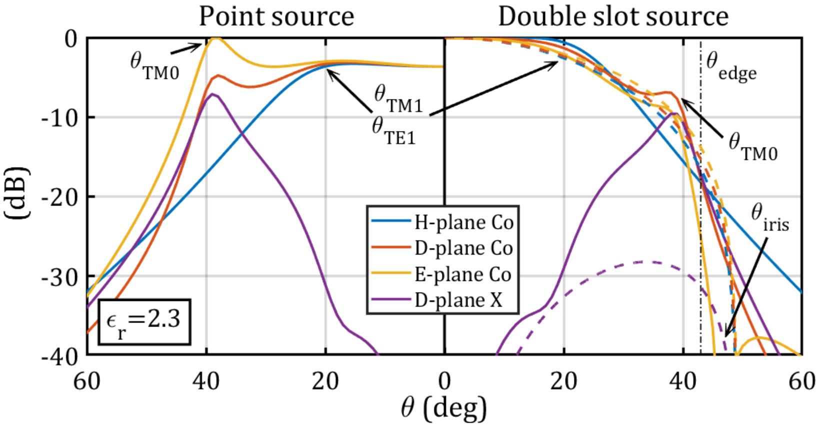

(b)

Figure 3.5: LWA far-field patterns, $\vec{E}_a$, for (a) $\varepsilon_r = 12$ and (b) $\varepsilon_r = 2.3$. The left side corresponds to an x-polarized elementary magnetic source; whereas the right side corresponds to a double slot iris source. The shown patterns are symmetric w.r.t. θ. For reference, $\vec{E}_{\mathrm{GO}}^{S_i}$ at S_i (dashed lines) is also plotted. All curves have been evaluated using the geometric parameters (cavity, double-slot, and lens) which maximize η_{il}. Those are $h_c = 0.56\lambda_0$, $\rho_0 = 0.5\lambda_0$, and $\theta_{\mathrm{edge}} = 43\,\mathrm{deg}$ for $\varepsilon_r = 2.3$, and $h_c = 0.57\lambda_0$, $\rho_0 = 0.64\lambda_0$, and $\theta_{\mathrm{edge}} = 11\,\mathrm{deg}$ for $\varepsilon_r = 12$.

in this case to reach a high η_{tap}. A cavity larger than the standard half wavelength, $h_c = 0.57\lambda_0$, contributes to the desired pattern form, as in this case the $\mathrm{TM}_1/\mathrm{TE}_1$ modes radiate towards larger angles (Fig. 3.5a on the left). The TM_0 mode radiation would reduce in this case the η_{tap}, and so the best compromise is to keep it out of the lens rim ($\theta_{\mathrm{edge}} < \theta_{\mathrm{TM}_0}$), as in [24, 109]. In this way the double slot should ideally fully cancel the effect of the TM_0, in order to reduce the spill-over, by introducing a null in the FT of its equivalent currents at $\theta_{\mathrm{iris}} \approx \theta_{\mathrm{TM}_0}$), as shown in Fig. 3.5a on the right. The optimum double-slot ρ_0 is in this case around $0.64\lambda_0$. This is the best compromise between cancelling completely the TM_0 (higher η_{so}), and keeping the pattern inside the lens rim as squared as possible (higher η_{tap}). The resulting optimum pattern for $\varepsilon_r = 12$ is shown in Fig. 3.5a on the right, where θ_{iris} can be clearly distinguished in the E-plane at $\theta = 15\,\mathrm{deg}$, lowering the TM_0 radiation peak in around $15\,\mathrm{dB}$. The position of θ_{iris} has in case of high ε_r materials similar dispersion characteristic as the LWA $\mathrm{TM}_1/\mathrm{TE}_1$ modes, and therefore does not impact significantly in the relative bandwidth of the lens η_{il}.

For $\varepsilon_r = 2.3$, the feed critical angle arrives at $41\,\mathrm{deg}$. The lens should be therefore truncated at $\theta_{\mathrm{edge}} \leq 41\,\mathrm{deg}$, in order to obtain a high η_{tap}. For this angular range, $\vec{E}_{\mathrm{GO}}^{S_i}$ presents an amplitude distribution at S_i which approaches a cosine with approximately $-15\,\mathrm{dB}$ taper (Fig. 2.3 and Fig. 3.5b). In this case it is more convenient to choose $\theta_{\mathrm{edge}} > \theta_{\mathrm{TM}_0}$, and only taper down the θ_{TM_0} contribution by means of the double-slot. The optimum ρ_0 is therefore $0.5\lambda_0$, for which the null in the FT of the double slot equivalent currents $\theta_{\mathrm{iris}} > \theta_{\mathrm{TM}_0}$ (Fig. 3.5b right). The resulting LWA pattern (Fig. 3.5b right) presents in this way a very similar taper to the incident field, reaching high η_{tap}. Here, θ_{iris} appears at around $45\,\mathrm{deg}$, and the TM_0 radiation is tapered down to $-8\,\mathrm{dB}$, being the high correlation between $\vec{E}_a$ and $\vec{E}_{\mathrm{GO}}^{S_i}$ evident. For low ε_r, the position for θ_{iris}, related to the optimum ρ_0, appears in the region beyond the feed critical angle, where very low power is radiated by the LWA. In this way, the narrow-band characteristic of the slot θ_{iris} has a small impact in the primary patterns. Their dispersion with frequency is consequently mostly related to the LW modes dispersion, which are very broadband for low ε_r. This fact provides these lenses with a very large η_{il} bandwidth.

Fig. 3.6 shows the maximum reachable lens η_{il} as a function of the double-slot distance, ρ_0 for several lens ε_r. We can observe that the overall maximum η_{il} appears for $\varepsilon_r = 2.3$ thanks to the very good field correlation explained previously, achieved by keeping the TM_0 inside the lens rim and a double slot distance of $\rho_0 \approx 0.5\lambda_0$. As we move to higher ε_r, a second relative maximum appears for $\rho_0 \approx 0.6\lambda_0$, becoming an absolute maximum for $\varepsilon_r = 12$, associated to the TM_0 radiating outside the lens rim. As the ε_r increases from 2.3 to 4, the taper in $\vec{E}_{\mathrm{GO}}^{S_i}$ decreases, demanding a lower value of amplitude taper to keep a high η_{tap}. The inflexion point between these two design strategies appears at around $\varepsilon_r = 6$, where a good compromise between η_{tap} and η_{so} can be reached for both $\theta_{\mathrm{edge}} < \theta_{\mathrm{TM}_0}$ (optimum $\rho_0 = 0.6$) and $\theta_{\mathrm{edge}} > \theta_{\mathrm{TM}_0}$ (optimum $\rho_0 = 0.4$). If a wideband design is pursued, the design with $\theta_{\mathrm{edge}} > \theta_{\mathrm{TM}_0}$ and $\rho_0 = 0.4$ should be chosen, for which the frequency dispersion of θ_{iris} has a lower impact in the η_{il} bandwidth.

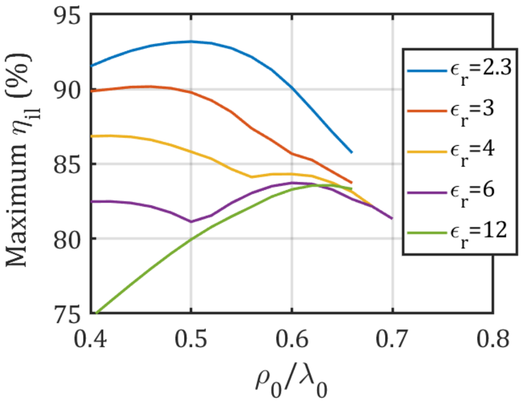

Figure 3.6: Maximum η_{il} versus double-slot distance ρ_0 normalized to λ_0. The rest of geometric parameters are optimized for every distance.

Following this design approach, the LWA lens antenna has been optimized as function of ε_r. The obtained parameters are summarized in Fig. 3.7a and Fig. 3.7b. The relative frequency bandwidth for which $\eta_{\mathrm{il}} > 80\%$ is achieved, as well as the maximum reached η_{il} are reported in Fig. 3.7c. Relative bandwidths higher than 40% can be achieved with $\varepsilon_r < 4$, whereas 15% bandwidth is reached with this criterion in case of using a lens with $\varepsilon_r \approx 12$.

3.5 Elliptical Lens Scanning Properties

By displacing the feed along the lens focal plane, a certain beam steering angle is achieved in the lens far-field (Fig. 3.8). The lens steering capability defines the maximum number of beams, overlapping at -3 dB, which can be generated with a single Fly's eye lens planar panel (Fig. 1.3). In this section, the maximum steering angle is derived with respect to the lens ε_r and truncation angle θ_{edge}, taking into account ideal optimized cosine feeds and for LWA feeds with air cavities.

In [110], the steering properties of extended hemispherical lenses were studied for double slot feeds. Here, instead, we investigate the steering capabilities of truncated elliptical lenses as function of the lens truncation angle, θ_{edge} (Fig. 2.1a), using ideal feeds adapted to each θ_{edge}. The scope is to derive the optimum θ_{edge} that maximizes the steering angle (accepting 3 dB scan loss) and aperture efficiencies by making a trade-off between the different loss mechanisms involved (taper, reflection, spill over). The considered lens materials are the same as in Section 3.4 (ε_r between 2 and 12). Finally, the steering capabilities for

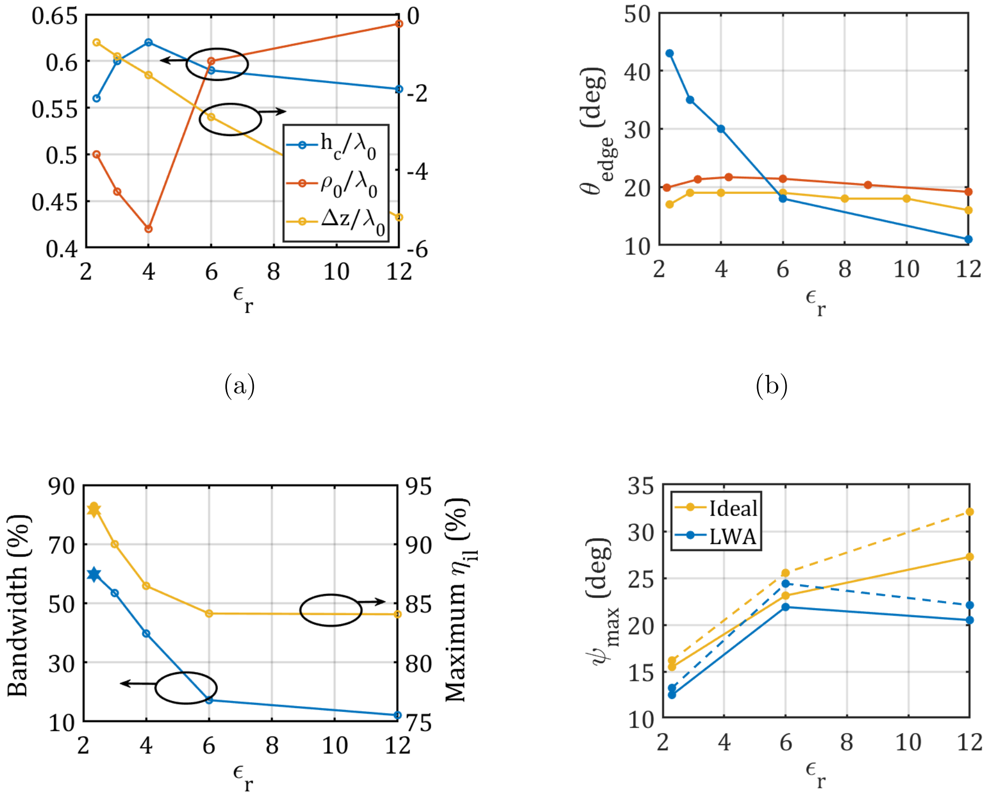

(a) (b)

(c) (d)

Figure 3.7: a) Optimum cavity height, double-slot distance, and LWA phase centre position for maximum η_{il} versus lens ε_r. b) Comparison of optimum lens edge truncation angles, θ_{edge}, as defined in Fig. 2.1 where the blue line is θ_{edge} for maximum η_{il} with the LWA as feed, the red line is θ_{edge} for maximum steering angle applying the geometric criteria and the yellow line is θ_{edge} for maximum steering angle with a cosine primary pattern estimated by PO. c) LWA relative bandwidth for lens $\eta_{\text{il}} > 80\%$ as a function of ε_r, for a design with the maximum η_{il}, and maximum η_{il} achieved vs. ε_r. The stars represent the simulated values reached with the HDPE prototype. d) Maximum steering achieved for truncated elliptical lenses. The colors correspond to the same cases evaluated in (b). Dashed line: E-plane. Solid line: H-plane.

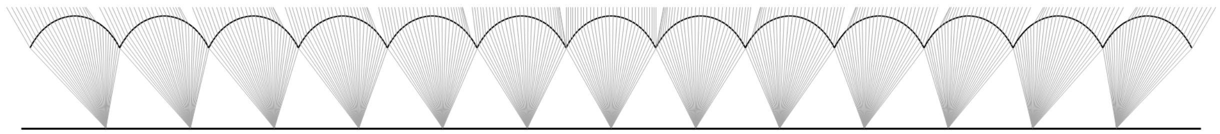

Figure 3.8: Fly's eye row example. 2D representation including ray tracing in transmission, showing the multi-beam capability for the lens row array with different feed displacements. 15 lenses are shown, covering a FoV of ±25 deg.

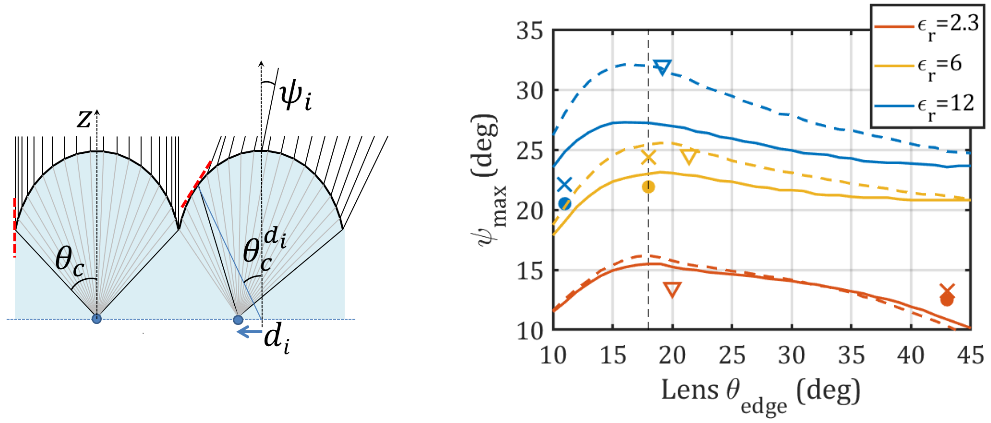

(a) (b)

Figure 3.9: a) Elliptical lens ray tracing example for on- and off-focus feeds, where the lens critical angles are shown for both cases: θ_c and $\theta_c^{d_i}$, respectively. b) Maximum steering angle $\psi_{\max}$ achieved in free space vs. lens θ_{edge}. Triangles: geometric approximation. Solid line: PO analysis with cosine illumination for H-plane steering; dashed line: same for E-plane. Circles: PO analysis with LW feed optimized for broadside for H-plane steering; crosses: same for E-plane.

lenses with different ε_r fed by the LWA are evaluated, completing the performance analysis for such feeds.

The beam steering angle ψ_i, achieved in the lens far-field for a certain feed displacement d_i along the lens focal plane (Fig. 3.9a), can be geometrically approximated by tracing the central ray as $\psi_i = \sin^{-1}(\sqrt{\varepsilon_r} d_i/F)$, being F the lens focal distance (Fig. 2.1a). It is clear that lower ε_r materials need higher feed displacements to achieve a certain steering angle. In order to avoid significant spill-over loss, the maximum feed displacement should be $d_{\max} = D/4$. On one hand, for a certain d_i, larger θ_{edge} (smaller F/D) leads to higher steering angles, ψ_i. On the other hand, θ_c appears at a smaller angle when the lens is illuminated off-focus ($\theta_c^{d_i}$ in Fig. 3.9a), and so the lens should be truncated at θ_{edge} smaller than $\theta_c^{d_i}$ (larger F/D) to avoid significant reflection loss. In this way, the optimum θ_{edge} which maximizes the steering angle should fulfil $\theta_{\text{edge}} = \theta_c^{d_{\max}}$, for $d_{\max} = D/4$. This criterion is independent from the lens D. Fig. 3.7b shows the optimum θ_{edge} for different ε_r, obtained with the described approach. For lenses with ε_r between 2 and 12, the optimum θ_{edge} stays around 20 deg in all cases. Fig. 3.9b shows the corresponding $\psi_{\max}$ calculated geometrically (triangles).

The calculated optimum θ_{edge} has been validated with a single-plane Physical Optics tool, deriving $\psi_{\max}$ for which η_{ap} decays 3 dB w.r.t. broadside. Lenses with $D = 18\lambda_0$ are considered, illuminated by cosine patterns with $-11\,\mathrm{dB}$ taper at the lens edge. The results are shown in Fig. 3.9b, being the optimum θ_{edge} near 18 deg for all studied cases, validating the geometric approximation (Fig. 3.7b). The maximum steering angles obtained here for $\varepsilon_r = 12$ are 27 deg and 30 deg for the H- and E-planes respectively, for truncated lenses with $\theta_{\mathrm{edge}} = 18$ deg and adapted ideal cosine feeds. These steering angles are higher than in the case of the silicon lenses considered in [110], where a maximum scan angle of 20 deg was reported for $\theta_{\mathrm{edge}} \approx 60$ deg (off-scale in Fig. 3.9b).

When using the LWA as a feed, and considering an air cavity, in the case of lenses with $\varepsilon_r = 6$ the optimum lens θ_{edge} values which maximize η_{il} at broadside and $\psi_{\max}$ for steering are nearly coincident (see Fig. 3.7b). In case of $\varepsilon_r < 6$, the optimum θ_{edge} for the lens broadside beam is larger than the optimum θ_{edge} for maximum steering. The maximum number of beams is limited, in this case, by the increment in the reflection loss due to the larger total-reflection area. In case of $\varepsilon_r > 6$, the optimum θ_{edge} for the broadside beam is smaller than the optimum θ_{edge} for steering. Here, the maximum steering angle reached is limited by the increasing spill-over loss, due to the larger F/D ratio.

The achieved steering angles using the LWA as feed, optimized for broadside, (patterns shown in Fig. 3.5 on the right) have been calculated using an ad-hoc PO tool considering the whole lens surface [111]. The results are plotted in Fig. 3.9b for $\varepsilon_r = 2.3$, 6, and 12 (circles). The PO simulated results for the LWA have been validated via FW simulations (no multiple reflections) carried out with the software EMPIRE-XPU [112]. The results are in good agreement, as shown in Fig. 3.10. Fig. 3.7d shows the maximum steering angle $\psi_{\max}$ for different ε_r achieved with θ_{edge} optimized to maximize η_{il} at broadside or to maximize the steering range. These curves confirm that the LWA feed optimized for maximum η_{ap} at broadside with a lens with $\varepsilon_r = 6$ is the nearest to the optimum steering range.

Coming back to the scope of this analysis, the number of beams achieved per plane considering LW feeds and lenses with $D = 18\lambda_0$ can be evaluated from the maximum steering angle and the $-3\,\mathrm{dB}$ beamwidth (~ 3.5 deg) as follows: 7 beams ($\psi_{\max} = 12.5$ deg) with $\varepsilon_r = 2.3$, 12 beams ($\psi_{\max} = 21.5$ deg) with $\varepsilon_r = 6$ and 11 beams ($\psi_{\max} = 19.75$ deg) with $\varepsilon_r = 12$. In a two dimensional circular planar array of lenses, those steering angles correspond to 40, 110 and 90 beams for $\varepsilon_r = 2.3$, 6, and 12, respectively. Nevertheless, this number of beams has been derived considering LWA feeds with air cavities. For a certain lens ε_r, the optimum θ_{edge} to maximize the η_{ap} at broadside increases if the LW feed cavity is filled with material with $\varepsilon_r > 1$, as the optimum θ_{edge} approaches the feed critical angle, θ_c^f, after which very low power is radiated. In order to maximize the number of beams for a certain lens ε_r, the LW feed θ_c^f may be chosen so that the optimum θ_{edge} to maximize η_{ap} at broadside is coincident with the optimum θ_{edge} estimated with ideal cosine feeds for

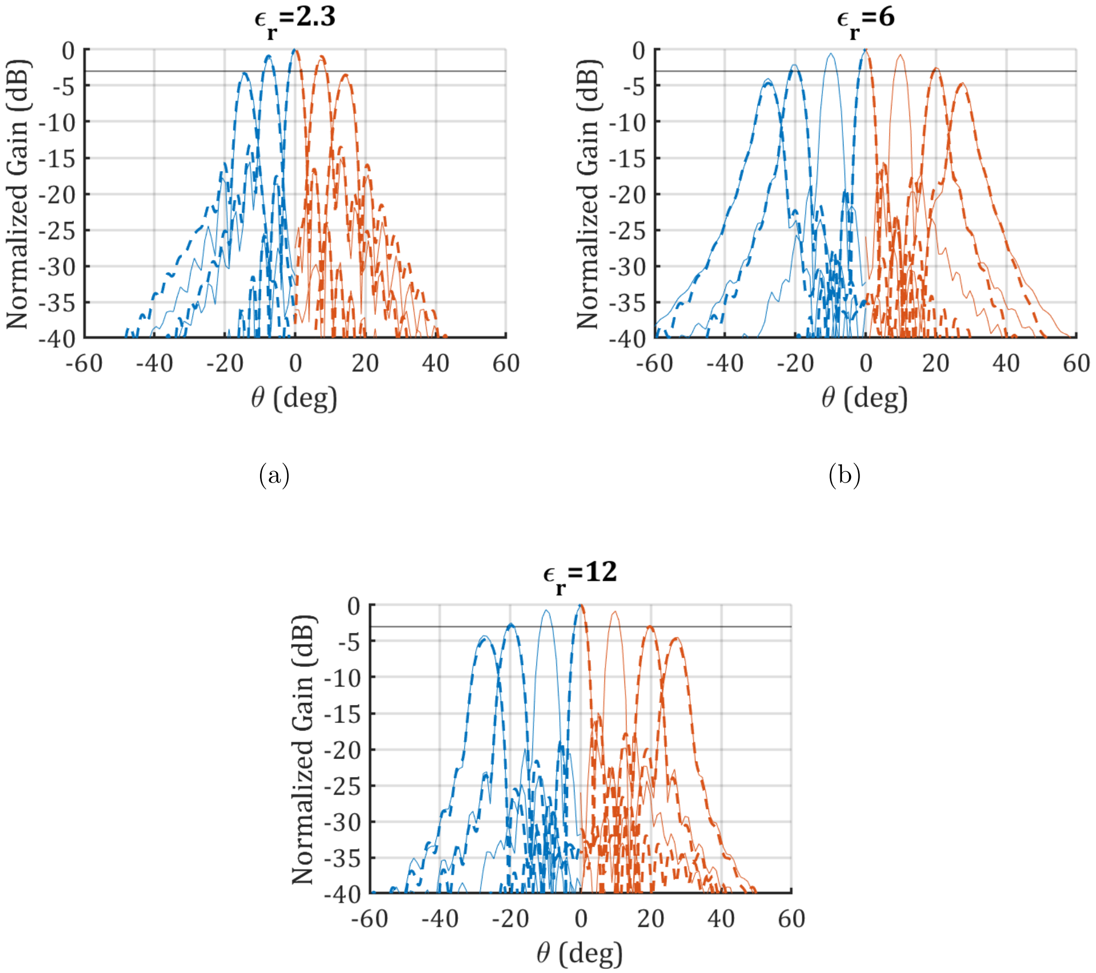

(a)

(b)

(c)

Figure 3.10: Lens far-field magnitude simulated with a 2D PO (solid line) and FW without multiple reflections (dashed line), normalized to the broadside beam. The lenses ($D = 18\lambda_0$) and LWA feeds are optimized for maximum η_{il} at broadside (Section 3.4) a) $\varepsilon_r = 2.3$ for $d = 0$, $0.08D$ and $0.16D$, b) $\varepsilon_r = 6$ for $d = 0$, $0.11D$, $0.23D$ and $0.30D$, c) $\varepsilon_r = 12$ for $d = 0$, $0.13D$, $0.25D$ and $0.34D$. Blue: E-plane. Red: H-plane. A black line marks the 3 dB scan loss criterion for maximum steering angle.

a maximum steering range. In the multi-fixed beam scenarios introduced in Section 1.3.1, each beam corresponds to one feed antenna and transceiver.

Chapter 4

Wideband Linearly-Polarized Plastic Lens

In this chapter, a LW fed HDPE lens antenna working at G-band which can be useful for future XG communications is presented. The proposed lens design enables the generation of up to 40 beams, with gains higher than 30 dB. The lens aperture efficiency has been optimized with the analysis in reception introduced in Chapter 2, validating the results via full wave simulations. The reached aperture efficiency for the broadside beam is higher than 80% over a 44% relative bandwidth. Measurement results for a fabricated prototype show excellent agreement with the simulated performance.

4.1 Introduction

In this work, we extend the LWA feed architecture presented in [43] for low ε_r lens materials. The goal is to achieve high gain with high aperture efficiency over a wide band, required for future wireless communication applications. The analysis in reception in Chapter 2 is applied to maximize the aperture efficiency of the lens antenna. We report an experimental validation of the performances derived in Chapter 3 for a low-density elliptical lens made with HDPE, leading to state-of-the-art results. Simulation results show an aperture efficiency higher than 80%, matching better than -10dB and dielectric losses lower than 0.5dB over 44% relative bandwidth. The measurements are in very good agreement with the simulations.

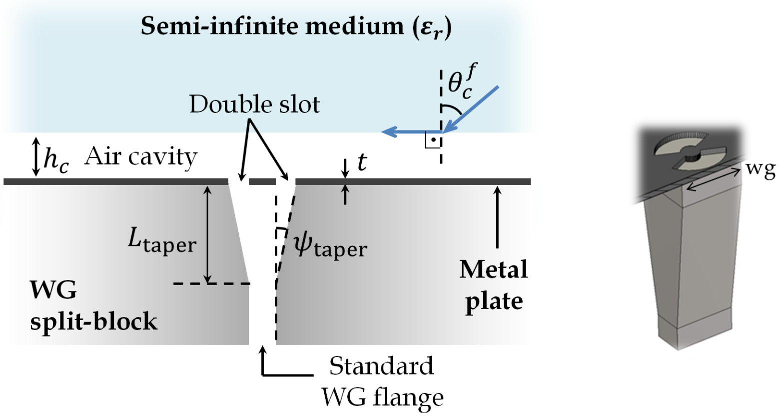

(a) (b)

Figure 4.1: a) LWA geometry. A semi-infinite dielectric-slab is located at a distance h_c $\lambda_0/2$ to create a Fabry-Pérot cavity illuminated by a tapered waveguide ($L_{\text{taper}} = 4.4\lambda_0$, $\psi_{\text{taper}} = 3\,\text{deg}$). θ_c^f is the feed critical angle, after which the cavity presents total reflection. The blue arrows represent incident and transmitted rays in the dielectric-air interface in reception. b) 3D view of the tapered waveguide and double slot in the ground plane.

The chapter is organized as follows: Section 4.2 explains the design of a prototype with low ε_r material; Section 4.3 describes the prototype far-field and gain characterization; and Section 4.5 provides some concluding remarks.

4.2 Broadband Prototype Design

The lens antenna geometry is displayed in Fig. 2.1, and the proposed feed geometry is shown in detail in Fig. 4.1. It consists of a resonant (Fabry-Pérot) air cavity between a ground plane and a lens dielectric medium. The excitation of the air cavity is performed by means of a squared waveguide TE_{01} mode illuminating a double-slot opening in the ground plane (Fig. 4.1), similar approach to the one used in [109, 113]. The double-slot is used to further shape the pattern in order to maximize the aperture efficiency, as explained in Section 3.4. It plays as well an important role in the impedance matching to the waveguide. The squared waveguide size is fixed to $\text{wg} = 0.8\lambda_0$ at the central frequency (Fig. 4.1b, Fig. 3.4), to avoid the excitation of higher order modes. The waveguide is then tapered to a standard flange as shown in Fig. 4.1. This tapering has minor impact on the radiation and impedance matching.

From the analyses in previous sections, the optimal lens material for this application seems to be $\varepsilon_r = 2.3$, since it presents the highest efficiency and widest bandwidth. In addition, due to the lens low ε_r there is no need to use a matching layer which, added to the lower material costs, results in the most cost-effective approach. The only compromise made when choosing a lens with low ε_r is the reduction in the potential field of view achievable with a Fly's eye array (Fig. 1.3), as discussed in Section 3.5. In this section, a design covering the whole G-band ($140 - 220\,\mathrm{GHz}$) is presented, using a HDPE lens ($\varepsilon_r = 2.3$, $\tan\delta = 0.00033$). This material has been chosen after characterizing several plastics in the frequency range of interest, as it presented the lowest measured dielectric loss. As a final step, a fine tuning of the double-slot geometry is carried out in order to achieve a good impedance matching to the waveguide over the whole frequency band. The analytic primary patterns calculation and lens aperture efficiency computation are validated for the final optimized model by means of full-wave (FW) simulations.

4.2.1 Feed Radiation Patterns and Impedance Matching

The final geometrical values of the optimized double-slot iris are set to $\alpha = 65.5$ deg, $\rho_0 = 0.54\lambda_0$, $w = 0.3\lambda_0$ (Fig. 3.4), $t = 0.08\lambda_0$, and the cavity $h_c = 0.56\lambda_0$ (Fig. 4.1), being λ_0 the wave-length at $f_0 = 180\,\mathrm{GHz}$. The slots have been widened to reach a good impedance matching; ρ_0 has been slightly increased with respect to the optimum. The impact of those small variations in the η_{il} is negligible, as will be shown in Section 4.2.2. Fig. 4.2 shows the radiation pattern magnitude and phase at f_0, while Fig. 4.3a shows the maximum directivity over frequency. In both cases there is a good agreement between analytically computed results (with SGF) and FW simulations, validating the approximate expression of the iris current distribution introduced in Eq. (3.1) (Chapter 3). The maximum variation of the LWA feed directivity over the entire frequency band is around 1 dB. Fig. 4.3b shows FW simulation results for the LWA reflection coefficient radiating in a semi-infinite medium and inside the lens (including multiple reflections [114]), in both cases lower than $-10\,\mathrm{dB}$ over the whole operational bandwidth. The FW simulation model is done with perfect electric conductor boundary conditions and includes a taper from a standard flange to a squared waveguide (Fig. 4.1).

4.2.2 Lens Radiation Performance

In this section the simulation results for a G-band HDPE lens with $D = 3\,\mathrm{cm}$ are shown. After tuning the double-slot geometry in order to achieve a good matching over the whole bandwidth, a fine retuning of the feed Δz and lens θ_{edge} has been performed to maximize

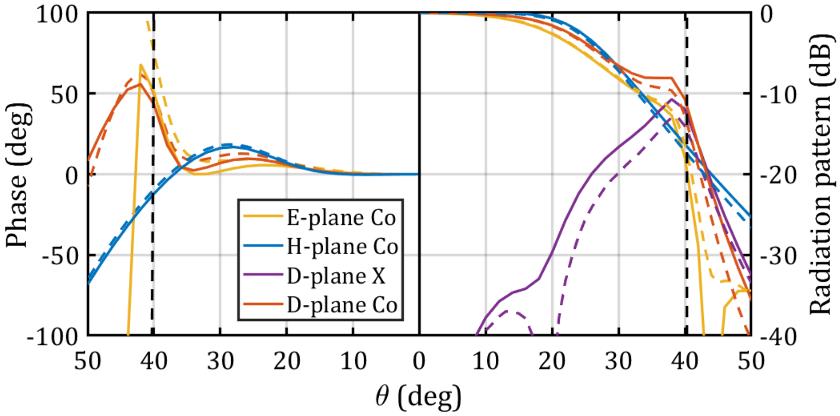

Figure 4.2: Feed radiation patterns and phase for the fabricated prototype at f_0. Solid lines: SGF solution, dashed lines: FW simulations. The prototype lens $\theta_{\rm edge}$ is marked with dashed black lines.

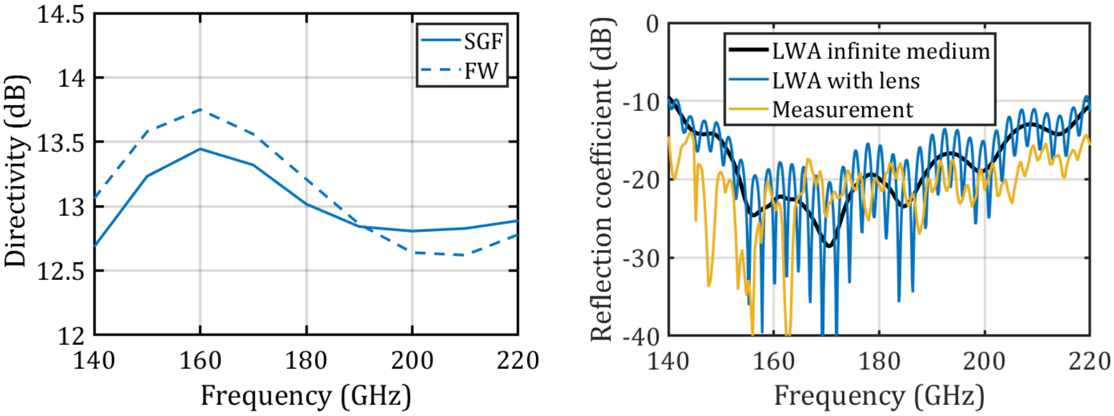

(a)

(b)

Figure 4.3: a) Maximum directivity over frequency for the prototype LWA radiating in the semi-infinite medium and b) LWA reflection coefficient.

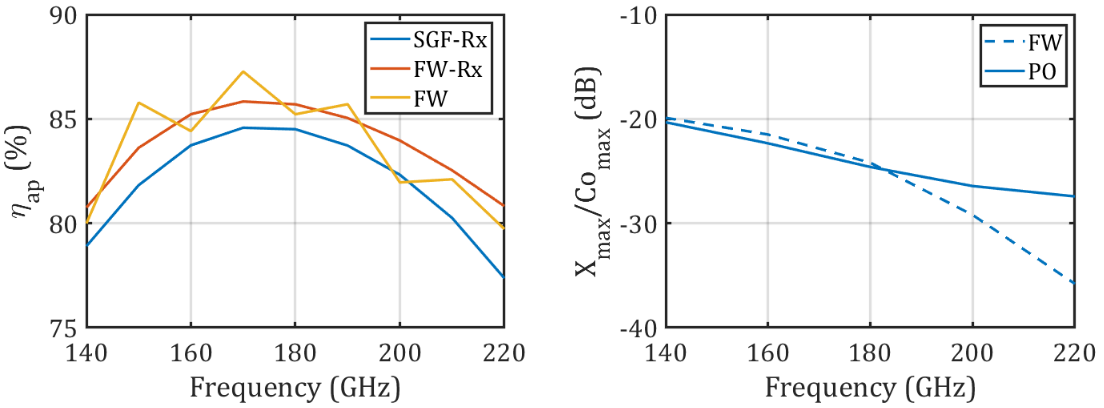

(a) (b)

Figure 4.4: a) Lens η_{ap} over frequency obtained with the reception analysis using: the SGF primary pattern with the double-slot current approximation (SGF-Rx); and the FW simulated primary pattern (FW-Rx), together with a FW simulation with multiple reflections, which introduce a small ripple. b) Ratio between the maximum lens cross-polar and co-polar levels evaluated over all azimuth and elevation angles with PO and FW simulations including multiple reflections.

the lens η_{ap}, applying the reception analysis described in Section 2.4. The final value for θ_{edge} is 40.3 deg, slightly smaller than the optimum displayed in Section 3.4 due to the higher taper in the E-plane, caused by the larger ρ_0. The final Δz has been set to –0.95 mm.

The resulting η_{ap} is displayed in Fig. 4.4a. Here, the analysis in reception has been applied on one side to the primary patterns calculated with the SGF convoluted with the current approximation for the double slot (SGF-Rx), and on the other side to the FW primary patterns (FW-Rx), validating Eq. (3.1) over the whole frequency band. FW simulations, including multiple reflections, have been performed in order to validate the lens η_{ap} optimization and analysis in reception (Fig. 4.4a), and to obtain the lens far-field radiation patterns (Fig. 4.5). The good agreement between the η_{ap} obtained through the analysis in reception and FW simulation proofs that the multiple reflections and possible spill-over do not have any significant impact on the lens antenna far-fields, due to the lens low ε_r. FW simulation results show η_{ap} higher than 80 % in the whole frequency band. The achieved bandwidth is also marked in Fig. 3.7c, reaching almost identic values w.r.t. the ideal case.

In Fig. 4.5, the normalized simulated co-polarized patterns for the broadside and two steered beams are shown. The highest lens cross-polar level at broadside normalized to the

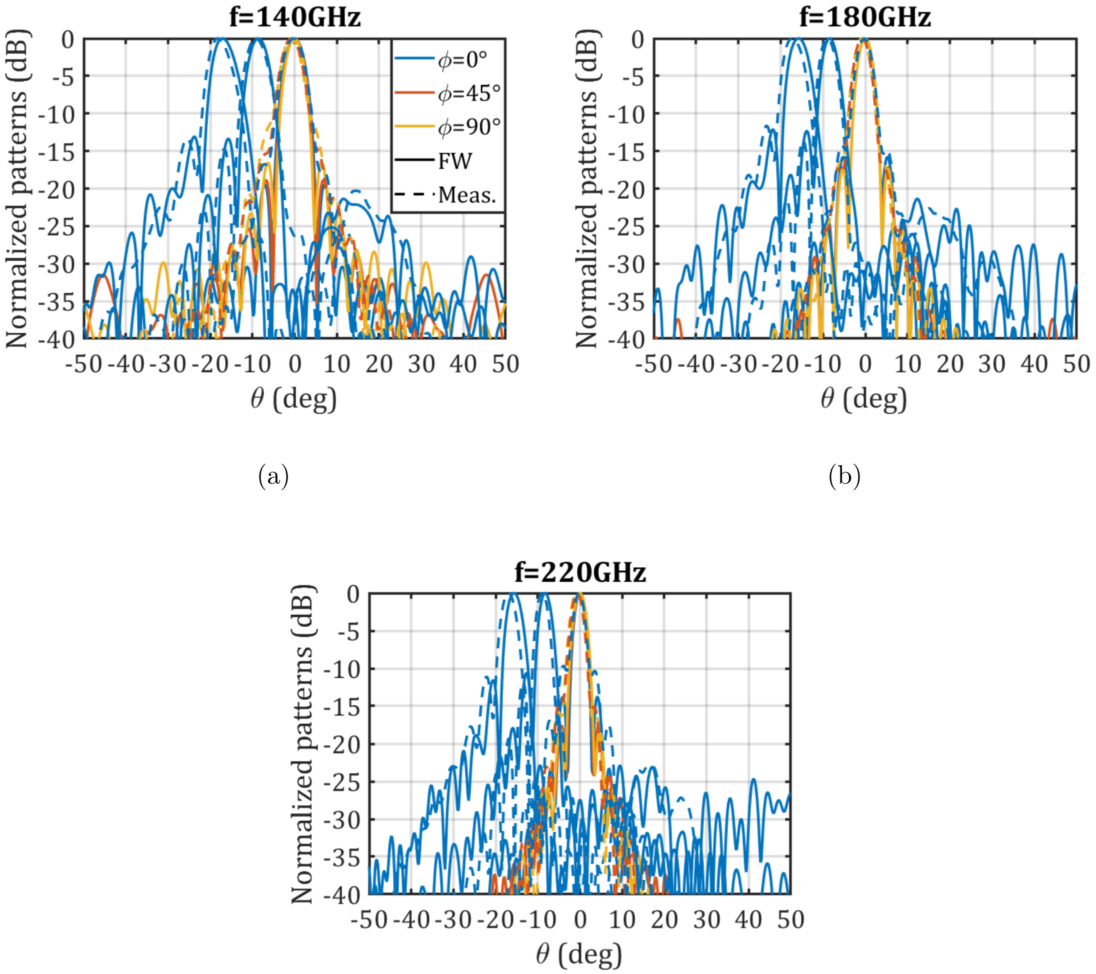

(a)

(b)

(c)

Figure 4.5: FW simulated (multiple reflections) and measured lens patterns normalized to each beam maximum. The steered beams correspond to feed displacements, $d = 2.8\,\text{mm}$ and $5.6\,\text{mm}$, for which the measured steering angle is respectively 9.25 deg and 18.25 deg for 140 GHz, 9 deg and 17.25 deg for 180 GHz, and 9 deg and 17 deg for 140 GHz.

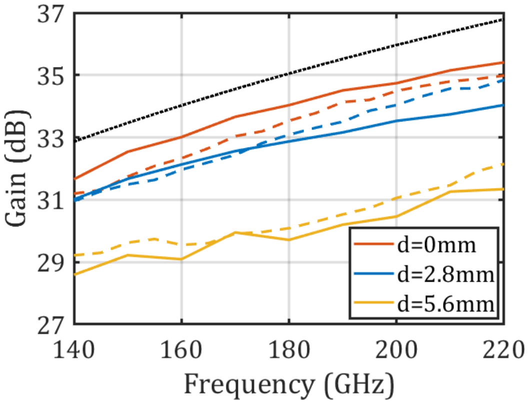

Figure 4.6: Gain over frequency for broadside and steered beams. Solid line: FW simulations. Dashed line: measurements. These results do not include loss in the waveguide. The dotted black curve represents the maximum directivity for a circular aperture with $D = 3\,\text{cm}$.

co-polar maximum directivity is –20 dB at 140 GHz, as shown in Fig. 4.4b. The co-polar gain over frequency is displayed in Fig. 4.6, corresponding the lens η_{ap} drop in the steered beams to the expected from the analysis in Section 3.5. The maximum estimated loss in the lens dielectric material is about 0.5 dB at the highest frequency (220 GHz). The ohmic losses in the 1 cm long waveguide are between 0.8 and 1.5 dB in the whole frequency band, for an estimated effective metal conductivity of $3.6e5\,\text{S/m}$. The conductor loss could be significantly reduced in an integrated design by shortening the waveguide and improving its roughness. Table 4.1 summarizes the estimated loss contributions for a single lens.

4.3 Prototype Fabrication and Measurements

Two identical prototypes have been fabricated consisting of three main parts: an aluminium split-block waveguide tapered to a standard waveguide flange, a thin metal plate containing the double-slot iris and the HDPE lens with the air cavity. Fig. 4.7 shows a picture of one of the fabricated prototypes. The waveguide and lens have been manufactured

Frequency (GHz)	Waveguide (dB)	Mismatch (dB)	Dielectric (dB)
140	1.5	0.3	0.2
180	0.9	0.0	0.3
220	0.9	0.1	0.4

Table 4.1: Losses in the fabricated prototype.

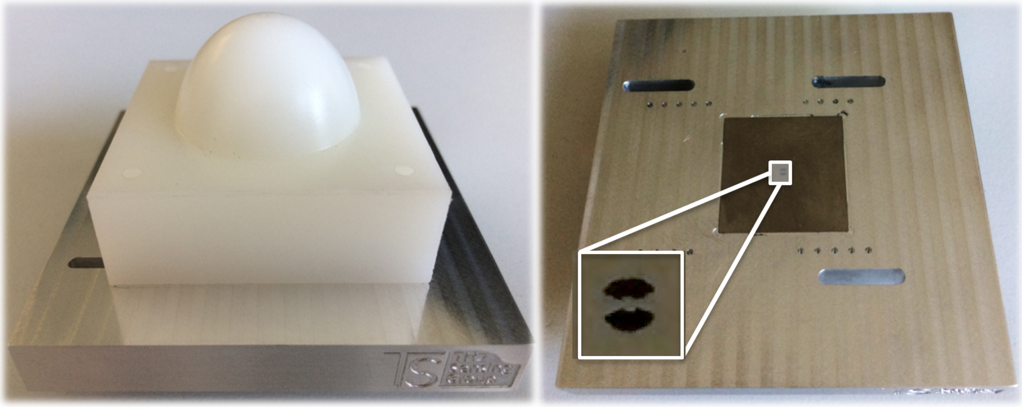

Figure 4.7: Lens antenna prototype. The left hand side shows the HDPE lens antenna, placed on the ground plane. On the right hand side, the double slot iris is shown. Positioning holes have been drilled at a constant distance of 1.4 mm, to displace the lens and measure the broadside and steered beams.

through standard milling techniques, whereas the double-iris slot has been realised by means of laser-cut. The measured reflection coefficient is in accordance with the simulations (Fig. 4.3b). The matching level shift between lossless FW simulations and measurements is related to the waveguide ohmic losses.

4.3.1 Lens-to-Lens Coupling

Applying the analysis in reception explained in the Chapter 2, the near-field coupling between two identical lenses, η_c, facing each other is calculated (Fig. 2.4a). This parameter, which can be measured with a simple setup, can be used to determine the single antenna radiation efficiency and therefore gain, and to evaluate the accuracy of the estimated losses in the lens and waveguide. Fig. 4.8b shows the lens-to-lens near-field coupling calculated semi-analytically, FW simulated and measured, with the reference plane at the standard waveguide flanges. In the semi-analytic calculation, mismatch loss, losses in the waveguide and dielectric loss in the lens (Table 4.1) have been added to the near-field coupling calculated with the analysis in reception. The transmission between two lenses in the FW simulation does not include multiple reflections. The difference between both curves shows the limitation in the accuracy of the GO approach used for the analytic calculation of the transmitted fields after the lens, $\vec{E}_{\mathrm{GO}}^{\mathrm{S_c}}$. In the lens-to-lens near-field coupling measurements, time gating has been applied to eliminate the contribution of multiple reflections in the lens-air interfaces. The time gating has been performed applying a window which considers only the first transmitted rays from one lens to the other as shown in Fig. 4.8a. All additional transmitted rays coming from multiple reflections inside the lenses or between

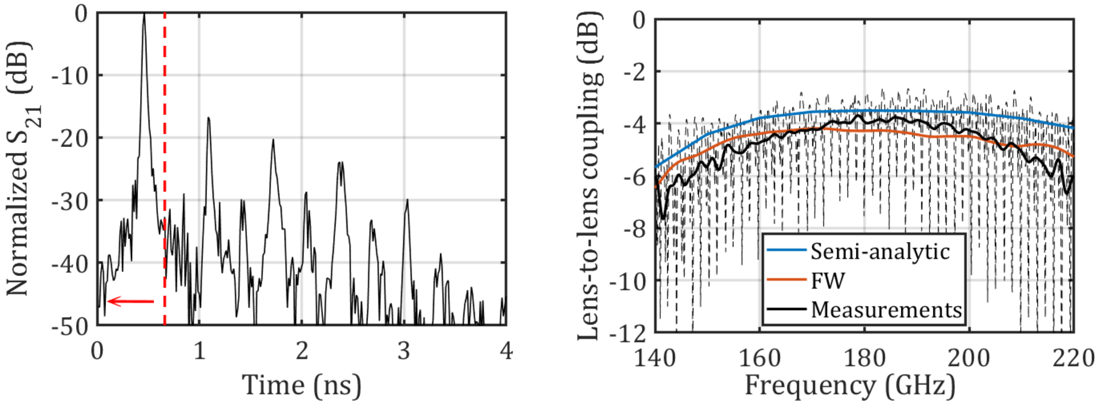

(a) (b)

Figure 4.8: a) Time-domain representation of the measured transmission between the two lenses. The red dashed line marks the applied time window. b) Lens-to-lens near-field coupling efficiency where the black lines correspond to the measured S_{21}: raw (dashed) and time-gated (solid).

them are filtered in time domain, and finally the resulting frequency response is calculated from the filtered results (plotted in Fig. 4.8b). Time-gated measurement results show an agreement with FW simulations within ± 1 dB in the worst case, which is translated in ± 0.5 dB for a single lens. This error includes the impact of tolerances in the measurement, fabrication and material properties estimation, such as lens $\tan\delta$ and waveguide effective conductivity.

A FW simulation has been performed eliminating the lenses and keeping the LWA feeds in the same position (the space between feeds is filled with dielectric). The transmission reached in this configuration is lower than -30 dB in the whole band. This value corresponds to the directivity of both feeds (13 ± 0.5 dB) minus the propagation loss in the dielectric material (55 to 59 dB). The presence of the lenses improves the coupling in 27–31 dB.

4.3.2 Near-Field Characterization

In order to obtain the lens far-field patterns, near-field measurements have been performed over a planar surface on top of the lens antenna, by means of a probe (i.e. an open-ended WR5 waveguide) placed on an automatic positioner. A squared surface with an area of $50 \times 50\,\mathrm{mm}^2$ has been measured at 8.5 cm distance from the lens, taking sampling points at 680 μm distance (half wavelength at the highest frequency, 220 GHz). Around the measuring probe, a hollow metallic diffraction cone has been installed, in order to minimize the effect of multiple reflections between the lens and measurement equipment. A standard probe correction has been then applied to remove the small impact of the probe in the measured far-field, with the same approach presented in [115]. Fig. 4.5 compares the measured and FW simulated lens far-field patterns for broadside and two steered beams, showing an excellent agreement over the whole frequency band. This can be also seen in the results for the maximum gain over frequency, shown in Fig. 4.6. The maximum antenna gain at broadside has been estimated by adding the dielectric loss, validated with the lens-to-lens coupling method, to the directivity calculated from the near-field measurements. In case of the steered beams, the gain has been evaluated by normalizing the radiation intensity with the power radiated and dielectric loss of the broadside case. The losses in the waveguide are not included in this plot. These results confirm that 7 beams in a linear array or 40 beams in a two dimensional array configuration can be achieved with an HDPE lens planar array, with a maximum scan loss of 3 dB. The maximum difference between the FW simulated and measured maximum directivity is 0.7 dB in the whole bandwidth and for all measured beams, which is related to the measurement and fabrication tolerances. Several measurements were performed changing the measurement plane height. Measurement repeatability showed changes in the estimated directivity of around 0.5 dB.

4.3.3 Far-Field Link Measurements

The transmission between two lenses placed at different distances (50 cm, 1 m, and 2 m) has been as well measured in order to validate the antenna gain estimation. Fig. 4.9 shows the raw and time gated measurement results compared to the transmission calculated with Friis equation. The measured results converge to the estimation with Friis equation when the link distance approaches 2 m, where both lenses can be considered to be at far-field distance. The link measurement with 2 m distance presents higher ripple, since it was performed with a single lens placed in front of a metal plate at 1 m distance, due to the lack of cables reaching this length. This measurement in reflection has been as well performed placing the metal plate at 50 cm distance, showing the same results as the measured transmission between two lenses at 1 m distance (Fig. 4.9).

Table 4.2 presents a summary of the performances for the most relevant designs of integrated lens antennas found in the literature.

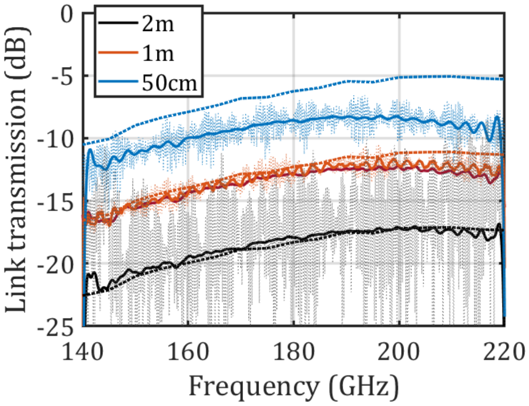

Figure 4.9: Measured and estimated transmission between two lenses placed at large distances. Thin dashed lines represent the raw transmission measurements; solid lines represent measurements after time-gating; dotted lines represent the results estimated with Friis equation. Results include both dielectric and conductor loss. For 1 m distance, light red: measurement in transmission; dark red: measurement in reflection.

4.4 Prototype Industrialization

The antenna concept presented was adapted to be suitable for larger scale production processes. Moreover, the design was scaled to D-band ($110-170$ GHz). In order to reduce the steps needed in the antenna fabrication, the double-slot was eliminated, leaving as main parts the waveguide split-block and the lens (Fig. 4.10). The elimination of the double-slot is only possible for lenses with low ε_r, as in this case the double-slot dimensions are almost

Ref.	f_0 [GHz]	BW [%]	Dir. f_0 [dB]	$\eta_{\mathrm{ap}}^{\mathrm{min}}$ [dB]	$L_{\mathrm{diel}}^{\mathrm{max}}$ [dB]	$\mathrm{SLL}^{\mathrm{max}}$ [dB]
[39]	246	-	29.9	-1.1	-	-16
[40]	60	16	19.9	-2.3^*	-	-16
[41]	400	1 : 3	27	-2.6^*	0.2	-8
[42]	50	1 : 5	19	-3.3^*	1.5	-12.5
[43]	550	18	22.2	-1^*	-	-15
[18]	77	10	24	-1.5^*	0.5	-15
[46]	30	12.5	25.9	-1.9^*	0.5	-14
[19]	73.5	7	37.3	-2.9^*	1	-
[47]	290	30	31.5	-4^*	-	-8
This work	**180**	**44**	**34**	**-1**	**0.5**	**-15**

Table 4.2: Simulated performances of integrated lens antennas. (*) Values estimated from the articles.

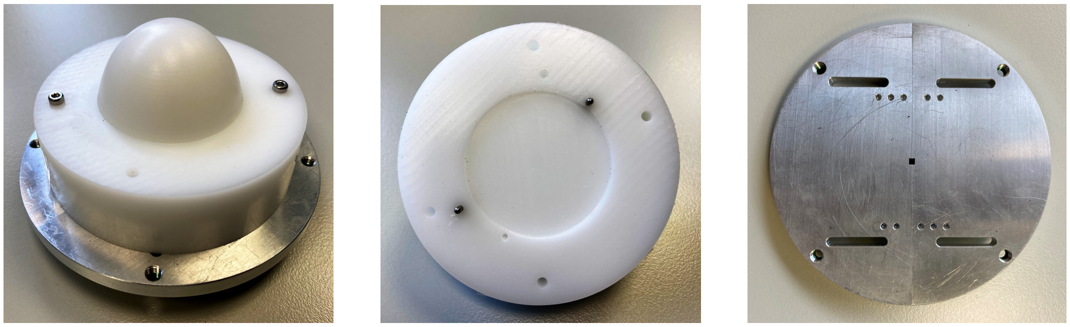

(a) (b) (c)

Figure 4.10: a) D-band prototype. b) D-band HDPE lens. c) D-band split-block.

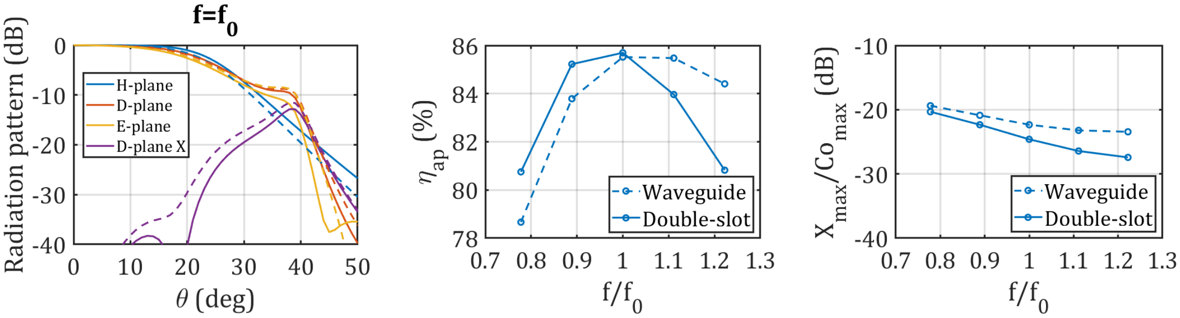

(a) (b) (c)

Figure 4.11: a) Primary patterns at f_0 with LW cavity $h_c = 0.56\lambda_0$ (Fig. 4.1). Comparison between double-slot feed ($\alpha = 65.5$ deg, $\rho_0 = 0.54\lambda_0$, $w = 0.3\lambda_0$ (Fig. 3.4), $t = 0.08\lambda_0$, and waveguide feed ($wg = 0.8\lambda_0$) λ_0 the wave-length at f_0. b) η_{ap} calculated with the analysis in reception for the double-slot and waveguide feeds from (a). c) Ratio between the maximum lens cross-polar and co-polar levels evaluated over all azimuth and elevation angles with PO simulations for the double-slot and waveguide feeds from (a).

covering the whole waveguide area. As a consequence, the Fourier transform of the source currents do not change significantly, attenuating the TM$_0$ mode in the same manner and preserving the radiation patterns. Fig. 4.11 compares the performance of the double-slot and waveguide feeds in terms of primary patterns, η_{ap} and cross-polar level. Despite the slightly higher cross-polar level in case of the waveguide feed, the simplicity advantage obtained in the fabrication is worthwhile.

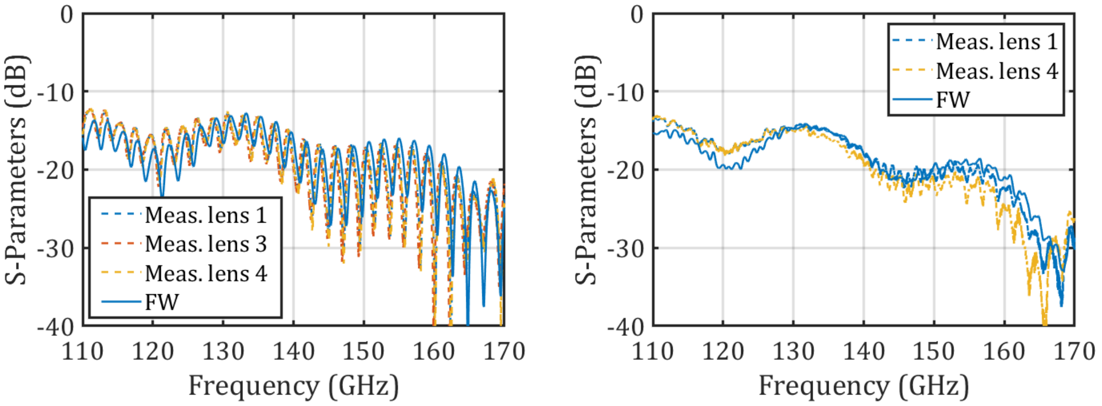

(a) (b)

Figure 4.12: D-band prototype S_{11} measurements and FW simulations for a) Broadside beam and b) beam pointing at 9 deg.

The antenna was scaled and FW simulated with EMPIRE XPU [112]. The lens has a diameter of 35 mm ($16.3\lambda_0$ at 140 GHz). The LW cavity height, h_c in Fig. 4.1, has been scaled to 1.2 mm, while the waveguide cross-section dimensions are $1.65 \times 1.8\,\mathrm{mm}^2$. These dimensions are tapered to a standard WR6 waveguide, with $\psi_{\mathrm{taper}} = 7.2$ deg and $L_{\mathrm{taper}} = 1.8\lambda_0$ (Fig. 4.1). The split-block and HDPE lens were fabricated with standard milling techniques. Several holes for positioning pins in the lens and waveguide split-block allow defining the displacement between the feed and lens focus.

Fig. 4.12 shows the simulated and measured antenna matching for the broadside beam and the beam pointing at 9 deg (feed displaced 3.6 mm), lower than -10 dB over the whole frequency band. Nevertheless, the matching level is slightly higher than in the G-band prototype, where the double-slot was used (Fig. 4.3b). In these figures, it is clear that the impact of multiple reflections from the lens is much lower for the off-focus feed [116]. The agreement between measurement and simulation results is excellent. Results for three prototypes are included, showing a high reproducibility in the antenna manufacturing process.

In Fig. 4.13, the FW simulated radiation patterns are displayed for the broadside beam and for a beam pointing at 9 deg. The FW simulated maximum directivity and gain for both beams are shown in Fig. 4.14, reaching more than 30 dB over the whole D-band. For the broadside beam, the simulated aperture efficiency is higher than 80 % over 42 % band-

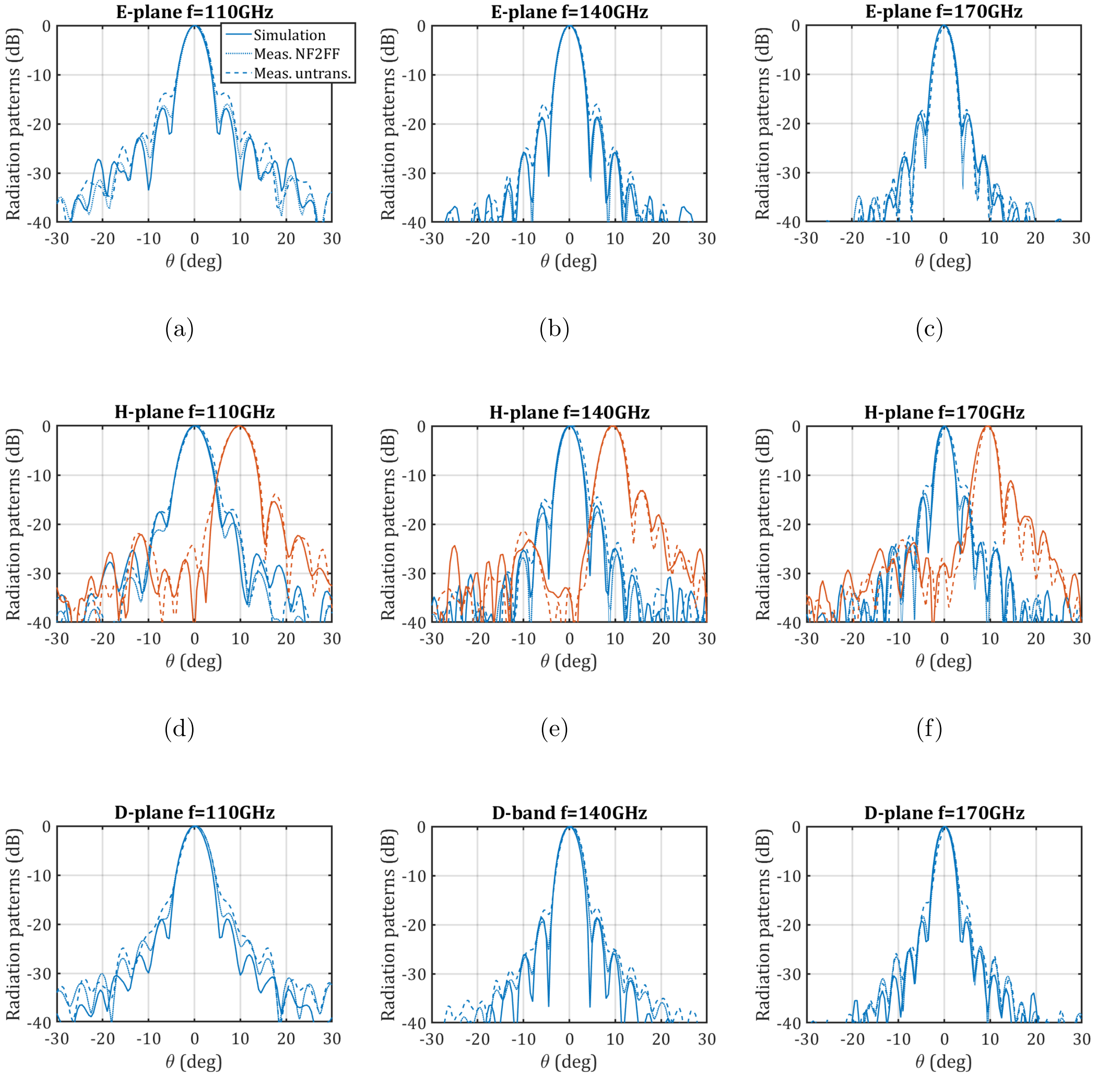

(a) (b) (c)

(d) (e) (f)

(g) (h) (i)

Figure 4.13: FW simulated and measured radiation patterns a) b) c) E-plane, broadside beam; d) e) f) H-plane, broadside (blue) and beam steering at 9 deg (red); g) h) i) D-plane, broadside beam.

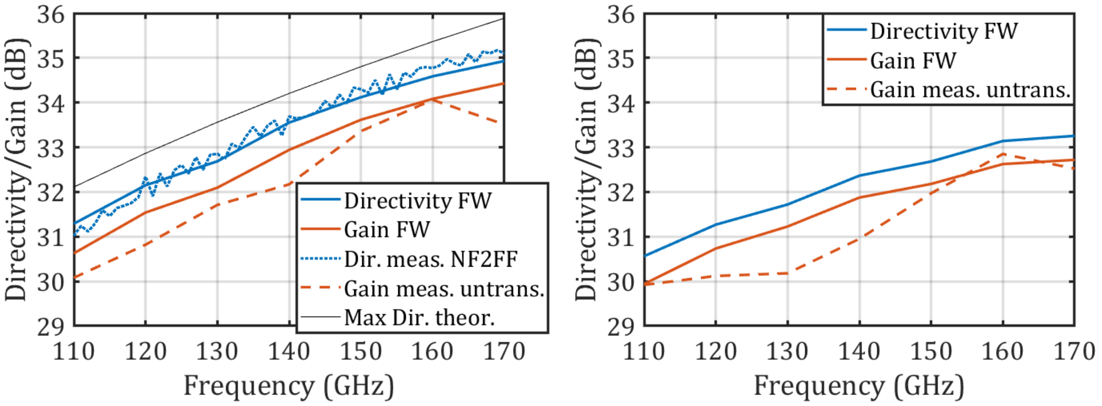

(a) (b)

Figure 4.14: D-band prototype maximum directivity and gain measurements and FW simulations for a) Broadside beam and b) beam pointing at 9 deg.

width, with a radiation efficiency higher than 86 %, including the losses in the waveguide and lens dielectric.

The radiation pattern characterization was performed with R&S®ATS1000 [117] measurement chamber (Fig. 4.15). More details about the measurement setup can be found in [118]. Two measurement approaches were employed: a direct far-field measurement, (untransformed measurement) and a near-field measurement with a near-field to far-field transformation (transformed measurement). Fig. 4.13 shows the measurement results with the two approaches, where an excellent agreement in the radiation patterns from the transformed measurements can be appreciated. The broadside beam maximum measured directivity from the transformed measurement is shown in Fig. 4.14a, also in very good agreement with FW simulated results. The broadside gain over frequency shown in Fig. 4.14a was obtained from the untransformed measurements, calibrated by means of a standard gain horn. A maximum difference of 1.3 dB appears between FW and measurement results, which may be related to the differences in the measured radiation patterns, or to tolerances in the antenna loss calculation. Fig. 4.13 shows as well the untransformed measurements for the beam pointing at 9 deg, in very good agreement with FW simulations. Fig. 4.14b shows the maximum gain over frequency obtained from the untransformed measurements, with a maximum difference of 1 dB w.r.t. FW simulations.

Despite the described small differences, the test results validate the full-wave simulation results, confirming the relevance and robustness of the concept. Overall, the design and


(a) (b)

Figure 4.15: a) R&S® ATS1000 measurement chamber with lens prototype prepared for testing. b) Lens prototype inside the measurement chamber.

modelling, manufacturing and measurement accuracy meet the challenging requirements in these high frequency bands.

4.5 Conclusions

A broadband integrated lens antenna is presented for future wireless communications at high frequencies. The proposed antenna is based on the resonant LW feed coupled to a HDPE elliptical lens. This design represents a trade-off with high efficiency, very large bandwidth and low cost, but limited number of off-focus beams. The lens achieves 34 dB gain at 180 GHz, reaching an aperture efficiency higher than 80 % and dielectric losses lower than 0.5 dB over 44 % relative bandwidth for the broadside beam. This design enables to generate up to 40 beams overlapping at -3 dB with a planar two dimensional Fly's eye array of lenses, keeping the gain higher than 30 dB at 180 GHz. The reflection coefficient is lower than -10 dB over the whole frequency band. The antenna has been fabricated and measured, showing excellent agreement with the simulated performances.

The lens antenna has been industrialized and scaled to D-band. Measurement results show a high repeatability among several prototypes and very good agreement with measurement results, confirming the robustness of this concept.

Chapter 5

Wideband Circularly Polarized Antenna with In-Lens Polarizer

In this chapter, a broadband G-band LW fed lens antenna with an integrated dielectric grid polarizer is presented. The proposed wideband polarizer unit cell geometry enables its fabrication at frequencies higher than 100 GHz, presenting high transmission properties and low axial ratio (AR). A quasi-analytic technique based on multi-layer Spectral Green's Function combined with a numerical Floquet modes solver is used to optimize the lens aperture efficiency and axial ratio. The proposed technique is validated via full wave simulations. A design is proposed in low dielectric permittivity material, achieving full-wave simulated aperture efficiency higher than 75 % over 44 % relative bandwidth, and an AR lower than 3 dB over 35 % relative bandwidth. The antenna is able to achieve multiple directive circularly-polarized beams, when fed by a focal plane array, preserving the AR bandwidth. A prototype was fabricated and measured, exhibiting an excellent agreement with quasi-analytic and full-wave simulations.

5.1 Introduction

In Chapter 4 an efficient, wide-band linearly polarized (LP) lens antenna with a LW feed was proposed in G-band (140–220 GHz) to be used in a Fly's Eye architecture, suitable for point-to-multipoint and dense small cells scenarios [20]. In order to enhance the wireless link efficiency, especially in scenarios with moving terminals, circularly polarized (CP) lens antennas are even better candidates to be used as single elements in the Fly's Eye lens arrays, as they minimize the loss due to polarization misalignment. However, wideband, low loss and cost-effective concepts are needed to generate circular polarization, in order

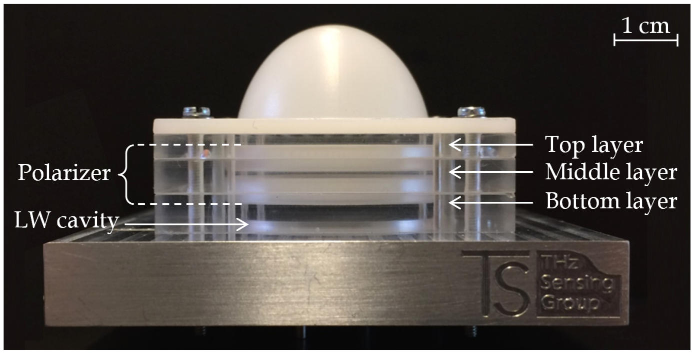

(a)

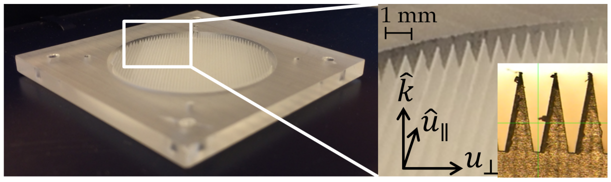

(b)

Figure 5.1: a) CP antenna prototype. From bottom to top: split-block waveguide, integrated polarizer in Topas material and lens fabricated with HDPE (lens diameter 3 cm). b) Bottom polarizer layer and side view of the polarizer pyramidal gratings.

not to compromise the performance reached with the LP lenses. The challenge to achieve these goals in the mm-wave and sub-mm-wave bands is addressed in this contribution.

An add-on polarizer based on the dielectric-grating concept is proposed to be integrated inside an elliptical plastic lens (Fig. 5.1a) and fed by the resonant LWA presented in Chapter 4. A new polarizer unit cell geometry is proposed, enabling the fabrication of wideband low dielectric permittivity polarizer gratings at G-band, with low-cost, low-loss plastic materials and standard milling techniques. In addition, this geometry improves the bandwidth and transmission with respect to the standard rectangular-grating used in [86]. Thanks to the LWA feed, which radiates most of the energy below the dielectric-air critical angle, total reflections in the lens dielectric-polarizer interface are avoided. The elliptical lens provides the antenna with high gain ($> 30\,\mathrm{dB}$) and steering capability, making it suitable for high-speed communication systems.

The combination of a high-directivity lens (diameter bigger than $15\lambda_0$) and a polarizer (containing sub-wavelength structures) in a single FW simulation, results in an extremely time-consuming model. In order to provide a fast optimization of the feed-polarizer-lens system, a quasi-analytic model based on multi-layer Spectral Green's Function (SGF) in anisotropic media (Appendix A) and an analysis of the lens in reception (Chapter 2), combined with a single unit-cell Floquet modes FW solver has been developed and used. The quasi-analytic approach for the lens analysis allows the estimation of the CP aperture efficiency and axial ratio after the lens. The fabricated antenna, optimized with this quasi-analytic method, achieves full-wave simulated aperture efficiency higher than 75 % over a 44 % relative bandwidth and an axial ratio lower than 3 dB over a 35 % relative bandwidth, with dielectric losses lower than 0.65 dB.

The chapter is organized as follows: Section 5.2 describes the overall antenna concept, the new polarizer grating geometry, and the analysis and optimization methodology applied; Section 5.3 shows the antenna prototype design and simulation results; Section 5.4 describes the measurement procedure used to characterize the antenna CP radiation patterns, AR, and gain.

5.2 Circularly Polarized Lens Antenna Concept

In this section, the concept of the dielectric lens with embedded polarizer, CP lens, is discussed. Circular polarization is achieved inside the dielectric lens by placing a dielectric-grating polarizer on top of a resonant LW feed, as shown in Fig. 5.1a. A novel wideband polarizer unit cell geometry, suitable to be fabricated at sub-mm wavelengths, is introduced here. In transmission, the lens is illuminated by a CP primary field (field of the LWA feed with polarizer, radiating inside the lens), collimating it to achieve high-gain.

The fast quasi-analytic methodology applied to optimize the full feed-polarizer-lens system performance is as well presented in this section. The CP primary patterns are calculated inside the lens by evaluating the multi-layer anisotropic structure with SGF (Appendix A). The optimization of the CP lens aperture efficiency and AR calculation are performed by means of the analysis of the antenna in reception presented in Chapter 2.

5.2.1 In-Lens Polarizer: Unit Cell

An add-on polarizer using dielectric gratings has been chosen to be embedded in the lens, due to its large bandwidth properties and its suitability for a cost-effective manufacturing at such small wavelengths. The dielectric gratings are fabricated in the same low relative dielectric permittivity ε_r material as the lens ($\varepsilon_r = 2.3$). The choice of this low ε_r improves the bandwidth of the polarizer transmission coefficients, enhancing as well the AR bandwidth. However, in terms of birefringence, lower ε_r values provide a lower contrast between the effective permittivity for the perpendicular and parallel field components ($\hat{u}_{\parallel}$ and $\hat{u}_{\perp}$ in Fig. 5.1b and Fig. 5.2b). This leads to higher grating heights, h in Fig. 5.2a, required to achieve the aimed 90 deg phase delay between the orthogonal LP components. On the other hand, the unit cell width or period, w, has to be small enough to avoid grating lobes ($\sim \lambda_d/2$). When choosing a standard rectangular grating geometry, these conditions result in a unit cell aspect ratio, h/w, higher than 14. The fabrication of such high h/w represents a big challenge at frequencies above 100 GHz. In order to facilitate the fabrication of the polarizer with standard milling techniques, a polarizer geometry with N separate layers of pyramids, each with a thickness of $h_i = (h - h_s)/N$, is proposed (where h_s is the thickness of the slab supporting the central pyramids). These layers are composed by identical extruded pyramids, piled to form the complete polarizer unit cell, as show in Fig. 5.2a. The pyramids' slope, determined by the milling tool tip angle, sets the maximum achievable height, and therefore phase delay per layer. For our current implementation, the polarizer is made out of $N = 4$ layers to reach the 90 deg phase delay. Further details regarding the polarizer fabrication have been given in [119]. The resulting polarizer unit cell geometry is shown in Fig. 5.2a. It can be fabricated in three parts: the bottom and top part, with gratings on one side, and the central part with gratings on both sides, as can be recognized as well in Fig. 5.1a. This tapered form provides the gratings with mechanical stability and represents as well a smooth transition between the air and plastic material characteristic impedances. This enhances the polarizer transmission properties w.r.t. a rectangular corrugation, making it unnecessary to perform a fine lateral alignment between the different polarizer layers.

The polarizer transmission properties have been analyzed by means of Floquet modes simulations for a single unit cell, with periodic boundary conditions. A 4-port S-parameters matrix can be calculated for each plane-wave angle of incidence, describing the coupling between TE and TM modes, as explained in Appendix A.

5.2.2 Leaky-Wave Feed with Add-on Polarizer

The CP feed, shown in Fig. 5.3 on the left, consists of the linearly-polarized (LP) LWA feed presented in Chapter 4 with the proposed add-on polarizer on top, as displayed in Fig. 5.2b and Fig. 5.3.

As explained in Section 3.2, the LWA feed is characterized by a critical angle, θ_c^f (Fig. 5.3), after which very low power is radiated. For $\varepsilon_r = 2.3$, θ_c^f appears at 41 deg, and as a consequence the patterns radiated by this feed inside the lens (LP primary patterns), present a taper higher than -12 dB at this angle. The polarizer presents effective

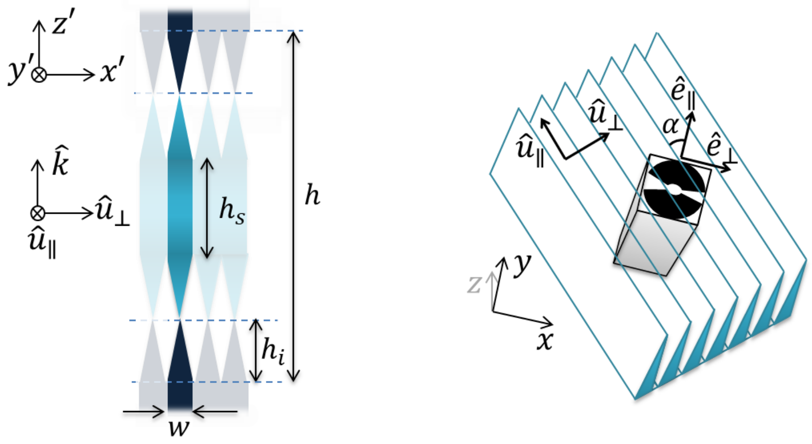

(a) (b)

Figure 5.2: a) Polarizer unit cell. The blue color represents the dielectric, whereas the white color the air. The dashed lines mark the separation of the polarizer in three pieces for its fabrication. $h = 4.26\lambda_0$, $h_i = 0.76\lambda_0$, $h_s = 1.2\lambda_0$ and $w = 0.5\lambda_d$, being λ_0 the free-space wavelength at $f_0 = 180\,\mathrm{GHz}$ and $\lambda_d = \lambda_0/\sqrt{\varepsilon_r}$. b) Wave-guide cross-section and double-slot with polarizer grid on top, oriented with an angle $\alpha = 45$ deg with respect to the double slot linear polarization $\hat{e}_\parallel$.

$\varepsilon_r > 1$ for both orthogonal field components, and therefore the critical angle in the interface between the polarizer and the dielectric medium, θ_c^p in Fig. 5.3 on the left, is always larger than θ_c^f. Thanks to the LWA properties, the polarizer is only illuminated with incident angles lower than θ_c^f ($\theta_{\mathrm{LW}} < \theta_c^f$). This avoids significant total reflections in the interface between the lens material and the polarizer gratings.

The add-on polarizer based on dielectric gratings is placed on top of the LP LWA at a coordinate $z = z_{\mathrm{bot}}$ (Fig. 5.3a), which is high enough to preserve the LW propagation properties. The polarizer gratings are oriented with an angle of 45 deg w.r.t. the LP LWA polarization (Fig. 5.2b).

The resulting anisotropic multi-layer structure shown in Fig. 5.3 on the left has been analysed with the SGF approach discussed in Appendix A. In order to calculate the CP primary patterns, the transmission line model in Fig. 5.3 on the right has been applied. The LW air cavity and lens dielectric medium in which the polarizer is inserted are modelled as isotropic media, with different transmission lines for the TE and TM mode propagation. The polarizer is treated as a homogeneous anisotropic slab inserted in the isotropic lens medium, with a certain height ($z_{\mathrm{top}} - z_{\mathrm{bot}}$). The polarizer S-parameters correspond to a 4×4 matrix coupling the TM and TE modes for each θ_i and ϕ_i incident angle. The S-parameters

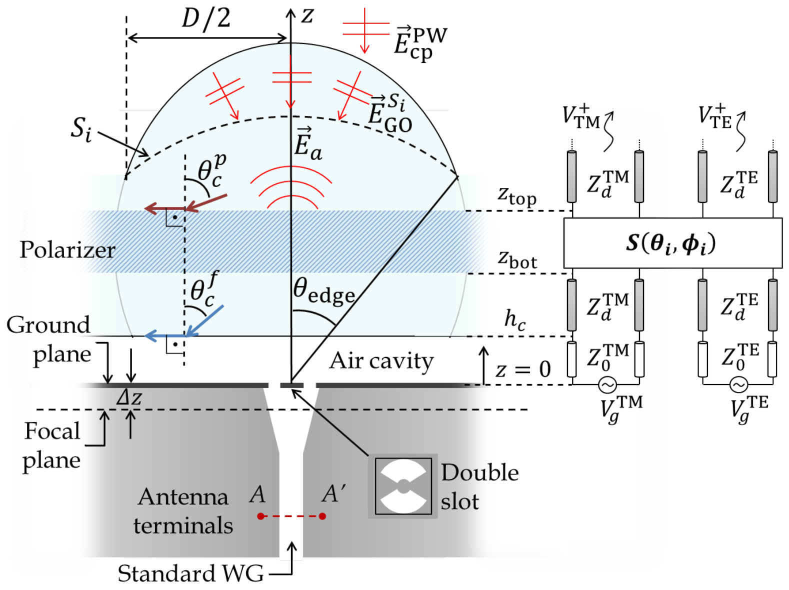

Figure 5.3: Left: Main parameters of the elliptical lens geometry with integrated polarizer, and LW feed. Optimized values: $h_c = 0.56\lambda_0$, $z_{\text{bot}} = 2.27\lambda_0, z_{\text{top}} = 6.53\lambda_0, \theta_{\text{edge}} = 40$ deg, $\Delta z = -2.8$ mm. The fields used for the lens aperture efficiency and axial ratio calculation are as well represented here ($\vec{E}_a$, $\vec{E}_{\text{GO}}^{S_i}$ and $\vec{E}_{\text{cp}}^{\text{PW}}$). Right: Equivalent transmission line model applied for the CP primary pattern calculation.

are calculated with FW Floquet modes based simulations for a single unit cell, for the different θ_i, ϕ_i. Finally, the lens is modelled as a semi-infinite dielectric medium (Fig. 5.3), neglecting the effect of multiple reflections in the lens-air interface. The transmission line model, calculation of the voltages and currents, and finally the computation of the far-field is explained with detail in Appendix A.

5.2.3 Optimization of the Lens with Integrated Polarizer

In order to obtain the high gain required for a wide-band communications scenario, a truncated elliptical lens (as in Chapter 4) is placed on top of the CP feed (LWA feed + polarizer). Once the CP primary patterns have been calculated, the elliptical lens and feed parameters can be optimized by applying an analysis of the antenna in reception (SGF-Rx), based on the same methodology described in Chapter 2 and applied in Chapter 4. This enables a fast optimization for the feed-polarizer-lens system, avoiding time-consuming FW simulations. The LW cavity height, h_c, the double slot geometry, the feed z position with respect to the focal plane, Δz, and lens truncation angle, θ_{edge} (Fig. 5.3), are the variables to maximize the CP lens aperture efficiency, η_{ap}. The lens θ_{edge} determines its focal length

F for a given lens diameter D, as the lens eccentricity e is given by its ε_r as $e = 1/\sqrt{\varepsilon_r}$ (Section 2.1).

The geometry and fields used in this evaluation are shown in Fig. 5.3 on the left. In this analysis, the voltage generated by an ideal CP plane wave at the open circuited antenna terminals AA', V_{oc}, in the antenna evaluated in reception, is derived to calculate the antenna efficiency η_{ap}. As explained in Chapter 2, V_{oc} is determined by performing a reaction integral over the surface S_i, inside the lens, between the CP primary patterns evaluated in transmission, $\vec{E}_a$, and the incoming field $\vec{E}_{\text{GO}}^{S_i}$ from the CP plane wave as

$$V_{\text{oc}} I_{\text{tx}} \approx \frac{2}{\zeta_d} \int_0^{2\pi} \int_0^{\theta_{\text{edge}}} \vec{E}_{\text{GO}}^{S_i}(\theta,\phi) \cdot \vec{E}_a^{\text{GP}}(\theta,\phi) e^{jk\Delta z \cos\theta} dS \tag{5.1}$$

where I_{tx} is the amplitude of the electric current feeding the antenna in transmission, θ_{edge} is the lens rim angle from the focus, $\zeta_d = \zeta_0/\sqrt{\varepsilon_r}$ and ζ_0 the wave impedance in vacuum. $\vec{E}_a^{\text{GP}}$ is calculated with the phase reference in the LW ground plane, and the term $e^{jk_d\Delta z \cos\theta}$ represents the z-displacement of the ground plane w.r.t. the lens focal plane, applied to place the actual feed phase centre on the lens focus ($\vec{E}_a = \vec{E}_a^{\text{GP}} e^{jk_d\Delta z \cos\theta}$). As explained in Chapter 2, I_{tx} can be arbitrary chosen (e.g. $I_{\text{tx}} = 1\,\text{A}$, becoming $V_{\text{oc}} I_{\text{tx}} = V_{\text{oc}}$). As we are aiming for a CP field, $\vec{E}_{\text{GO}}^{S_i}$ is calculated in this case with a CP incident plane-wave, $\vec{E}_{\text{cp}}^{\text{PW}}$ (Fig. 5.3 on the left). In this way, two orthogonally CP plane waves are defined as

$$\vec{E}_{\text{RH}}^{\text{PW}} = \frac{E_0^{\text{PW}}}{\sqrt{2}} \left(\hat{x} + j\hat{y}\right) \tag{5.2a}$$

$$\vec{E}_{\text{LH}}^{\text{PW}} = \frac{E_0^{\text{PW}}}{\sqrt{2}} \left(\hat{x} - j\hat{y}\right) \tag{5.2b}$$

being $\vec{E}_{\text{RH}}^{\text{PW}}$ right-handed CP and $\vec{E}_{\text{LH}}^{\text{PW}}$ left-handed CP, with propagation vector $-\hat{z}$. The corresponding $\vec{E}_{\text{GO}}^{S_i}$ is evaluated analytically as derived in [98].

η_{ap} is estimated relating the power captured by the lens from the co-polarized CP plane-wave impinging the lens from broadside, P_{in}, to the power which is actually delivered to the load at the feed, P_L, applying Eq. (5.1), Eq. (2.3) and Eq. (2.4).

The resulting η_{ap} includes the taper, phase, reflection, spill-over and polarization efficiencies, being equivalent to the difference between the achieved directivity and the maximum directivity for this circular aperture.

In order to derive the lens AR, V_{oc} is calculated for both orthogonal CP plane waves. The far-field at broadside for each CP component is proportional to its corresponding V_{oc} (reciprocity theorem), and therefore the lens AR at broadside can be approximated, e.g. for a right-handed CP antenna, in a similar way as in [120]

$$\mathrm{AR} \approx \frac{|V_{\mathrm{oc}}^{\mathrm{RH}}| + |V_{\mathrm{oc}}^{\mathrm{LH}}|}{|V_{\mathrm{oc}}^{\mathrm{RH}}| - |V_{\mathrm{oc}}^{\mathrm{LH}}|} \tag{5.3}$$

5.3 Prototype Design and Fabrication

Applying the described analysis methodology based on SGF and an analysis of the antenna in reception, a CP lens antenna has been designed in G-band, centered in 180 GHz, with a diameter $D = 18\lambda_0$ (Fig. 5.3). In this section, the final geometry and simulation results are shown for the polarizer unit cell, the CP feed radiating in a semi-infinite dielectric medium and, finally, for the complete CP lens antenna.

5.3.1 Unit Cell Performance

The unit cell dimensions for the polarizer are reported in Fig. 5.2a. The unit cell period w avoids the grating lobes for incident angles up to 52 deg, until 200 GHz. The resulting pyramid h_i/w is 2.3. The polarizer S-parameters are estimated from Floquet modes simulations performed with CST Studio Suite [121] for the unit cell, using the first two Floquet modes (TE_1 and TM_1), as described in Appendix A. As shown in Fig. 5.4a, the polarizer unit cell is almost “transparent” to the incident wave amplitude up to $\theta_c^f = 41$ deg, after which the LWA is radiating very low power. The AR is lower than 3 dB in both principal planes for incident angles lower than 25 deg. Fig. 5.4b shows the unit cell AR over the whole frequency band, for different incident angles. In this figure, the AR is displayed for unit cells with aligned and fully misaligned pyramid layers, showing the robustness of the concept against misalignment.

5.3.2 Leaky-Wave Feed with Polarizer: Radiation Patterns and AR

Fig. 5.5 shows the CP primary patterns, calculated applying the SGF model discussed in Appendix A. The validation with FW simulations with EMPIRE XPU [112] shows an excellent agreement with the SGF results, in both phase and amplitude, over the whole

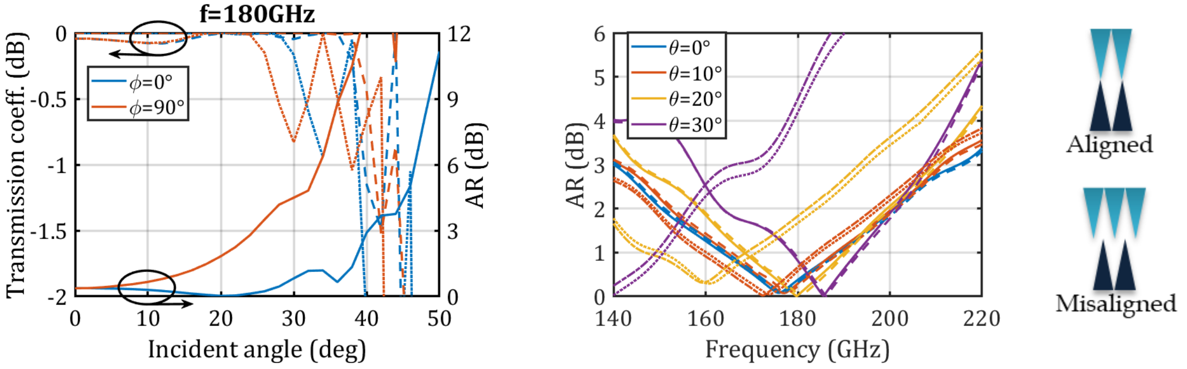

(a) (b)

Figure 5.4: a) Left axis: unit cell transmission coefficients of the fundamental Floquet modes vs. plane-wave incident angles at 180 GHz. Dashed line: TM mode; dotted line: TE mode. Right axis: AR calculated from the complex unit cell transmission coefficients. b) Unit cell AR over frequency for different angles of incidence, evaluated from the Floquet modes simulations. Solid line: $\phi = 0$ deg incidence with aligned pyramids; dashed line: $\phi = 0$ deg misaligned pyramids; dash-dotted line: $\phi = 90$ deg aligned pyramids; dotted line: $\phi = 90$ deg misaligned pyramids. The unit cell coordinate system is taken as in Fig. 5.2, aligned with its periodicity.

frequency band. The CP primary patterns are very close to the LP ones (see Chapter 4), thanks to the polarizer good transmission properties and low AR. This can be seen as well in the directivity comparison for the feed with (CP) and without polarizer (LP), which differ in maximum 1 dB, as shown in Fig. 5.6. The simulated feed maximum directivity over frequency has a variation lower than 2 dB in the whole band, being the AR at broadside lower than 3 dB from 150 GHz to 220 GHz (Fig. 5.6).

5.3.3 Lens with Integrated Polarizer: Radiation Patterns and AR

Using the analysis in reception as described in Section 5.2.3, the CP lens geometry has been optimized to maximize η_{ap}. As the polarizer does not significantly modify the CP primary pattern amplitude with respect to the LP ones (Fig. 5.5), the double-slot geometry and lens truncation angle θ_{edge} have not been modified w.r.t. the LP design in Chapter 4. However, the CP feed phase center changes with respect to the LP feed, due to the polarizer lower effective ε_r, being the optimum feed phase center position with respect to the lens focal plane $\Delta z = -2.8$ mm. The final results for the lens η_{ap} and AR have been validated by means of FW simulations performed with EMPIRE XPU (with multiple reflections),

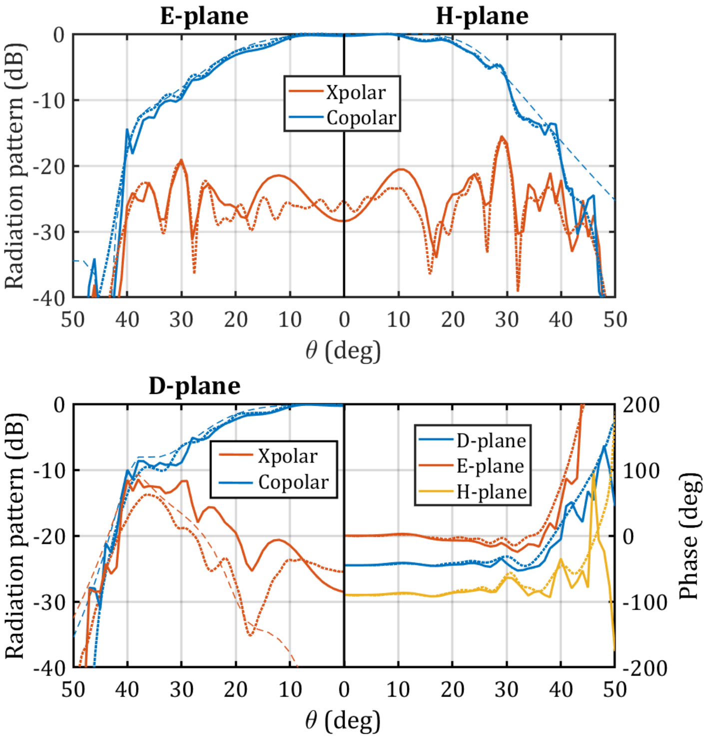

Figure 5.5: CP primary field amplitude and phase (considering the lens as infinite medium). Solid line: SGF model. Dotted line: FW simulations. Dashed line (in radiation pattern plots): linear polarized primary patterns (without polarizer), SGF model. E-, H-, and D-planes are defined here with respect to the LP feed polarization.

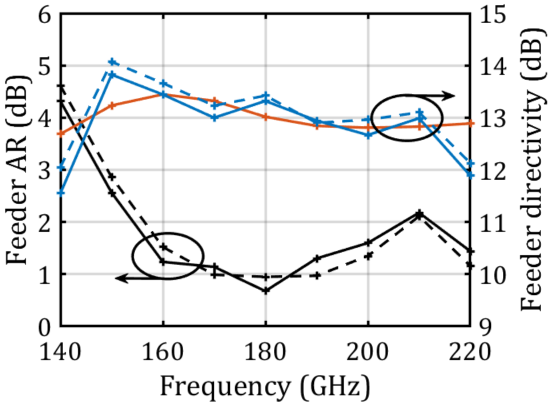

Figure 5.6: Left axis: Axial ratio at broadside for LWA feed with polarizer. Right axis: LWA feed directivity with (CP) and without polarizer (LP). Solid line: SGF model. Dashed line: FW simulations. Red line: LP feed directivity (without polarizer).

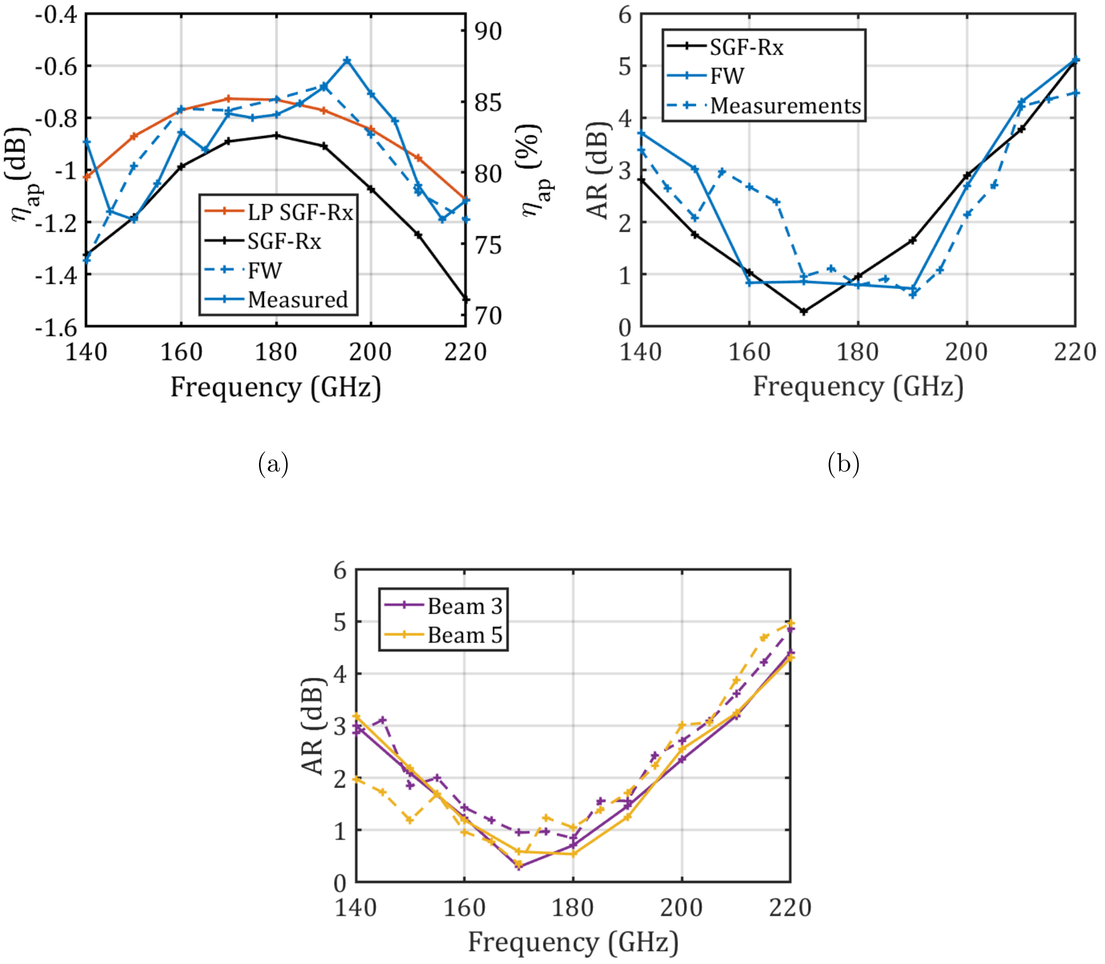

(a)

(b)

(c)

Figure 5.7: a) Broadside aperture efficiency for the CP lens. In red, the SGF-Rx simulations for the LP lens are reported for reference. b) CP lens axial ratio at broadside. c) CP lens AR for the beams steering at 8.4 deg (beam 3) and 16 deg (beam 5) (corresponding respectively to feed displacements, $d = 0.09D$ and $0.19D$). Solid line: FW simulations; dashed line: far-field from near-field measurements.

showing very good agreement. Fig. 5.7a shows that the lens η_{ap}, is not degraded with the use of the polarizer, remaining very close to the η_{ap} for the LP lens. In Fig. 5.7b, the resulting AR is reported, compared as well with the AR evaluated with the lens FW simulated radiation patterns. Results show a lens $\eta_{\text{ap}} > 75\,\%$ over $44\,\%$ bandwidth and AR $< 3\,\text{dB}$ over $35\,\%$ bandwidth.

Fig. 5.8 shows the CP FW simulated radiation patterns at broadside for the lens with integrated polarizer, with side-lobe levels (SLL) lower than $-15\,\mathrm{dB}$ up to $200\,\mathrm{GHz}$. The feed has been displaced off-focus, as explained in Section 3.5, in order to perform beam steering with the elliptical lens. By placing the polarizer below the lens, the polarizer is illuminated in the same manner regardless which is the feed position over the lens focal plane. In this way, the feed AR, and therefore also the lens AR bandwidth, do not change when performing beam steering, as it can be appreciated in Fig. 5.7c. Moreover, the impact of multiple reflections in the AR is in case of the steered beams lower, as the reflected waves do not propagate in the main beam direction. Fig. 5.9 shows the CP lens radiation patterns for the steered beams, with very similar SLL to the LP patterns presented in Chapter 4. Fig. 5.10a displays the maximum gain over frequency for the broadside and steered beams, showing as well very similar performance to the LP lens. This fact implies that the maximum steering angle achieved with the lens, or number of beams suitable to cover a communication scenario, as discussed in Section 1.3.1, is not degraded w.r.t. the LP lens (±12 deg).

In Fig. 5.10b the CP lens antenna reflection coefficient seen from the standard waveguide flange is displayed, being this $-10\,\mathrm{dB}$ over the whole frequency band.

The CP lens antenna prototype makes use of the same split-block waveguide and double slot manufactured for the LP design in Chapter 4. The polarizer has been fabricated in Topas material, on top of which a HDPE lens has been placed (Fig. 5.1a), both materials presenting $\varepsilon_r = 2.3$. HDPE has been chosen for the lens fabrication due to its very low loss properties ($\tan\delta = 3.4\times10^{-4}$); Topas material ($\tan\delta = 1.2\times10^{-3}$) has been chosen for the polarizer fabrication, as its hardness facilitates the milling process [119]. The maximum dielectric loss in the lens, evaluated with the FW simulated gain, is $0.65\,\mathrm{dB}$ at $220\,\mathrm{GHz}$.

5.4 Measurements

In this section, the measurement campaign carried out to characterize the CP lens antenna prototype is described.

The antenna reflection coefficient has been measured at the split-block standard waveguide interface, being the results in agreement with simulations (Fig. 5.10b). In order to make a first validation of the antenna polarization performance, the lens self-coupling (power reflected from a metal plate) has been measured, using an approach similar to [122], but placing the metal plate directly in the near-field instead of the far-field. In order to validate the lens radiation efficiency η_{rad} (to calculate the antenna gain) and with the aim of performing a first AR measurement, a phase-amplitude method has been applied [123],

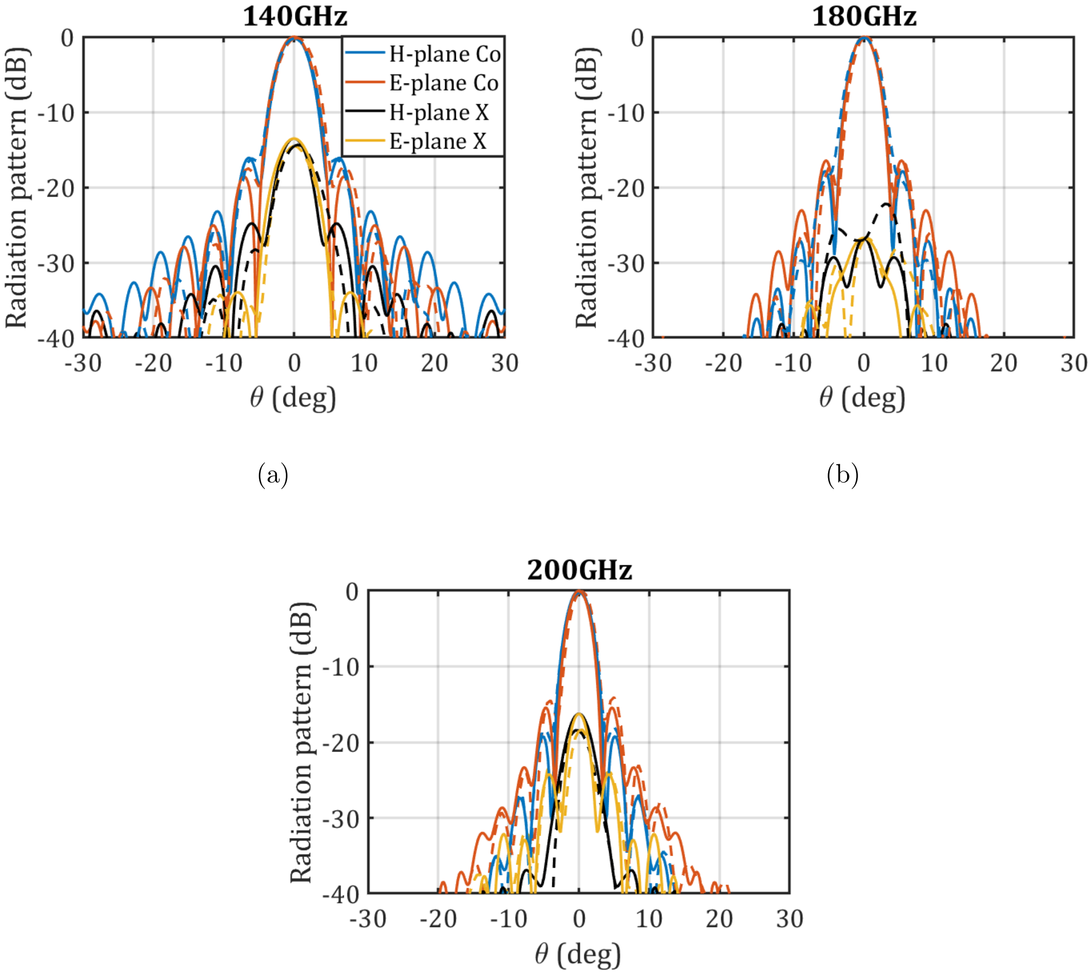

(a)

(b)

(c)

Figure 5.8: Lens CP far-field patterns for the broadside beam. Solid line: FW simulations; dashed line: far-field from near-field measurements. E-, H-, and D-planes are defined here with respect to the double-slot linear polarization.

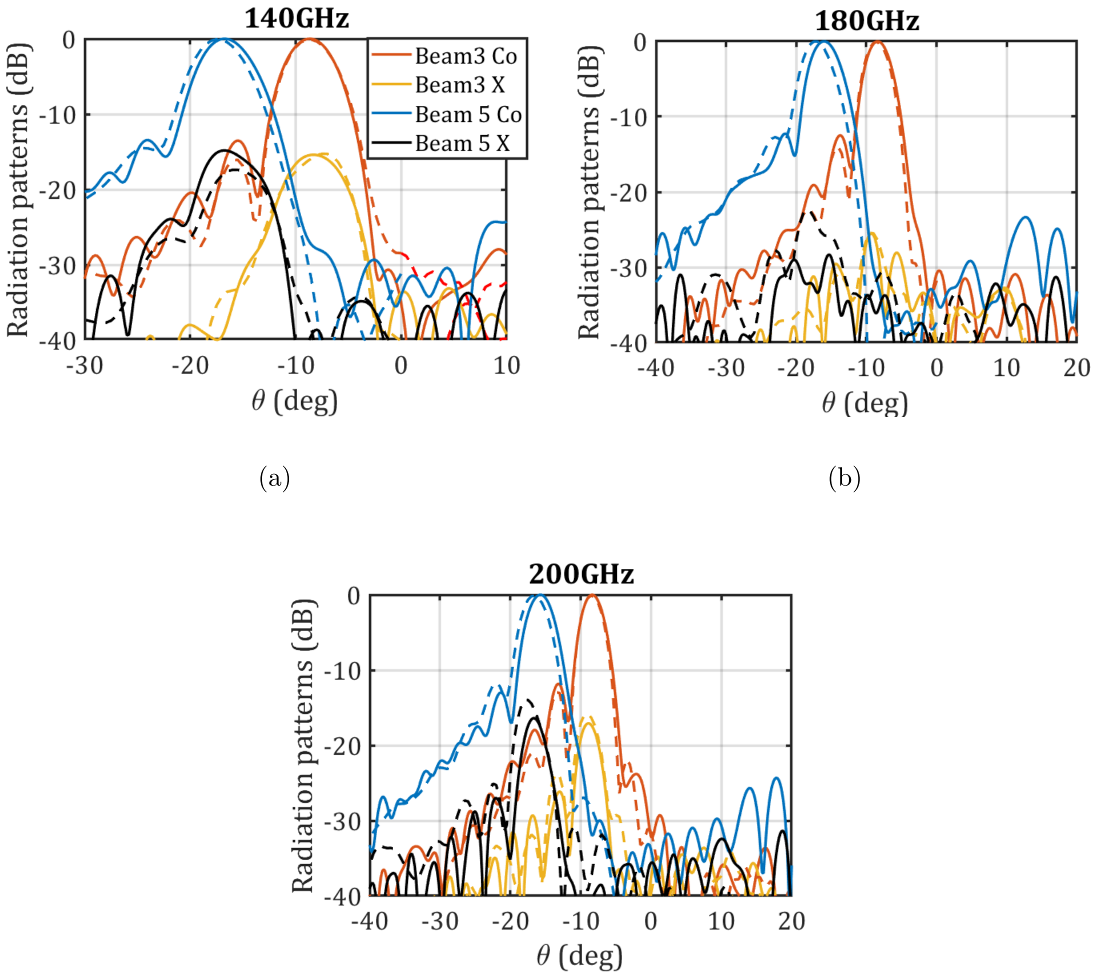

(a)

(b)

(c)

Figure 5.9: Lens CP far-field patterns for the beams steering at 8.4 deg (beam 3) and 16 deg (beam 5), normalized to their maximum co-polar amplitude. The steering is performed within the LP double-slot H-plane. The beams correspond to feed displacements, $d = 0.09D$ and $0.19D$. Solid line: FW simulations; dashed line: far-field from near-field measurements.

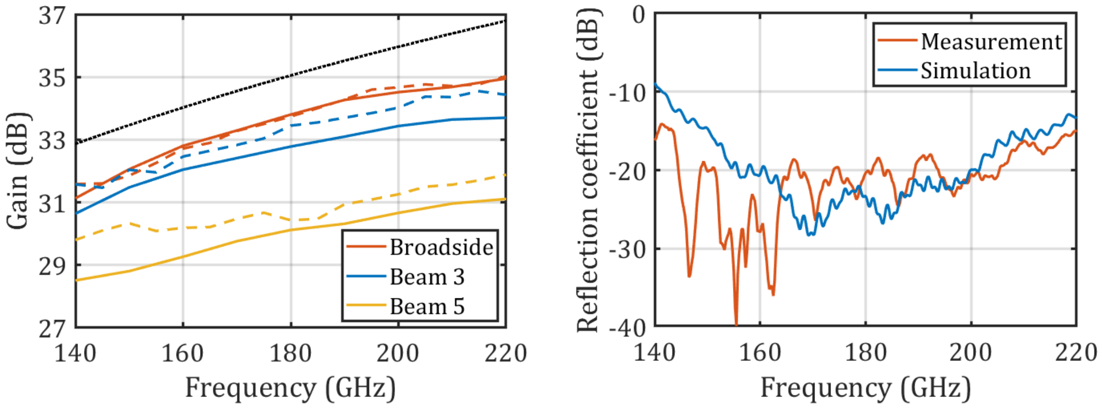

(a) (b)

Figure 5.10: a) Maximum gain for the lens CP co-polar components. Solid line: FW simulations; dashed line: measurements. Dotted black line: maximum possible directivity for this circular equivalent aperture. b) Reflection coefficient for the CP lens.

measuring the coupling to the LP lens in Chapter 4. In this approach, the LP lens is rotated 90 deg to measure both orthogonally LP field components. Here, a very accurate relative phase characterization and positioning between the two LP measurements is needed to characterize the CP fields. The strategy to perform the phase calibration between the two measurements, which is very challenging in this frequency band, is explained in this section. Profiting from this calibration and using as well the phase-amplitude method, two near-field measurements with a LP near-field probe were performed for each beam to obtain the CP radiated fields. The CP lens radiation patterns, maximum gain, and AR validation by means of coupling and near-field measurements is presented for the broadside and steered beams, with an excellent agreement with quasi-analytic and FW simulations.

5.4.1 Antenna Self-Coupling: Measurement in Reflection

A first verification of the antenna polarization purity has been performed by measuring the signal reflected on a metal plate, coming back to the CP lens (setup in Fig. 5.11a). This measurement is equivalent to the one of the transmission between two orthogonally CP polarized lenses. A similar approach was proposed in [122], where reflection measurements were performed in the antenna far-field using a metal plate and a corner reflector, and estimating the CP antenna AR. Here instead we propose to place the metal reflector in the lens near-field region, at 1 cm distance from the lens equivalent aperture, where

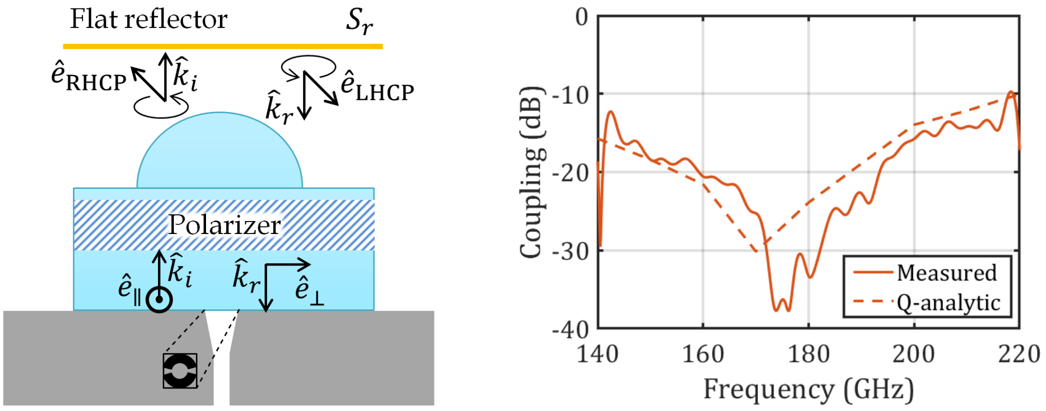

(a)

(b)

Figure 5.11: a) Measurement setup for CP lens self-coupling. The fields and propagation constants are reported for the central ray. $\hat{e}_{||}$ and $\hat{e}_{\perp}$ are defined as in Fig. 5.2b. b) CP lens self-coupling results. Quasi-analytic: reaction integral between PO fields. Measurements: reflection coefficient time gated to consider only first order reflected rays, and to eliminate reflections at WG taper and double-slot.

the radiated fields are well-collimated with nearly planar phase front, thanks to the high aperture efficiency of the proposed lens antenna (Fig. 5.7a). In that case, the field can be well predicted by performing a GO propagation. This assumption was validated in Section 4.3.1 by measuring the coupling between two LP lenses, and comparing with FW simulations.

The CP lens self-coupling can be calculated quasi-analytically with the analysis of the antenna in reception, as explained in Section 2.5.2. Both reflected and transmitted fields can be formulated in terms of CP components, as proposed in [122]. In this way, the dot product $\vec{E}_{\mathrm{GO}}^{S_r,\mathrm{Tx}} \cdot \vec{E}_{\mathrm{GO}}^{S_r,\mathrm{Rx}} = 4E_{\mathrm{RH}}E_{\mathrm{LH}}$, being E_{RH} and E_{RH} the amplitudes of the right and left handed polarized field components, respectively. Although the AR cannot be calculated from this single measurement [122], the AR and measured coupling minima are coincident when the AR equals 0 dB (see Fig. 5.7b).

The results of this analysis are shown in Fig. 5.11b, with a minimum coupling at 170 GHz, where the calculated lens AR optimum appears (Fig. 5.7b). The estimated waveguide loss Table 4.1 and dielectric loss in the lens, obtained from FW simulations, have been added to the quasi-analytic calculation, in order to perform a fair comparison with the measured results. Time gating has been applied to the measured signal, in order to cancel the effect of multiple reflections and account only for the first reflected wave in the metal plate, as in the quasi-analytic evaluation. The time-gated measurement results are reported in Fig. 5.11b, showing a very good agreement with the quasi-analytic calculation.

5.4.2 Coupling CP-LP Lenses

The near-field coupling between the LP lens presented in Chapter 4 and the fabricated CP lens has been measured with two purposes: derive the lens AR and validate the simulated lens η_{rad}, in order to estimate the lens maximum gain. This coupling can be as well calculated semi-analytically with the analysis of the antenna in reception described in Section 2.5.1.

The field radiated by the LP lens, $\vec{E}^{S_c}_{\mathrm{GO-LP}}$, is calculated in the plane between both lenses, S_c in Fig. 5.12a, with a GO approach, and taken as incident field impinging on the CP lens. In the same way, the field transmitted by the CP lens, $\vec{E}^{S_c}_{\mathrm{GO-CP}}$, is calculated at S_c, where the reaction integral is performed to calculate V_{oc} as

$$V_{\mathrm{oc}} \approx \int_0^{2\pi} \int_0^{D/2} \vec{E}^{S_c}_{\mathrm{GO-LP}}(\rho,\phi) \cdot \vec{E}^{S_c}_{\mathrm{GO-CP}}(\rho,\phi) \rho d\rho d\phi \tag{5.4}$$

and the coupling efficiency can be calculated as in Eq. (2.10).

V_{oc} is calculated with the LP lens in two polarization orientations, parallel and orthogonal to the CP lens feed ($V_{\mathrm{oc}}^{\parallel}$ and $V_{\mathrm{oc}}^{\perp}$), as shown in Fig. 5.12a. Fig. 5.13a shows the amplitude of the calculated coupling efficiency for both LP orientations, $c_{\parallel}$ and $c_{\perp}$, where the estimated waveguide and dielectric loss have been as well added to perform a fair comparison with the measurement results. Fig. 5.13a shows as well the phase difference between $V_{\mathrm{oc}}^{\parallel}$ and $V_{\mathrm{oc}}^{\perp}$.

The CP lens AR at broadside can be calculated using $V_{\mathrm{oc}}^{\mathrm{RH}} = V_{\mathrm{oc}}^{\parallel} - jV_{\mathrm{oc}}^{\perp}$ and $V_{\mathrm{oc}}^{\mathrm{LH}} = V_{\mathrm{oc}}^{\parallel} + jV_{\mathrm{oc}}^{\perp}$ in equation Eq. (5.3). The field generated by the LP lens, impinging on the CP lens, is very close to the one of an ideal LP plane wave. Therefore, the AR derived from this measurement is almost overlapping with the AR calculated from the coupling to an ideal plane-wave (Section 5.3.3), as shown in Fig. 5.13b. The small difference between both AR calculations is related to the different field amplitude taper and phase with respect to the ideal plane-wave case, taken as incident field in the analysis of the antenna in reception.

The coupling measurements have been performed placing the lenses at 2 cm distance. From these measurements, complex coupling coefficients between both lenses, $c_{\parallel}$ and $c_{\perp}$, are evaluated. In order to rotate the LP lens polarization direction, a waveguide twist has been introduced between the Vector Network analyser (VNA) and the lens antenna. In this

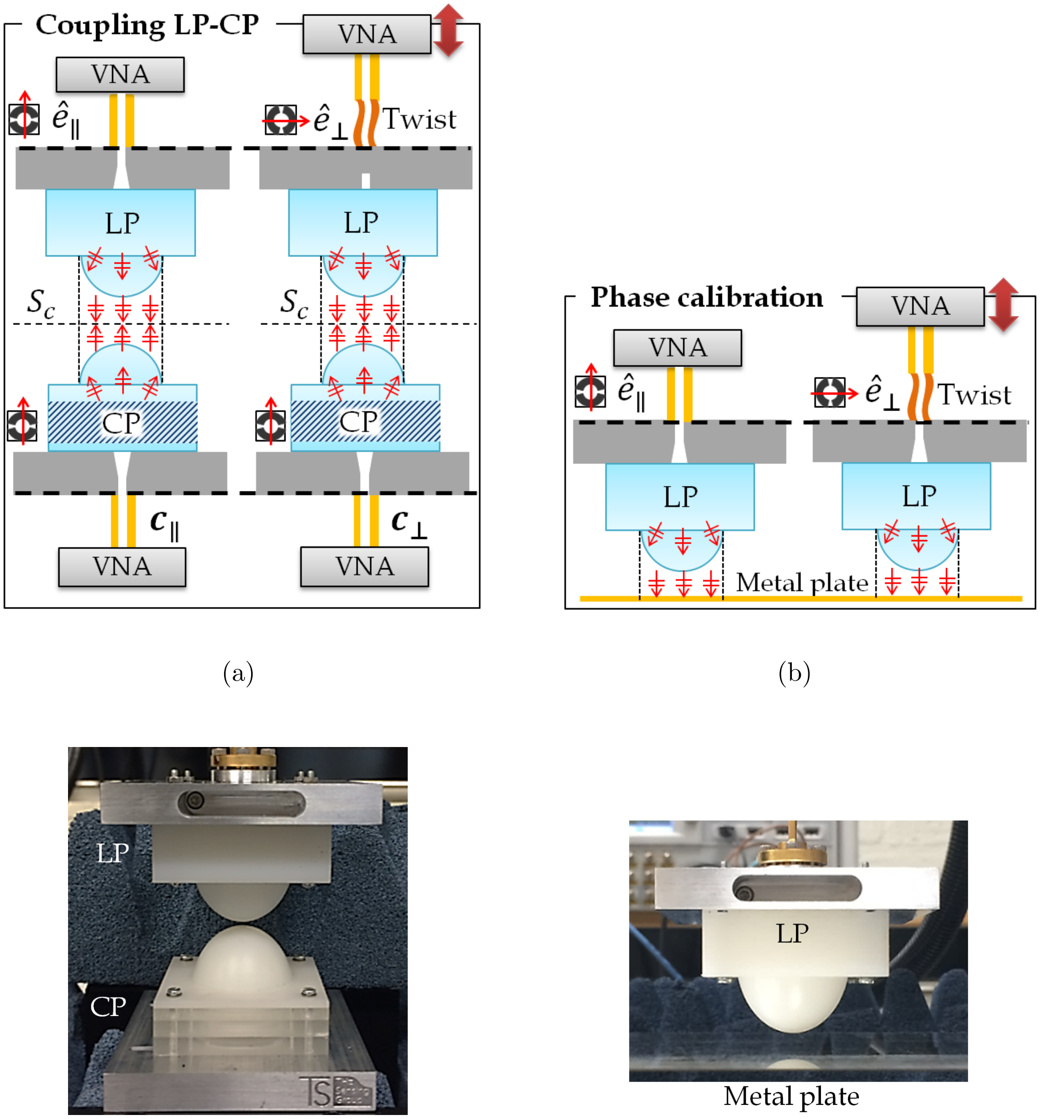

(a) (b)

(c) (d)

Figure 5.12: Measurement setup for a) coupling between LP and CP lenses, and b) phase calibration between parallel and orthogonal coupling measurements. The top view of the LW feed double-slot and E-field unit vector is shown for each lens. Calibration planes are marked with dashed lines. c) Picture of measurement setup for coupling between LP and CP lenses. d) Picture of measurement setup for phase calibration.

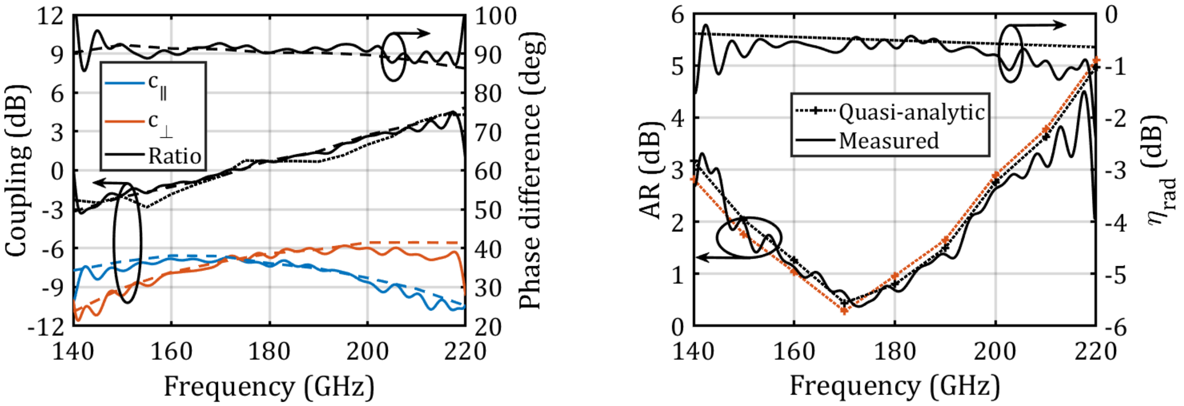

(a) (b)

Figure 5.13: a) Left axis: $c_{\|}$ and $c_{\perp}$ amplitude. Solid line: measurements. Dashed line: quasi-analytic calculation. All include dielectric and waveguide loss. The ratio between $c_{\|}$ and $c_{\perp}$ is displayed as well. Dotted line: for comparison, radiated power ratio between parallel and orthogonal near-field measurements is also shown. Right axis: phase difference between $c_{\|}$ and $c_{\perp}$; solid line: time-gated measurements, dotted line: quasi-analytic model. b) Left axis: AR estimated from coupling to a LP lens field (black) and to a plane wave with uniform amplitude (red). Right axis: CP lens antenna radiation efficiency, excluding waveguide ohmic losses.

way, the VNA does not need to be rotated, which could degrade the VNA phase calibration. The twist has been characterized with one-port Short-Open-Load (SOL) measurements, and the results used to calibrate $c_{\perp}$.

Phase calibration: To obtain a good relative phase measurement between $c_{\|}$ and $c_{\perp}$, not only the twist S-parameters should be known, but also its exact length, so that both measurements are performed with the LP and CP lenses at the exact same distance. A fine correction of the twist estimated length was done by measuring the phase of the reflected wave from a metal plate, as shown in Fig. 5.12b. In order to consider only the first order waves reflected at the metal plate, time gating has been applied to both measurements. After correcting the twist estimated length in +50μm, the phase error decreases from 15 deg to 2 deg in the whole frequency band. The reproducibility of this length correction has been verified by mounting the setup and performing the coupling measurements several times, and later on with near-field measurements.

Coupling measurements: In the quasi-analytic model, only the first order transmitted rays are considered. Therefore, time gating has been applied to the measurements, performed with the setup reported in Fig. 5.12a, in order to cancel the effect of multiple reflections. Fig. 5.13a shows the time-gated measurement for $c_{\parallel}$ and $c_{\perp}$ and the phase difference between both, in good agreement with quasi-analytic results. The AR has been calculated from the coupling measurements using $V_{\mathrm{oc}}^{\parallel} = c_{\parallel}$ and $V_{\mathrm{oc}}^{\perp} = c_{\perp}$, showing good agreement with the quasi-analytic results (Fig. 5.13b). Being $c_{\parallel}$ and $c_{\perp}$ the couplings related to respectively orthogonal field components, the power coupled from both measurements can be used to validate the antenna η_{rad}. The estimated η_{rad} and the one obtained from the coupling measurements are shown in Fig. 5.13b, excluding waveguide loss. The maximum difference between both is 0.5 dB, which includes measurement tolerances (coupling and twist characterization), tolerances in both LP and CP prototypes fabrication, and errors in the estimation of waveguide and dielectric losses. Both measurement setups are shown in Fig. 5.12c and Fig. 5.12d.

5.4.3 Near-Field Measurements

In order to obtain the far-field patterns for the broadside and steered beams, the lens near-fields have been measured with a linear polarized open-ended waveguide probe. Several positioning holes in the split-block allow placing the lens with integrated polarizer at different lateral positions w.r.t. the feed, in order to generate the broadside and steered beams, as shown in Chapter 4. Two measurements have been performed for each beam, rotating the LP probe polarization to characterize both orthogonal components. The twist S-parameters and length have been considered and compensated likewise. The near-fields have been measured on a $50 \times 50\,\mathrm{mm}^2$ plane with 680 µm distance between samples, 50 mm above the lens equivalent aperture. For the beams steering at 8.4 deg and 16 deg, the near-field measurement plane has been displaced laterally respectively 8 mm and 17 mm w.r.t. the lens center, in order to properly measure the field associated to the tilted rays.

The power ratio between both orthogonal LP near-field measurements for the broadside beam is coincident with the one estimated from the coupling measurements, as shown in Fig. 5.13a, confirming the consistency between both results. The normalized CP far-field patterns obtained from each pair of LP near-field measurements are shown in Fig. 5.8 and Fig. 5.9, with good agreement with the FW simulation results. Fig. 5.10a displays the measured maximum gain for the broadside and steered beams, including dielectric loss in the polarizer and lens. The gain has been estimated with the maximum directivity from the far-field measurements and the FW η_{rad} (Fig. 5.13b), validated with the coupling measurements. The gain for the steered beams has been normalized to the measured power radiated by the broadside beam, in order to account for the power scattered outside of the measurement plane. The differences between FW simulated and measured results are related to the measurement tolerances in the two near-field measurements, their relative position and phase, and fabrication tolerances. Fig. 5.7a shows the measured η_{ap} for the broadside beam, higher than 75 % in the whole frequency band. In Fig. 5.7b, the AR obtained from the measured CP far-field at broadside and steered beams is displayed, reaching a 3 dB AR relative bandwidth of 35 %. The measured far-field AR includes the effect of multiple reflections, as no time-gating has been applied. All results present good agreement with FW simulation results, validating the prototype performance, as well the phase calibration method applied (Fig. 5.12b). Table 5.1 presents a summary of the performance reached in our design, compared to the most relevant designs of CP antennas found in the literature.

5.5 Conclusions

In this chapter, a G-band lens with an integrated dielectric grid polarizer has been presented, achieving full-wave simulated aperture efficiency higher than 75 % and axial ratio lower than 3 dB over 35 % relative bandwidth. The CP lens reaches more than 30 dB of gain with only 0.65 dB dielectric loss. The proposed new polarizer unit cell presents excellent transmission properties over the whole bandwidth, and can be easily fabricated for these high frequency bands through standard milling techniques.

A semi-analytical model has been used to analyse the full system feed-polarizer-lens, based on SGF and an analysis in reception of the lens. This approach allows us to make a very time-efficient optimization of the feed-polarizer-lens system and presents very good agreement with the measurements. Thanks to this analysis and the novel polarizer unit cell, state-of-the-art performances have been reached with this CP lens antenna.

Ref.	f_0 (GHz)	Gain f_0 (dB)	-3 dB AR BW (%)	$\eta_{\text{ap}}^{\text{min}}$ (%)	L_σ^{max} (dB)	SLL$^{\text{max}}$ (dB)
[83]	29	20.8	> 14.6	17	2.3	-15
[86]	58.5	21.4	29	87.5	3	-12
[87]	34/500	11.2	> 35	-	-	-15
[32]	115	18	37	-	-	-10
[88]	140	31.7	> 28	55	1.9	-13
[46]	30	23.4	2.6	65	2	-10
This work	**180**	**34**	**35**	**75**	**0.6**	**−15**

Table 5.1: Measured performances of CP antennas. References in bolt present multi-beam capability. Values in italic have been estimated from the articles. L_σ comprises ohmic and dielectric loss.

Chapter 6

Dielectric Gratings Enhancing the Field of View in Low Dielectric Permittivity Elliptical Lenses

Low relative permittivity plastic elliptical lenses in combination with integrated focal plane arrays are a promising solution to be used in the future mm- and sub-mm wave systems, due to the availability of materials with moderate loss, light weight and cost-effective manufacturing techniques. However, the achievable scanning angular range is relatively small with low permittivity lenses. In this contribution, we explore the use of dielectric gratings with modulated height integrated in the lens material, with the aim of enlarging the steering angle. The dielectric gratings synthesize a tilted feed pattern, reducing the reflection loss and spill-over when illuminating the lens off-focus. A quasi-analytic approach based on Floquet mode analysis of the gratings is used to synthesize the grating profile in combination with an analysis in reception of the lens antenna. A wideband prototype in G-band (140–220 GHz) has been fabricated, achieving a Field-of-View of ±25 deg with gain larger than 30 dB at the center frequency.

6.1 Introduction

The growing interest for mm- and sub-mm- waves in mass-market applications, such as communications and radar, demands the development of low-cost system and front-end concepts. In these higher frequencies bands, high-gain antennas are required to compensate for the higher path spreading loss and lower available output power. Plastic lenses with low relative dielectric permittivity ($\varepsilon_r \sim 2.3$) represent attractive candidates to achieve

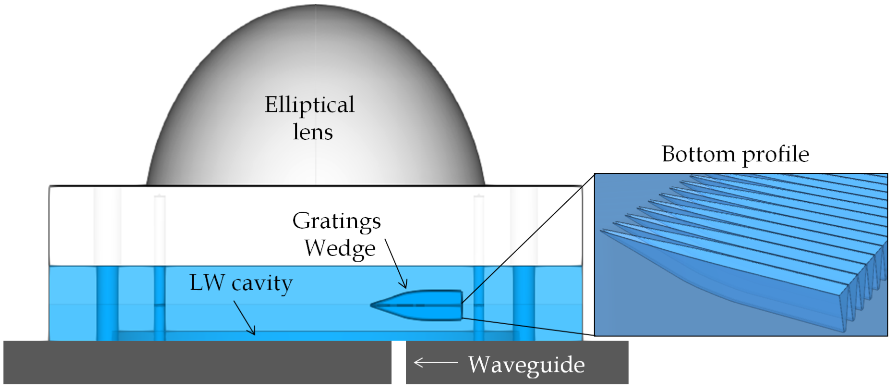

Figure 6.1: Dielectric gratings with modulated height integrated in an elliptical lens. On the right, detail of one of the grating layers.

the required high gain, due to their cost-effectiveness, light weight, and availability of materials with moderate loss. It has already been demonstrated that aperture efficiencies larger than 75 % can be achieved over 40 % bandwidth in linearly and circularly polarized elliptical lens designs, shown in Chapter 4 and Chapter 5. However, the low ε_r brings some penalty in terms of the beam steering achieved when displacing the feed within the focal plane. The particular case of truncated elliptical lenses with high aperture efficiency (η_{ap}) for the broadside beam was studied in Section 3.5. To reach high η_{ap} at broadside, a taper illumination of around -11 dB should be reached at the lens rim when placing the feed on the focus. This implies increasing spill-over and reflection losses when displacing the feed along the focal plane.

In this chapter, the use of dielectric gratings with modulated height, integrated inside a low ε_r elliptical lens, as shown in Fig. 6.1, is investigated. The aim is to enlarge the angular field of view achieved with the elliptical lens over a wideband, while maximizing η_{ap} over the whole scan range. This enables the implementation of multi-beam planar Fly's eye elliptical lens arrays sharing a common ground plane, as discussed in Chapter 1 for beyond 5G communications applications (Fig. 1.3), reaching a compact array size. In this work, we propose to reduce the spill-over and reflection loss performing a lateral displacement of the feed phase center by integrating, inside the elliptical lens, a wedge composed of dielectric gratings, on top of the wideband LW feed presented in Chapter 4. For this aim, gratings with decreasing effective permittivity create a linear phase shift in the feed fields inside the lens. The lower effective permittivity introduces as well a phase center displacement in z direction, which is taken into account in the optimization of the steered beams. The use of dielectric gratings has been proposed in the literature to synthesize planar lenses and reflectarrays [124, 125], polarizers [86] (and Chapter 5 in this dissertation), or lens matching layers [40, 126].

The antenna architecture is shown in Fig. 6.1, where the dielectric gratings are also displayed. This pyramidal grating geometry in one dimension is based on the one used to build the polarizer in Chapter 5, as it was proven to be suitable to be fabricated with standard milling techniques at frequencies higher than 100 GHz. This geometry presents good transmission properties over the whole frequency band, preserving the wideband capability. The dielectric-grating wedge (GW) is synthesized considering the incident field angles from the LW feed near-field calculated resorting to the multi-layer Spectral Green's Function, and applying a Floquet modes analysis of the grating, based on the Effective Medium Theory (EMT) [127, 128, 129, 130, 131, 132, 133, 134, 135, 136]. The scan loss for each steered beam in the elliptical lens is minimized with the analysis in reception (Chapter 2), performing a reaction integral on a flat surface defined inside the lens between the incident fields associated to an oblique plane-wave with the targeted beam steering, and the field radiated by the feed in transmission. The incident field is calculated inside the elliptical lens with the Geometrical Optics tool presented in [137].

A prototype at G-band has been fabricated and measured, showing ±25 deg of beam steering with 3.6 dB scan loss at the center frequency (180 GHz), which represents 4 dB improvement w.r.t. the case where the feed without GW is displaced along the focal plane. This improvement is achieved over a wide band. A Fly's eye row design with six lenses is proposed, covering ±25 deg FoV with 15 beams.

The chapter is organized as follows: Section 6.2 describes the dielectric-grating wedge concept and geometry; Section 6.3 describes the GW synthesis methodology; Section 6.4 describes the scan loss optimization with the analysis in reception; Section 6.5 shows the design of a complete Fly's eye row; Section 6.6 presents the prototype fabrication and measurements validating the concept; Section 6.7 provides some concluding remarks.

6.2 Dielectric-Grating Wedge Concept

In this section, the GW concept developed to enhance the FoV in elliptical lenses with low ε_r is discussed. The strategy followed in this work is to add a linear phase shift to the LW feed by using a non-periodic dielectric grating geometry (GW) integrated in the elliptical lens medium. The introduced linear phase shift, in turn, corresponds to a lateral displacement of the feed phase center, which enables a reduction of the spill-over and reflection losses for a certain steering angle.

The 1D pyramidal grating geometry which has been chosen is described as well in this section, analysing its transmission properties in a periodic configuration, with emphasis on the originated phase shift, for different wave incident angles and polarizations.

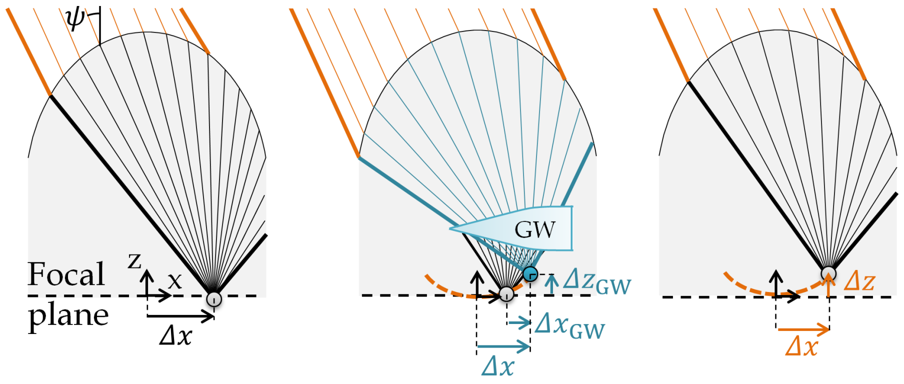

(a) (b) (c)

Figure 6.2: Conceptual ray tracing representation of a) feed phase center displaced Δx along the elliptical lens focal plane, b) gratings wedge integrated in the elliptical lens, introducing a virtual phase center displacement $[\Delta x_{\mathrm{GW}}, \Delta z_{\mathrm{GW}}]$ with respect to the original feed, and c) feed phase center optimized laterally and axially.

6.2.1 Leaky-Wave Feed with Dielectric Gratings Wedge

It is well known that by displacing the feed off-focus in integrated elliptical lenses, a beam steering is achieved in the lens radiation pattern [110]. The lateral feed displacement Δx required to achieve a beam steering angle ψ in a lens with focal distance F and dielectric permittivity ε_r, can be approximated as $\Delta x \approx F \sin\psi/\sqrt{\varepsilon_r}$ (Fig. 6.2a). For lenses with low ε_r, large displacements are required, and therefore, for a certain scan loss requirement, a small Field of View (FoV) is reached [110]. In Section 3.5, it is shown that for elliptical lenses with optimized truncation angles θ_{edge}, the FoV achieved with 3 dB scan loss when displacing the feed along the focal plane is ±15 deg with $\varepsilon_r = 2.3$, and reaches respectively ±27 deg and ±32 deg in the H- and E-planes for $\varepsilon_r = 12$.

The scope of this work is to enhance the steering capability of the elliptical lens with $\varepsilon_r = 2.3$, fed by the LW feed, presented in Chapter 4. Here, the LW is excited by a squared waveguide through a double-slot in the ground plane. For the broadside beam, this concept reaches 80 % η_{ap} over 40 % relative bandwidth, but due to the low ε_r it presents a relatively small FoV (±14 deg). In order to enhance the beam steering capability in this elliptical lens, dielectric gratings in the same low ε_r material ($\varepsilon_r = 2.3$) will be integrated on top of the LW feed, as shown in Fig. 6.1 and Fig. 6.2b. The gratings are designed to generate a linearly increasing phase shift in the LW feed field, inducing the desired phase center lateral displacement in the feed radiation pattern.

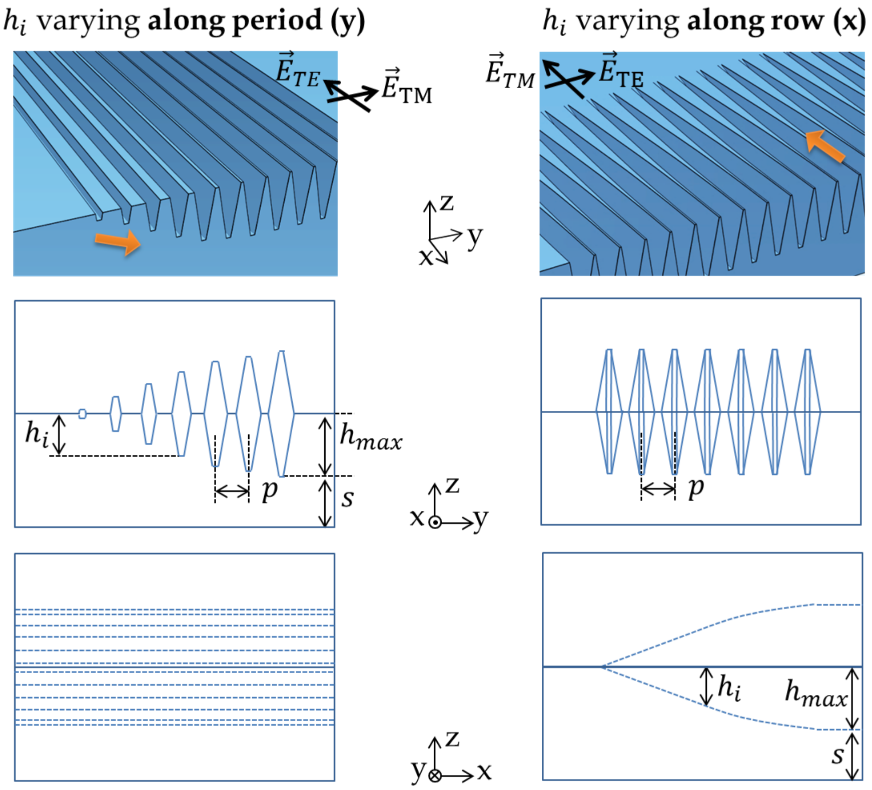

Figure 6.3: Gratings fabrication with different heights. The maximum pyramid height ($h_{\max} = 1.3\,\mathrm{mm}$) is set by the period between gratings and the tool angle ($\alpha = 9.3$ deg). The pyramidal grating height varies along a) the period or b) each row. The steering takes place in the TM plane.

Similar pyramidal gratings were used in Chapter 5 to produce circular polarization, exploiting the effective permittivity anisotropy in the gratings to generate 90 deg phase shift between two orthogonal linearly polarized waves. In this chapter, the height of the gratings is modulated, as shown in Fig. 6.3, leading to different effective permittivity. In contrast to the polarizer application, in this case the anisotropy axes are aligned with the field polarization, in order to avoid changes in the polarization. The use of this grating geometry is enabled by the fact that the LW feed radiates most of the energy below the critical angle between air and $\varepsilon_r = 2.3$. The low ε_r gratings provide wideband transmission coefficients (Chapter 5), and the feed impedance remains unchanged, enabling wideband steering enhancement.

By introducing a GW with varying height, leading to a linearly increasing phase shift, the initial feed phase center is displaced for the new system LW feed-GW in lateral and axial directions, as shown in Fig. 6.2b (Δx_{GW} and Δz_{GW}). Δx_{GW} is related to the linear phase shift introduced by the GW, and increases for larger phase variation; Δz_{GW} is caused by the lower effective permittivity of the GW with respect to the dielectric material, as already observed in Chapter 5. Thanks to this phase center displacement, the feed which should be originally placed on the coordinates $[\Delta x, \Delta z]$ to generate a beam pointing to ψ after the elliptical lens (Fig. 6.2c), will be now placed at $[\Delta x - \Delta x_{\mathrm{GW}}, \Delta z - \Delta z_{\mathrm{GW}}]$ to generate the same steering angle after the elliptical lens. In this way spill-over and reflection loss are reduced, increasing the taper efficiency, as shown in Fig. 6.2b. The goal is therefore to maximize the linear phase shift slope generated by the gratings wedge (GW), in order to minimize the scan loss. The position of the new system LW feed-GW w.r.t. the lens focus $[\Delta x, \Delta z]$ is optimized with the analysis in reception as explained in Section 6.4, considering an oblique incident plane-wave with the desired impinging angle. The optimum displacement $[\Delta x, \Delta z]$ for different steering angles defines a curved surface which allows a reduction of the phase loss, as shown in [48]. This effect is similar to what happens in optical systems, where different steering angles lead to the definition of the Petzval surface [138].

6.2.2 Gratings Geometry and Orientation

The gratings wedge is based on double-sided pyramids fabricated with constant slant angle, α, as set by the standard milling tool slant angle [119]. The geometry of one pyramid is shown in the inset of Fig. 6.4b, where the only variable is the grating height h, related to the tool penetration in the dielectric. The grating rows are milled at a periodic distance $p = 550\mu\mathrm{m}$, avoiding grating lobes for incident angles up to 40 deg until 215 GHz. For larger incidence angles the LW feed presents very low radiated power Chapter 4. t_{bot} and α are set by the tool tip width and slant angle respectively. The maximum height achieved in the gratings for the chosen tool slant angle $\alpha = 9.3$ deg is $h_{\max} = 1.27\,\mathrm{mm}$, set by the minimum $t_{\mathrm{top}} = 30\mu\mathrm{m}$ (Fig. 6.4b), to avoid breaking the grating in the milling process. $h_{\max}$ sets the maximum phase shift that can be achieved with one layer of gratings.

The grating height variation can be performed along each row or along the period, as shown in Fig. 6.3. 1D gratings present anisotropic properties in their effective dielectric permittivity [127], and therefore depending on the grating orientation with respect to the field polarization, different phase shifts are reached for the same geometry. In order to perform an estimation of the transmission coefficients for a certain pyramid height, plane-wave incident angle, and field polarization, a Floquet mode model (FqW) assuming local periodicity has been implemented, based on a z-discretization of the pyramid in infinitesimal dielectric cubes, each of them modelled with EMT (EMT-FqW). The methodology, which takes into account the structure anisotropy, is discussed in Appendix B.

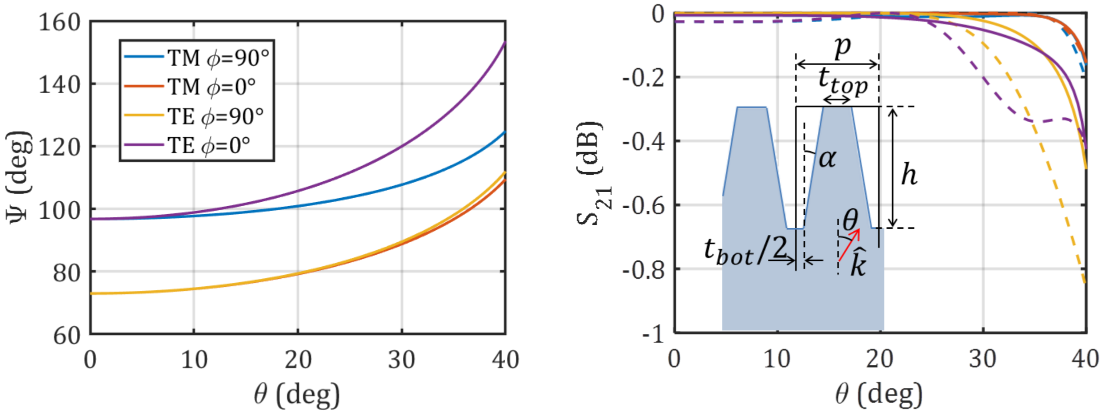

(a) (b)

Figure 6.4: a) Phase shift Ψ introduced by the pyramidal unit cell with $h = h_{\max}$ w.r.t. a unit cell of the same height filled with dielectric, w.r.t. the angle in the dielectric θ and the azimuth steering angle ϕ. The reference system and field polarization are shown in Fig. 6.3. b) Unit cell transmission coefficient (S_{21}) for the same polarization and ϕ steering planes as in a). Solid lines: single pyramid with $h = h_{\max}$. Dashed lines: two pyramids with $h = h_{\max}$ facing each other. Inset: Grating geometry, where $p = 550\,\mu\text{m}$, $t_{\text{bot}} = 100\,\mu\text{m}$, $\alpha = 9.3$ deg, and $t_{\text{top}} = p - t_{\text{bot}} - 2h\tan\alpha$.

The linear phase shift synthesized on top of the GW is evaluated, assuming local periodicity, as the phase difference between the phase of the field radiated by the LW in a homogeneous medium and the one of the LW in the presence of the grating geometry, at the same plane. Therefore the relevant design parameter is the phase shift Ψ, along the longitudinal component z, between a pyramidal unit cell with height h and a unit cell of the same height filled with dielectric. This is calculated with respect to the incident angle θ in the homogeneous medium and the polarization as follows:

$$\Psi(\theta, h) = k_{zd}h - \Phi^{\text{TE/TM}}(\theta, h) \tag{6.1}$$

where $k_{zd} = k_d \cos\theta$, k_d is the propagation constant in the dielectric and $\Phi^{\text{TE/TM}}$ is the phase of the scattering parameter $S_{21} = |S_{21}|e^{j\Phi}$ calculated by EMT-FqW for the evaluated grating, for the TE or TM mode. Assuming local periodicity and plane wave incidence, the phase shift associated to the transversal propagation component (k_ρ) cancels out and is therefore not present in Eq. (6.1), as it is derived from Snel's law. The resulting phase shifts for different polarizations and cell orientations are plotted in Fig. 6.4a for $h = h_{\max}$, for the range of incident elevation angles where the LW feed radiates significant power. This phase shift is the maximum that can be implemented in a single layer of gratings. The phase shift increases for larger elevation angles. On top of that, for scanning enhancement in the E-plane (TM mode), the favorable grating modulation plane to maximize the phase shift is $\phi = 90$ deg, whereas for the H-plane (TE mode) the optimum is $\phi = 0$ deg (reference system in Fig. 6.3). Fig. 6.4b shows the unit cell transmission amplitude properties for the same cases considered in Fig. 6.4a.

By using pairs of mirrored gratings, as displayed in Fig. 6.3, the transmission coefficients of the GW embedded in the elliptical lens are enhanced, as shown in Fig. 6.4b (dashed lines), and the maximum synthesizable phase shift is at the same time doubled.

6.3 Grating Wedge Synthesis

In this Section, the synthesis procedure to design the GW profiles is described. A GW with a pair of mirrored grating layers and $\phi = 0$ deg orientation to enhance the steering in the H-plane is designed, as shown in Fig. 6.5 on the right. The GW synthesis is performed iteratively using an approximated ray tracing via the application of the implemented EMT-FqW model for the gratings (Appendix B). First, the requirements in terms of phase shift to be introduced by the GW are derived. Next, the steps to design the GW profile, to reach the given phase profile at its top, are clarified, together with the taken approximations in the ray tracing procedure. Finally, the synthesis and results are shown, comparing the achieved phase profile in a FW simulation with the required one.

6.3.1 Phase Shift Requirement for Gratings Wedge

The linear phase shift requirement on top of the GW, Ψ_t, is defined at $z_t = 4.54\,\text{mm}$ (Fig. 6.5 on the center) within $x = \pm 3.34\,\text{mm}$, where the LW near-field amplitude edge taper is $-8\,\text{dB}$ at z_t (Fig. 6.6a). The coordinates z_b, z_c, and z_t in Fig. 6.5 are known, assuming that each grating layer will reach the height $h_{\max}$ at its edge, and considering that the grating should be supported by a dielectric layer of at least 1 mm thickness, due to fabrication restrictions (s in Fig. 6.3 and Fig. 6.5). The chosen amplitude taper results in a good compromise between maximizing the phase slope synthesized and preserving the near-field amplitude after the GW, as it will be discussed in Section 6.4. Let's define Ψ_t as the linear phase associated to a θ_{FF} steering angle in the feed far-field inside the lens as

$$\Psi_t(x) = k_d x \sin\theta_{\text{FF}} \tag{6.2}$$

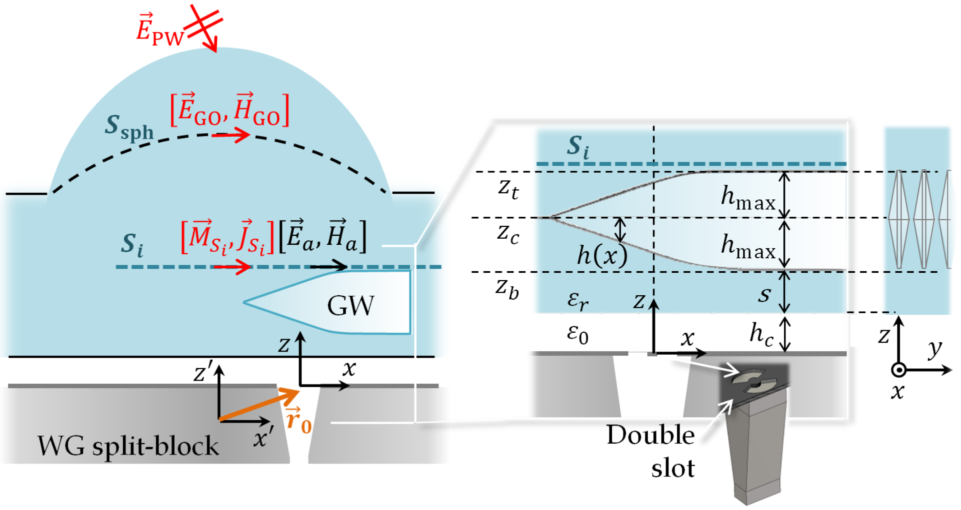

Figure 6.5: Left: antenna geometry, fields and currents used for the analysis in reception. The coordinate system $[x', z']$ is centered in the ellipse focus; $[x, z]$ is centered in the double-slot feed. Right: 2D drawing of the synthesized gratings wedge. The gratings height varies along each row, as shown in Fig. 6.3 on the right. The blue area represents the dielectric, the shaded area the pyramids and the white area the air. $h_c = 940\,\mu\text{m}$, $h_{\text{max}} = 1.27\,\text{mm}$, $s = 1\,\text{mm}$, $z_t = 4.54\text{mm}$, S_i at $z = 4.7\,\text{mm}$. The side view of the gratings is shown, where the pairs of mirrored pyramids to reduce reflection are visible.

The GW, which is thick in terms of wavelength ($2h_{\text{max}} > 2\lambda_d$, being λ_d the wavelength in the dielectric), is divided in two mirrored layers. Each layer will be assigned with half of the required phase shift, and thus the requirement defined at z_t, Ψ_t, is propagated backwards to z_c and divided by two, in order to synthesize the mirrored profiles. This backward propagation is performed with an approximated ray tracing, using the wave propagation direction in the homogeneous medium of the LW without gratings, as shown in Fig. 6.7a. The mapped phase requirement at z_c, Ψ_c, is calculated as

$$\Psi_c(x) = \Psi_t(x \pm \Delta x_0(x))/2 \tag{6.3}$$

for $x \gtrless 0$, where $\Delta x_0(x) = h_{\text{max}} \tan \theta_t(x)$, being θ_t calculated from the LW feed wave propagation vector at $z = z_t$, $\hat{k}_t$.

The wave propagation angles, for the requirement mapping as well as later on for the lens synthesis, are approximated by using the Poynting vector direction of the LW feed near-field without lens (Fig. 6.6b), calculated as $\theta = \cos^{-1}(\hat{z} \cdot \hat{k})$, where $\hat{k} = \vec{S}/|\vec{S}|$ with $\vec{S} = 1/2\,\mathfrak{Re}\{\vec{E} \times \vec{H}^*\}$, being $\vec{E}$ and $\vec{H}$ the LW feed electric and magnetic near-fields. The LW feed near-fields are calculated integrating the corresponding SGF (Eq. (A.1) in Appendix A) and current distribution of the LW feed (Eq. (3.1)). Although the far-field

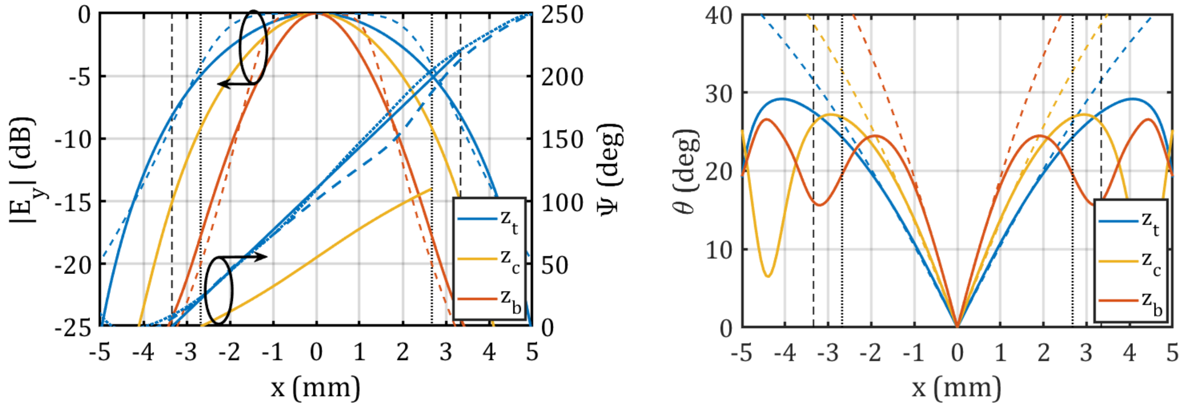

(a)

(b)

Figure 6.6: a) Left axis: LW feed field amplitude (without GW) in the H-plane at 180 GHz at the z coordinates marked in Fig. 6.5. Solid line: near-field calculation. Dashed line: far-field calculation projected in the z-planes. Right axis: phase shift w.r.t. the LW without GW. Solid: requirements Ψ_t (blue line) and Ψ_c (yellow line). Dashed: FW simulations with the first calculated profile, h_0. Dotted: FW simulations with the final calculated profile, h. b) Poynting vector direction for the field and planes shown in a). Solid: calculated from the near-fields. Dashed: geometric approximation ($\theta = \tan^{-1}[x/(z-\Delta z)]$), being $\Delta z = -950\,\mu\text{m}$ the far-field phase center displacement in z w.r.t. the LW ground plane. In both plots, vertical dashed lines mark the limits within Ψ_t is defined, and vertical dotted lines where Ψ_c is defined.

approximation gives already relatively good results for the field amplitude taper at z_i, as shown in Fig. 6.6a, the near-field propagation direction is more accurate at the grating edges, as shown in Fig. 6.6b.

In order to approximately estimate the maximum phase shift that can be obtained at the edge of the GW, the incident angles of the field that impinges each layer at the maximum x_n should be considered. The first profile iteration is calculated with the phase requirement defined at z_c, Ψ_c. Therefore, the x-boundaries calculated with the approximate ray tracing, within Ψ_c is defined, will be taken as reference (marked in Fig. 6.6 with vertical dotted lines). In Fig. 6.6b, it can be seen that, at these boundaries, the incident angle stays below 25 deg and 30 deg in z_b, z_c, and z_t. Considering these incident angles, and the phase shift reached with a grating with $h_{\max}$ (Fig. 6.4a), it can be concluded that a maximum phase shift of 110 deg −120 deg can be achieved per grating layer. For the two layers, we finally set a linearly increasing phase shift requirement Ψ_t from 0 deg to 220 deg at z_t (Fig. 6.6a). This corresponds to approximately $\theta_{\text{FF}} = 5.7$ deg at 180 GHz Eq. (6.2). Fig. 6.6a shows the phase shift requirements at z_t and z_c.

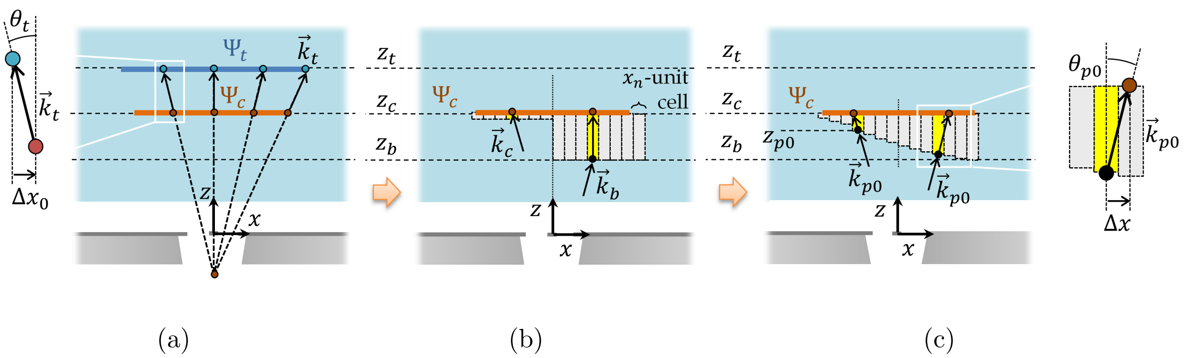

Figure 6.7: a) Phase requirement at GW top and center z-planes. b) Unit cell mapping and incident angles for GW profile synthesis in first iteration, c) Unit cell mapping and incident angles in second iteration.

6.3.2 Synthesis of Grating Wedge Profile

In the following, we describe the synthesis process for the grating layer pair forming the GW (Fig. 6.5). As explained in the previous section, the phase shift requirement has been defined at z_c, where the GW is centered, as Ψ_c (Fig. 6.7a). The GW is discretized in unit cells with x-coordinates x_n, representing two mirrored pyramids (Fig. 6.5 on the right) with respectively unknown height $h(x_n)$, being $h_{\max}$ is the maximum achievable height (Fig. 6.5). The grating height $h(x_n)$ can be determined applying the EMT-FqW model, starting from a certain incident angle and required phase shift on each unit cell.

However, the assignment of the phase shift requirement to a certain unit cell and the unit cell height calculation cannot be decoupled, as they are related by the gratings geometry itself. The definition of a grating surface equation to find this relationship is not a trivial task, for several reasons: 1) the propagation angle inside the pyramid changes with z and does not have a closed form (see Appendix B); 2) when considering unit cells with infinitesimal width, each ray crosses laterally unit cells with different heights, which should be considered in form of a graded effective permittivity in x direction; 3) the incident wave has a spherical phase front, and consequently different incident angles along x direction should be taken into account.

In this work, a simplified iterative approach is proposed to derive the gratings profile, reaching sufficient accuracy in the synthesized phase shift feature with two iterations. The lateral wave propagation cannot be neglected due to the grating significant and variable thickness (up to $\sim 0.75\lambda_0$ per layer) and the wide incident angles associated to the LW feed (up to 30 deg). Therefore, already in the first iteration, displayed in Fig. 6.7b, the lateral propagation is taken into account by evaluating the phase requirement at the center of the layer pair, z_c in Fig. 6.5.

The phase shift requirements are assigned to each x_n-unit cell as shown in Fig. 6.7b, and the pyramid height h_0 at each x_n is then approximated solving

$$\Psi_c(x_n) = k_d \cos[\theta(x_n)] h_0(x_n) - \Phi^{\mathrm{TE}}[\theta(x_n), h_0(x_n)] \tag{6.4}$$

where k_d is the propagation constant in the dielectric, $\theta(x_n)$ is the propagation angle in the dielectric considered for the x_n-unit cell and $\Phi^{\mathrm{TE}}(\theta, h_0)$ is the phase evaluated with the equivalent EMT-FqW model at z_c.

As the gratings profile is unknown, to evaluate the incident angle in the first step, we assume that the lens will reach the maximum thickness on the right side, $h_{\max}$, and we divide the grating surface in two regions:

- For $x_n < 0$, it is assumed that the gratings will have a small height, as the required phase difference is small in this region. Therefore, a good approximation for the incident angle on the unknown grating surface, $h(x_n, z_n)$, is the one dictated by the LW feed Poynting vector at z_c ($\hat{k}_c(x_n)$ in Fig. 6.7b).
- For $x_n > 0$, it is assumed that the gratings will have a large height, to create large phase shifts. A good approximation for the incident angle on the unknown grating surface, $h(x_n, z_n)$, is the one dictated by the LW feed Poynting vector at $z_b = z_c - h_{\max}$ ($\hat{k}_b(x_n)$ in Fig. 6.7b).

Assuming these incident angles, resorting to Eq. (6.4), we estimate the first approximation for the profile, h_0, shown in Fig. 6.8.

After that a first approximation for the profile is known, $z_{p0}(x_n) = z_c - h_0(x_n)$, a refinement with a second iteration is performed. This time, the incident angle and phase requirement can be evaluated along the GW bottom profile calculated in the first iteration, z_{p0}, as shown in Fig. 6.7c. In this way, the final grating profile h is synthesized solving

$$\Psi_c[x_n \pm \Delta x(x_n)] = k_d \cos[\theta_{p0}(x_n)] h(x_n) - \Phi^{\mathrm{TE}}[\theta_{p0}(x_n), h(x_n)] \tag{6.5}$$

for $x \gtrless 0$, where $\Delta x(x_n) = h_0(x_n) \tan[\theta_{p0}(x_n)]$, and θ_{p0} is calculated from $\hat{k}_{p0}$ (Fig. 6.7c). By approximating the propagation vector inside the gratings by the propagation vector $\hat{k}_{p0}$ in the dielectric (denser medium), an error is introduced in the calculated Δx. The maximum error can be evaluated comparing Δx estimated with $\hat{k}_{p0}$ in the dielectric, with

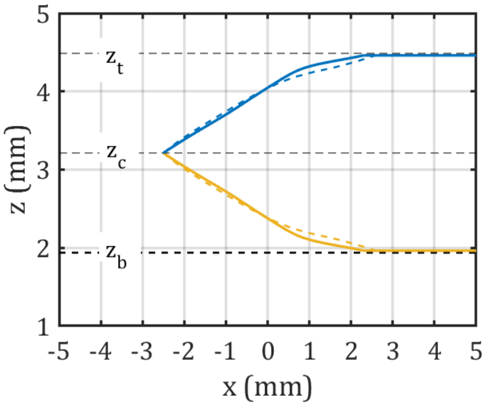

Figure 6.8: Initial (dashed line) and final (solid line) GW profiles, h_0 and h, respectively.

the transmitted angle in a unit cell with the lowest effective permittivity, $\varepsilon_{\text{eff}} \sim 1.4$ (for $h_i = h_{\max}$). Taking into account the maximum angle in the dielectric, $\theta_{p0} \sim 30$ deg, the transmitted angle for $\varepsilon_{\text{eff}} \sim 1.4$ is 38 deg, resulting in a committed error in Δx of 270 µm ($< \lambda_d/4$).

The initial and final calculated layer profiles are shown in Fig. 6.8. As shown as well in Fig. 6.5, for $x > 0$ the lens is extended further with dummy gratings with maximum height until the field taper reaches -20 dB at z_t (5.5 mm) at the center frequency. This avoids an abrupt change in the boundary conditions, which would degrade the grating transmission properties. For the same reason, in y-direction, the gratings are periodically repeated to cover the area with a field taper larger than -20 dB (± 5.2 mm).

6.3.3 Full-Wave Simulation Results

The synthesized GW in the presence of the LW feed has been FW simulated with EMPIRE XPU [112]. The FW simulations include the effects of multiple reflections in the GW. The phase difference obtained between the LW near-fields without and with gratings at S_i, $z = 4.7$ mm, is shown in Fig. 6.6a, in good agreement with the defined Ψ_t. For the profile calculated in the first iteration, h_0, the maximum error in the synthesized phase shift is 20 deg, whereas for the profile calculated in the second iteration, h, the error is reduced to 7 deg. The impact of this accuracy in the scan loss of the elliptical lens will be evaluated in Section 6.4.

The LW near-field amplitude and phase without and with GW at S_i are shown in Fig. 6.9, with the reference system in Fig. 6.5. The results correspond to the profile

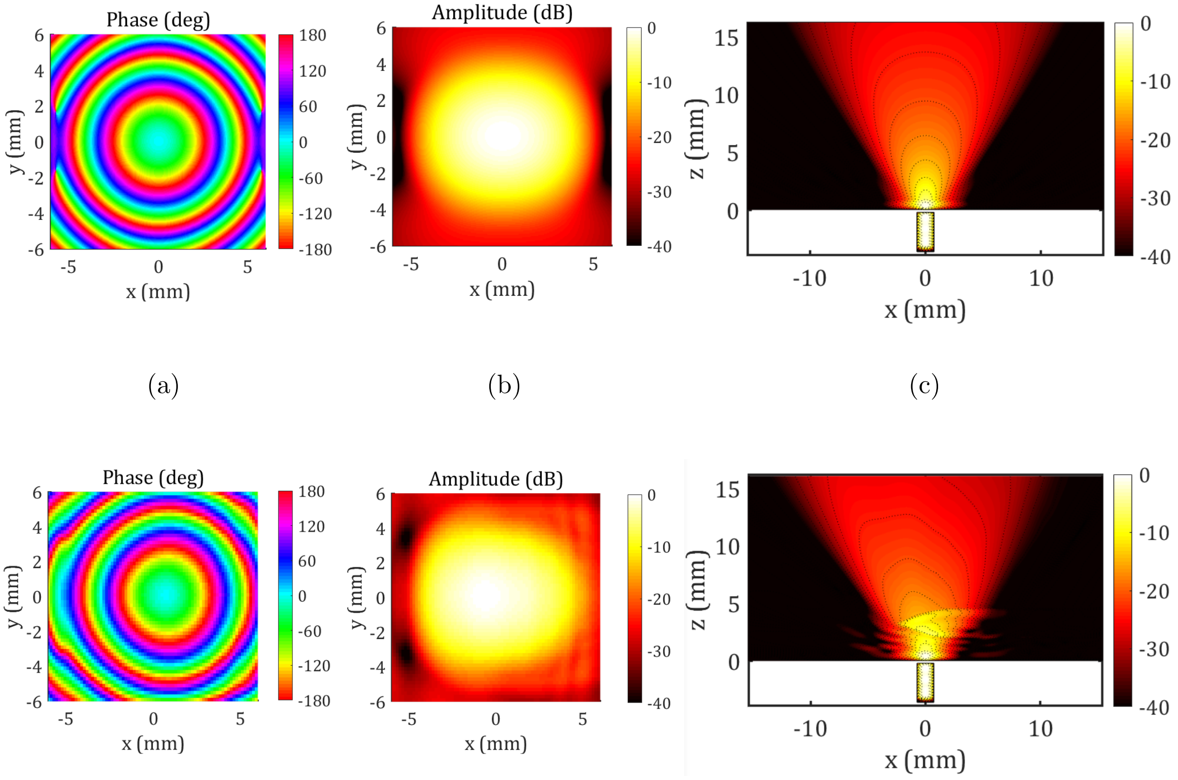

(a) (b) (c)

(d) (e) (f)

Figure 6.9: Near-field phase and amplitude at S_i and $y = 0$ (Fig. 6.5) for a), b), c) LW feed without GW, d),e), and f) LW feed with GW.

calculated in the second iteration. It can be seen that the near-field amplitude changes after the GW with respect to the LW field radiating in a homogeneous medium. This effect is related to the tilt in the field propagation, associated to the synthesized linear phase, which is already visible after the GW (Fig. 6.9f). The obtained amplitude effect is positive in terms of the lens scan loss, as it will be discussed in Section 6.4. The near-field obtained at S_i after the GW in the FW simulations is used in the analysis in reception explained in Section 6.4 to minimize the scan loss for a certain beam steering direction.

6.4 Scan Loss Optimization: Analysis in Reception

In order to maximize the elliptical lens η_{ap} for a beam steering to a certain angle, an analysis in reception of the full antenna system (LW feed, GW, and elliptical lens) is proposed (Chapter 2). The optimization parameter is the displacement vector $\vec{r_0}$ of the LW feed-GW system inside the elliptical lens, with respect to its focus (Fig. 6.5 on the left).

The η_{ap} can be calculated dividing the power P_L delivered to the matched load connected to the feed in reception operative mode, from a plane wave $\vec{E}_{\text{PW}}$ with a certain oblique incident direction, $(\vec{k}_i)$. In order to optimize the scanning performance in a certain direction, the fields $[\vec{E}_{\text{GO}}, \vec{H}_{\text{GO}}]$ are evaluated at S_{sph} (Fig. 6.5 on the left) using the tool in [137] for a plane wave incident from the targeted direction.

In Chapter 2, $|V_{\text{oc}} I_{\text{tx}}|$ is calculated by performing a reaction integral over a spherical surface inside the elliptical lens centered on the focus, S_{sph} in Fig. 6.5, between the Geometrical Optics field, $[\vec{E}_{\text{GO}}, \vec{H}_{\text{GO}}]$, generated by a plane wave incident onto the lens, and the fields radiated by the lens feed in an infinite medium, $[\vec{E}_a, \vec{H}_a]$. In the case considered in this chapter, since the proposed grating is electrically thick, one cannot use a far field approximation to evaluate the fields $[\vec{E}_a, \vec{H}_a]$ in S_{sph}. It is therefore more convenient in this case to calculate the reaction integral directly over S_i (instead of S_{sph}), using the FW simulation of the GW, as follows:

$$V_{\text{oc}} I_{\text{tx}} = \iint_{S_i} (\vec{H}_a \cdot \vec{M}_{S_i} - \vec{E}_a \cdot \vec{J}_{S_i}) dS \tag{6.6}$$

where $[\vec{E}_a, \vec{H}_a]$ are the feed near-fields in S_i including the GW, estimated with FW simulations including multiple reflections (Fig. 6.9), and $[\vec{M}_{S_i}, \vec{J}_{S_i}]$ are the equivalent currents induced at S_i by the fields $[\vec{E}_{\text{GO}}, \vec{H}_{\text{GO}}]$ for the specific analysed plane wave direction. The fields at S_{sph}, $[\vec{E}_{\text{GO}}, \vec{H}_{\text{GO}}]$, are propagated inside the lens and calculated at S_i with the Green's Function for homogeneous media to obtain the incident fields at S_i, $[\vec{E}_i, \vec{H}_i]$. The induced currents at S_i can be calculated as $\vec{J}_{S_i} = \hat{n} \times \vec{H}_i$ and $\vec{M}_{S_i} = -\hat{n} \times \vec{E}_i$ where $\hat{n}$ is the normal to the surface S_i, in our case $\hat{n} = \hat{z}$.

The reaction integral in Eq. (6.6), and therefore η_{ap}, is maximized when the conjugate of $[\vec{E}_a, \vec{H}_a]$ is equal to $[\vec{E}_i, \vec{H}_i]$. For a known $[\vec{E}_a, \vec{H}_a]$ over a plane, and a known incident plane wave angle, the plane where $[\vec{E}_i, \vec{H}_i]$ presents an optimum match with $[\vec{E}_a, \vec{H}_a]$ in terms of phase and amplitude should be found inside the elliptical lens. The vector $\vec{r_0}$ defines the optimum relative position between $[x', z']$ and $[x, z]$ (Fig. 6.5) where the LW feed-GW system should be displaced to minimize the scan loss.

Applying the described analysis in reception, $\vec{r_0}$ for the LW feed-GW system has been optimized for the beam steering at 25 deg to minimize the scan loss. The lens diameter ($18\lambda_0 = 30\,\text{mm}$), elliptical lens truncation angle (40 deg) and LW feed geometry correspond to the reported in Chapter 4. The resulting optimum displacement is $\vec{r_0} = \Delta x \hat{x} + \Delta z \hat{z}$,

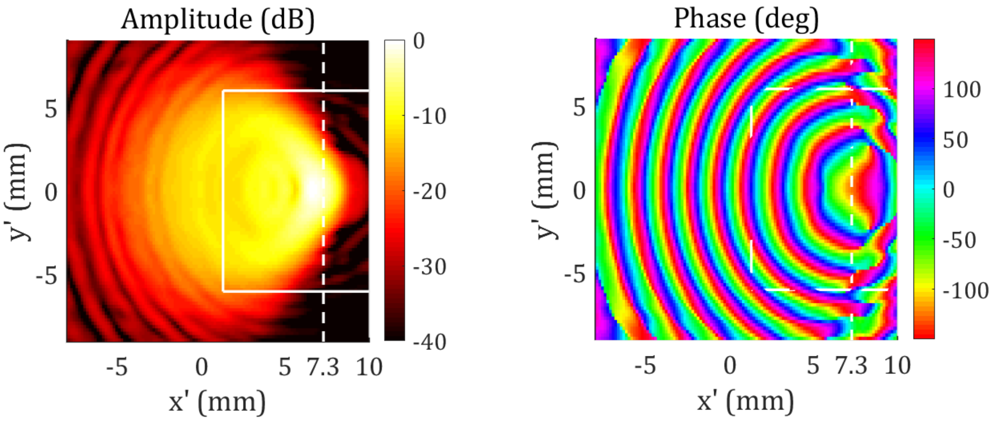

(a)

(b)

Figure 6.10: Incident field $\vec{E}_i$ at $z' = 8.7\,\text{mm}$ for a y-polarized plane-wave with 25 deg oblique incidence, considering an elliptical lens with $\varepsilon_r = 2.3$, $D = 30\,\text{mm}$ and truncation angle 40 deg, at 180 GHz. a) Amplitude, b) Phase. Reference system $[x', y']$ as defined in Fig. 6.5. For reference, the plane $y = 0$ for the LW feed-GW system has been marked with dashed white lines, and the range where Fig. 6.9e is plotted with solid white lines.

with $\Delta x = 7.3\,\text{mm}$ and $\Delta z = 4\,\text{mm}$. Fig. 6.10 shows the incident field amplitude and phase for a 25 deg incident plane-wave in the plane $z' = 8.7\,\text{mm}$, where the best field match to the field transmitted after the gratings at S_i (Fig. 6.9), $z = 4.7\,\text{mm}$ in Fig. 6.5, is found.

The η_{ap} in the beam pointing at 25 deg for the optimized feed with GW is $-4.4\,\text{dB}$ at 180 GHz, estimated with the analysis in reception. The contributions to η_{ap} are: phase efficiency $-1\,\text{dB}$, spill-over and reflection efficiency $-2.6\,\text{dB}$, taper and polarization efficiency: $-0.7\,\text{dB}$. This leads to a scan loss, with respect to the η_{ap} of the broadside beam reported in Chapter 4 with the same LW feed, of only $-3.6\,\text{dB}$, which is a significant improvement w.r.t the $-7.8\,\text{dB}$ that one would get by displacing the feed in the focal plane, as in Section 3.5. The good performance was achieved by choosing a good compromise between field taper at the edge of the grating and phase slope. Indeed, considering the same feed location, optimized for the feed with gratings, the amplitude modification in the LW feed field originated by the gratings (Fig. 6.9e) enhances the taper efficiency in approx. 1 dB, with respect to the amplitude characteristic in the LW feed without gratings (Fig. 6.9b).

For the sake of comparison, the analysis in reception has been as well applied to optimize $\vec{r}_0$ for 25 deg steering for the LW feed without gratings. The cases where the feed is displaced along the focal plane (Fig. 6.2a) and where its position has also been optimized axially (Fig. 6.2c) have been evaluated. Fig. 6.11a compares the FW simulated radiation

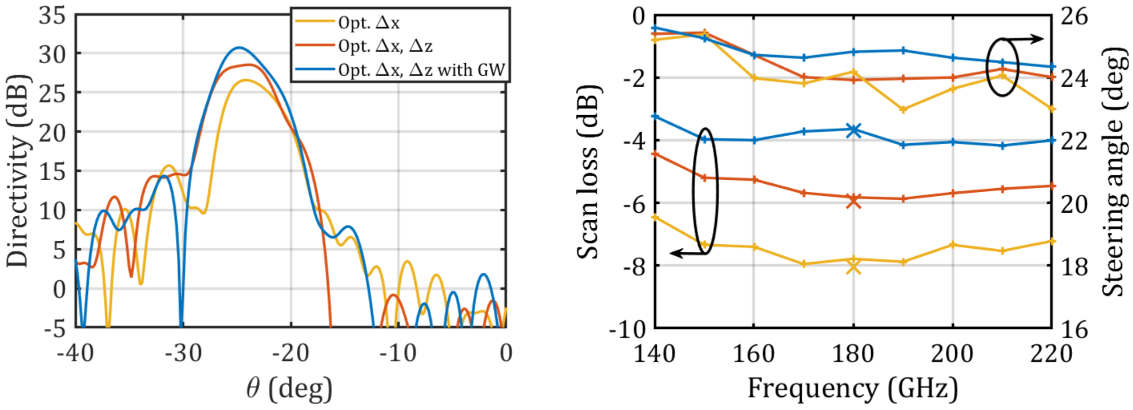

(a) (b)

Figure 6.11: a) FW simulated radiation pattern comparison for beam steering to 25 deg on the H-plane at 180 GHz for 1) the LW feed displacing along the focal plane (yellow line), 2) the LW feed position optimized laterally and axially (red line), and 3) the LW feed with GW optimized laterally and axially (blue line). b) FW simulated scan loss (w.r.t. the η_{ap} of the broadside beam reported in Chapter 4) and scan angle over frequency for the beam pointing at 25 deg, for the three configurations listed in a). The crosses represent the scan loss calculated with the analysis in reception.

patterns at the center frequency for the beams pointing at 25 deg for 1) the LW feed displacing along the focal plane ($\Delta x = 8.9\,\mathrm{mm}$) (yellow line), 2) the LW feed position optimized laterally and axially ($\Delta x = 7.6\,\mathrm{mm}$, $\Delta z = 5\,\mathrm{mm}$) (red line), and 3) the LW feed with GW optimized laterally and axially ($\Delta x = 7.3\,\mathrm{mm}$, $\Delta z = 4\,\mathrm{mm}$) (blue line). Here, the beam symmetry and directivity improvement with the GW can be appreciated. Moreover 2 dB higher aperture efficiency is achieved at the center frequency thanks to the proposed GW.

In Fig. 6.11b, the scan loss and steering angle over frequency are displayed for the 25 deg beams, showing wideband scan loss improvement. The scan loss is better than $-4.1\,\mathrm{dB}$ in the whole frequency band, with respect to the broadside beam reported in Chapter 4. The improvement w.r.t. the cases without GW is higher than 1.2 dB over the whole bandwidth. The steering angle is more stable for the lens with GW over the whole frequency band, due to the lower impact of multiple reflections.

Fig. 6.12 shows the FW simulated radiation patterns. The the maximum level of the cross-polar with respect to the maximum of the co-polar is lower than $-15\,\mathrm{dB}$ over the whole frequency band. The FW simulated ratio between the maximum cross- and co-polar levels has been displayed in Fig. 6.12d for the broadside beam presented in Chapter 4, for

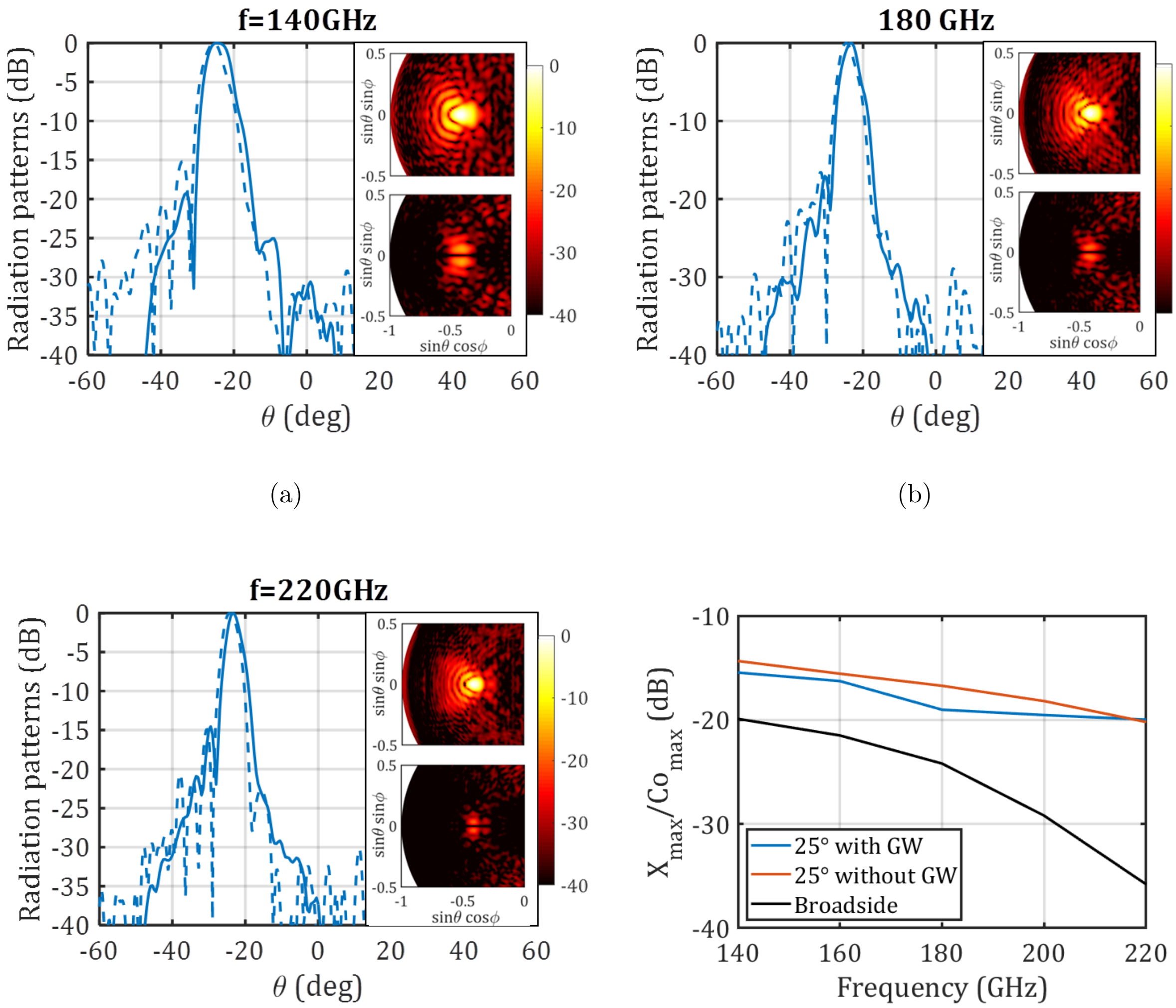

(a) (b)

(c) (d)

Figure 6.12: Radiation patterns for the elliptical lens with integrated GW. Dashed line: FW simulations; solid line: measurements. The inset shows the FW simulated far-field: co-polar (top) and cross-polar (bottom). a) 140 GHz, b) 180 GHz, c) 220 GHz. d) FW simulated ratio between the maximum cross- and co-polar level. The curve without GW corresponds to the feed position optimized laterally and axially.

the beam pointing at 25 deg with the feed positioned in the optimized phase center (axially and laterally), and for the beam pointing at 25 deg with the feed with GW, positioned as well in the optimized phase center. It can be concluded that the cross-polar level does not increase with the use of the GW, but due to the off-focus displacement of the feed.

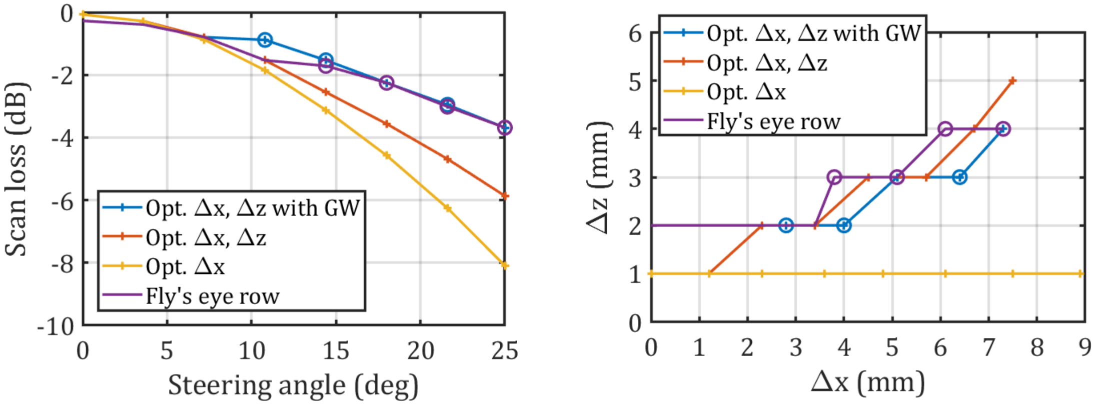

(a) (b)

Figure 6.13: a) Scan loss comparison for elliptical lens steering on the H-plane with 1) the LW feed displacing along the focal plane (yellow line), 2) the LW feed position optimized laterally and axially (red line), 3) the LW feed with GW optimized laterally and axially (blue line), and 4) compact Fly's eye row (purple line). b) Δx and Δz for the beams reported in a). The circles represent the cases where the GW has been used. The scan loss is calculated w.r.t. the broadside beam from Chapter 4 (lens without GW), displayed in Fig. 6.14.

Applying the analysis in reception, $\vec{r}_0$ has been optimized in terms of scan loss for different steering angles, in order to cover the whole targeted steering range (± 25 deg) with multiple simultaneous beams crossing at -3 dB. For an elliptical lens with 30 mm diameter (~ 34 dB directivity at the center frequency), a steering range of ± 25 deg can be covered with 15 beams. The LW feed geometry and elliptical lens truncation angle are for all beams the same as in Chapter 4.

The scan loss for each beam, calculated with the analysis in reception, is shown in Fig. 6.13a, and the corresponding Δx and Δz values in Fig. 6.13b. Only the beams with scan loss higher than 3 dB have been provided with a GW. For the sake of comparison, the results for the LW feed without GW, optimized along the focal plane and also axially, are also shown. Fig. 6.14 shows the radiation patterns with GW for the beams pointing at 14.4 deg, 21.6 deg and 25 deg estimated with FW simulations.

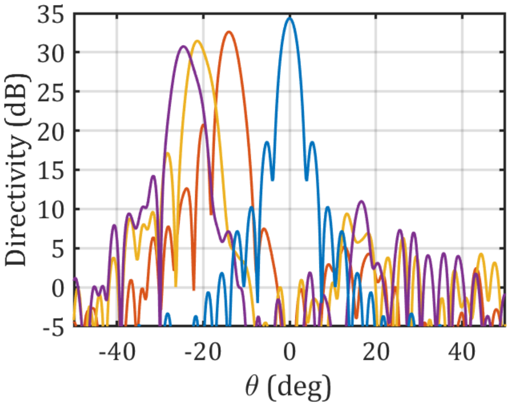

Figure 6.14: Directivity including multiple reflections for the beams pointing at 14.4 deg (red line), 21.6 deg (yellow line), and 25 deg (purple line), all for the lens with GW, simulated with EMPIRE XPU (H-plane). The broadside beam from Chapter 4 (without GW) has been included as reference (blue line). The feed Δx and Δz corresponds to the one reported in Fig. 6.14b (optimized Δx and Δz with GW).

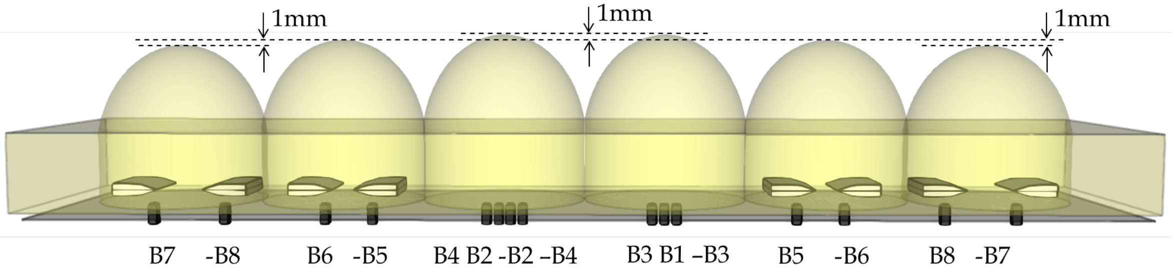

Figure 6.15: Compact Fly's eye row.

6.5 Fly's Eye Array

Applying the analysis in reception introduced in Section 6.4, a planar Fly's eye row of lenses has been optimized in terms of scan loss in order to cover the whole targeted steering range (±25 deg) with multiple simultaneous beams crossing at -3 dB. Here, feeds sharing a common ground plane have been considered (Fig. 1.3). In order to reach a more compact Fly's eye row, the 15 beams can be distributed in only 6 lenses as shown in Fig. 6.15. Only the beams with scan loss higher than 3 dB have been provided with a GW. Note that, in order to integrate two beams under the same lens, sharing a common ground plane, the same Δz should be set for both. This compromise, which impacts minimally in the scan loss performance, enables as well the fabrication of all layers of gratings in the Fly's eye array in the same layer of dielectric.

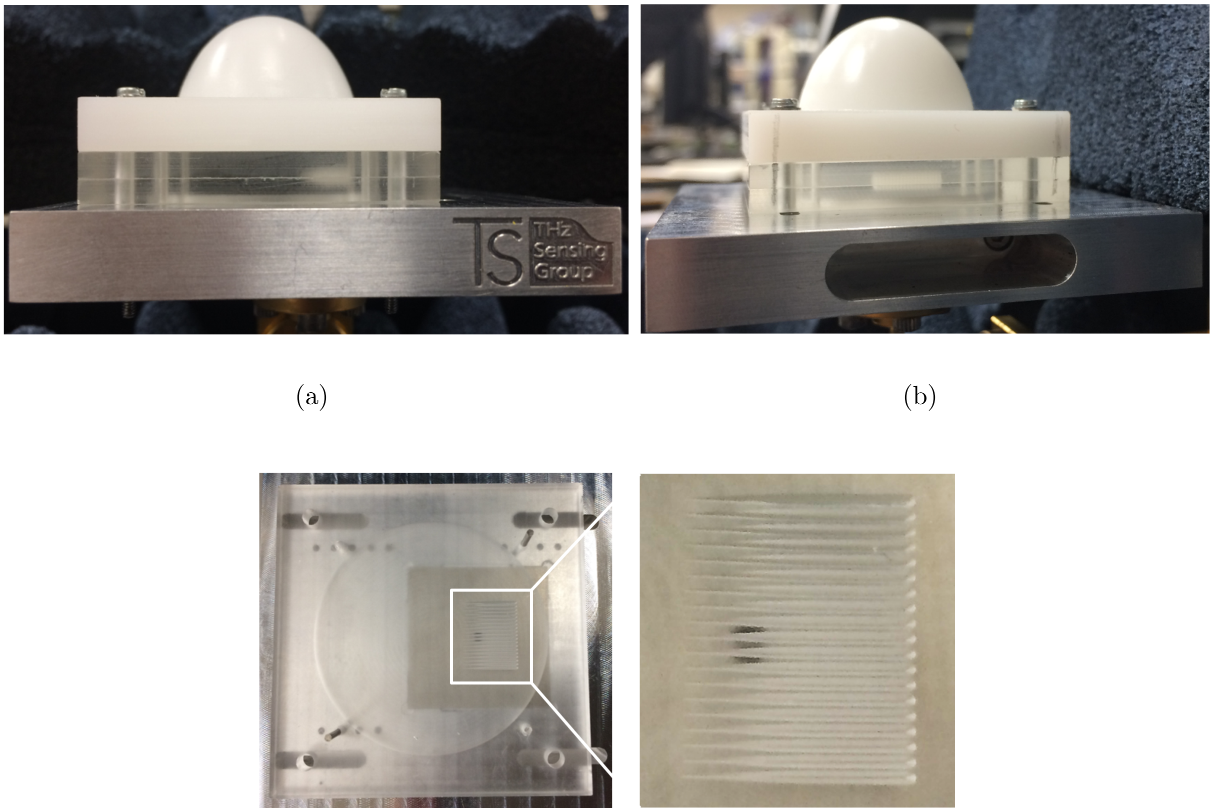

(a)

(b)

(c)

Figure 6.16: a) Prototype front view (see Fig. 6.1). b) Prototype side view. c) Top view of fabricated dielectric gratings. The feed double-slot on top of the waveguide can be appreciated in black below the Topas layer.

The results for the η_{ap} along the whole Fly's eye row are shown in Fig. 6.13a, and the corresponding Δx and Δz values in Fig. 6.13b.

6.6 Prototype Fabrication and Measurements

A prototype has been fabricated in order to validate the performance of the lens with integrated GW, for the beam steering at 25 deg (Fig. 6.16). The waveguide split-block and double-slot introduced in Chapter 4 are used as well in this prototype. The waveguide split-block presents several positioning holes where the lens can be fixed w.r.t. the feed for the different beam steering, as shown in Chapter 4. The elliptical lens has been fabricated

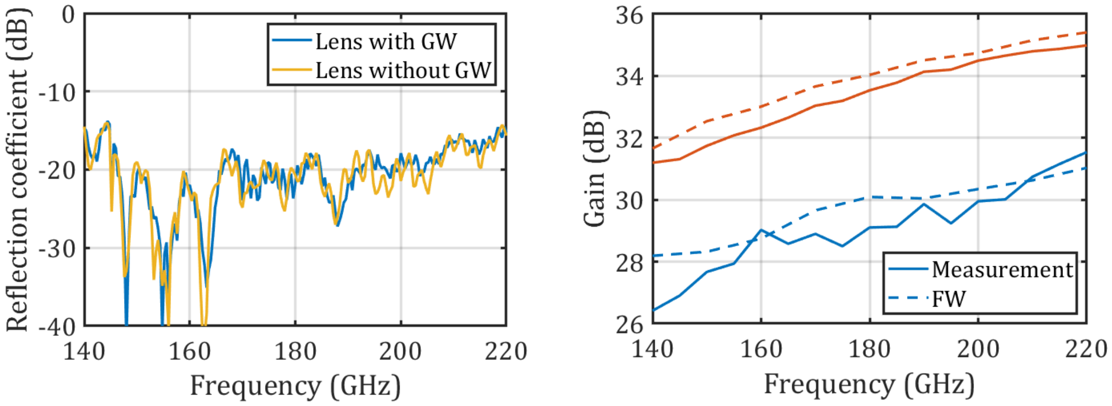

(a) (b)

Figure 6.17: a) Measured reflection coefficient for the elliptical lens with GW, compared to the measurements without GW from Chapter 4. b) Measured and FW simulated maximum gain for the radiation patterns steering to 25 deg in Fig. 6.12 (blue lines). The measured and FW simulated gain for the broadside beam in Chapter 4 is also shown as reference (red lines).

in HDPE material (High Density Polyethylene, $\varepsilon_r = 2.3$) due to its very low loss properties ($\tan\delta = 3.4 \times 10^{-4}$); the gratings layers have been fabricated in Topas material ($\varepsilon_r = 2.3$, $\tan\delta = 1.2 \times 10^{-3}$), due to the material hardness which enables the fabrication with standard milling, as mentioned in Chapter 5.

The antenna reflection coefficient has been measured and compared to the reflection coefficient of the lens without GW. The results, displayed in Fig. 6.17a, show that the use of the GW does not modify the impedance matching results.

The far-field patterns have been characterized by measuring the near-field on a plane on top of the lens antenna, by means of an open-ended waveguide. The sampling is performed by an automatic positioner, to which the VNA with the open-ended waveguide is fixed. A plane with $50 \times 50\,\text{mm}^2$ area has been measured, displaced 30 mm w.r.t. the ellipse symmetry axis, in order to capture the energy corresponding to the main beam. In Fig. 6.12, the FW simulated and measured radiation patterns are compared, showing good agreement.

Fig. 6.17b shows the maximum gain over frequency for the beam pointing at 25 deg. In order to account for the power lost in spill-over and not captured in the measurement plane, the directivity has been normalized by the power radiated by the antenna at broadside in

Chapter 4. The gain of this antenna is known, as reported in Chapter 4, and therefore its radiated power can serve as a reference.

6.7 Conclusion

In this chapter, a new approach to enhance the scan range in low ε_r lenses is presented. A wedge of dielectric gratings is integrated inside the elliptical lens, reducing the spill-over and reflection loss for the off-axis beams. The analysis in reception introduced in Chapter 2 is extended to optimize the optimum position of the feed and gratings wedge, minimizing the scan loss. The scan loss reached for the beam pointing at 25 deg is $-3.6\,\mathrm{dB}$, calculated w.r.t. the broadside beam from Chapter 4, with $-0.8\,\mathrm{dB}$ aperture efficiency. This represents an improvement of $4\,\mathrm{dB}$ w.r.t. the scan loss for the feed without gratings wedge displaced along the focal plane. A prototype at G-band with a beam steering of 25 deg has been fabricated and characterized, validating the FW simulation results.

Chapter 7

H-band Quartz-Silicon Leaky-Wave Lens with Air-Bridge Interconnect to GaAs Front-End

In this contribution, a wideband H-band (220–320 GHz) silicon lens antenna illuminated by an integrated quartz-cavity LW feed is presented. A novel air-bridge chip interconnect technology based on spray coating and laser lithography is introduced. This interconnection acts as a wideband, low loss transition between the GaAs front-end and the quartz antenna, avoiding the use of expensive waveguide split-blocks. An antenna prototype including the interconnect has been manufactured and characterized, validating the potential performance for an integrated H-band LW with aperture efficiency higher than 74 % over 34 % bandwidth, and radiation efficiency higher than 70 % over 37 % of bandwidth.

7.1 Introduction

While allowing for larger bandwidths, the use of higher frequencies comes with increased propagation spreading loss and lower output power, which can be compensated with high-gain and efficient antennas. Additionally, the efficiency in the transition between the antenna and the front-end becomes especially meaningful. In this chapter, a wideband antenna-in-package at H-band is proposed, shown in Fig. 7.1, employing the multi-layer quartz technology presented in [73] and exploiting leaky waves [24]. The use of quartz technology allows the development of more complex antenna concepts, thanks to the lower ohmic loss and the possibility to fabricate thicker and multiple substrate layers. A new approach for the air-bridge interconnect technology is introduced in this chapter, achieving

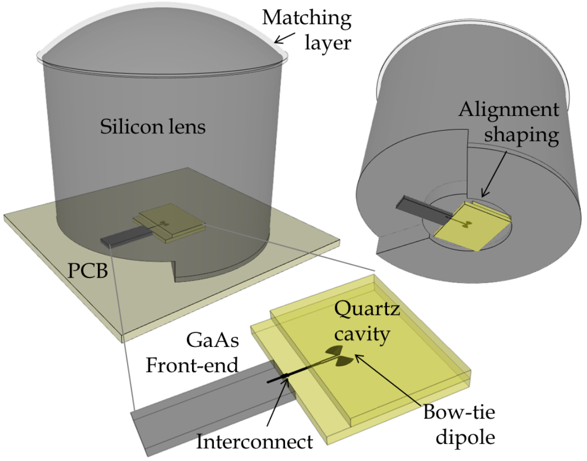

Figure 7.1: Lens antenna concept with quartz LW feed and interconnect to GaAs front-end.

a low-loss, wideband connection from the antenna to the front-end chip, enabling the implementation of efficient off-chip antennas. The novel air-bridge interconnect technology, based on spray coating and laser lithography, achieves higher fabrication precision than [72]. The proposed technology introduces a considerable performance advantage w.r.t. bond-wire transitions (transition loss lower than 0.2 dB over the whole H-band), and can be implemented with large-scale suitable processes.

In order to cover the wideband high aperture efficiency requirement, a resonant LW antenna is proposed as lens feed. A similar antenna was proposed in Chapter 4 using a plastic lens and air cavity fed by a split-block waveguide, reaching 80 % aperture efficiency over more than 40 % bandwidth. In this work, the LW feed is implemented in the multi-layer quartz technology presented in [73], using the novel air-bridge interconnect. The proposed LW antenna is composed of a quartz cavity and a silicon lens. The LW feed features high directivity inside the lens, enabling the use of a truncated lens with shallow shape. The quartz LW cavity is excited by a dipole, enabling a wideband differential interconnection from the quartz to the front-end chip, with no need of ground connection. Moreover, the presented antenna-in-package concept allows mounting the front-end chips and implementing the transitions between them on top of a low-cost Printed Circuit Board (PCB) (e.g. FR4). The lens can be as well placed on top of the antenna quartz chip as a surface-mount component (Fig. 7.1), facilitating considerably its assembly.

A quartz LW antenna including an interconnect to a GaAs chip has been designed with minimized cavity size (integrated design). Full-wave simulations for this design show wideband impedance matching and stable patterns, reaching potentially more than 74 % aperture efficiency over 34 % relative bandwidth for an integrated prototype. Thanks to the low loss characteristic of both interconnect and transmission line on quartz, more than 70 % radiation efficiency could be reached in the whole bandwidth with this integrated antenna. Simulation results for a Fly's eye row covering ±25 deg FoV are shown. A prototype dedicated to the characterization has been fabricated, elongating the dipole transmission line to allow measuring the antenna with landing probes. Measurement results for this prototype are in very good agreement with FW simulations, validating the results for the integrated design.

The chapter is organized as follows: Section 7.2 focuses on the LW feed concept; Section 7.3 presents the antenna-in-package technology, as well as the LW feed and lens analysis and design; Section 7.4 describes the antenna prototype fabrication and characterization; Section 7.5 shows the feeding line, interconnect and balun characterization; Section 7.6 provides some concluding remarks.

7.2 Wideband Leaky-Wave Antenna Concept

The proposed antenna geometry is sketched in Fig. 7.1. The quartz chip, which acts as lens feed, is placed beside the active front-end chip, and connected to it by means of the air-bridge interconnect technology presented here. The antenna consists of a resonant LW quartz cavity ($\varepsilon_r^c = 3.8$), comprised between a ground plane and the silicon lens ($\varepsilon_r^l = 11.9$), fed by a bow tie dipole. By choosing a dipole antenna as excitation of the LW cavity, we can benefit from the differential mode in the transition to the GaAs chip. The differential transition does not need any ground reference (hence no via connection), enabling wideband performance. Moreover, the chosen stack-up does not support the propagation of surface waves. In this section, the antenna concept is described more in detail.

As discussed in Chapter 3, the feed directivity enhancement increases for a higher ε_r contrast between the cavity and lens material. This effect is linked to the critical angle in the interface between the cavity and the lens ($\theta_c^f = 34$ deg for quartz-silicon), after which very low power is radiated by the LW antenna. The feed directivity improvement is however achieved at a cost of decreasing the antenna bandwidth [24]. The combination quartz-silicon presents a similar ε_r contrast to the one present in concepts using a lens with low ε_r (~ 2.5) and an air cavity, where relative bandwidths larger 40 % have been achieved in Chapter 4. The dispersion diagrams for both cases (quartz-silicon and air-HPDE stratifications) were compared in Section 3.2 (Fig. 3.2), showing very similar characteristics. However, the use of a silicon lens is advantageous in multi-beam architectures, as it enlarges the achieved field-of-view with respect to lenses with low ε_r, as derived in [110] and Section 3.5. Indeed, as discussed in Section 3.5, 25 deg of steering could be achieved with a silicon lens truncated at an angle of $\sim$ 30 deg (seen from the focus), almost double as the 12 deg achieved with the plastic lens presented in Chapter 4.

The LW cavity is fed by a dipole antenna, placed in its center (Fig. 7.1) and at half distance between the ground plane and the silicon (Fig. 3.1b and Fig. 7.2). Having the cavity half-wavelength height, the distance from the dipole to the ground plane is quarter-wavelength, optimum for the wideband impedance matching of the dipole. Two layers of quartz, with equal height $h_c/2$, are stacked for this aim. A bow-tie dipole has been chosen to enhance the antenna impedance bandwidth.

The LW modes power attenuates inside the cavity along ρ as $e^{-2\alpha\rho}$, being with $\alpha = \mathfrak{Im}[k_\rho]$ [103, 104]. The TM_0 presents the smallest α, and it sets therefore the antenna effective area, when it propagates. Considering a quartz cavity and a silicon lens, the TM_0 attenuation related to the mode radiation, $e^{-2\alpha\rho}$, reaches -10 dB at $\rho = 6\lambda_d$ over the whole bandwidth. If the TM_0 does not propagate, as it is the case with a dipole excitation, the effective area is given by the TE_1 mode, hence significantly reduced. In this case, -10 dB attenuation is reached at a maximum $\rho = 1.4\lambda_d$ at 320 GHz. This smaller effective area allows truncating the LW cavity (here the quartz chip) at a much smaller size without affecting the radiation characteristic.

7.3 Leaky-Wave Antenna-in-Package

In this section, the stratification and geometry for the quartz chip, GaAs chip and interconnect used between them are explained in detail. The quartz LW feed and lens design methodology are as well described, and their final geometry and FW simulation results are shown for the design at H-band (220 – 320 GHz).

7.3.1 Antenna-in-Package Technology

The geometry and layer stack-up for the LW quartz feed, GaAs chip and interconnect are shown in Fig. 7.2. The top view shows the quartz chip, where the quartz top layer is transparent to show the dipole on the bottom layer. The top quartz layer is truncated at a length $sp = 300$ µm shorter than the bottom, in order to leave space to implement the interconnect to the GaAs chip. The dipole is manufactured on the bottom quartz layer, with a ground plane below. The antenna is realized in a 100 mm wafer technology using low loss fused silica substrates. The final wafer thickness is 135 µm with 3 µm thick plated Au layers on front and back side. The Au structures are defined using laser lithography and wet etching. Both quartz layers are bonded with a thin layer of thermoplastic glue

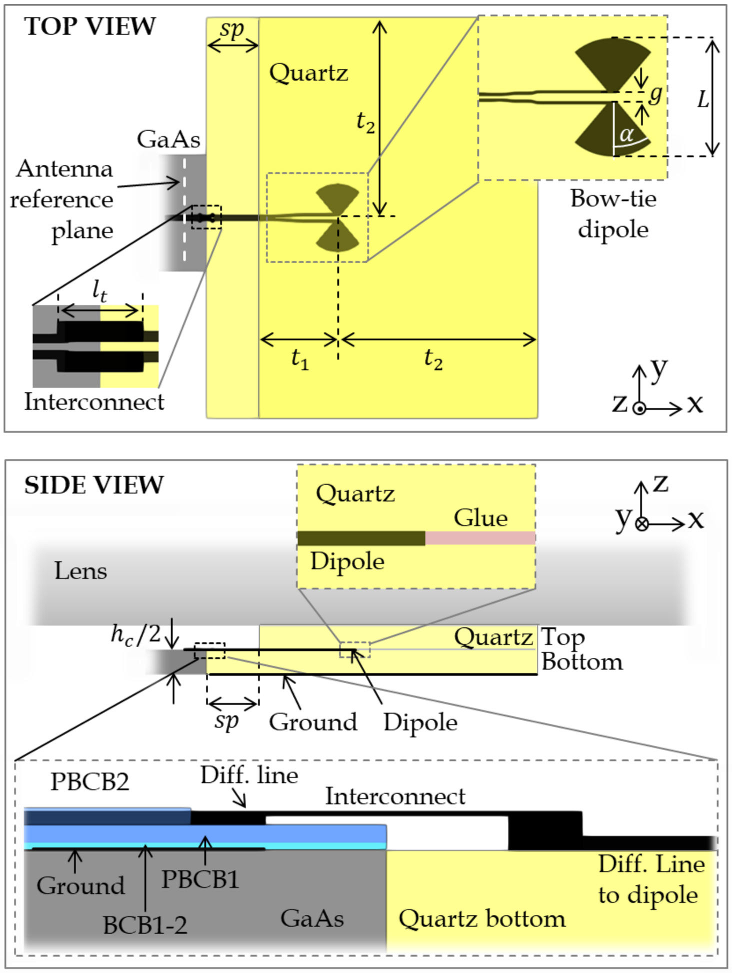

Figure 7.2: LW feed geometry and stratification. Metallic structures (gold) are drawn in black. Top view: geometric parameters quartz chip: $sp = 300\,\mu\text{m}$, $t_1 = 440\,\mu\text{m}$, $t_2 = 1.13\,\text{mm}$, $h_c = 270\,\mu\text{m}$. Side view: 1) GaAs: gold thickness ground: $0.35\,\mu\text{m}$, differential line: $3\,\mu\text{m}$; substrate thicknesss and ε_r: BCB1-2: $1.7\,\mu\text{m}$, $\varepsilon_r = 2.7$, $\tan\delta = 0.002$, PBCB1: $3.5\,\mu\text{m}$, $\varepsilon_r = 3.2$, PBCB2: $4\,\mu\text{m}$, $\varepsilon_r = 3.2$, $\tan\delta = 0.015$. 2) Interconnect gold thickness: $0.8\,\mu\text{m}$. 3) Quartz: gold thickness: $3\,\mu\text{m}$, roughness: $0.08\,\mu\text{m}$; glue: $\varepsilon_r \sim 3$, $3\,\mu\text{m}$.

($3\,\mu\text{m}$), which allows the two quartz chips to get in direct contact. It has been observed that an air gap remains between the glue and the outer side of the Au differential line strips, and no glue penetrates in the gap between both strips. This has been taken into consideration in the antenna design.

The GaAs MMIC and the quartz antenna are glued side-by-side using silver epoxy. The GaAs chip is manufactured with the same height as the bottom quartz chip, $h_c/2 = \lambda_d/4$, in order to allow for a flat interconnect, as it is shown in the side view. Alternatively, a

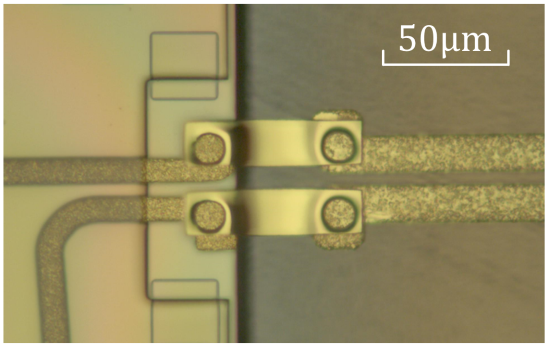

Figure 7.3: Micrograph of a differential air-bridge interconnect between a GaAs MMIC (on the left) and a quartz chip (on the right).

preform may be placed below the GaAs chip in order to reach the desired height. In the detailed view of the stack-up, the metal and substrate layers in the GaAs are displayed. The differential line in the GaAs MMIC is embedded in photo-BCB material (PBCB). A ground plane shields the transmission line from the GaAs substrate.

In order to implement the interconnect, the photo resist is spray coated over the chips and structured using high-resolution laser lithography to open the contact pads where the chip-to-antenna interconnect is to be placed. A metal stack layer is deposited by evaporating Ti/Au (30/500 nm, respectively) followed by the second lithography step, where the 20 µm wide interconnect metal stripes are defined. The length of the interconnect stripes, $l_t = 70\,\mu\text{m}$, is tailored to match the distance between the chips. In the final step, the metal layer is etched away, leaving the defined chip-to-antenna interconnects. As a result, the metal stripes are running from the contact pads of the front-end GaAs chip over the supporting photoresist layer to the contact pad on the quartz bottom layer. Fig. 7.3 shows a micrograph of a prototype realization of a GaAs-quartz interconnect, after the final metal etching step.

The loss in the air-bride interconnect has been estimated by means of FW simulations, resulting less than 0.2 dB over the whole frequency band. The loss in the differential transmission line in quartz has been measured as explained in the Section 7.5, going from 0.8 dB/mm at 220 GHz to 1.3 dB/mm at 320 GHz.

7.3.2 Leaky-Wave Feed and Lens: Analysis and Design

As a first step in the LW antenna design, the LW feed radiation patterns inside the lens (primary patterns) have been estimated with an asymptotic evaluation of the SGF in stratified media (Appendix A), using the equivalent transmission line in Fig. 3.1b. This model considers an ideal dipole without transmission line, a non-truncated quartz cavity and the lens as a semi-infinite silicon medium. As a first approximation, the dipole has been modelled as a line with length $L = 0.5\lambda_d$ and width $W = 0.1\lambda_d$, being λ_d the wavelength in quartz at the center frequency (270 GHz). The current distribution is assumed to be sinusoidal along the line length, and a square function along its width. A first optimization of the LW feed cavity height and phase center, and the lens truncation angle was carried out applying the analysis of the antenna in reception described in Chapter 2, considering a silicon lens with 8 mm diameter. Although the diameter chosen to validate the concept does not provide the antenna gain values derived for the use cases evaluated in Section 1.3.1, the lens can be easily scaled keeping identical feed geometry. The analysis in reception allows a fast optimization of the lens η_{ap}, including taper, phase, reflection, and spill-over efficiencies. After this first evaluation, the cavity height was set to $h_c = 0.47\lambda_d$.

As a second step, the bow-tie dipole, placed at $z = h_c/2$, and transmission line were optimized by means of FW simulations to maximize the impedance bandwidth. The dipole geometry parameters were set to $L = 0.66\lambda_d$, $\alpha = 40$ deg, and $g = 28\,\mu\mathrm{m}$ (Fig. 7.2), providing a wideband matching to a 150 Ω differential line. In the GaAs front-end, 100 Ω differential impedance is provided (8 µm width and 8 µm gap). The dipole feeding line has been tapered in two steps to transform 150 Ω into 100 Ω differential impedance. In the region where no top quartz layer is present, the differential line parameters were adapted to preserve the 100 Ω differential impedance. Initially, a BCB layer was planned to cover this piece of transmission line, which was dimensioned with 10 µm width and 10 µm gap to provide 100 Ω. This BCB layer was finally not used, becoming the impedance here 125 Ω. The small impact of this mismatch is included in the simulations. The interconnect is implemented with two stripes with 20 µm width and 10 µm gap (Fig. 7.3). This does not affect significantly the impedance matching, since the impedance variation is less than 15 % and the interconnect is short in terms of wavelength ($l_t = 0.06\lambda_0$). The obtained scattering parameters (S-parameters) at the antenna reference plane (Fig. 7.2 top view) are shown in Fig. 7.4.

After fixing the dipole and line geometry, the analysis in reception was applied to the primary patterns obtained from FW simulations with semi-infinite silicon medium and non-truncated quartz cavity. The goal was to fine tune the lens truncation angle and feed phase center in order to maximize η_{ap} over the whole bandwidth. The resulting optimum ellipse truncation angle is 30 deg, and the feed phase center $0.64\lambda_d$ below the ground plane.

Finally, the truncation size of the quartz cavity was optimized. The truncation length on the differential line side should minimize the transmission line loss, while preserving the primary patterns and impedance matching. The cavity truncation on the transmission line

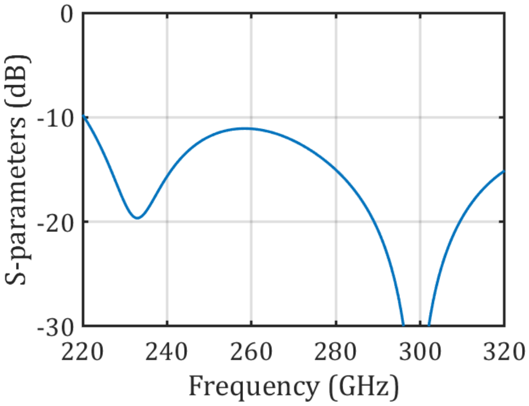

Figure 7.4: Reflection coefficient of LW feed with the silicon lens modelled as semi-infinite medium. Both models include the 730 µm long transmission line. The reference impedance is 100 Ω differential, taken at the GaAs chip in the reference plane shown in Fig. 7.2

side (H-plane) can be performed at $t_1 = 0.75\lambda_d$ distance from the dipole at the center frequency, where the TE_1 mode attenuation due to the radiation reaches -10 dB at 270 GHz, and -6.5 dB at 320 GHz. Applying the analysis in reception to the FW primary patterns including the truncated cavity, it has been estimated that the antenna η_{ap} is degraded in less than 0.1 dB at 320 GHz with this truncation. This is also partly thanks to the additional, length $\mathrm{sp} = 0.64\lambda_d$ needed on the bottom quartz layer for the implementation of the interconnect (Fig. 7.2), which enlarges the effective truncation length. The resulting transmission line length is 730 µm, with a maximum estimated loss of 0.9 dB at 320 GHz. The opposite side and perpendicular w.r.t. the transmission line may be truncated at a larger dimension ($t2 = 1.13$ mm), in order to mechanically support the silicon lens, which lies on the quartz chip (Fig. 7.2).

The FW primary patterns including the truncated quartz cavity, bow-tie dipole, differential line and interconnect, are shown in Fig. 7.5a at the center frequency. This figure displays as well as a reference the primary patterns calculated with SGF for an ideal dipole with the same length L, without cavity truncation or transmission line. Fig. 7.5b displays the directivity at broadside over the whole frequency band for both cases, with a maximum variation of 2 dB. The final results are still in good agreement with the ideal model after including all the non-ideal effects. The most significant difference is the cross-polar level, which increases in the FW model, due to the transmission line radiation.

The lens radiation patterns have been calculated applying the described SGF model with an ideal dipole and Physical Optics (SGF-PO), as well as with the complete FW model in EMPIRE XPU [112] with multiple reflections, including the truncated quartz cavity,

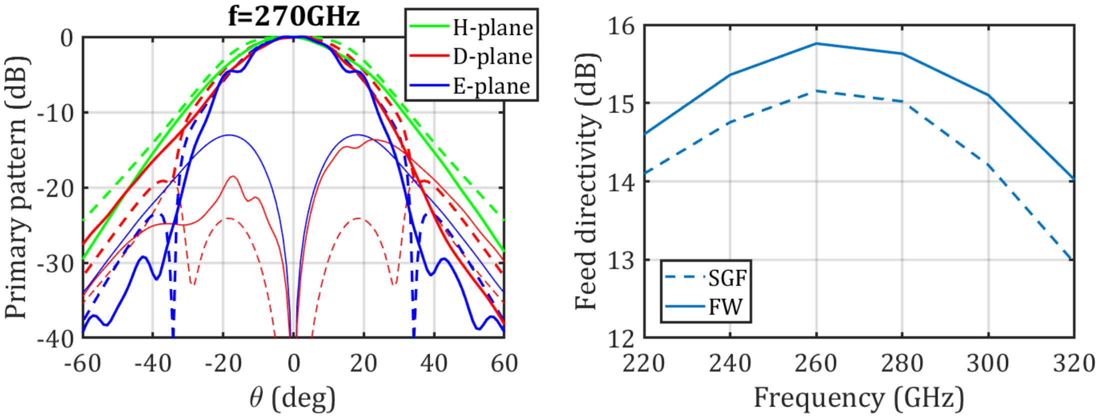

(a) (b)

Figure 7.5: a) Feed radiation patterns inside the lens (lens modelled as semi-infinite medium). Solid lines: FW simulations including the truncated quartz cavity, bow-tie dipole, differential line and interconnect. Dashed lines: SGF model with ideal thin dipole. Thick lines: co-polar. Thin lines: cross-polar. b) Feed directivity over frequency at broadside for the models in a).

bow-tie dipole, differential line and interconnect (Fig. 7.6). A standard $\lambda/4$ matching layer with $\varepsilon_r = 2.8$ has been considered in both PO and FW simulations. The matching layer ε_r corresponds to SUEX material [139], which later on will be used in the fabrication. The cross-polar level increase due to the feeding line radiation is also visible in the lens patterns. Fig. 7.7a shows the maximum directivity results from both analyses, which are in good agreement. The gain includes losses in the interconnect ($< 0.2\,\text{dB}$), differential line ($< 0.9\,\text{dB}$), and lens ($< 0.4\,\text{dB}$). The loss from the differential line is estimated via measurements as described in Section 7.5. The η_{ap} estimated with FW simulations for the feed and the analysis in reception (FW-Rx), validated with FW simulations including the lens, is higher than 74 % over 34 % bandwidth, as shown in Fig. 7.7b. The η_{ap} is not significantly degraded w.r.t. the one obtained with SGF and the analysis in reception for an ideal dipole (SGF-Rx), as shown in Fig. 7.7b. η_{ap} is here defined as the ratio between the directivity obtained with the lens, and the maximum directivity possible for this circular aperture. The efficiency decay at the higher part of the band is related to phase and polarization loss introduced by the feeding line. The power lost in cross-polar is always lower than 0.5 dB. The overall antenna radiation efficiency, η_{rad}, (ohmic and dielectric losses) is higher than 70 % over the whole frequency band, as also displayed in Fig. 7.7b.

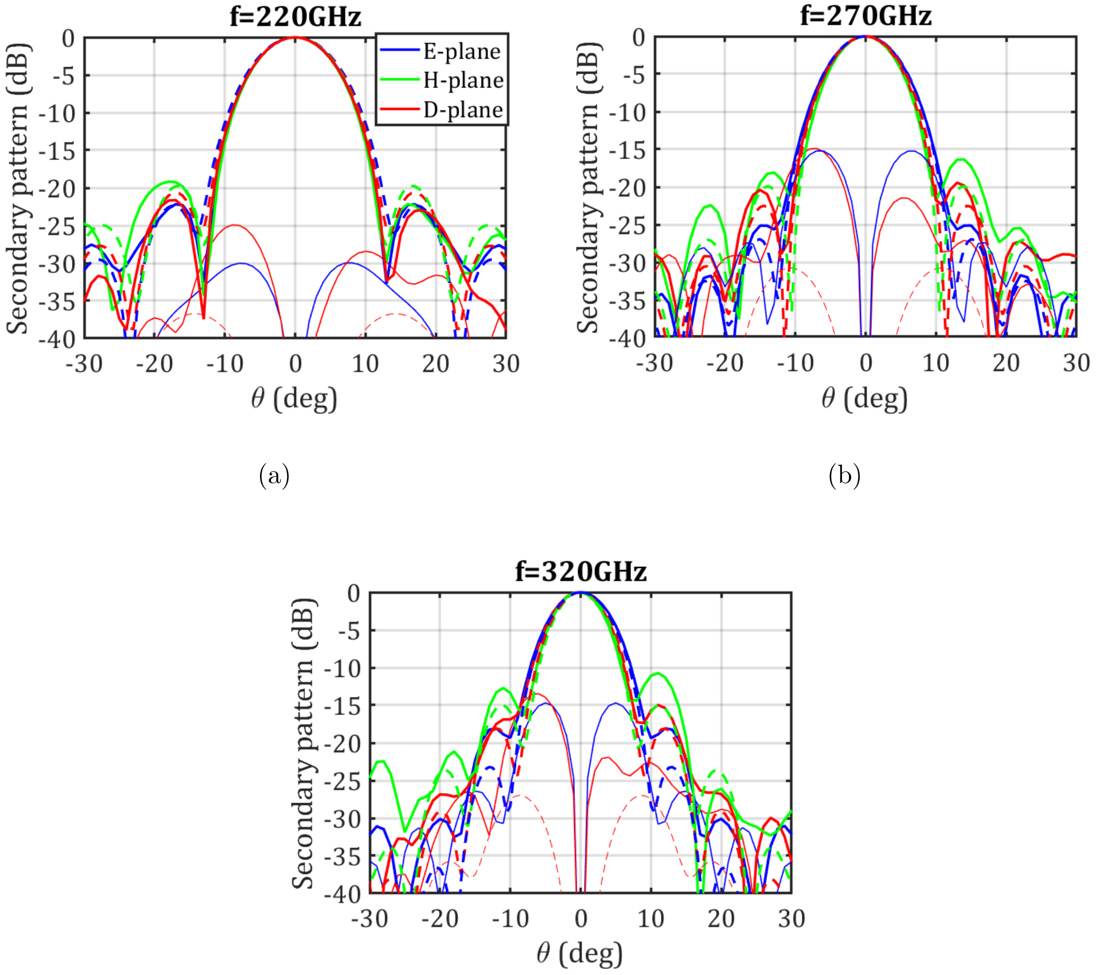

(a)

(b)

(c)

Figure 7.6: Lens radiation patterns for the integrated prototype at a) 220 GHz, b) 270 GHz, c) 320 GHz. Solid lines: FW simulations with multiple reflections, including the lens with matching layer, truncated quartz cavity, bow-tie dipole, differential line and interconnect. Dashed lines: SGF-PO model, PO with the primary patterns for an ideal dipole obtained with SGF. Thick lines: co-polar. Thin lines: cross-polar.

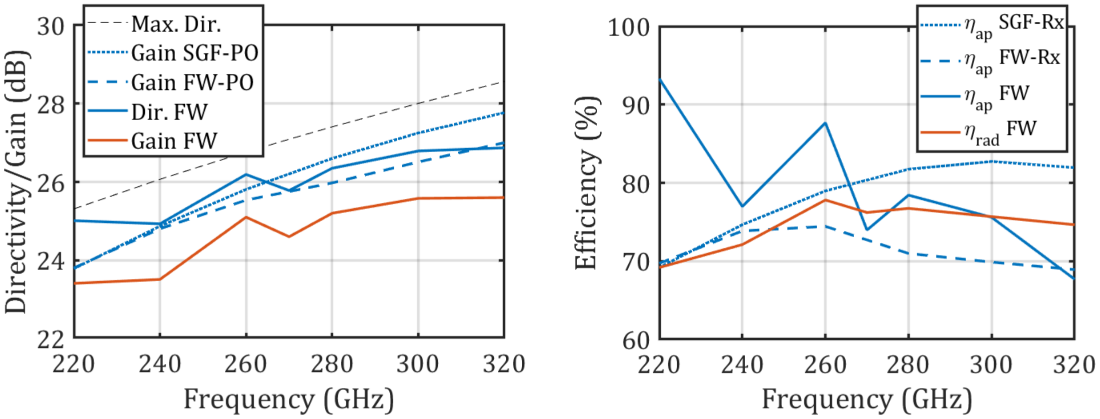

(a) (b)

Figure 7.7: a) Lens directivity and gain over frequency. The maximum directivity for the equivalent circular aperture has been plotted as reference in dashed black line. SGF-PO: PO with the primary patterns for an ideal dipole obtained with SGF. FW-PO: PO with the FW simulated primary patterns for the dipole with interconnect, feeding line and truncated cavity. FW: simulation with multiple reflections, including interconnect, feeding line, truncated cavity and lens with matching layer. b) Lens aperture efficiency and radiation efficiency (dielectric and ohmic loss) including the truncated quartz cavity, bow-tie dipole, feeding line and interconnect. SGF-Rx: analysis in reception applied to the primary patterns for an ideal dipole obtained with SGF. FW-Rx: analysis in reception applied to the FW simulated primary patterns for the dipole with interconnect, feeding line and truncated cavity. FW: simulation with multiple reflections, including interconnect, feeding line, truncated cavity and lens with matching layer.

7.3.3 Antenna Self-Coupling

As explained in Section 2.5.2, Eq. (2.11), a good estimation for the lens aperture and radiation efficiency can be obtained by calculating the power received back in the feed when placing a metallic reflector on top of the lens, in the near-field (Fig. 7.8a).

Applying the analysis in reception in Section 2.5.2, η_c has been calculated for the ideal dipole and infinite quartz cavity (SGF-Rx in Fig. 7.8b), as well as for the FW simulated dipole with truncated cavity, bow-tie dipole, feeding line, and interconnect, radiating in a semi-infinite silicon medium (FW-Rx in Fig. 7.8b). For the sake of comparison, no dielectric or ohmic losses (η_{rad}) have been considered in the FW-Rx calculation. The difference between the FW η_c and the ideal case corresponds to additional phase and polarization loss introduced by the dipole feeding line, as previously mentioned.

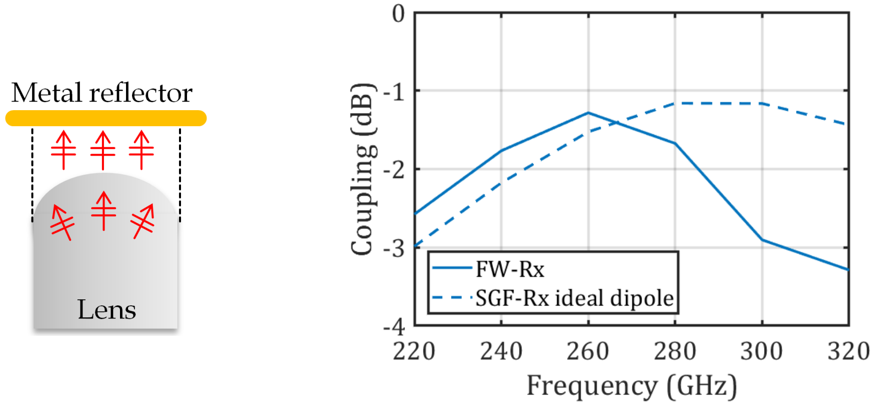

(a) (b)

Figure 7.8: Lens self-coupling (no dielectric or ohmic loss) evaluated with the analysis in reception. The FW feed model includes the truncated quartz cavity, bow-tie dipole, feeding line, and interconnect.

7.3.4 Fly's Eye Array

As discussed in Section 3.5, the use of a silicon lens is advantageous in terms of the steering achieved, thanks to the high ε_r. Taking into account the lens truncation angle, $\theta_{\text{edge}} = 30$ deg, the steering range achieved in a lens with $D = 18\lambda_0$ (2 cm for $f_0 = 270$ GHz) could reach 25 deg in the H-plane and almost 28 deg in the E-plane, as shown in Fig. 3.9 (calculations without matching layer). In this analysis, the lens D considered is larger as in the fabricated prototype. This has been chosen so that it provides the gain values required in the use cases evaluated in Section 1.3.1.

Fig. 7.9a shows the directivity calculated for the broadside beam and for the beam pointing at 25 deg, for a lens with 2 cm diameter. The performance of an ideal dipole feed as well as the feed design presented in Section 7.3.2 have been evaluated in reception, applying the tool presented in [137]. A lens with the same matching layer used in Section 7.3.2 has been considered. To achieve 25 deg steering, the feed has been displaced 2.5 mm off-focus in the E- and H-plane respectively, along the focal plane. Fig. 7.9b shows the scan loss in both planes, for the two evaluated feeds. As predicted, the scan loss is ~ 3 dB at the center frequency, being this in the evaluated case with matching layer even slightly lower in the H-plane.

The scan loss for the beam pointing at 25 deg in the H-plane has been also FW simulated for the designed LW feed and silicon lens with $D = 8$ mm ($7.2\lambda_0$). Fig. 7.10a shows the directivity and gain for the beam pointing at 25 deg in the H-plane, together with the

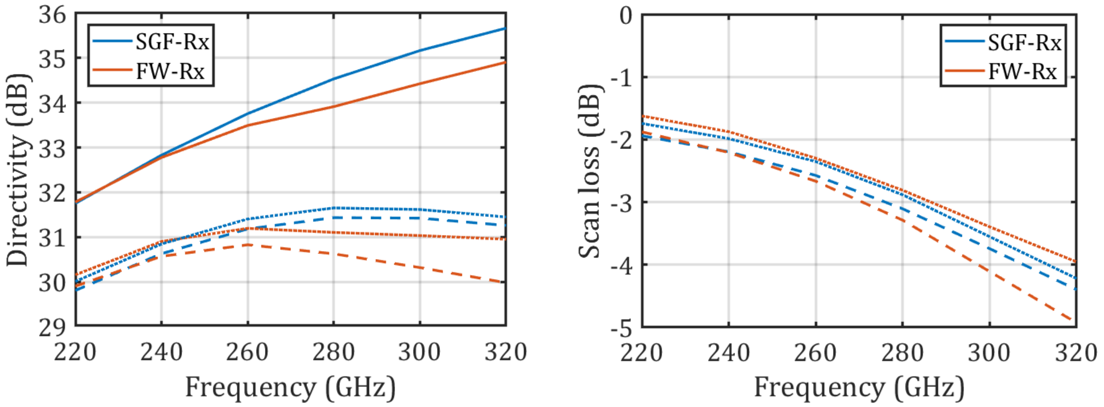

(a) (b)

Figure 7.9: a) Simulated directivity for the broadside beam and for the beam pointing at 25 deg for the ideal dipole (SGF-Rx) and the integrated design with truncated cavity, bow-tie dipole, feeding line, and interconnect (FW-Rx), with a lens with $D = 2\,\mathrm{cm}$. Solid line: broadside. Dashed line: 25 deg E-plane scanning. Dotted line: 25 deg H-plane scanning. b) Scan loss for the beam pointing at 25 deg, calculated from the directivity curves in (a).

broadside directivity and gain. In this case, the feed has been displaced 1.05 mm off-focus to generate the beam steering to 25 deg. In Fig. 7.10b, the scan loss over frequency is displayed, staying always above $-3\,\mathrm{dB}$. The steering range turns out larger than predicted in Fig. 3.9, as the designed lens has a smaller diameter than the one used in the calculations in Section 3.5 ($7.2\lambda_0$ instead of $18\lambda_0$). A smaller lens diameter leads to lower phase loss for the off-focus beams, reducing the scan loss.

Fig. 7.11a shows the radiation patterns obtained for the E- and H-plane scanning. It can be seen that the side-lobe level increases in the H-plane for both the ideal dipole and the dipole with feeding line and truncated cavity. This could eventually reduce the scanning range. In Fig. 7.11b, a possible integration approach for the 15 beams under two lenses is displayed, fitting respectively 7 and 8 beams each. This spacing would be allowed by the dipole dimensions. However, it has to be pointed out that the simulations have been done considering a single dipole, and effects in the embedded patterns due to mutual coupling, known in leaky antennas [113], are not included.

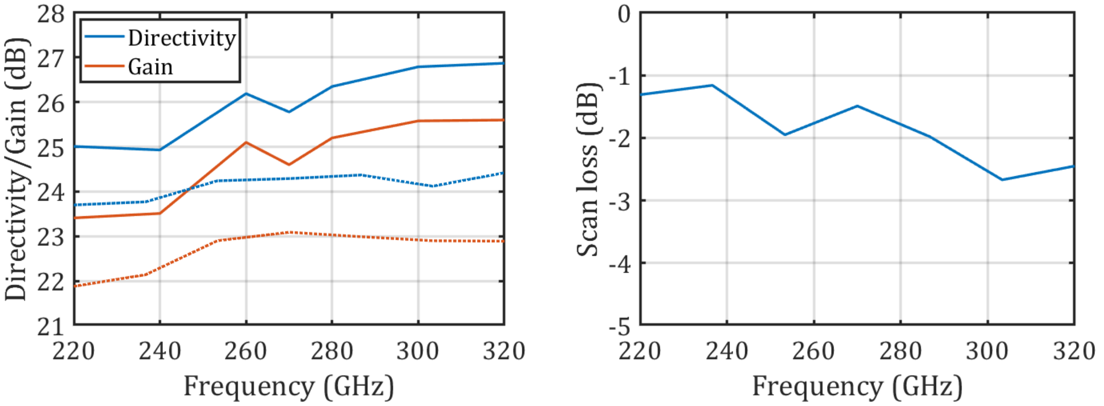

(a)

(b)

Figure 7.10: a) FW simulated directivity and gain for the broadside beam (solid line) and for the beam pointing at 25 deg in the H-plane (dotted line), for the integrated design with truncated cavity, bow-tie dipole, feeding line and interconnect, with a lens with $D = 8\,\mathrm{mm}$. b) Scan loss for the beam pointing at 25 deg, calculated from the directivity curves in (a).

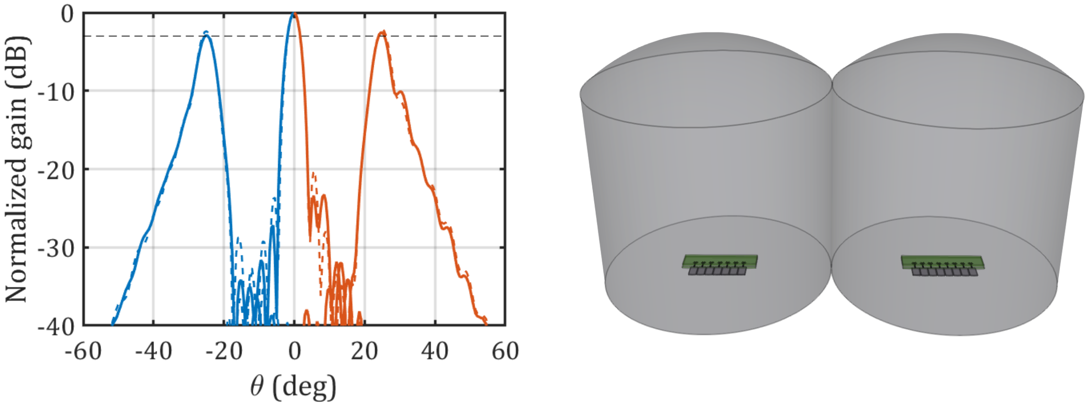

(a)

(b)

Figure 7.11: a) Simulated gain normalized to the broadside beam for the broadside and beam pointing at 25 deg with the 2 cm lens. Blue: E-plane scanning. Red: H-plane scanning. Solid line: FW-Rx (feed including feeding line and cavity truncation). Dashed line: SGF-Rx (ideal dipole). b) Possible Fly's eye feed integration for one row with ±25 deg FoV.

7.4 Antenna Prototype and Measurements

In this section, the prototype fabricated to validate the integrated antenna performance shown in Section 7.3.2 is described, containing a longer transmission line to enable landing probe measurements. The measurements performed to validate the antenna matching, radiation patterns and gain, are as well explained. The one-port S-parameters and coupling measurements are calibrated with the SOL (Short-Open-Load) method until the probe landing pads by means of standard Quartz calibration wafers [140].

7.4.1 Antenna Prototype

In order to enable the characterization of the lens antenna, a longer quartz chip dedicated to the measurements was manufactured, with a feeding line length of 6.4mm, allowing contacting the antenna with the probes from the top side (Fig. 7.12a and Fig. 7.12d). The fabricated quartz antenna is connected with the novel interconnect to the GaAs chip which later will contain the front-end. A delay-line balun in the GaAs chip enables the antenna characterization with single-ended WR3 landing probes (Fig. 7.12b). The delay-line balun is implemented in the GaAs stratification shown in Fig. 7.2, and its characterization is shown in Section 7.5. Fig. 7.12c shows a detail of the fabricated dipole embedded between the two quartz chips, where the mentioned air gap between the glue and the gold structures can be appreciated.

A silicon lens has been fabricated with diamond turning. On the bottom side of the lens, a circular profile with diameter equaling the diagonal dimension of the quartz chip enables an accurate alignment between the dipole and the lens focus (Fig. 7.1). A deeper opening was realized with laser cut on the side where the antenna is connected to the active front-end, in order to leave space for the rest of front-end chips and surface mount components, as shown in Fig. 7.1. The accuracy in this opening is not critical, as the LW lens feed does not illuminate the lens bottom area. After all front-end chips have been mounted on the PCB, the lens can be placed on top without the need of a microscope, allowing to speed up the fabrication process.

The lens has been provided with a matching layer realized with 165 μm thick SUEX coating, following the procedure described in [139]. As shown in Fig. 7.12a, only the top part of the lens has been covered, as very low energy is present in the lateral lens area, thanks to the directive LW feed radiation patterns inside the lens. This facilitates considerably the matching layer implementation.

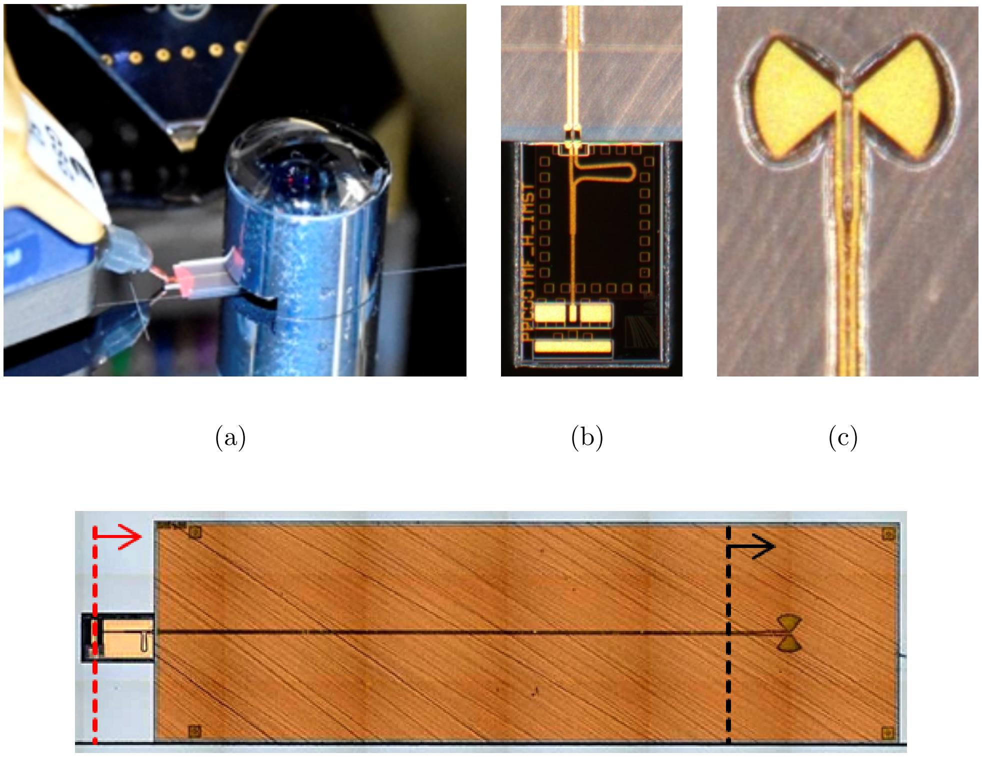

(a) (b) (c)

(d)

Figure 7.12: a) Silicon lens with longer quartz feed (6.4 mm transmission line) for S-parameter and near-field characterization. b) GaAs delay-line balun connected to the antenna transmission line in the quartz chip. c) Micrograph of the fabricated dipole. d) Full view of the long quartz antenna fabricated for characterization purposes. The red dashed line marks the measurement reference plane. The black dashed line marks the size of the antenna to be integrated in the final system (Fig. 7.2).

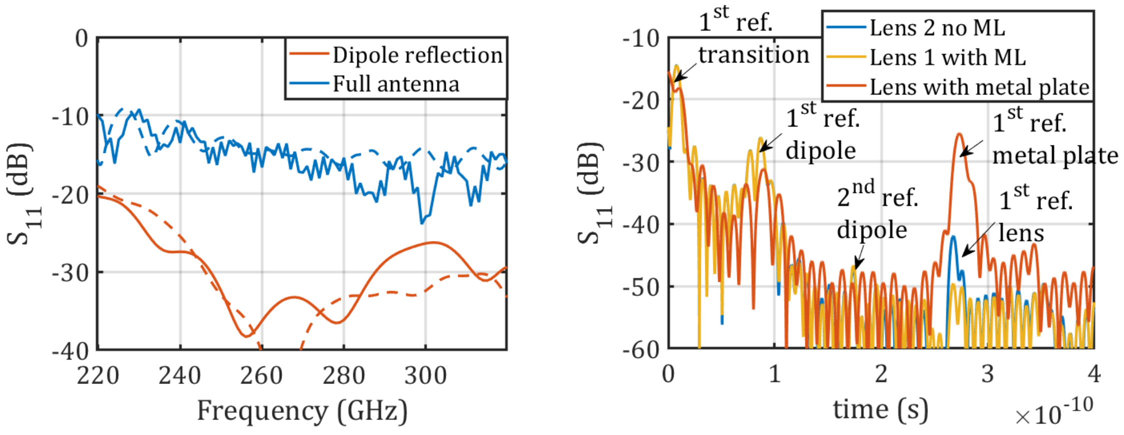

(a) (b)

Figure 7.13: a) Antenna reflection coefficient for the prototype in Fig. 7.12, at the marked reference plane. Dashed: FW simulations. Solid: measurements. The FW simulated S_{11} does not include the effect of multiple reflections in the lens. In both FW and measurements, the dipole reflection is calculated applying a time window from 0.05 ns to 0.12 ns. b) Antenna reflection coefficient measurement in time-domain, for lenses with and without matching layer (ML). The reflections in the different interfaces have been marked, indicating the reflection order.

7.4.2 Antenna Scattering Parameters

The measured antenna impedance matching is shown in Fig. 7.13a, for a lens with matching layer, compared to FW simulations with the same antenna geometry (6.4 mm transmission line length), including the interconnect and GaAs delay-line balun (reference plane shown in Fig. 7.12d). Both results show good agreement. Fig. 7.13b shows the measured antenna S_{11} in time domain. Here, reflections from the different interfaces in the design have been identified. The S_{11} for a lens without and with matching layer are compared, showing the reduction in the first reflection coming from the lens interface in case of using matching layer. The result of time-gating the reflection corresponding to the dipole, for the lens with matching layer, is as well displayed in Fig. 7.13a. The level of the time-gated reflection in the dipole is as well in good agreement in FW simulations and measurements. This is a second validation of the accurate loss estimation with the transmission line in the quartz chip done in Section 7.5.

7.4.3 Far-Field Measurements

The characterization of the lens antenna far-field was performed by measuring the near-field on top of the lens with an open ended WR3 waveguide probe, as shown in Fig. 7.14a. An area of $22 \times 22\mathrm{mm}^2$ was scanned with steps of $440\,\mu\mathrm{m}$ at $1.5\,\mathrm{cm}$ distance from the lens equivalent aperture. Both co- and cross-polar near-fields have been measured over the same plane and area, introducing a twist to rotate the waveguide probe polarization in case of the co-polar measurement. The resulting far-field patterns are shown in Fig. 7.15, compared to the ones estimated with FW simulations, showing good agreement. The loss introduced by the twist, estimated to be 1 dB, has been calibrated in the co-polar measurement. A beam steering of 3 deg was observed in the radiation patterns, corresponding to $-120\mu\mathrm{m}$ feed shift in x-direction (reference system in Fig. 7.2). The measured radiation patterns have been centered in Fig. 7.15 for the sake of comparison. Fig. 7.16a shows the measured and FW simulated directivity over frequency in good agreement. The measured co-polar directivity has been normalized to the power measured for both co- and cross-polar components, as it is the case in the FW simulation. Fig. 7.16b compares the measured and FW simulated polarization loss, calculated as the ratio between the co-polar power and the total radiated power, showing good agreement. The polarization loss increases in the higher part of the band, due to the common mode excited by the non-ideal balun, and the longer transmission line length used in this prototype dedicated to characterization. A FW simulation substituting the balun by an ideal differential excitation shows cross-polarization loss lower than 0.5 dB (Fig. 7.16b).

7.4.4 Antenna Gain: Self-Coupling Measurement

In order to validate the simulated antenna gain, the power coupled from the reflection from a metal plate on top of the lens has been measured. The measurement setup is shown in Fig. 7.14b, where the metallic reflector is placed at $500\,\mu\mathrm{m}$ distance from the lens equivalent aperture. Using this setup, only one-port needs to be calibrated. Moreover, as shown in Eq. (2.11), this measurement setup is proportional to η_{rad}^2, simplifying the antenna efficiency measurements. The antenna efficiency terms contributing to the self-coupling were explained in Section 2.5.2. Here, the reference plane is located as shown in Fig. 7.12d, and therefore the coupling includes the delay-line balun and long transmission line loss. Fig. 7.13b shows the measured S_{11} in time domain, where the reflection coming from the metallic reflector has been identified. A FW simulation, including dielectric and ohmic loss, reproducing the measurement setup has been performed, using a perfect electric conductor as reflector. The $-120\mu\mathrm{m}$ estimated off-focus displacement of the feed has been included in the FW simulation, in order to consider the corresponding phase

(a) (b)

Figure 7.14: a) Near-field measurement setup. b) Measurement setup for self-coupling. Top: sketch of the prototype and reflector. Bottom: photo of the setup, showing the lens and copper bridge acting as reflector.

loss coming from the plate reflection. The results, time-gated to evaluate the reflection coming from the metallic reflector, are shown over frequency in Fig. 7.17 for both FW simulation and measured results, showing good agreement. The differences between FW and measurement results are related to the tolerances in the measurements, dielectric and ohmic losses modelling, and prototype fabrication (balun, interconnect, quartz antenna, silicon lens and matching layer).

Table 7.1 shows a summary of the different loss contributions in the antenna with short transmission line (730 µm) for the integrated front-end, and the antenna with long transmission line (6.4 mm) for characterization purposes. Those have been validated via the self-coupling measurement, together with the near-field and feeding line characterization.

Feeding line length (µm)	Frequency (GHz)	Balun (dB)	Interconnect (dB)	Feeding line (dB)	Lens and ML (dB)	Polarization (dB)
730	220	1.3	0.2	0.6	0.4	0.0
	320	1.6	0.2	0.9	0.4	0.3
6400	220	1.3	0.2	5.1	0.4	0.4
	320	1.6	0.2	8.3	0.4	1.8

Table 7.1: Antenna loss contributions

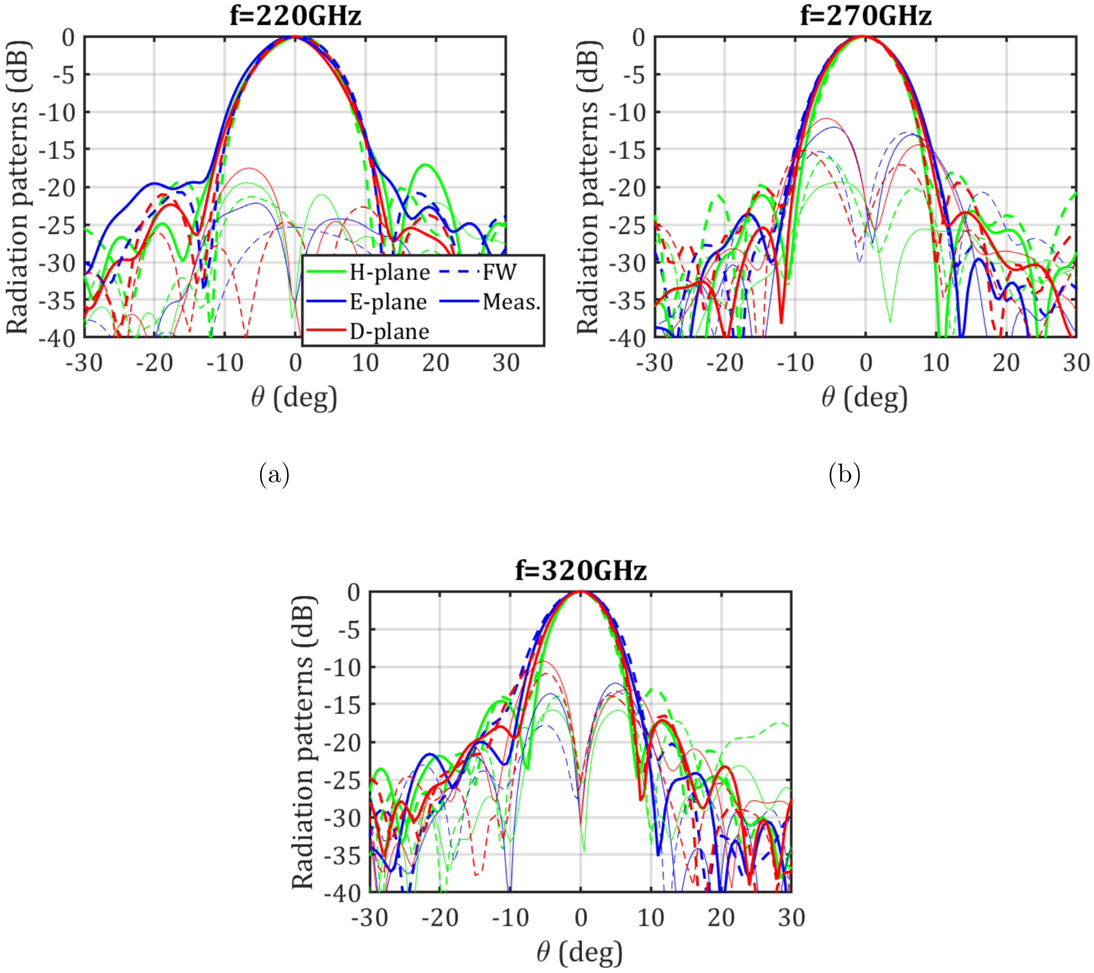

(a)

(b)

(c)

Figure 7.15: Lens far-field patterns for the prototype dedicated to characterization (Fig. 7.12). Thick line: co-polar. Thin line: cross-polar. a) 220 GHz, b) 270 GHz, c) 320 GHz.

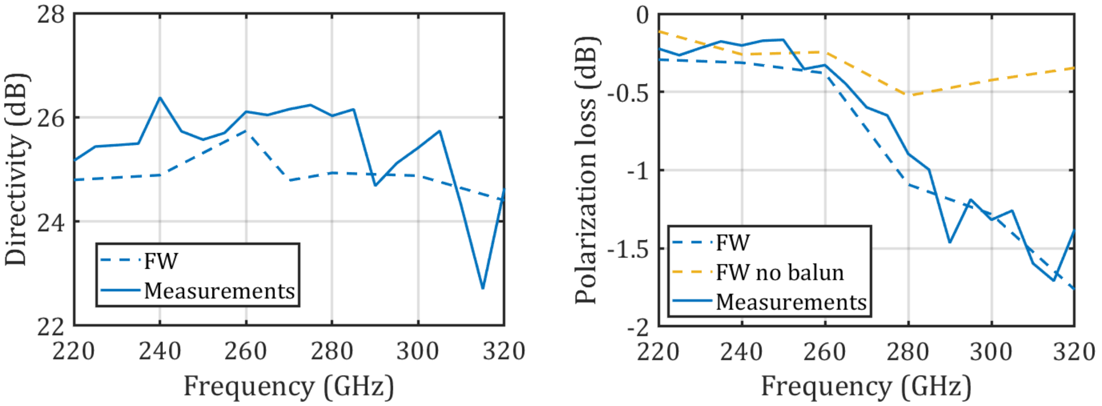

(a) (b)

Figure 7.16: a) Lens antenna directivity and b) lens antenna polarization loss (ratio between power radiated in co-polar and total radiated power). All curves correspond to the long antenna prototype dedicated to the characterization (reference plane shown in Fig. 7.12d). The FW simulation without balun in b) is performed substituting the balun with a differential port.

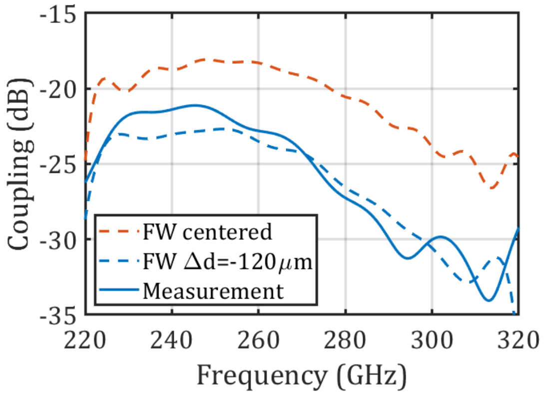

Figure 7.17: Time-gated S_{11} of the lens antenna with a metallic reflector placed at 500 μm from the lens top (measurement setup in Fig. 7.14b). The time domain signal is shown in Fig. 7.13. A window from 0.23ns to 0.32ns has been applied, to account only for the first reflected wave.

7.5 Feeding Line, Interconnect and Balun Characterization

In this section, the validation of the estimated losses in the interconnect between the quartz and GaAs chip, the quartz differential transmission line feeding the dipole, and baluns used for the characterization, is described. In order to enable the use of single-ended WR3 landing probes, baluns implemented in the GaAs MMICs have been included in all measurements to transform the differential mode into single-ended. The delay-balun used in the antenna measurements has been as well characterized, in order to de-embed its contribution. The two-port S-parameters measurements have been calibrated until the probe landing pads with the TRL (Through-Reflect-Line) method on a commercial impedance standard substrate (ISS).

7.5.1 Feeding Line and Interconnect Characterization

The losses in the differential transmission line in quartz were characterized by measuring 1) a back-to-back structure with two rat-race baluns (Fig. 7.18a), and 2) the same baluns with a quartz differential transmission line in between (Fig. 7.18c), connected with air-bridge interconnects. The 2.75 mm long transmission line is implemented in the same quartz stratification with bottom and top layers where the antenna is embedded, shown in Fig. 7.2. The differential line has the same impedance as will later be used in the antenna transmission line (100 Ω). The rat-race balun was designed in the GaAs MMIC with the stratification shown in Fig. 7.2. The balun provides a single-ended input impedance of 50 Ω and transfers this to 100 Ω differential impedance.

Fig. 7.19 shows the FW simulated and measured S-parameters for both back-to-back structures, with good agreement over the whole frequency band (average error 1 dB). Note that FW simulations do not include the effect of the landing pads, which originate the mentioned difference with the measured results. Fig. 7.20 displays the transmission for the 2.75 mm differential line and two interconnects, calculated as the ratio between the S_{21} measurements for both back-to-back structures (Fig. 7.18a and Fig. 7.18c). By applying this ratio, the effect of the landing pads is mostly compensated. The results are compared with the ones estimated from FW simulations, showing good agreement. Taking into account 0.2 dB loss for a single interconnect, estimated with FW simulations, the calculated loss in the differential transmission line in quartz goes from 0.8 dB/mm at 220 GHz to 1.3 dB/mm at 320GHz (Fig. 7.20).

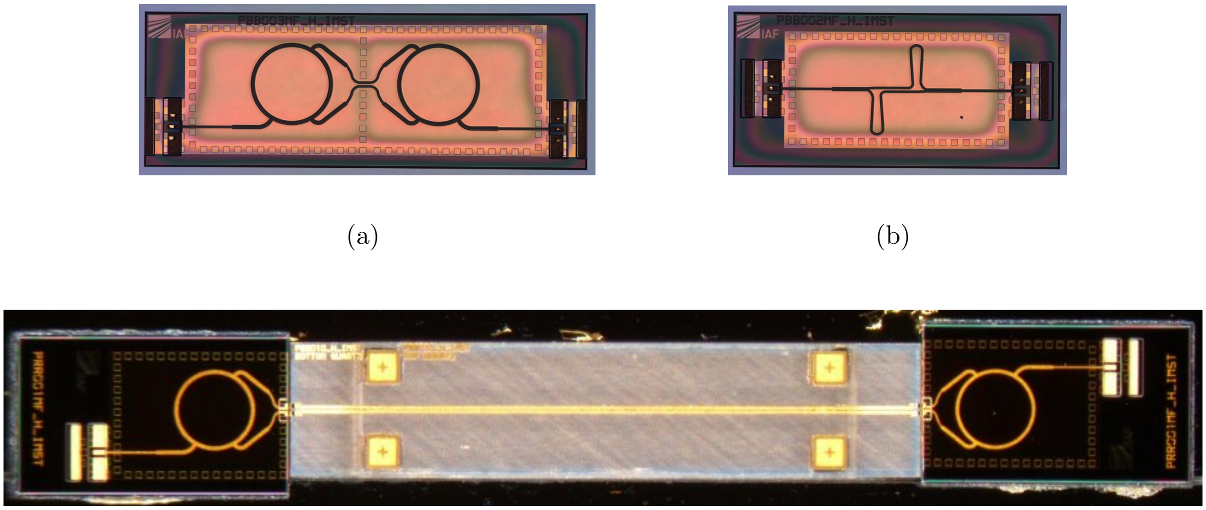

(a)

(b)

(c)

Figure 7.18: Fabricated back-to-back structures a) Rat-race baluns for interconnect and quartz differential transmission line characterization. b) Delay-line baluns used in the antenna characterization. c) Rat-race baluns with 2.75 mm long quartz transmission line (two interconnects).

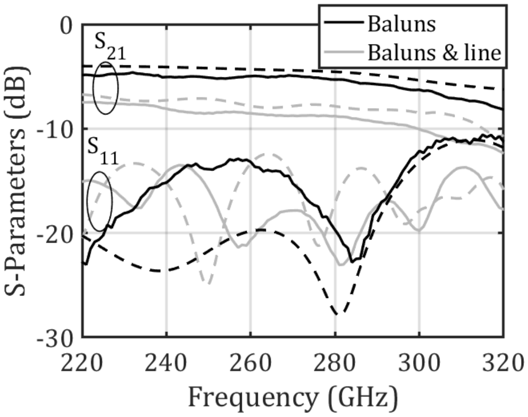

Figure 7.19: S-parameters for the back-to-back rat race balun (Fig. 7.18a) and back-to-back rate race balun with quartz differential line and two interconnects (Fig. 7.18c). Dashed line: FW simulations. Solid line: measurements.

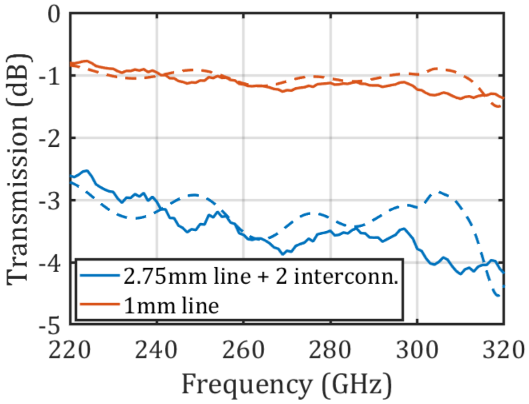

Figure 7.20: Transmission for the 2.75 mm transmission line and two interconnects (back-to-back) estimated from the S_{21} measurements in Fig. 7.19, and calculated transmission for 1 mm transmission line. Dashed line: FW simulations. Solid line: measurements.

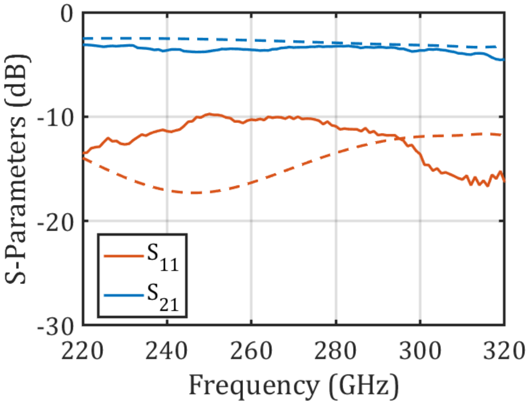

Figure 7.21: Delay-line balun S-parameters. Dashed line: FW simulations. Solid line: measurements.

7.5.2 Delay-Line Balun for Antenna Measurements

The delay-line balun loss was validated with measurements by means of a back-to-back structure, shown in Fig. 7.18b, showing good agreement with FW simulations (Fig. 7.21). The effect of the landing pads is comparable to the one observed in Fig. 7.19.

7.6 Conclusion

In this chapter, a wideband H-band LWA with a quartz cavity fed by a dipole is presented, to be used as silicon lens feed. The quartz antenna is connected to the active GaAs front-end by means of a novel air-bridge interconnect technology based on spray coating and laser lithography. The new proposed packaging approach avoids the use of waveguide split-blocks, and facilitates the front-end assembly. Full-wave antenna simulations show good impedance matching, aperture efficiency higher than 74 % over 34 % bandwidth, and radiation efficiency higher than 70 % over 37 % bandwidth for an integrated antenna. The radiation efficiency accounts for losses in the GaAs-quartz interconnect, dipole feeding line and lens. A prototype dedicated to the characterization has been fabricated. Scattering parameters, near-field and coupling measurement have been performed, validating the performance of the proposed integrated antenna-in-package solution at H-band.

Chapter 8

Conclusions and Future Outlook

This work focuses in the design of lens antennas at frequencies higher than 100 GHz, for point-to-multipoint and small cell applications in Beyond 5G and 6G communications. New design methodologies, based on spectral Green's function for stratified media and an analysis in reception, are introduced to enable the fast optimization of large lenses. Applying this methodology, four lens antenna designs are developed at G-band and H-band, featuring some of the properties required in the use cases evaluated: wide bandwidth, high directivity, high efficiency, circular polarization, enhanced steering range, and low-loss interface with the active front-end. All four designs make use of resonant LW feeds in order to achieve high aperture efficiency over a wideband. New measurement approaches based on coupling between lenses in the near-field are proposed, enabling the characterization of the lens antenna gain and axial ratio at these high frequencies.

In this chapter, an overview of the conclusions and most significant results of this dissertation is given, and recommendations regarding future research paths are discussed.

8.1 Optimization Methodology: Analysis of the Lens in Reception and Spectral Green's Functions

In this thesis, an analysis in reception, combined with spectral Green's function for stratified media, is proposed to optimize integrated lenses with LW feeds in terms of aperture efficiency. In this evaluation the aperture efficiency (taper, spill-over, and reflection efficiencies) is calculated as the coupling to a plane wave, by performing a reaction integral between the GO field associated to the plane wave, and the field radiated by the feed. When designing lenses with large dimensions in terms of wavelength, the computational effort of the quasi-analytic calculation is much lower than the one in full-wave simulations, in which these optimizations would become extremely time-consuming.

Applying this methodology, described in Chapter 2, the design rules for truncated elliptical lenses with LW feeds, aiming for maximum aperture efficiency at the broadside beam, were derived in Chapter 3. From this evaluation, the bandwidth characteristics of the lenses with LW feeds were obtained, showing that aperture efficiencies higher than 80 % can be achieved in lenses with $\varepsilon_r \sim 2.3$. This methodology has been applied in Chapter 4 to optimize the lens truncation angle, feed phase center and feed geometry with the aim of maximizing the lens aperture efficiency.

The analysis in reception with spectral techniques has been extended in Chapter 5 and Appendix A to enable the optimization of the circularly polarized lens presented in Chapter 5, in terms of aperture efficiency and axial ratio. In this case, the coupling to circularly polarized plane waves was calculated, from which the axial ratio has been estimated. The advantage in terms of computational effort with respect to full-wave simulations is in this case even larger. The polarizer structures are small in terms of wavelength and should be finely discretized, becoming the model extremely heavy for a full-wave optimization.

In Chapter 6, this methodology has been applied to minimize the scan loss for a certain beam steering in the elliptical lens with gratings wedge. In this case, the feed fields are evaluated in the near-field, in contrast with previous implementations, where an asymptotic evaluation of the feed far-field was used.

An analysis in reception has been as well applied to estimate the coupling between lenses, or the reflected power from a metallic reflector located on top of the lens. Those calculations were useful to characterize and validate the developed lens prototypes.

8.2 Wideband Lens Solutions with Leaky-Wave Feeds

Applying the design methodology explained in the previous section, four integrated lens prototypes were developed, fabricated and characterized within this dissertation, which are described in Chapter 4, Chapter 5, Chapter 6, and Chapter 7. In order to derive realistic specifications for the prototypes, link-budgets for real use cases were calculated, as explained in Chapter 1. All four design focus on some of the main aspects required in mm- and sub-mm-wave Fly's eye lenses for Beyond 5G and 6G applications: wideband characteristic, high aperture efficiency, multi-beam capability, low loss. Besides, every prototype makes emphasis in additional features which are useful as well in the studied use cases: large steering range with low scan loss, circular polarization, and efficient transition from the antenna to the active front-end.

In order to achieve high aperture efficiency over a wideband, resonant LW feeds were used in all designs presented in this thesis. As explained in Chapter 3, this feed is based on a resonant cavity located between a ground plane and the lens dielectric, where several LW modes propagate while radiating energy into the lens. This effect enlarges the feed effective area, hence its directivity, achieving a highly efficient lens illumination.

The trade-offs in terms of bandwidth, aperture efficiency and steering range were studied in Chapter 3 depending on the LW feed cavity and lens ε_r. This study served as a reference for the lens designs developed within this thesis. The dispersion characteristic of the LW feed is more wideband for lower contrast between the cavity and lens ε_r. It is therefore that low contrast has been chosen for all designs, aiming for relative bandwidths higher than 35 %.

In the following, the lens designs and the performance achieved are described. Measurement results for all four prototypes validate the design methodology based on the analysis in reception, applied within this dissertation.

8.2.1 Wideband Linearly Polarized Plastic Lens (G-Band)

In Chapter 4, a broadband integrated lens antenna at G-band ($140 - 220\,\mathrm{GHz}$) was presented, fabricated in low-cost HDPE material. The lens, with $18\lambda_0$ diameter, is fed by a resonant LW feed based on an air cavity, excited by a waveguide through a double-slot in the ground plane. This design achieves a gain larger than 31 dB at broadside over 44 % relative bandwidth, reaching aperture efficiency higher than 80 % and dielectric loss lower than 0.5 dB over the whole frequency band. The lens is able to steer up to 12 deg with 3 dB scan loss, which enables the generation of 40 beams overlapping at $-3\,\mathrm{dB}$ on a two-dimensional Fly's eye planar panel. The reflection coefficient is lower than $-10\,\mathrm{dB}$ over the whole bandwidth. In this prototype, the configuration with an air cavity and a lens with low ε_r allows reaching high efficiency and bandwidth (state-of-the-art performances), at the cost of limited steering range. Measurement results for the fabricated prototype have validated the described performances.

8.2.2 Wideband Circularly Polarized Plastic Lens (G-Band)

Chapter 5 introduced a wideband circularly polarized lens design at G-band, building on the design presented in Chapter 4. Circular polarization is generated by integrating a dielectric grid polarizer inside the lens, achieving a compact design. The new polarizer unit cell proposed features excellent transmission properties over a broadband, and enables its fabrication with standard milling techniques at frequencies higher than 100 GHz. The circularly-polarized lens reaches state-of-the-art performances, with an aperture efficiency higher than 75 % and axial ratio lower than 3 dB over 35 % relative bandwidth. The broadside beam achieves more than 31 dB gain over the whole bandwidth, with less than 0.65 dB dielectric loss. Thanks to integrating the polarizer inside the lens, the lens steering range is preserved w.r.t. the linearly polarized design presented in Chapter 4. A prototype has been fabricated and characterized, validating the described performance.

8.2.3 Plastic Lens with Enhanced Steering Range (G-Band)

Chapter 6 introduced a strategy to enhance the steering range of the low ε_r lens designs presented in Chapter 4 and Chapter 5. For this aim, a wedge of dielectric gratings with modulated height is integrated inside the plastic lens, on top of the LW feed. The gratings wedge causes beam steering in the feed radiation pattern inside the lens, displacing its phase center laterally and axially, and enabling a reduction in the spill-over and reflection loss for the off-focus beams. An iterative synthesis procedure for the gratings wedge is presented, taking into account the feed spherical wave propagation. The gratings are analysed resorting to effective medium theory, representing each grating with a series of equivalent transmission lines.

The design reaches 25 deg steering with 3.6 dB scan loss w.r.t. the broadside beam in Chapter 4. This represents an improvement of 4.2 dB w.r.t. displacing the feed in the focal plane in the lens without gratings wedge, and 2.2 dB w.r.t. optimizing the feed position laterally and axially, also without gratings wedge. This improvement is visible over a wideband, with a scan loss lower than 4.1 dB over the whole bandwidth. Measurement results for the fabricated prototype have validated the described performances. The gratings wedge could be as well integrated below the polarizer introduced in Chapter 5, enhancing the steering in the circularly polarized lens.

8.2.4 Silicon Lens with Integrated Quartz Feed (H-Band)

In Chapter 7, a silicon lens design was presented in H-band ($220-320$ GHz), making use of a quartz chip to implement the cavity of the resonant LW feed. Thanks to the low contrast between the quartz cavity and silicon lens, large bandwidths can be reached, similar to the ones achieved with the plastic prototypes presented previously. However, in this case larger steering angles are achieved (25 deg) due to the use of a lens with high ε_r. The

LW feed is excited by a dipole, located at the center of the cavity, at quarter wavelength distance of the ground plane. The differential approach allows implementing a symmetric connection to the active front-end chip, with no need of ground connection. A new air-bridge interconnect technology, based on spray coating and laser lithography, provides a wideband, low-loss transition, enabling a highly efficient off-chip antenna concept which facilitates the front-end and lens assembly.

Full-wave antenna simulations for an integrated antenna show aperture efficiency higher than 74 % over 34 % bandwidth, and radiation efficiency higher than 70 % over 37 % bandwidth. The radiation efficiency accounts for losses in the GaAs-quartz interconnect, dipole feeding line and lens. The lens is in this case smaller in terms of wavelength as in previous designs ($7.2\lambda_0$), achieving 24.5 dB gain at the center frequency. Nevertheless, the lens could be easily scaled to achieve larger gains, with similar performance in terms of aperture and radiation efficiency. The reflection coefficient is lower than -10 dB over 37 % bandwidth. Power lost due to cross-polar radiation due to the dipole feeding lines stays below 0.5 dB over the whole frequency band. A prototype dedicated to the characterization has been fabricated and measured, validating the integrated antenna performance.

8.3 Lens Characterization Strategies at Sub-THz Frequencies

In the frame of the development of antennas for Beyond 5G and 6G communications, not only new antenna concepts are needed, but also advances in antenna characterization techniques. In this dissertation, new methods based on near-field coupling were proposed to estimate the lens gain and axial ratio. In all described coupling measurements, time gating is applied in order to account only for the first order rays.

In Chapter 4, a method was proposed to estimate the radiation efficiency in dielectric lenses, in order to validate the antenna gain. The approach consists in measuring the coupling in the near-field between two identical lenses. Alternatively, in Chapter 7, the reflection coefficient of a lens with a flat metallic reflector on top, at near-field distance, is measured to perform the same estimation. To perform the validation, the coupling can be calculated with the analysis in reception or by means of full-wave simulations for the first order ray.

In Chapter 5, the coupling between a circularly polarized lens and a linearly polarized lens in two orthogonal polarizations was measured (phase-amplitude method), in order to validate the antenna gain and axial ratio. The coupling to the linearly polarized lens can be as well calculated with the analysis in reception. A strategy to perform a fine phase calibration between the two orthogonally oriented measurements has been introduced in Chapter 5. This calibration method has been used as well for the characterization of the circularly polarized near-fields.

In Chapter 5, it was also proposed to estimate the antenna polarization purity with a single coupling measurement, by characterizing the reflection coefficient of the circularly polarized antenna with a flat metallic reflector on top. In this way, no phase calibration is needed.

8.4 Future Outlook

The future perspectives for this thesis are summarized in the following:

- In this thesis, an extensive study of truncated lens antennas in terms of aperture efficiency and steering capability has been carried out, in order to be applied in Fly's eye array configurations. However, the construction and characterization of the Fly's eye array itself is still not completed. The coupling between different feeds or the far-field characterization of the beams embedded in the array are some of the parameters which may be studied. The performance of multiple feeds integrated under one lens should be still evaluated in detail.

- In the context of the construction of a full Fly's eye array, the integration of the polarizer in Chapter 5 and the gratings wedge in Chapter 6 under the lenses would enable circularly polarized beams with enhanced steering capability. The array optimization, fabrication and characterization should be carried out.

- All the designs presented in this thesis feature a single polarization. Dual polarized designs are of interest in communications, as they allow doubling the link capacity or enable the integration of transmitter and receiver antennas under the same aperture. The extension of the LW feed concepts to achieve two orthogonal polarizations would bring challenges in terms of antenna design, as enough decoupling between polarizations should be achieved, and wideband antenna feeding concepts.

- The integration of multiple active front-ends in array configuration under one lens might require alternative antenna feeding strategies or further innovation in the transition from the front-end to the antenna. This is one of the challenges which remain open for future developments.

- The steering enhancement strategy for low ε_r lenses presented in Chapter 6 of this dissertation has been applied only to one polarization (H-plane), and it should be still investigated for the E- and D-planes. For this aim, the modelling of anisotropic pyramidal gratings described in Appendix B for the principal planes should be extended to any arbitrary plane. This would also enable to expand the gratings wedge design capability from a 2D to a 3D profile, enhancing the phase efficiency further.

- The Fly's eye antenna concept studied in this dissertation applies to fixed beam applications. An extension to architectures enabling dynamic beam steering can be carried out by introducing mechanical displacement of the lenses, or switchable feeding networks. The steering enhancement concepts should be adapted or extended for those cases.

8.5 Impact of the Research

The work described in this dissertation has led to a number of journal and conference publications (see List of Publications in page 173). In total four peer-reviewed journal publications are published or submitted, together with 17 conference publications. The research performed in the work described in Chapter 5 was nominated for the *Best Antenna Design and Application Award* in the European Conference on Antennas and Propagation (EuCAP), Krakow, Poland, 2019.

Appendix A

Spectral Green's Functions in Stratified Isotropic and Anisotropic Media

In this appendix, the evaluation of the fields radiated by a source in the presence of both isotropic and anisotropic stratified media is summarized. This analysis has been applied to calculate the near-fields and far-fields of the leaky-wave feed radiating directly inside the lens, and for the feed radiating through the dielectric grating polarizer inside the lens.

A.1 Evaluation of Spectral Fields in Stratified Media

The $[\vec{E}, \vec{H}]$ field radiated by a source in an observation point defined by $[\rho, z]$ can be expressed as a 2D Fourier transform of the spectral fields $[\tilde{\vec{E}}, \tilde{\vec{H}}]$ with respect to the variables x and y as

$$\vec{E}(\vec{\rho}, z) = \frac{1}{4\pi^2} \int_{-\infty}^{\infty} \int_{-\infty}^{\infty} \tilde{\vec{E}}(\vec{k}_\rho, z) e^{-j\vec{k}_\rho \cdot \vec{\rho}} dk_x dk_y \tag{A.1a}$$

$$\vec{H}(\vec{\rho}, z) = \frac{1}{4\pi^2} \int_{-\infty}^{\infty} \int_{-\infty}^{\infty} \tilde{\vec{H}}(\vec{k}_\rho, z) e^{-j\vec{k}_\rho \cdot \vec{\rho}} dk_x dk_y \tag{A.1b}$$

where $\vec{k}_\rho = k_x \hat{x} + k_y \hat{y}$ and $\vec{\rho} = x\hat{x} + y\hat{y}$.

The far-field can be calculated applying an the asymptotic evaluation of the spectral integral in Eq. (A.1a) as follows

$$\vec{E}_{\text{far}}(\vec{r}) \approx 2jk_{\text{zs}}\tilde{\vec{E}}\left(\vec{k}_{\rho s}, z\right) e^{jk_{\text{zs}}z}\frac{e^{-jk_d r}}{4\pi r} \tag{A.2}$$

where $k_d = k_0\sqrt{\epsilon_r}$, $k_{\rho s} = k_d \sin\theta$ and $k_{\text{zs}} = k_d \cos\theta$.

The spectral electric and magnetic fields $[\tilde{\vec{E}}, \tilde{\vec{H}}]$ in stratified media can be evaluated in the i-medium via the introduction of an equivalent transmission line that represents the stratification in z [141] as

$$\tilde{\vec{E}}_{\text{TM}}(\vec{k}_\rho, z) = -\frac{j\zeta^{(i)}k_\rho^2}{k^{(i)}} I^{(i)}_{\text{TM}}(\vec{k}_\rho, z)\hat{z} + \frac{j\zeta^{(i)}k_z^{(i)}}{k} k_\rho I^{(i)}_{\text{TM}}(\vec{k}_\rho, z)\hat{k}_\rho \tag{A.3a}$$

$$\tilde{\vec{E}}_{\text{TE}}(\vec{k}_\rho, z) = -jk_\rho V^{(i)}_{\text{TE}}(\vec{k}_\rho, z)\hat{\alpha} \tag{A.3b}$$

$$\tilde{\vec{H}}_{\text{TM}}(\vec{k}_\rho, z) = jk_\rho I^{(i)}_{\text{TM}}(\vec{k}_\rho, z)\hat{\alpha} \tag{A.3c}$$

$$\tilde{\vec{H}}_{\text{TE}}(\vec{k}_\rho, z) = -\frac{jk_\rho^2}{\zeta^{(i)}k^{(i)}} V^{(i)}_{\text{TE}}(\vec{k}_\rho, z)\hat{z} + \frac{jk_z^{(i)}}{\zeta^{(i)}k^{(i)}} k_\rho V^{(i)}_{\text{TE}}(\vec{k}_\rho, z)\hat{k}_\rho \tag{A.3d}$$

where $\zeta^{(i)}$ is the i-medium characteristic impedance, $k_z^{(i)} = \sqrt{k^{(i)2} - k_\rho^2}$, $\hat{k}_\rho = \frac{1}{k_\rho}(k_x\hat{x} + k_y\hat{y})$ and $\hat{\alpha} = \frac{1}{k_\rho}(k_x\hat{y} - k_y\hat{x})$. The transmission line characteristic impedances are defined as

$$Z^{(i)}_{\text{TM}} = \frac{k_z^{(i)}\zeta^{(i)}}{k^{(i)}} \tag{A.4a}$$

$$Z^{(i)}_{\text{TE}} = \frac{k^{(i)}\zeta^{(i)}}{k_z^{(i)}} \tag{A.4b}$$

Fig. A.1 shows the equivalent transmission line models for the LW feed excited with a dipole (Fig. A.1a) and a slot (Fig. A.1b).

A source represented with an equivalent electric current density distribution, $\tilde{\vec{J}}_s(\vec{k}_\rho)$, can be introduced in the transmission line via a pair of current generators, I_g^{TE} and I_g^{TM}, with the following amplitude

$$I_g^{\text{TE}} = \frac{\tilde{\vec{J}}_s \cdot \hat{k}_\rho}{jk_\rho} \tag{A.5a}$$

$$I_g^{\text{TM}} = -\frac{\tilde{\vec{J}}_s \cdot \hat{\alpha}}{jk_\rho} \tag{A.5b}$$

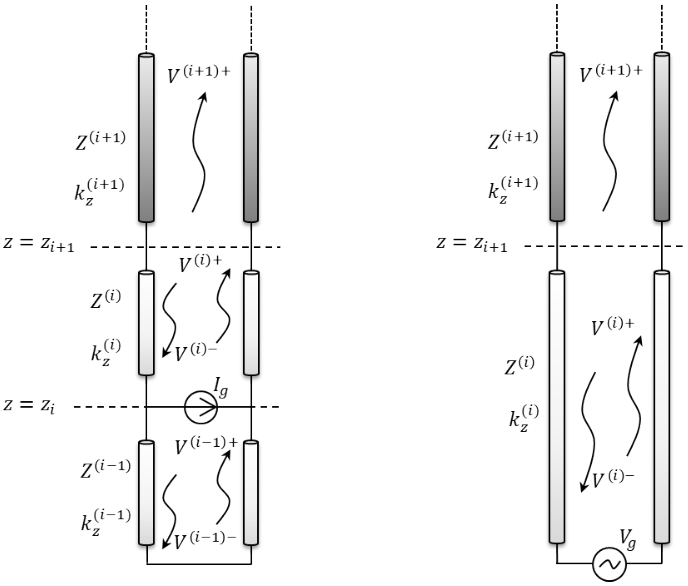

(a) (b)

Figure A.1: Equivalent transmission line model for the LW feed with a) an electric source and b) a magnetic source. The transmission lines apply for both TE and TM modes.

being $\tilde{\vec{J}}_s$ the Fourier transform of the equivalent electric currents. Note that I_g^{TE} and I_g^{TM} include information about the source amplitude and polarization orientation. In the LW feed in Chapter 7, $\tilde{\vec{J}}_s$ for the bow-tie dipole is approximated with the current of an ideal line dipole, giving a good first estimation of the primary fields.

Dually, a source represented with an equivalent magnetic current density distribution, $\tilde{\vec{M}}_s(\vec{k}_\rho)$, can be introduced in the transmission line via a pair of voltage generators, V_g^{TE} and V_g^{TM}, with the following amplitude

$$V_g^{\mathrm{TE}} = -\frac{\tilde{\vec{M}}_s \cdot \hat{k}_\rho}{jk_\rho} \tag{A.6a}$$

$$V_g^{\mathrm{TM}} = -\frac{\tilde{\vec{M}}_s \cdot \hat{\alpha}}{jk_\rho} \tag{A.6b}$$

being $\tilde{\vec{M}}_s$ the Fourier transform of the equivalent magnetic currents. The approximated expression for the double-slot spatial currents in the LW feed is given in Chapter 3 and validated in Chapter 4.

A.1.1 Application to Isotropic Stratified Media

In case of dealing with isotropic media, the source polarization determines the field polarization in any z-coordinate along the transmission line model. We can therefore normalize the solutions of the transmission line to the amplitude and polarization of the described current generators.

If the equivalent source currents are electric, the currents and voltages are normalized with the amplitude and polarization of the current generators I_g^{TE} and I_g^{TM} as

$$i_{\mathrm{TE}} = \frac{I_{\mathrm{TE}}}{I_g^{\mathrm{TE}}} = \frac{I_{\mathrm{TE}} j k_\rho}{J_s \hat{p} \cdot \hat{\alpha}} \tag{A.7a}$$

$$v_{\mathrm{TE}} = \frac{V_{\mathrm{TE}}}{I_g^{\mathrm{TE}}} = \frac{V_{\mathrm{TE}} j k_\rho}{J_s \hat{p} \cdot \hat{\alpha}} \tag{A.7b}$$

$$i_{\mathrm{TM}} = \frac{I_{\mathrm{TM}}}{I_g^{\mathrm{TM}}} = -\frac{I_{\mathrm{TM}} j k_\rho}{J_s \hat{p} \cdot \hat{k}_\rho} \tag{A.7c}$$

$$v_{\mathrm{TM}} = \frac{V_{\mathrm{TM}}}{I_g^{\mathrm{TM}}} = -\frac{V_{\mathrm{TM}} j k_\rho}{J_s \hat{p} \cdot \hat{k}_\rho} \tag{A.7d}$$

In this way, we obtain current generators with unitary amplitude, $i_g^{\mathrm{TE}} = i_g^{\mathrm{TM}} = 1$.

Substituting these equations in the spectral electric and magnetic field expressions, we can derive the spectral Green's function dyadic, which relates the electric or magnetic fields at any z-quote with the electric current source as

$$\tilde{\vec{H}}(\vec{k}_\rho, z) = \underline{\underline{\tilde{G}}}^{hj}(\vec{k}_\rho, z, z')\tilde{\vec{J}}(\vec{k}_\rho, z') \tag{A.8a}$$

$$\tilde{\vec{E}}(\vec{k}_\rho, z) = \underline{\underline{\tilde{G}}}^{ej}(\vec{k}_\rho, z, z')\tilde{\vec{J}}(\vec{k}_\rho, z') \tag{A.8b}$$

The Green's function dyadics, assuming that the source is in the xy plane, result in

$$\underline{\underline{\tilde{G}}}^{hj}(\vec{k}_\rho, z, z') = \begin{bmatrix} \frac{(i_{\mathrm{TM}} - i_{\mathrm{TE}}) k_x k_y}{k_\rho^2} & \frac{i_{\mathrm{TE}} k_x^2 + i_{\mathrm{TM}} k_x^2}{k_\rho^2} \\ \frac{i_{\mathrm{TE}} k_x^2 + i_{\mathrm{TM}} k_x^2}{k_\rho^2} & \frac{(i_{\mathrm{TE}} - i_{\mathrm{TM}}) k_x k_y}{k_\rho^2} \\ \frac{k_y v_{\mathrm{TE}}}{\zeta k} & \frac{k_x v_{\mathrm{TE}}}{\zeta k} \end{bmatrix} \tag{A.9a}$$

$$\underline{\underline{\tilde{G}}}^{ej}(\vec{k}_\rho, z, z') = \begin{bmatrix} -\frac{v_{\mathrm{TM}} k_x^2 + v_{\mathrm{TE}} k_x^2}{k_\rho^2} & \frac{(v_{\mathrm{TE}} - v_{\mathrm{TM}}) k_x k_y}{k_\rho^2} \\ \frac{(v_{\mathrm{TE}} - v_{\mathrm{TM}}) k_x k_y}{k_\rho^2} & -\frac{v_{\mathrm{TE}} k_x^2 + v_{\mathrm{TM}} k_x^2}{k_\rho^2} \\ \frac{\zeta k_x i_{\mathrm{TM}}}{k} & \frac{\zeta k_y i_{\mathrm{TM}}}{k} \end{bmatrix} \tag{A.9b}$$

If the equivalent source currents are magnetic, the currents and voltages are normalized with the amplitude and polarization of the voltage generators V_g^{TE} and V_g^{TM} as

$$v_{\mathrm{TE}} = \frac{V_{\mathrm{TE}}}{V_g^{\mathrm{TE}}} = -\frac{V_{\mathrm{TE}} j k_\rho}{M_s \hat{p} \cdot \hat{k}_\rho} \tag{A.10a}$$

$$i_{\mathrm{TE}} = \frac{I_{\mathrm{TE}}}{V_g^{\mathrm{TE}}} = -\frac{I_{\mathrm{TE}} j k_\rho}{M_s \hat{p} \cdot \hat{k}_\rho} \tag{A.10b}$$

$$v_{\mathrm{TM}} = \frac{V_{\mathrm{TM}}}{V_g^{\mathrm{TM}}} = -\frac{V_{\mathrm{TM}} j k_\rho}{M_s \hat{p} \cdot \hat{\alpha}} \tag{A.10c}$$

$$i_{\mathrm{TM}} = \frac{I_{\mathrm{TM}}}{V_g^{\mathrm{TM}}} = -\frac{I_{\mathrm{TM}} j k_\rho}{M_s \hat{p} \cdot \hat{\alpha}} \tag{A.10d}$$

In this way, we obtain current generators with unitary amplitude, $v_g^{\mathrm{TE}} = v_g^{\mathrm{TM}} = 1$.

Substituting these equations in the spectral electric and magnetic field expressions, we can extract the spectral Greens function dyadic, which relates the electric or magnetic fields at any z-quote with the magnetic current source as

$$\vec{\tilde{E}}(\vec{k}_\rho, z) = \underline{\underline{\tilde{G}}}^{em}(\vec{k}_\rho, z, z')\vec{\tilde{M}}(\vec{k}_\rho, z') \tag{A.11a}$$

$$\vec{\tilde{H}}(\vec{k}_\rho, z) = \underline{\underline{\tilde{G}}}^{hm}(\vec{k}_\rho, z, z')\vec{\tilde{M}}(\vec{k}_\rho, z') \tag{A.11b}$$

The Greens function dyadic, assuming that the source is in the xy plane, results in

$$\underline{\underline{\tilde{G}}}^{em}(\vec{k}_\rho, z, z') = \begin{bmatrix} \frac{(v_{\mathrm{TM}} - v_{\mathrm{TE}})k_x k_y}{k_\rho^2} & -\frac{v_{\mathrm{TE}} k_x^2 + v_{\mathrm{TM}} k_x^2}{k_\rho^2} \\ \frac{v_{\mathrm{TE}} k_x^2 + v_{\mathrm{TM}} k_x^2}{k_\rho^2} & \frac{(v_{\mathrm{TE}} - v_{\mathrm{TM}})k_x k_y}{k_\rho^2} \\ -\frac{\zeta k_y i_{\mathrm{TM}}}{k} & \frac{\zeta k_x i_{\mathrm{TM}}}{k} \end{bmatrix} \tag{A.12a}$$

$$\underline{\underline{\tilde{G}}}^{hm}(\vec{k}_\rho, z, z') = \begin{bmatrix} -\frac{i_{\mathrm{TM}} k_x^2 + i v_{\mathrm{TE}} k_x^2}{k_\rho^2} & \frac{(i_{\mathrm{TM}} - i_{\mathrm{TE}})k_x k_y}{k_\rho^2} \\ \frac{(i_{\mathrm{TM}} - i_{\mathrm{TE}})k_x k_y}{k_\rho^2} & -\frac{i_{\mathrm{TM}} k_x^2 + i_{\mathrm{TE}} k_x^2}{k_\rho^2} \\ \frac{k_x v_{\mathrm{TE}}}{\zeta k} & \frac{k_y v_{\mathrm{TE}}}{\zeta k} \end{bmatrix} \tag{A.12b}$$

These dyadic spectral Greens Functions select the field polarization at any z-quote, corresponding to the chosen source orientation. The spatial fields can be then derived by calculating the Fourier transform of the spectral fields with respect to k_ρ, k_α as described previously, or in the far-field with the asymtotic evaluation of the integral.

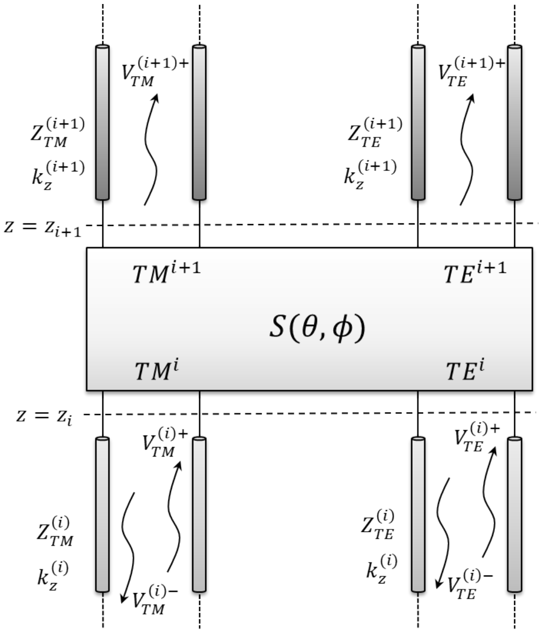

Figure A.2: Equivalent transmission line model with S-parameter matrix describing interaction between TE and TM modes in anisotropic media.

A.1.2 Application to Anisotropic Stratified Media

If the analysed stratification includes anisotropic media, the field polarization does not only depend on the source orientation. Anisotropic media present different effective dielectric permittivity (ε_r) for different field polarization vectors, fact which origins couplings between the TE and TM field components and therefore polarization change. It is therefore not possible to normalize the source and consequently the voltage and currents solutions at any z-quote with the equivalent generator amplitude and polarization, as we would lose the information about the field polarization changes. The sources used in the transmission line should be therefore I_g^{TE} and I_g^{TM}, in case of electric surface currents, or V_g^{TE} and V_g^{TM}, in case of magnetic surface currents, as defined previously.

In order to take into account the transmission and reflection between TE and TM components in the anisotropic media, an S-parameter matrix is introduced, which couples both TE and TM equivalent transmission lines.

The voltages and currents before and after the anisotropic media are related through the following equations

$$V_{\mathrm{TM}}^{(i+1)} = V_{\mathrm{TM}}^{(i+1)+} e^{-jk_z^{(i+1)} z} = \left(s_{\mathrm{TM-TM}} V_{\mathrm{TM}}^{(i)+} + s_{\mathrm{TM-TE}} \sqrt{\frac{Z_{\mathrm{TM}}^{(i+1)}}{Z_{\mathrm{TE}}^{(i)}}} V_{\mathrm{TE}}^{(i)+} \right) e^{jk_z^{(i+1)}(z_{i+1}-z_i)} e^{-jk_z^{(i+1)} z} \tag{A.13a}$$

$$I_{\mathrm{TM}}^{(i+1)} = \frac{V_{\mathrm{TM}}^{(i+1)-} e^{-jk_z^{(i+1)} z}}{Z_{\mathrm{TM}}^{(i+1)}} \tag{A.13b}$$

$$V_{\mathrm{TE}}^{(i+1)} = V_{\mathrm{TM}}^{(i+1)+} e^{-jk_z^{(i+1)} z} = \left(s_{\mathrm{TE-TM}} \sqrt{\frac{Z_{\mathrm{TE}}^{(i+1)}}{Z_{\mathrm{TM}}^{(i)}}} V_{\mathrm{TM}}^{(i)+} + s_{\mathrm{TE-TE}} V_{\mathrm{TE}}^{(i)+} \right) e^{jk_z^{(i+1)}(z_{i+1}-z_i)} e^{-jk_z^{(i+1)} z} \tag{A.13c}$$

$$I_{\mathrm{TE}}^{(i+1)} = \frac{V_{\mathrm{TE}}^{(i+1)-} e^{-jk_z^{(i+1)} z}}{Z_{\mathrm{TE}}^{(i+1)}} \tag{A.13d}$$

After finding the solutions for the voltages and currents in every z-quote, the spectral fields can be calculated with Eq. (A.3). The spatial fields can be then derived by calculating the Fourier transform of the spectral fields with respect to k_ρ, k_α as described previously, or in the far-field with the asymtotic evaluation of the integral.

A.2 Floquet Mode Scattering Matrix

The polarizer transmission coefficients are calculated by Floquet-mode CST simulations [121] for the polarizer unit cell. In those Floquet-mode simulations, the S-parameters for the transmission and reflection between the first two modes (TE_1 and TM_1) are calculated with periodic boundary conditions. Those fulfil the equations listed in Appendix A.1.2 for the voltages at the input and output. It has been verified that the TE and TM field vector definition in CST follow the same convention as the transmission line model, i.e. the transmission and reflection coefficients are calculated only for the transverse components. However, In CST, the S-parameters correspond to the transmission and reflection between TE and TM E-field transverse components. In order to use them to relate the voltages, a minus sign is needed in the crossed terms (TM-TE), as only the TE voltage has contrary sign with respect to the TE electric field (Eq. (A.3)).

In the unit cell simulations with periodic boundary conditions, the polarizer anisotropy axes are aligned with the coordinate system. In order to use the anisotropy to create

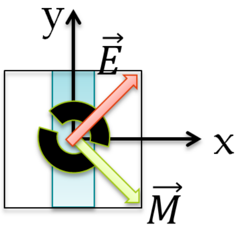

Figure A.3: Coordinate system used for the unit cell and slots in CST Floquet mode simulations, and in the SGF modelling.

circular polarization, the source linear polarization should be rotated 45 deg with respect to the polarizer unit cell Fig. A.3. Defining the slot rotation angle γ from the y-axis, the magnetic currents for both slots can be expressed as

$$\vec{m}_s(\rho, \phi) \approx \frac{1}{\rho} \cos\left[\frac{\pi}{2\alpha}\left(\phi \pm \frac{\pi}{2} - \gamma\right)\right] \operatorname{rect}\left(\phi \pm \frac{\pi}{2} - \gamma, 2\alpha\right) \operatorname{rect}\left(\rho - \frac{\rho_0}{2}, w\right) (\cos\gamma\hat{x} + \sin\gamma\hat{y}) \tag{A.14}$$

Appendix B

Dielectric Gratings Modelling

B.1 Introduction

The electromagnetic wave propagation along periodic sub-wavelength dielectric gratings can be modelled as the propagation through equivalent homogeneous media. The EMT derives the electromagnetic properties of the equivalent homogeneous media for a given grating geometry (e.g. effective dielectric permittivity). Closed-form solutions for the EMT effective permittivity of 1D rectangular or lamellar gratings [128], 2D rectangular gratings [129], cylindrical perforations [130], pyramidal gratings with different bases [131] or arbitrary 1D structures [132] have been derived in the literature. Besides, 1D gratings can be evaluated more accurately as a stack of multiple thin layers with rectangular lamellar geometry, as already proposed in [127, 133, 134] for circular rods, triangular, sinusoidal, or arbitrary profiles. In this work, this approach will be followed to calculate the phase of the transmitted wave along the pyramidal gratings.

B.2 Discretization and Effective Medium Theory

Fig. B.1 shows the representation of a grating as a stack of $n = 1 : N$ 1D rectangular gratings with height $l \ll h$, where each of them can be approximated as a uniaxial anisotropic medium, where the axes are aligned with the grating symmetry axes. The effective permittivity tensor is defined for the n-th layer as

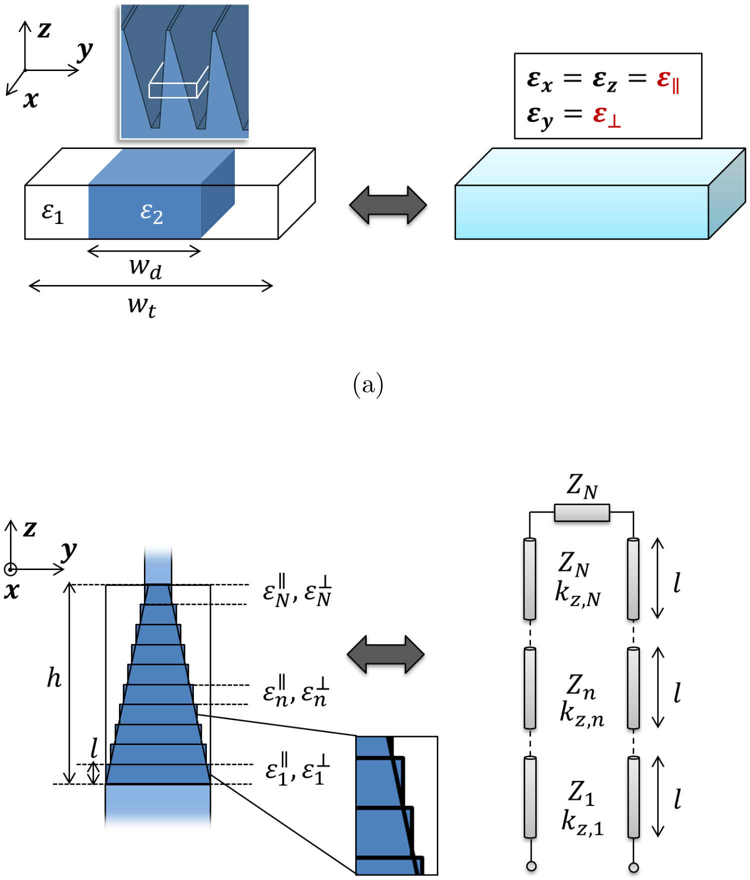

(a)

(b)

Figure B.1: a) Dielectric squared grating and its equivalent homogeneous anisotropic medium. b) Pyramid-pair discretization and equivalent transmission line model.

$$\underline{\underline{\varepsilon_n}} = \begin{pmatrix} \varepsilon_r^{\parallel} & 0 & 0 \\ 0 & \varepsilon_r^{\perp} & 0 \\ 0 & 0 & \varepsilon_r^{\parallel} \end{pmatrix} \tag{B.1}$$

with the coordinate system in Fig. B.1. As the grating period is not extremely small with respect to the wavelength ($0.6\lambda_d$ at the highest frequency), a second-order solution respect to the period-to-wavelength ratio, α, has been considered to calculate the effective permittivity [127]. The expressions for $\varepsilon_n^{\parallel}$ and $\varepsilon_n^{\perp}$, depend as well on its dielectric material fill factor in the n-th layer, $f_n = w_d/w_t$ (Fig. B.1), the ε_r in both the dense medium, ε_2, and the medium where the gratings are immerse, ε_1, as

$$\varepsilon_n^{\parallel} = \varepsilon_n^0 + \frac{\pi^2}{3}\left[(1-f_n)(\varepsilon_2-\varepsilon_1)\right]^2\alpha^2 \tag{B.2a}$$

$$\varepsilon_n^{\perp} = \frac{1}{a_n^0} + \frac{\pi^2}{3}\left[f_n(1-f_n)\frac{\varepsilon_2-\varepsilon_1}{\varepsilon_2\varepsilon_1}\right]^2\frac{\varepsilon_0}{(a_n^0)^3}\alpha^2 \tag{B.2b}$$

where $\varepsilon_n^0 = \varepsilon_2 f_n + \varepsilon_1(1-f_n)$ and $a_n^0 = f_n/\varepsilon_2 + (1-f_n)/\varepsilon_1$. In the design in Chapter 6, $\varepsilon_1 = 1$ and $\varepsilon_2 = 2.3$. This model assumes that only the fundamental mode is supported in the gratings layer, and therefore the grating depth does not appear as a variable [135]. The dependency of the effective permittivity with respect to the angle of incidence [132], [136] has been as well neglected. The error introduced by these assumptions will be later on quantified comparing the EMT model with FW Floquet mode simulations.

B.3 Equivalent Transmission Line Model

In order to evaluate the reflection and transmission properties of the stack of thin uniaxial anisotropic media, methods such as the thin-film theory [133] or linearization of Ricatti differential equation for small reflections [134] have been proposed in the literature. In this work, we propose to apply an equivalent transmission line (TL) model with N-sections in z of thickness l, and so account for all multiple reflections in the pyramidal structure. The TL model is applied in the two principal planes, aligned with the anisotropy axis (planes $\phi = 0$ deg and $\phi = 90$ deg in Fig. B.1). In these planes the transmitted field for an incident plane-wave can be described as well as a single plane-wave [142], and TE and TM modes are de-coupled. The propagation constants and characteristic impedances for the TE and TM equivalent transmission lines have been estimated from the theory of wave propagation in anisotropic multi-layer media at oblique incidence [143].

For each layer in the stack, the propagation in the $\phi = 0$ deg plane can be described considering different effective permittivity for the TM and TE modes, as $\varepsilon_n^{\mathrm{TM}} = \varepsilon_n^{\parallel}$ and $\varepsilon_n^{\mathrm{TE}} = \varepsilon_n^{\perp}$. As $\varepsilon_n^x = \varepsilon_n^z = \varepsilon_n^{\parallel}$, the effective permittivity for the TM mode is independent from the incident angle. The propagation constant in a n-th section of the TL is then calculated as

$$k_{\mathrm{z,n}}^{\mathrm{TM/TE}} = \sqrt{\varepsilon_n^{\mathrm{TM/TE}}k_0^2 - k_\rho^2} \tag{B.3}$$

where $k_\rho = k_0\sqrt{\varepsilon_2}\sin\theta$, being θ the wave vector direction in the host dielectric. The impedances for the TE and TM modes in $\phi = 0$ deg are defined for this section as

$$Z_n^{\mathrm{TM}} = \frac{\zeta_0}{\sqrt{\varepsilon_n^{\mathrm{TM}}}}\frac{k_{z,n}^{\mathrm{TM}}}{k_n^{\mathrm{TM}}} \tag{B.4a}$$

$$Z_n^{\mathrm{TE}} = \frac{\zeta_0}{\sqrt{\varepsilon_n^{\mathrm{TE}}}}\frac{k_n^{\mathrm{TE}}}{k_{z,n}^{\mathrm{TE}}} \tag{B.4b}$$

where $k_n^{\mathrm{TM/TE}} = \sqrt{\varepsilon_n^{\mathrm{TM/TE}}}k_0$, and ζ_0 is the wave impedance in vacuum. In the plane $\phi = 90$ deg, $k_{z,n}^{\mathrm{TE}}$ and Z_n^{TE} can be defined as above, this time with $\varepsilon_n^{\mathrm{TE}} = \varepsilon_n^{\parallel}$. However, for the TM mode, as $\varepsilon_n^y = \varepsilon_n^{\perp} \neq \varepsilon_n^z$, $\varepsilon_n^{\mathrm{TM}}$ is dependent on the wave vector direction in the evaluated n-th layer, θ_n, as reported in [143]

$$\varepsilon_n^{\mathrm{TM}} = \frac{\varepsilon_n^{\perp}\varepsilon_n^{\parallel}}{\varepsilon_n^{\perp}\sin^2\theta_n + \varepsilon_n^{\parallel}\cos^2\theta_n} \tag{B.5}$$

where θ_n is calculated with the Snel's law for multilayer anisotropic media, as reported in [143]

$$\sin\theta_n = \frac{\sqrt{\varepsilon_{n-1}^{\perp}\varepsilon_{n-1}^{\parallel}\varepsilon_n^{\parallel}}\sin\theta_{n-1}}{\sqrt{\varepsilon_n^{\perp}\varepsilon_n^{\parallel}\left(\varepsilon_{n-1}^{\perp} - \varepsilon_{n-1}^{\parallel}\right) - \varepsilon_{n-1}^{\perp}\varepsilon_{n-1}^{\parallel}\left(\varepsilon_n^{\perp} - \varepsilon_n^{\parallel}\right)\sin^2\theta_{n-1} + \varepsilon_n^{\perp}\varepsilon_n^{\parallel}\varepsilon_{n-1}^{\parallel}}} \tag{B.6}$$

where $\varepsilon_{n-1}^{\perp}$ and $\varepsilon_{n-1}^{\parallel}$ are the yy and zz tensor components and θ_{n-1} the incident angle in the medium where the incident wave propagates. $k_{z,n}^{\mathrm{TM}}$ is calculated with $\varepsilon_n^{\mathrm{TM}}$ from Eq. (B.5) in the same way as in the $\phi = 0$ deg plane. Instead, the equation for the calculation of Z_n^{TM} becomes for $\phi = 90$ deg

$$Z_n^{\mathrm{TM}} = \frac{\zeta_0\sqrt{\varepsilon_n^{\mathrm{TM}}}}{\varepsilon_n^{\perp}}\frac{k_{z,n}^{\mathrm{TM}}}{k_n^{\mathrm{TM}}} \tag{B.7}$$

Once the propagation constants and characteristic impedances have been calculated for each layer, the computation of the transmission matrix (ABCD) for the full stack is calculated with a standard concatenation of ABCD matrices as

$$\begin{bmatrix} A_T & B_T \\ C_T & D_T \end{bmatrix} = \prod_{1}^{N} \begin{bmatrix} A_n & B_n \\ C_n & D_n \end{bmatrix} \tag{B.8}$$

where $A_n = \cos(k_{z,n}^{\mathrm{TE/TM}} l)$, $B_n = jZ_n^{\mathrm{TE/TM}} \sin(k_{z,n}^{\mathrm{TE/TM}} l)$, $C_n = (j/Z_n^{\mathrm{TE/TM}}) \sin(k_{z,n}^{\mathrm{TE/TM}} l)$ and $D_n = A_n$ [144]. The Scattering parameters (S-parameters) are calculated from the resulting ABCD matrix. For a single pyramid, the reference impedance for the S-parameter calculation is the one in the dielectric for the pyramid base side, and the one of the last slab in the pyramid tip, which would be the boundary condition when using mirrored pyramids. For two mirrored pyramids, the reference impedance is the one in the dielectric on both sides, as they will be embedded in the elliptical lens dielectric.

The transmission line model has been validated with full-wave (FW) Floquet mode simulations in CST Studio Suite [121] for a unit cell with periodic boundary conditions. S-parameter results for a pyramid-pair for broadside and oblique incidence are shown in Fig. B.2. The validation is shown for gratings with $h_{\max} = 1.27\,\mathrm{mm}$. The accuracy of the analytic results is sufficient for the application discussed in Chapter 6.

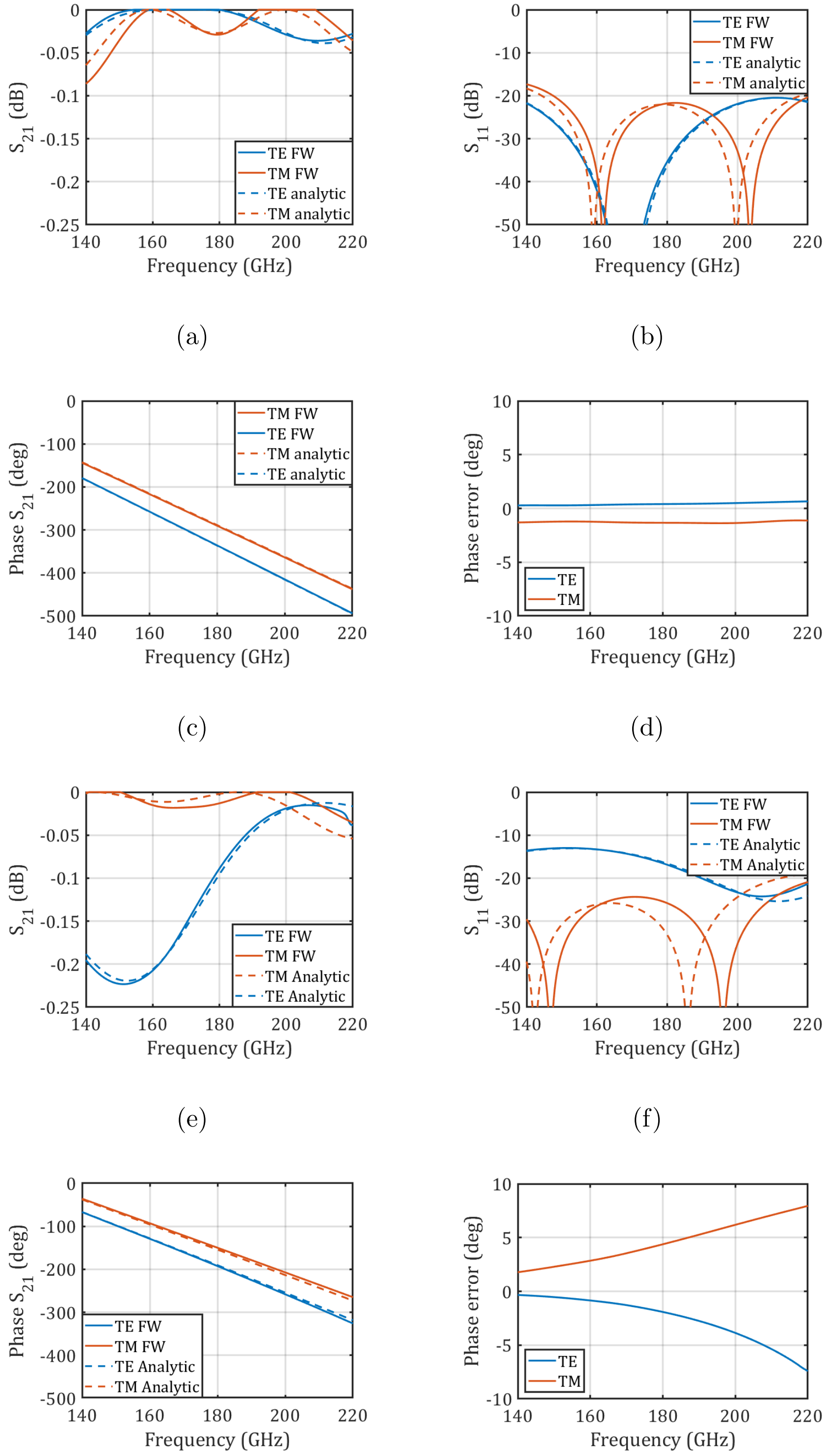

(a) (b)

(c) (d)

(e) (f)

(g) (h)

Figure B.2: Transmission coefficients for two dielectric pyramids with height 1275 µm a)-d) Broadside incidence e)-h) Obliques incidence for $\phi = 90$ deg, $\theta = 30$ deg. The phase error refers to the difference between FW and analytic results for the S_{21} phase.

Bibliography

[1] M. Giordani, M. Polese, M. Mezzavilla, S. Rangan, and M. Zorzi, "Toward 6G networks: Use cases and technologies," *IEEE Communications Magazine*, vol. 58, no. 3, pp. 55–61, 2020.

[2] T. S. Rappaport, Y. Xing, O. Kanhere, S. Ju, A. Madanayake, S. Mandal, A. Alkhateeb, and G. C. Trichopoulos, "Wireless communications and applications above 100 GHz: Opportunities and challenges for 6G and beyond," *IEEE Access*, vol. 7, pp. 78729–78757, 2019.

[3] "5G spectrum. gsma public policy position," Available: `https://www.gsma.com/spectrum/wp-content/uploads/2020/03/5G-Spectrum-Positions.pdf`, Accessed: 2020. [Online].

[4] J. Edstam, S. Hansryd, S. Carpenter, T. Emanuelsson, Y. Li, and H. Zirath, "Microwave Backhaul Evolution: Reaching Beyond 100 GHz," in *Ericsson Technology Review*, Stockholm, Sweden, Februar 2017.

[5] S. Dang, O. Amin, B. Shihada, and M.S. Alouini, "What should 6G be?," *Nature Electronics*, vol. 3, no. 1, pp. 20–29, 2020.

[6] M. Xiao, S. Mumtaz, Y. Huang, L. Dai, Y. Li, M. Matthaiou, G. K. Karagiannidis, E. Björnson, K. Yang, C. I, and A. Ghosh, "Millimeter wave communications for future mobile networks," *IEEE Journal on Selected Areas in Communications*, vol. 35, no. 9, pp. 1909–1935, 2017.

[7] K. M. S. Huq, S. A. Busari, J. Rodriguez, V. Frascolla, W. Bazzi, and D. C. Sicker, "Terahertz-enabled wireless system for Beyond-5G ultra-fast networks: A brief survey," *IEEE Network*, vol. 33, no. 4, pp. 89–95, 2019.

[8] I. F. Akyildiz, J. M. Jornet, and C. Han, "Terahertz band: Next frontier for wireless communications," *Physical Communication*, vol. 12, pp. 16–32, 2014.

[9] M. H. Alsharif, A. H. Kelechi, M. A. Albreem, S. A. Chaudhry, M. S. Zia, and S. Kim, "Sixth generation (6G) wireless networks: Vision, research activities, challenges and potential solutions," *Symmetry*, vol. 12, no. 4, pp. 676, 2020.

[10] M. Polese, J. Jornet, T. Melodia, and M. Zorzi, "Toward end-to-end, full-stack 6G terahertz networks," *arXiv preprint arXiv:2005.07989*, 2020.

[11] H. Viswanathan and P. E. Mogensen, "Communications in the 6G era," *IEEE Access*, vol. 8, pp. 57063–57074, 2020.

[12] "IEEE standard for high data rate wireless multi-media networks–amendment 2: 100 gb/s wireless switched point-to-point physical layer," *IEEE Std 802.15.3d-2017 (Amendment to IEEE Std 802.15.3-2016 as amended by IEEE Std 802.15.3e-2017)*, pp. 1–55, 2017.

[13] "Ericsson mobility report june 2020," Available: `https://www.ericsson.com/en/mobility-report`, Accessed: 2020. [Online].

[14] W. Saad, M. Bennis, and M. Chen, "A vision of 6G wireless systems: Applications, trends, technologies, and open research problems," *IEEE network*, vol. 34, no. 3, pp. 134–142, 2019.

[15] T. Kürner et al., "Applications requirement document (ARD)," IEEE 802.15 TG3d, `https://mentor.ieee.org/802.15/documents`, 2015, DCN: 15-14-0304-16-003d.

[16] H.Wang *et al.*, "Power Amplifiers Performance Survey 2000-Present," Available: `https://gems.ece.gatech.edu/PA_survey.html`, Accessed: 2020. [Online].

[17] R. Chu and K. Shinihara, *Semiconductors and Semimetals. III-Nitride Electronic Devices*, Academic Press, Cambridge, United States, 1 edition, 2019.

[18] A. Artemenko, A. Mozharovskiy, A. Maltsev, R. Maslennikov, A. Sevastyanov, and V. Ssorin, "Experimental characterization of e-band two-dimensional electronically beam-steerable integrated lens antennas," *IEEE Antennas and Wireless Propagation Letters*, vol. 12, pp. 1188–1191, 2013.

[19] J. Ala-Laurinaho, J. Aurinsalo, A. Karttunen, M. Kaunisto, A. Lamminen, J. Nurmiharju, A. V. Räisänen, J. Säily, and P. Wainio, "2-D beam-steerable integrated lens antenna system for 5G E-band access and backhaul," *IEEE Transactions on Microwave Theory and Techniques*, vol. 64, no. 7, pp. 2244–2255, 2016.

[20] N. Llombart, D. Emer, M. Arias Campo, and E. McCune, "Fly's eye spherical antenna system for future Tbps wireless communications," in *Proceedings of the 11th European Conference on Antennas and Propagation (EuCAP)*, 2017.

[21] W. Simon, D. Schaefer, S. Bruni, M. Arias Campo, O. Litschke, S. Otto, and S. Holzwarth, "Compact and modular Ka-band front-end concept for SATCOM and 5G," in *Proceedings of the 14th European Conference on Antennas and Propagation (EuCAP)*, 2020.

[22] Duncan A. Robertson, David G. Macfarlane, Robert I. Hunter, Scott L. Cassidy, Nuria Llombart, Erio Gandini, Tomas Bryllert, Mattias Ferndahl, Hannu Lindström, Jussi Tenhunen, Hannu Vasama, Jouni Huopana, Timo Selkälä, and Antti-Jussi Vuotikka, "The CONSORTIS 16-channel 340-GHz security imaging radar," in *Passive and Active Millimeter-Wave Imaging XXI*, David A. Wikner and Duncan A. Robertson, Eds. International Society for Optics and Photonics, 2018, vol. 10634, pp. 58 – 67, SPIE.

[23] K. B. Cooper, R. J. Dengler, N. Llombart, B. Thomas, G. Chattopadhyay, and P. H. Siegel, "THz imaging radar for standoff personnel screening," *IEEE Transactions on Terahertz Science and Technology*, vol. 1, no. 1, pp. 169–182, 2011.

[24] N. Llombart, G. Chattopadhyay, A. Skalare, and I. Mehdi, "Novel terahertz antenna based on a silicon lens fed by a leaky wave enhanced waveguide," *IEEE Transactions on Antennas and Propagation*, vol. 59, no. 6, pp. 2160–2168, 2011.

[25] A. Hosseini, F. De Flaviis, and F. Capolino, "Design formulas for planar Fabry–Pérot cavity antennas formed by thick partially reflective surfaces," *IEEE Transactions on Antennas and Propagation*, vol. 64, no. 12, pp. 5487–5491, 2016.

[26] G. Minatti, M. Faenzi, M. Sabbadini, and S. Maci, "Bandwidth of gain in metasurface antennas," *IEEE Transactions on Antennas and Propagation*, vol. 65, no. 6, pp. 2836–2842, 2017.

[27] K. Pham, N. T. Nguyen, A. Clemente, L. Di Palma, L. Le Coq, L. Dussopt, and R. Sauleau, "Design of wideband dual linearly polarized transmitarray antennas," *IEEE Transactions on Antennas and Propagation*, vol. 64, no. 5, pp. 2022–2026, 2016.

[28] Y. Yang, O. D. Gurbuz, and G. M. Rebeiz, "An eight-element 370–410-GHz phased-array transmitter in 45-nm CMOS SOI with peak EIRP of 8–8.5 dBm," *IEEE Transactions on Microwave Theory and Techniques*, vol. 64, no. 12, pp. 4241–4249, 2016.

[29] W. Shin, B. Ku, O. Inac, Y. Ou, and G. M. Rebeiz, "A 108–114 ghz 4 $\times 4$ wafer-scale phased array transmitter with high-efficiency on-chip antennas," *IEEE Journal of Solid-State Circuits*, vol. 48, no. 9, pp. 2041–2055, 2013.

[30] A. Sarkar, A. Sharma, A. Biswas, and M. J. Akhtar, “EMSIW-based compact high gain wide full space scanning LWA with improved broadside radiation profile,” *IEEE Transactions on Antennas and Propagation*, vol. 67, no. 8, pp. 5652–5657, 2019.

[31] Y. Geng, J. Wang, Y. Li, Z. Li, M. Chen, and Z. Zhang, “New design of beam-formed leaky-wave antenna based on substrate integrated waveguide in a confined space,” *IEEE Transactions on Antennas and Propagation*, vol. 66, no. 11, pp. 6334–6339, 2018.

[32] S. Bhardwaj and J. L. Volakis, “Hexagonal waveguide based circularly polarized horn antennas for sub-mm-wave/terahertz band,” *IEEE Transactions on Antennas and Propagation*, vol. 66, no. 7, pp. 3366–3374, 2018.

[33] N. Llombart, K. B. Cooper, R. J. Dengler, T. Bryllert, and P. H. Siegel, “Confocal ellipsoidal reflector system for a mechanically scanned active terahertz imager,” *IEEE Transactions on Antennas and Propagation*, vol. 58, no. 6, pp. 1834–1841, 2010.

[34] H. Hasani, M. Tamagnone, S. Capdevila, C. F. Moldovan, P. Maoddi, A. M. Ionescu, C. Peixeiro, J. R. Mosig, A. K. Skrivervik, and J. Perruisseau-Carrier, “Tri-band, polarization-independent reflectarray at terahertz frequencies: Design, fabrication, and measurement,” *IEEE Transactions on Terahertz Science and Technology*, vol. 6, no. 2, pp. 268–277, 2016.

[35] G. Perez-Palomino, P. Baine, R. Dickie, M. Bain, J. A. Encinar, R. Cahill, M. Barba, and G. Toso, “Design and experimental validation of liquid crystal-based reconfigurable reflectarray elements with improved bandwidth in F-band,” *IEEE Transactions on Antennas and Propagation*, vol. 61, no. 4, pp. 1704–1713, 2013.

[36] M. Faenzi, D. González-Ovejero, and S. Maci, “Wideband active region metasurface antennas,” *IEEE Transactions on Antennas and Propagation*, vol. 68, no. 3, pp. 1261–1272, 2020.

[37] “JMA wireless. Case study: Levi’s stadium,” Available: `https://www.nxp.com/docs/en/supporting-information/LEVIS-STADIUM-CS.pdf`, Accessed: 2020. [Online].

[38] “Interesting facts about Levi’s® stadium wifi, mobile app and ninerds [web blog post],” Available: `https://www.levisstadium.com/2014/09/progress-tk-interesting-facts-levis-stadium-wifi-mobile-app-ninerds`, Accessed: 2020. [Online].

[39] D. F. Filipovic, S. S. Gearhart, and G. M. Rebeiz, "Double-slot antennas on extended hemispherical and elliptical silicon dielectric lenses," *IEEE Transactions on Microwave Theory and Techniques*, vol. 41, no. 10, pp. 1738–1749, 1993.

[40] N. T. Nguyen, N. Delhote, M. Ettorre, D. Baillargeat, L. Le Coq, and R. Sauleau, "Design and characterization of 60-GHz integrated lens antennas fabricated through ceramic stereolithography," *IEEE Transactions on Antennas and Propagation*, vol. 58, no. 8, pp. 2757–2762, 2010.

[41] A. J. Alazemi, H. Yang, and G. M. Rebeiz, "Double bow-tie slot antennas for wideband millimeter-wave and terahertz applications," *IEEE Transactions on Terahertz Science and Technology*, vol. 6, no. 5, pp. 682–689, 2016.

[42] A. Neto, "UWB, non dispersive radiation from the planarly fed leaky lens antenna—part 1: Theory and design," *IEEE Transactions on Antennas and Propagation*, vol. 58, no. 7, pp. 2238–2247, 2010.

[43] N. Llombart, C. Lee, M. Alonso-del Pino, G. Chattopadhyay, C. Jung-Kubiak, L. Jofre, and I. Mehdi, "Silicon micromachined lens antenna for THz integrated heterodyne arrays," *IEEE Transactions on Terahertz Science and Technology*, vol. 3, no. 5, pp. 515–523, 2013.

[44] J. R. Costa and C. A. Fernandes, "Broadband slot feed for integrated lens antennas," *IEEE Antennas and Wireless Propagation Letters*, vol. 6, pp. 396–400, 2007.

[45] J. R. Costa, M. G. Silveirinha, and C. A. Fernandes, "Evaluation of a double-shell integrated scanning lens antenna," *IEEE Antennas and Wireless Propagation Letters*, vol. 7, pp. 781–784, 2008.

[46] X. Wu, G. V. Eleftheriades, and T. E. van Deventer-Perkins, "Design and characterization of single- and multiple-beam mm-wave circularly polarized substrate lens antennas for wireless communications," *IEEE Transactions on Microwave Theory and Techniques*, vol. 49, no. 3, pp. 431–441, 2001.

[47] K. Konstantinidis, A. P. Feresidis, C. C. Constantinou, E. Hoare, M. Gashinova, M. J. Lancaster, and P. Gardner, "Low-THz dielectric lens antenna with integrated waveguide feed," *IEEE Transactions on Terahertz Science and Technology*, vol. 7, no. 5, pp. 572–581, 2017.

[48] N. T. Nguyen, A. V. Boriskin, L. Le Coq, and R. Sauleau, "Improvement of the scanning performance of the extended hemispherical integrated lens antenna using a double lens focusing system," *IEEE Transactions on Antennas and Propagation*, vol. 64, no. 8, pp. 3698–3702, 2016.

[49] G. C. Trichopoulos, G. Mumcu, K. Sertel, H. L. Mosbacker, and P. Smith, “A novel approach for improving off-axis pixel performance of terahertz focal plane arrays,” *IEEE Transactions on Microwave Theory and Techniques*, vol. 58, no. 7, pp. 2014–2021, 2010.

[50] A. V. Boriskin and R. Sauleau, “Numerical investigation into the design of shaped dielectric lens antennas with improved angular characteristics,” *Prog. Electromagn. Res. B*, vol. 30, no. 7, pp. 279–292, 2011.

[51] K. Liu, S. Yang, S. Qu, C. Chen, and Y. Chen, “Phased hemispherical lens antenna for 1-D wide-angle beam scanning,” *IEEE Transactions on Antennas and Propagation*, vol. 67, no. 12, pp. 7617–7621, 2019.

[52] J. G. Marin and J. Hesselbarth, “Lens antenna with planar focal surface for wide-angle beam-steering application,” *IEEE Transactions on Antennas and Propagation*, vol. 67, no. 4, pp. 2757–2762, 2019.

[53] M. Seo, M. Urteaga, J. Hacker, A. Young, Z. Griffith, V. Jain, R. Pierson, P. Rowell, A. Skalare, A. Peralta, R. Lin, D. Lin, and M. Rodwell, “InP HBT IC technology for terahertz frequencies: Fundamental oscillators up to 0.57 THz,” *IEEE Journal of Solid-State Circuits*, vol. 46, no. 10, pp. 2203–2214, 2011.

[54] A. Tessmann, A. Leuther, V. Hurm, I. Kallfass, H. Massler, M. Kuri, M. Riessle, M. Zink, R. Loesch, M. Seelmann-Eggebert, M. Schlechtweg, and O. Ambacher, “Metamorphic HEMT MMICs and modules operating between 300 and 500 GHz,” *IEEE Journal of Solid-State Circuits*, vol. 46, no. 10, pp. 2193–2202, 2011.

[55] L. Samoska, W. R. Deal, G. Chattopadhyay, D. Pukala, A. Fung, T. Gaier, M. Soria, V. Radisic, X. Mei, and R. Lai, “A submillimeter-wave hemt amplifier module with integrated waveguide transitions operating above 300 GHz,” *IEEE Transactions on Microwave Theory and Techniques*, vol. 56, no. 6, pp. 1380–1388, 2008.

[56] K. M. K. H. Leong, W. R. Deal, V. Radisic, X. B. Mei, J. Uyeda, L. Samoska, A. Fung, T. Gaier, and R. Lai, “A 340–380 GHz integrated CB-CPW-to-waveguide transition for sub millimeter-wave MMIC packaging,” *IEEE Microwave and Wireless Components Letters*, vol. 19, no. 6, pp. 413–415, 2009.

[57] A. Tessmann, V. Hurm, A. Leuther, H. Massler, R. Weber, M. Kuri, M. Riessle, H. P. Stulz, M. Zink, M. Schlechtweg, O. Ambacher, and T. Närhi, “A 243 GHz low-noise amplifier module for use in next-generation direct detection radiometers,” in *2013 European Microwave Integrated Circuit Conference*, 2013, pp. 220–223.

[58] R. Han, Y. Zhang, Y. Kim, D. Y. Kim, H. Shichijo, E. Afshari, and K. K. O, “Active terahertz imaging using schottky diodes in CMOS: Array and 860-GHz pixel,” *IEEE Journal of Solid-State Circuits*, vol. 48, no. 10, pp. 2296–2308, 2013.

[59] H. S. Bakshi, P. R. Byreddy, K. O. Kenneth, A. Blanchard, M. Lee, E. Tuncer, and W. Choi, “Low-cost packaging of 300 GHz integrated circuits with an on-chip patch antenna,” *IEEE Antennas and Wireless Propagation Letters*, vol. 18, no. 11, pp. 2444–2448, 2019.

[60] C. Li and T. Chiu, “340-GHz low-cost and high-gain on-chip higher order mode dielectric resonator antenna for THz applications,” *IEEE Transactions on Terahertz Science and Technology*, vol. 7, no. 3, pp. 284–294, 2017.

[61] X. Deng, Y. Li, C. Liu, W. Wu, and Y. Xiong, “340 GHz on-chip 3-D antenna with 10 dBi gain and 80radiation efficiency,” *IEEE Transactions on Terahertz Science and Technology*, vol. 5, no. 4, pp. 619–627, 2015.

[62] X. Deng, Y. Li, W. Wu, and Y. Xiong, “340-GHz SIW cavity-backed magnetic rectangular slot loop antennas and arrays in silicon technology,” *IEEE Transactions on Antennas and Propagation*, vol. 63, no. 12, pp. 5272–5279, 2015.

[63] X. Deng, Y. Li, H. Tang, W. Wu, and Y. Xiong, “Dielectric loaded endfire antennas using standard silicon technology,” *IEEE Transactions on Antennas and Propagation*, vol. 65, no. 6, pp. 2797–2807, 2017.

[64] S. Van Berkel, S. Malotaux, C. De Martino, M. Spirito, D. Cavallo, A. Neto, and N. Llombart, “Wideband double leaky slot lens antennas in CMOS technology at submillimeter wavelengths,” *IEEE Transactions on Terahertz Science and Technology*, pp. 1–1, 2020.

[65] B. Goettel, P. Pahl, C. Kutschker, S. Malz, U. R. Pfeiffer, and T. Zwick, “Active multiple feed on-chip antennas with efficient in-antenna power combining operating at 200–320 GHz,” *IEEE Transactions on Antennas and Propagation*, vol. 65, no. 2, pp. 416–423, 2017.

[66] N. Sarmah, J. Grzyb, K. Statnikov, S. Malz, P. Rodriguez Vazquez, W. Föerster, B. Heinemann, and U. R. Pfeiffer, “A fully integrated 240-GHz direct-conversion quadrature transmitter and receiver chipset in sige technology,” *IEEE Transactions on Microwave Theory and Techniques*, vol. 64, no. 2, pp. 562–574, 2016.

[67] H. Song, J. Kim, K. Ajito, M. Yaita, and N. Kukutsu, “Fully integrated ASK receiver MMIC for terahertz communications at 300 GHz,” *IEEE Transactions on Terahertz Science and Technology*, vol. 3, no. 4, pp. 445–452, 2013.

[68] M. H. Eissa, A. Malignaggi, R. Wang, M. Elkhouly, K. Schmalz, A. C. Ulusoy, and D. Kissinger, "Wideband 240-GHz transmitter and receiver in BiCMOS technology with 25-Gbit/s data rate," *IEEE Journal of Solid-State Circuits*, vol. 53, no. 9, pp. 2532–2542, 2018.

[69] S. Bosma, M. Alonso-del Pino, C. Jung-Kubiak, D. Blanco, and N. Llombart, "Scanning lens phased array for submillimeter wavelengths," in *2019 44th International Conference on Infrared, Millimeter, and Terahertz Waves (IRMMW-THz)*, 2019, pp. 1–2.

[70] S. Beer, H. Gulan, C. Rusch, and T. Zwick, "Coplanar 122-GHz antenna array with air cavity reflector for integration in plastic packages," *IEEE Antennas and Wireless Propagation Letters*, vol. 11, pp. 160–163, 2012.

[71] A. Bhutani, B. Göttel, A. Lipp, and T. Zwick, "Packaging solution based on low-temperature cofired ceramic technology for frequencies beyond 100 GHz," *IEEE Transactions on Components, Packaging and Manufacturing Technology*, vol. 9, no. 5, pp. 945–954, 2019.

[72] N. Chahat, A. Tang, C. Lee, R. Sauleau, and G. Chattopadhyay, "Efficient CMOS systems with beam–lead interconnects for space instruments," *IEEE Transactions on Terahertz Science and Technology*, vol. 5, no. 4, pp. 637–644, 2015.

[73] A. Dyck, M. Rösch, A. Tessmann, A. Leuther, M. Kuri, S. Wagner, B. Gashi, J. Schäfer, and O. Ambacher, "A transmitter system-in-package at 300 GHz with an off-chip antenna and GaAs-based MMICs," *IEEE Transactions on Terahertz Science and Technology*, vol. 9, no. 3, pp. 335–344, 2019.

[74] N. Yoneda, R. Miyazaki, I. Matsumura, and M. Yamato, "A design of novel grooved circular waveguide polarizers," *IEEE Transactions on Microwave Theory and Techniques*, vol. 48, no. 12, pp. 2446–2452, 2000.

[75] S. Wang, C. Chien, C. Wang, and R. Wu, "A circular polarizer designed with a dielectric septum loading," *IEEE Transactions on Microwave Theory and Techniques*, vol. 52, no. 7, pp. 1719–1723, 2004.

[76] M. Letizia, B. Fuchs, A. Skrivervik, and J. R. Mosig, "Circularly polarized homogeneous lens antenna system providing multibeam radiation pattern for haps," *URSI Radio Science Bulletin*, vol. 2010, no. 333, pp. 18–28, 2010.

[77] Y. Cai, Y. Zhang, Z. Qian, W. Cao, and S. Shi, "Compact wideband dual circularly polarized substrate integrated waveguide horn antenna," *IEEE Transactions on Antennas and Propagation*, vol. 64, no. 7, pp. 3184–3189, 2016.

[78] X. Cheng, Y. Yao, T. Yu, Z. Chen, J. Yu, and X. Chen, "Analysis and design of a low-cost circularly polarized horn antenna," *IEEE Transactions on Antennas and Propagation*, vol. 66, no. 12, pp. 7363–7367, 2018.

[79] J. Wu, Y. J. Cheng, H. B. Wang, Y. C. Zhong, D. Ma, and Y. Fan, "A wideband dual circularly polarized full-corporate waveguide array antenna fed by triple-resonant cavities," *IEEE Transactions on Antennas and Propagation*, vol. 65, no. 4, pp. 2135–2139, 2017.

[80] M. Joyal and J. Laurin, "Analysis and design of thin circular polarizers based on meander lines," *IEEE Transactions on Antennas and Propagation*, vol. 60, no. 6, pp. 3007–3011, 2012.

[81] S. M. A. Momeni Hasan Abadi and N. Behdad, "Wideband linear-to-circular polarization converters based on miniaturized-element frequency selective surfaces," *IEEE Transactions on Antennas and Propagation*, vol. 64, no. 2, pp. 525–534, 2016.

[82] D. Blanco and R. Sauleau, "Broadband and broad-angle multilayer polarizer based on hybrid optimization algorithm for low-cost Ka-Band applications," *IEEE Transactions on Antennas and Propagation*, vol. 66, no. 4, pp. 1874–1881, 2018.

[83] L. Di Palma, A. Clemente, L. Dussopt, R. Sauleau, P. Potier, and P. Pouliguen, "Circularly-polarized reconfigurable transmitarray in Ka-Band with beam scanning and polarization switching capabilities," *IEEE Transactions on Antennas and Propagation*, vol. 65, no. 2, pp. 529–540, 2017.

[84] S. Mener, R. Gillard, R. Sauleau, A. Bellion, and P. Potier, "Dual circularly polarized reflectarray with independent control of polarizations," *IEEE Transactions on Antennas and Propagation*, vol. 63, no. 4, pp. 1877–1881, 2015.

[85] J. Wang, z. Shen, W. Wu, and K. Feng, "Wideband circular polarizer based on dielectric gratings with periodic parallel strips," *Optics Express*, vol. 23, no. 10, pp. 12533–12543, 2015.

[86] K. X. Wang and H. Wong, "Design of a wideband circularly polarized millimeter-wave antenna with an extended hemispherical lens," *IEEE Transactions on Antennas and Propagation*, vol. 66, no. 8, pp. 4303–4308, 2018.

[87] Y. Liu, H. Lu, Y. Wu, M. Cui, B. Li, P. Zhao, and X. Lv, "Millimeterwave and terahertz waveguide-fed circularly polarized antipodal curvedly tapered slot antennas," *IEEE Transactions on Antennas and Propagation*, vol. 64, no. 5, pp. 1607–1614, 2016.

[88] M. M. Zhou and Y. J. Cheng, "D-band high-gain circular-polarized plate array antenna," *IEEE Transactions on Antennas and Propagation*, vol. 66, no. 3, pp. 1280–1287, 2018.

[89] M. Euler, V. Fusco, R. Dickie, R. Cahill, and J. Verheggen, "Sub-mm wet etched linear to circular polarization fss based polarization converters," *IEEE Transactions on Antennas and Propagation*, vol. 59, no. 8, pp. 3103–3106, 2011.

[90] M. Mutlu, A. E. Akosman, and E. Ozbay, "Broadband circular polarizer based on high-contrast gratings," *Optics Letters*, vol. 37, no. 11, pp. 2094–2096, 2012.

[91] T. Kämpfe, P. Sixt, D. Renaud, A. Lagrange, F. Perrin, and O. Parriaux, "Broadband circular polarizer based on high-contrast gratings," *Optical Engineering*, vol. 53, no. 10, pp. 107105–1–107105–2, 2014.

[92] K. B. Cooper, N. Llombart, G. Chattopadhyay, B. Dengler, R. E. Cofield, C. Lee, S. Filchenkov, and E. Koposova, "A grating-based circular polarization duplexer for submillimeter-wave transceivers," *IEEE Microwave and Wireless Components Letters*, vol. 22, no. 3, pp. 108–110, 2012.

[93] E. Doumanis, G. Goussetis, R. Dickie, R. Cahill, P. Baine, M. Bain, V. Fusco, J. A. Encinar, and G. Toso, "Electronically reconfigurable liquid crystal based mm-wave polarization converter," *IEEE Transactions on Antennas and Propagation*, vol. 62, no. 4, pp. 2302–2307, 2014.

[94] V. Rumsey, "On the design and performance of feeds for correcting spherical aberration," *IEEE Transactions on Antennas and Propagation*, vol. 18, no. 3, pp. 343–351, 1970.

[95] A. Neto, O. Yurduseven, N. Llombart, and A. Freni, "Antennas in reception," in *Proceedings of the 9th European Conference on Antennas and Propagation (EuCAP)*, 2015.

[96] P. Burghignoli, "A leaky-wave analysis of the phase center in Fabry-Pérot cavity antennas," *IEEE Transactions on Antennas and Propagation*, vol. 60, no. 5, pp. 2226–2233, 2012.

[97] A. Freni, N. Llombart, O. Yurduseven, and A. Neto, "On the use of Thevenin circuits in distributed transmission lines and its consequences for antennas in reception," in *Proceedings of the 10th European Conference on Antennas and Propagation (EuCAP)*, 2016.

[98] N. Llombart, B. Blázquez, A. Freni, and A. Neto, “Fourier optics for the analysis of distributed absorbers under THz focusing systems,” *IEEE Transactions on Terahertz Science and Technology*, vol. 5, no. 4, pp. 573–583, 2015.

[99] A. Neto, N. Llombart, G. Gerini, M. D. Bonnedal, and P. de Maagt, “EBG enhanced feeds for the improvement of the aperture efficiency of reflector antennas,” *IEEE Transactions on Antennas and Propagation*, vol. 55, no. 8, pp. 2185–2193, 2007.

[100] A. Neto and N. Llombart, “Wideband localization of the dominant leaky wave poles in dielectric covered antennas,” *IEEE Antennas and Wireless Propagation Letters*, vol. 5, pp. 549–551, 2006.

[101] C. A. Balanis, *Antenna Theory: Analysis and Design*, John Wiley & Sons, Inc., New Jersey, USA, 3 edition, 2005.

[102] D. R. Jackson, A. A. Oliner, and A. Ip, “Leaky-wave propagation and radiation for a narrow-beam multiple-layer dielectric structure,” *IEEE Transactions on Antennas and Propagation*, vol. 41, no. 3, pp. 344–348, 1993.

[103] A. Polemi and S. Maci, “On the polarization properties of a dielectric leaky wave antenna,” *IEEE Antennas and Wireless Propagation Letters*, vol. 5, pp. 306–310, 2006.

[104] D. Jackson and A. A. Oliner, *”Leaky-wave antennas,” in Modern Antenna Handbook, C. Balanis*, chapter 7, pp. 325–367, Wiley, New York, 2008.

[105] M. A. Hickey, Meide Qiu, and G. V. Eleftheriades, “A reduced surface-wave twin arc-slot antenna for millimeter-wave applications,” *IEEE Microwave and Wireless Components Letters*, vol. 11, no. 11, pp. 459–461, 2001.

[106] D. Blanco, E. Rajo-Iglesias, S. Maci, and N. Llombart, “Directivity enhancement and spurious radiation suppression in leaky-wave antennas using inductive grid metasurfaces,” *IEEE Transactions on Antennas and Propagation*, vol. 63, no. 3, pp. 891–900, 2015.

[107] M. Kominami, D. Pozar, and D. Schaubert, “Dipole and slot elements and arrays on semi-infinite substrates,” *IEEE Transactions on Antennas and Propagation*, vol. 33, no. 6, pp. 600–607, 1985.

[108] D. Blanco, E. Rajo-Iglesias, A. Montesano Benito, and N. Llombart, “Leaky-wave thinned phased array in pcb technology for telecommunication applications,” *IEEE Transactions on Antennas and Propagation*, vol. 64, no. 10, pp. 4288–4296, 2016.

[109] N. Llombart, A. Neto, G. Gerini, M. Bonnedal, and P. De Maagt, "Leaky wave enhanced feed arrays for the improvement of the edge of coverage gain in multibeam reflector antennas," *IEEE Transactions on Antennas and Propagation*, vol. 56, no. 5, pp. 1280–1291, 2008.

[110] D. F. Filipovic, G. P. Gauthier, S. Raman, and G. M. Rebeiz, "Off-axis properties of silicon and quartz dielectric lens antennas," *IEEE Transactions on Antennas and Propagation*, vol. 45, no. 5, pp. 760–766, 1997.

[111] O. Yurduseven, D. Cavallo, A. Neto, G. Carluccio, and M. Albani, "Parametric analysis of extended hemispherical dielectric lenses fed by a broadband connected array of leaky-wave slots," *IET Microwaves, Antennas Propagation*, vol. 9, no. 7, pp. 611–617, 2015.

[112] "EMPIRE XPU," Available: `http://www.empire.de`, Accessed: 2020. [Online].

[113] N. Llombart, A. Neto, G. Gerini, M. Bonnedal, and P. De Maagt, "Impact of mutual coupling in leaky wave enhanced imaging arrays," *IEEE Transactions on Antennas and Propagation*, vol. 56, no. 4, pp. 1201–1206, 2008.

[114] A. Neto, S. Maci, and P. J. I. De Maagt, "Reflections inside an elliptical dielectric lens antenna," *IEE Proceedings - Microwaves, Antennas and Propagation*, vol. 145, no. 3, pp. 243–247, 1998.

[115] E. Joy, W. Leach, and G. Rodrigue, "Applications of probe-compensated near-field measurements," *IEEE Transactions on Antennas and Propagation*, vol. 26, no. 3, pp. 379–389, 1978.

[116] M. J. M. van der Vorst, P. J. I. de Maagt, A. Neto, A. L. Reynolds, R. M. Heeres, W. Luinge, and M. H. A. J. Herben, "Effect of internal reflections on the radiation properties and input impedance of integrated lens antennas-comparison between theory and measurements," *IEEE Transactions on Microwave Theory and Techniques*, vol. 49, no. 6, pp. 1118–1125, 2001.

[117] "R&S®ATS1000 antenna test system," Available: `https://www.rohde-schwarz.com/fi/product/ats1000-productstartpage_63493-394432.html`, Accessed: 2020. [Online].

[118] B. Derat, S. Schmitz, S. Lachner, M. Arias Campo, and S. Bruni, "Numerical modelling and experimental validation of a D-band lens-based antenna design for Beyond 5G communications," in *2020 Antenna Measurement Techniques Association Conference (AMTA)*, 2020.

[119] M. Arias Campo, G. Carluccio, D. Blanco, S. Bruni, O. Litschke, and N. Llombart, "Dielectric-grating in-lens polarizer for beyond 5G communications," in *2019 44th International Conference on Infrared, Millimeter, and Terahertz Waves (IRMMW-THz)*, 2019, pp. 1–2.

[120] C. A. Balanis, *Advanced Engineering Electromagnetics*, John Wiley & Sons, Inc., New Jersey, USA, 1 edition, 1989.

[121] "CST Studio Suite," Available: `https://www.3ds.com/productsservices/simulia/products/cst-studio-suite.`, Accessed: 2020. [Online].

[122] S. Bhardwaj, N. K. Nahar, and J. L. Volakis, "Novel phaseless gain characterization for circularly polarized antennas at mm-wave and THz frequencies," *IEEE Transactions on Antennas and Propagation*, vol. 63, no. 10, pp. 4263–4270, 2015.

[123] B. Y. Toh, R. Cahill, and V. F. Fusco, "Understanding and measuring circular polarization," *IEEE Transactions on Education*, vol. 46, no. 3, pp. 313–318, 2003.

[124] M. Imbert, A. Papió, F. De Flaviis, L. Jofre, and J. Romeu, "Design and performance evaluation of a dielectric flat lens antenna for millimeter-wave applications," *IEEE Antennas and Wireless Propagation Letters*, vol. 14, pp. 342–345, 2015.

[125] M. K. T. Al-Nuaimi and W. Hong, "Discrete dielectric reflectarray and lens for E-band with different feed," *IEEE Antennas and Wireless Propagation Letters*, vol. 13, pp. 947–950, 2014.

[126] H. Yi, S. Qu, K. Ng, C. H. Chan, and X. Bai, "3-D printed millimeter-wave and terahertz lenses with fixed and frequency scanned beam," *IEEE Transactions on Antennas and Propagation*, vol. 64, no. 2, pp. 442–449, 2016.

[127] P. Lalanne, "Effective medium theory applied to photonic crystals composed of cubic or square cylinders," *Appl. Opt.*, vol. 35, no. 27, pp. 5369–5380, 1996.

[128] S. Rytov, "Electromagnetic properties of a finely stratified medium," *Soviet Physics JEPT*, vol. 2, pp. 466–475, 1956.

[129] E. B. Grann, M. G. Moharam, and D. A. Pommet, "Artificial uniaxial and biaxial dielectrics with use of two-dimensional subwavelength binary gratings," *J. Opt. Soc. Am. A*, vol. 11, no. 10, pp. 2695–2703, 1994.

[130] M. Mrnka and Z. Raida, "An effective permittivity tensor of cylindrically perforated dielectrics," *IEEE Antennas and Wireless Propagation Letters*, vol. 17, no. 1, pp. 66–69, 2018.

[131] A. Deinega, I. Valuev, B. Potapkin, and Y. Lozovik, "Minimizing light reflection from dielectric textured surfaces," *J. Opt. Soc. Am. A*, vol. 28, no. 5, pp. 770–777, 2011.

[132] P. Lalanne and J.P. Hugonin, "High-order effective-medium theory of subwavelength gratings in classical mounting: application to volume holograms," *J. Opt. Soc. Am. A*, vol. 15, no. 7, pp. 1843–1851, 1998.

[133] X. Jing, J. Ma, S. Liu, Y. Jin, H. He, Ji. Shao, and Z. Fan, "Analysis and design of transmittance for an antireflective surface microstructure," *Opt. Express*, vol. 17, no. 18, pp. 16119–16134, 2009.

[134] D. H. Raguin and G. M. Morris, "Analysis of antireflection-structured surfaces with continuous one-dimensional surface profiles," *Appl. Opt.*, vol. 32, no. 14, pp. 2582–2598, 1993.

[135] P. Lalanne and D. Lemercier-Lalanne, "Depth dependence of the effective properties of subwavelength gratings," *J. Opt. Soc. Am. A*, vol. 14, no. 2, pp. 450–459, 1997.

[136] C. W. Haggans, L. Li, and R. K. Kostuk, "Effective-medium theory of zeroth-order lamellar gratings in conical mountings," *J. Opt. Soc. Am. A*, vol. 10, no. 10, pp. 2217–2225, 1993.

[137] H. Zhang, S. O. Dabironezare, G. Carluccio, A. Neto, and N. Llombart, "A Fourier optics tool to derive the plane wave spectrum of quasi-optical systems," *IEEE Antennas and Propagation Magazine*, accepted for publication.

[138] M. Born and E. Wolf, *Principles of Optics*, Pergamon, Oxford, United Kingdom, 6 edition, 1980.

[139] S. Sahin, N. K. Nahar, and K. Sertel, "Thin-film suex as an antireflection coating for mmW and THz applications," *IEEE Transactions on Terahertz Science and Technology*, vol. 9, no. 4, pp. 417–421, 2019.

[140] M. Spirito, G. Gentile, and A. Akhnoukh, "Multimode analysis of transmission lines and substrates for (sub)mm-wave calibration," in *82nd ARFTG Microwave Measurement Conference*, 2013, pp. 1–6.

[141] L. B. Felsen, M. Mongiardo, and P. Russer, *Electromagnetic field computation by network methods*, Springer Science & Business Media, 2009.

[142] G. Tyras, *Radiation and propagation of electromagnetic waves*, Academic Press, London, United Kingdom, 1969.

[143] S. J. Orfanidis, *Electromagnetic Waves and Antennas*, Rutgers University, New Brunswick, United States, 1999.

[144] D. M. Pozar, *Microwave Engineering*, John Wiley & Sons, New York, United States, 1998.

List of Publications

Journal Papers

J1. M. Arias Campo, D. Blanco, S. Bruni, A. Neto, and N. Llombart, “On the use of Fly’s eye lenses with leaky wave feeds for wideband wireless communications,” *IEEE Trans. Antennas Propag.*, vol. 68, no. 4, pp. 2480–2480, Apr. 2020.

J2. M. Arias Campo, G. Carluccio, D. Blanco, O. Litschke, S. Bruni, and N. Llombart, “Wideband circularly polarized antenna with in-lens polarizer for high-speed communications,” *IEEE Trans. Antennas Propag.*, Early Access.

J3. M. Arias Campo, K. Holc, R. Weber, C. De Martino, M. Spirito, A. Leuther, S. Bruni, and N. Llombart, “H-band quartz-silicon leaky-wave lens with air-bridge interconnect to GaAs front-end,” *IEEE Trans. THz Sci. and Technol.*, accepted for publication.

J4. M. Arias Campo, G. Carluccio, S. Bruni, and N. Llombart, “Dielectric gratings enhancing the field of view in low dielectric permittivity elliptical lenses,” *IEEE Trans. Antennas Propag.*, under review.

Conference Papers

C1. M. Arias Campo, G. Carluccio, S. Bruni, and N. Llombart, “In-lens dielectric gratings wedge enhancing the beam steering in low dielectric permittivity lenses,” *in Proc. of 15th European Conference on Antennas and Propagation (EuCAP)*, Düsseldorf, Germany, Mar. 22-26, 2021.

C2. M. Arias Campo, K. Holc, R. Weber, C. De Martino, M. Spirito, A. Leuther, S. Bruni, and N. Llombart, “Measurements of H-band quartz-silicon leaky-wave lens with off-chip air-bridge interconnect," *in Proc. of 15th European Conference on Antennas and Propagation (EuCAP)*, Düsseldorf, Germany, Mar. 22-26, 2021.

C3. M. Arias Campo, K. Holc, A. Leuther, R. Weber, S. Bruni, and N. Llombart, "H-band silicon lens antenna with quartz leaky-wave feeder and novel chip interconnect," *in Proc. of 45th International Conference on Infrared, Millimeter and Terahertz Waves (IRMMW THz-2020)*, Buffalo, New York, United States, Nov. 8-13, 2020.

C4. M. Arias Campo, G. Carluccio, D. Blanco, O. Litschke, S. Bruni, and N. Llombart, "Fly's eye lenses for wideband Beyond 5G communications," *in Proc. of 45th International Conference on Infrared, Millimeter and Terahertz Waves (IRMMW THz-2020)*, Buffalo, New York, United States, Nov. 8-13, 2020.

C5. B. Derat, S. Schmitz, S. Lachner, M. Arias Campo, and S. Bruni, "Numerical modelling and experimental validation of a D-Band lens-based antenna design for Beyond 5G communications," *2020 Antenna Measurement Techniques Association Conference (AMTA)*, Newport, Rhode Island, United States, Nov. 1-6, 2020.

C6. M. Arias Campo, G. Carluccio, D. Blanco, O. Litschke, S. Bruni, and N. Llombart, "Wideband Fly's eye lenses for Beyond 5G applications," *in Proc. of International Symposium on Antennas and Propagation (AP-S–URSI 2020)*, Montreal, Canada, Jul. 5-10, 2020.

C7. M. Arias Campo, K. Holc, A. Leuther, R. Weber, S. Bruni, and N. Llombart, "H-band quartz-cavity leaky-wave lens feeder with novel chip interconnect," *in Proc. of 14th European Conference on Antennas and Propagation (EuCAP)*, Copenhagen, Denmark, Mar. 15-20, 2020.

C8. M. Arias Campo, S. Bruni, G. Carluccio, and N. Llombart, "On the use of dielectric gratings for enlarging the field of view in low dielectric permittivity lenses," *in Proc. of 14th European Conference on Antennas and Propagation (EuCAP)*, Copenhagen, Denmark, Mar. 15-20, 2020.

C9. M. Arias Campo, G. Carluccio, D. Blanco, S. Bruni, O. Litschke and N. Llombart, "Experimental characterization of a wideband G-Band circularly polarized lens antenna," *in Proc. of 14th European Conference on Antennas and Propagation (EuCAP)*, Copenhagen, Denmark, Mar. 15-20, 2020.

C10. M. Arias Campo, G. Carluccio, D. Blanco, S. Bruni, O. Litschke and N. Llombart, "Dielectric-grating in-lens polarizer for Beyond 5G communications," *in Proc. of 44th International Conference on Infrared, Millimeter and Terahertz Waves (IRMMW THz-2019)*, Paris, France, Sep. 1-6, 2019.

C11. M. Arias Campo, D. Blanco, G. Carluccio, S. Bruni, O. Litschke and N. Llombart, "Wideband in-lens polarizer for future high-speed wireless communications," *in Proc. of 13th European Conference on Antennas and Propagation (EuCAP)*, Krakow, Poland, Apr. 22-26, 2019.

C12. D. Blanco, M. Arias Campo, and N. Llombart, "Low-permittivity elliptical lens fed by a broadband leaky-wave antenna for communications applications," *in Proc. of International Symposium on Antennas and Propagation (AP-S–URSI 2018)*, Boston, United States, Jul. 8-13, 2018.

C13. D. Blanco, M. Arias Campo, and N. Llombart, "Low-Permittivity Elliptical Lens Fed by a Resonant Leaky-Wave Antenna for Wireless Communications," *in Proc. of 12th European Conference on Antennas and Propagation (EuCAP)*, London, United Kingdom, Apr. 9-13, 2018.

C14. D. Blanco, M. Arias Campo, and N. Llombart, "Broadband Low-Permittivity Elliptical Lens Fed by a Leaky-Wave Antenna for Communications Applications," *in Proc. of 43th International Conference on Infrared, Millimeter and Terahertz Waves (IRMMW THz-2018)*, Nagoya, Japan, Sep. 9-14, 2018.

C15. M. Arias Campo, D. Blanco, G. Carluccio, O. Litschke, S. Bruni, and N. Llombart, "Circularly Polarized Lens Antenna for Tbps Wireless Communications," *48th European Microwave Conference (EuMC)*, Madrid, Spain, Sep. 25-27, 2018.

C16. M. Arias Campo, D. Emer, G. Carluccio and N. Llombart, "3D lens antenna array for Tbps communications," *in Proc. of International Symposium on Antennas and Propagation (AP-S–URSI 2017)*, San Diego, United States, Jul. 9-14, 2017.

C17. N. Llombart, D. Emer, M. Arias Campo, and E. McCune, "Fly's eye spherical antenna system for future Tbps wireless communications," *in Proc. of 11th European Conference on Antennas and Propagation (EuCAP)*, Paris, France, Mar. 19-24, 2017.

Summary

On the Design of Fly's Eye Lenses at sub-THz Frequencies for Wideband Communications

The expanding demand for high-speed wireless communications is pushing current networks and systems close to their limits. The use of sub-THz bands, where large bandwidth is available, is pointed out as one of the key strategies to cope with the huge amount of data transfer in the next Beyond 5G and 6G communications generations. Despite the promising properties of these high frequency bands, many challenges arise with their exploitation. The increasing loss due to propagation spreading, as well as the higher atmospheric and rain loss, should be compensated with highly directive antenna concepts. Besides, the lower output power provided by the transceivers in this spectrum and the increasing noise figure of the receiving devices magnifies the importance of achieving highly efficient antennas and transitions to the active front-end. The implementation of multi-beam architectures becomes specially challenging when moving to higher frequencies. The chip area does not decrease with frequency as passive RF structures do, due to the decreasing electronics efficiency, hindering the integration of the active circuitry together with the antennas. The harnessing of the large bandwidths available should be supported by all system and network layers, which will require breakthroughs in the related fields.

This dissertation focuses in the development of wideband, efficient antenna concepts with multi-beam capability for the next communication generations. The use of elliptical lens antennas with resonant leaky-wave feeders is proposed, reaching aperture efficiencies higher than $70\,\%$ over more than $35\,\%$ bandwidth, for the first time with leaky-waves. Fly's eye lens architectures are introduced to cover small cell or point-to-multipoint use cases, where multiple, static beams are required. In order to evaluate the feeder and lens performance, an analysis in reception combined with spectral Green's functions is applied, enabling the optimization of lenses with diameters of $\sim 20\lambda$. Making use of this methodology, four lens designs have been developed, fabricated, and characterized at G-band ($140 - 220\,\mathrm{GHz}$) and H-band ($220 - 320\,\mathrm{GHz}$). The lens concepts presented concentrate on some of the main requirements to be integrated in the envisioned Fly's eye

arrays: wide bandwidth, high aperture efficiency, low loss (antenna and transition to front-end), circular polarization, large scan range. New measurement strategies are presented, applicable to the characterization of lens antennas in the sub-THz bands.

The use of plastic lenses with leaky-wave feeders is explored in this thesis, aiming for low-cost antenna solutions. Three plastic lenses have been developed in this frame in G-band. The first lens, linearly polarized, consists of a leaky-wave feed with a double-slot excitation, fed by a split-block waveguide, and a High-Density Polyethylene (HDPE) truncated elliptical lens. Thanks to the leaky-wave feed and low lens permittivity, and applying the mentioned analysis in reception, 80 % aperture efficiency is reached over 44 % bandwidth, for the first time using leaky-waves. In the second plastic design, a dielectric grating polarizer in Topas material is integrated inside the HDPE lens, in order to generate circular polarization. A pyramidal unit cell has been designed, enabling its fabrication with standard processes at frequencies higher than 100 GHz. The aperture efficiency reached with the circular polarized lens is 75 % over 44 % relative bandwidth, and the axial ratio is lower than 3 dB over 35 % relative bandwidth. Finally, the third plastic lens design focuses in enhancing the lens steering range, which is intrinsically low in lenses with low dielectric permittivity. For this aim, a wedge of dielectric gratings is integrated inside the lens, on top of the leaky-wave feed. The wedge induces a beam tilt in the feed pattern, reducing spill-over and reflection loss, and therefore the scan loss for off-focus beams. Thanks to the optimization with the analysis in reception, a scan loss reduction of 4 dB is achieved at the center frequency, w.r.t. the case where the feeder is displaced along the focal plane. This improvement is visible over the whole G-band. A scan range of ±25 deg is reached with 3.6 dB scan loss at the center frequency.

Finally, the integration of the leaky-wave feed concept with an active front-end is investigated at H-band. A leaky-wave feed consisting on a quartz cavity is used to feed a silicon lens. The cavity is implemented on a quartz chip with two layers, and fed by a dipole printed on the bottom one. The quartz chip is connected to a GaAs front-end by means of a novel air bridge interconnect technology developed at Fraunhofer IAF. The loss estimated for this interconnect is lower than 0.2 dB, enabling an efficient off-chip antenna concept. Measurement results for a fabricated prototype validate the performance of an integrated design with more than 74 % aperture efficiency over 34 % bandwidth, and a radiation efficiency higher than 70 % over 37 % bandwidth, accounting for the interconnect, dipole feeding line and lens losses. Thanks to the use of a silicon lens (high dielectric permittivity), 25 deg of beam steering are reached with this antenna, with less than 3 dB scan loss over the whole bandwidth.

Samenvatting

De groeiende vraag naar draadloze communicatie met hoge snelheid duwt de huidige netwerken en systemen naar hun grenzen. Het gebruik van sub-THz-banden, waar veel bandbreedte beschikbaar is, wordt genoemd als een van de belangrijkste strategieën om het hoofd te bieden aan de enorme doorvoersnelheden in de aanstaande Beyond 5G- en 6G-communicatiegeneraties. Ondanks de veelbelovende eigenschappen van deze hoogfrequente banden, doen zich bij de exploitatie ervan veel uitdagingen voor. Hogere verliezen als gevolg van voortplantingsverspreiding, evenals het hogere atmosferische verlies en regenverlies, moeten worden gecompenseerd met zeer richtingsgevoelige antenneconcepten. Het lagere uitgangsvermogen van de zendontvangers in dit spectrum en het toenemende ruisgetal van de ontvangende apparaten vergroten het belang van zeer efficiënte antennes en de overgang naar actieve front-ends. De implementatie van architecturen met meerdere bundels wordt een bijzondere uitdaging bij de transitie naar hogere frequenties. Het chipoppervlak neemt niet af met de frequentie, zoals passieve RF-structuren doen, vanwege de afnemende elektronica-efficiëntie. Hierdoor wordt de integratie van de actieve schakelingen en antennes belemmerd. Het benutten van de grote beschikbare bandbreedtes moet worden ondersteund door alle systeem- en netwerklagen, wat doorbraken op de gerelateerde gebieden vereist.

Dit proefschrift richt zich op de ontwikkeling van breedbandige, efficiënte antenneconcepten met meedere stralingsbundels voor de volgende generatie communicatiesystemen. Het gebruik van elliptische lensantennes gevoed door resonerende lekgolven wordt voorgesteld, waardoor een diafragma-efficiëntie van meer dan 70 % over een bandbreedte van meer dan 35 % wordt bereikt, voor het eerst met lekkende golven. Een vliegenoogarchitectuur wordt geïntroduceerd om gebruik te worden voor kleine dekkingsgebieden ('small cell') of punt-naar-punten scenario's, waarin meerdere statische bundels nodig zijn. Om de prestaties van de voeding en de lens te beoordelen, wordt een ontvangstanalyse gecombineerd met de spectrale Greense functie-aanpak, waardoor lenzen met een diameter van ~ 20 golflengten kunnen worden geoptimaliseerd. Gebruikmakend van deze methodologie zijn vier lensantenne ontwerpen ontwikkeld, vervaardigd en gekarakteriseerd in de G-band ($140-220$ GHz) en de H-band ($220-320$ GHz). De gepresenteerde lensconcepten spitsen zich toe op enkele van de belangrijkste vereisten die moeten worden geïntegreerd in de beoogde vliegenoog-arrays: grote bandbreedte, hoge diafragma-efficiëntie, lage verliezen (in de antenne en de overgang naar de front-end), circulaire polarisatie, groot stuurbereik . Nieuwe meetstrategieën worden gepresenteerd, die toepasbaar zijn op de karakterisering van lensantennes in de sub-THz banden.

In dit proefschrift wordt het gebruik van kunststof lenzen gevoed door lekgolven, gericht op goedkope antenne-oplossingen, onderzocht. In dit verband zijn in de G-band drie kunststof lenzen ontwikkeld. De eerste lens, lineair gepolariseerd, bestaat uit een lekgolftoevoer van twee gleuven, gevoed door een golfpijp vervaardigd uit een gespleten blok, en een afgeknotte elliptische lens van hogedichtheidpolyethyleen (HDPE). Dankzij de lekgolftoevoer, de lage lenspermittiviteit, en het toepassen van de genoemde ontvangstanalyse, wordt 80 % diafragma-efficiëntie bereikt over een bandbreedte van 44 %, voor het eerst met behulp van lekgolven. In het tweede plastic ontwerp is een diëlektrische roosterpolarisator van Topas-materiaal geïntegreerd in de HDPE-lens om circulaire polarisatie op te wekken. Er is een piramidevormige eenheidscel ontworpen, die de fabricage mogelijk maakt met de gebruikelijke processen voor frequenties hoger dan 100 GHz. De diafragma-efficiëntie die wordt bereikt met de circulair gepolariseerde lens is 75 % in een relatieve bandbreedte van 44 %, en de axiale verhouding is lager dan 3 dB in een relatieve bandbreedte van 35 %. Tot slot is het derde kunststof lensontwerp geent op het vergroten van het lensstuurbereik, dat intrinsiek laag is bij lenzen met een lage diëlektrische permittiviteit. Voor dit doel is een wig van diëlektrische roosters geïntegreerd in de lens, boven de lekgolftoevoer. De wig veroorzaakt een bundelkanteling in het voedingspatroon, waardoor een groter deel van de bundel het lensoppervlak bereikt en weerkaatsingsverliezen worden verminderd, waarmee het stuurverlies voor afneemt. Dankzij de optimalisatie met de ontvangtsanalyse wordt een stuurverliesreductie van 4 dB bereikt op de ontwerpfrequentie, t.o.v. het geval waarin de voeding wordt verplaatst in het brandvlak. Deze verbetering is zichtbaar over de gehele G-band. Een stuurbereik van ±25 deg wordt bereikt waarbij 3.6 dB scanverlies optreedt op de ontwerpfrequentie.

Ten slotte wordt de integratie van het lekgolfvoedingsconcept met een actieve front-end in de H-band onderzocht. Een lekgolftoevoer bestaande uit een kwartsholte wordt gebruikt om een siliciumlens te voeden. De holte is geïmplementeerd op een kwartschip met twee lagen en wordt gevoed door een dipoolantenne die op de onderste laag is gedrukt. De kwartschip is verbonden met een GaAs front-end door middel van een nieuwe luchtbrug-verbindingstechnologie die is ontwikkeld door Fraunhofer IAF. Het geschatte verlies voor deze verbinding is lager dan 0.2 dB, waardoor de plaatsing van de antenne buiten de chip met lage verliezen mogelijk wordt. De meetresultaten van een gefabriceerd prototype bevestigen de prestaties van een geïntegreerd ontwerp met een diafragma-efficiëntie van meer dan 74 % over een bandbreedte van 34 % en een stralingsrendement van meer dan

70 % over een bandbreedte van 37 %, rekening houdend met de verbingen, de dipooltoevoerleiding en lensverliezen. Door het gebruik van een silicium lens (hoge diëlektrische permittiviteit) wordt met deze antenne een stuurbereik van 25 deg bereikt, met minder dan 3 dB scanverlies over de hele bandbreedte.

Propositions Accompanying the Doctoral Thesis

I The resonant leaky-wave feed is currently the most efficient wideband solution to illuminate integrated elliptical lenses with low dielectric permittivity (~ 2.5) (this proposition pertains to this dissertation).

II A dielectric grating polarizer integrated in an elliptical lens with a leaky-wave feed can provide circular polarization with comparable performance to the linearly polarized lens with the same diameter and eccentricity (this proposition pertains to this dissertation).

III The steering range of plastic truncated elliptical lenses with low permittivity (~ 2.5) can be almost doubled when integrating a wedge of dielectric gratings inside the elliptical lens, without reducing the bandwidth (this proposition pertains to this dissertation).

IV As long as there is still anyone surprised about a woman choosing an engineering career, there can be no hope for women to be respected as engineers in the same way as men.

V *"The more I know, the more I realize I know nothing."* – Socrates. A person's knowledge can be considered as a circle surrounded by unknown matter. The smaller the knowledge is, the less border exists to the unknown, which remains therefore unnoticed. Expanding the knowledge widens at the same time the awareness of the own ignorance. Nevertheless, only modest people will admit they have seen the border.

VI It is a shame that, even in developed countries, people's success does not only depend on their talent, but also heavily on their family's level of education and income.

VII A Ph.D. thesis is the result of the work of many people, to whom one should be always grateful. Also, *"I am thankful for all of those who said no to me. It's because of them I'm doing it myself."* – Wayne Dyer.

VIII If you listen to people who discourage you to follow your dreams, you lose the battle before even starting it. *"You may never know what results come of your actions, but if you do nothing, there will be no results."* – Mahatma Gandhi.

IX If you count the hours that you actually worked in your Ph.D., you will realize that it was the most expensive project in your career. But also your best investment.

X *"If you can't explain it to a six year old, you don't understand it yourself."* – attributed to Richard Feynman.

These propositions are considered opposable and defendable, and as such have been approved by the promotors Prof. dr. N. Llombart Juan and Prof. dr. A. Neto.

About the Author

Marta Arias Campo was born on July 13, 1986 in León, Spain. She received her M.Sc. degree in Telecommunications Engineering from the Technical University of Madrid, Madrid, Spain in September 2009. During her master she specialized in radiocommunication systems and circuits. She performed her M.Sc. thesis at the Radiation Group at the Technical University of Madrid, under the supervision of Prof. Dr. Manuel Sierra Pérez. During her M.Sc. thesis, she worked in the transmit and receive modules for a conformal array antenna at L-band for satellite communications.

In October 2009, she joined the Antennas and EM Modeling Department, IMST GmbH, where she currently works as a Research and Development Antenna Engineer in the Antenna Front-Ends Team, with the main focus on the design of active planar antenna arrays and front-ends for radar and communications.

In 2016, she joined the Terahertz Sensing Group, Technical University of Delft, Delft, The Netherlands, where she is working towards her Ph.D. degree, in collaboration with IMST GmbH. Her research has been carried out in under the supervision of Prof. Dr. N. Llombart and Prof. Dr. A. Neto as promotors, and co-supervised by Dr. S. Bruni and Dr. G. Carluccio. This work resulted in four manufactured prototype demonstrators, four journal publications and seventeen papers in international conferences. She was selected as one of the four finalists to compete for the *Best Antenna Design and Application Award* in the 13th edition of EUCAP, Krakau, Poland (22-26 Apr. 2019).

Her research interests include the analysis and design of lens antennas and quasi-optical structures at sub-THz frequencies for high-speed wireless communications and radar applications.

She is currently serving as a reviewer for *IEEE Transactions on Antennas and Propagation.*

Acknowledgements

The unconventional constellation under which this thesis started made it a very attractive matter for bets and gambles, for and against a possible successful ending. Having reached this point, I still almost cannot believe it myself how lucky I was during all this time... lucky to have so many people around me who made it possible, who supported me, and who fought with me to bring this project to such a rewarding outcome.

I would like to start thanking Prof. Nuria Llombart. I simply could not imagine how many things one can learn from someone in four years' time. You have pushed my boundaries, and showed me that I could reach much further than I thought. I admire your passion for engineering, your amazing capability of approaching and solving problems, your incredible memory and capacity to manage uncountable parallel activities. Thank you for teaching me so many useful skills, and for not giving up on me despite the difficult working configuration.

My great experience in Delft would not have been possible without the consent of Prof. Andrea Neto. Thank you for welcoming me in the Terahertz Sensing Group, for the fruitful discussions and for your valuable feedback.

The fact that I could even think about starting this adventure, was thanks to the full support that I got since the beginning in IMST from my head of department, Prof. Matthias Geissler, and my team leader, Oliver Litschke. I am so grateful that you gave me this opportunity, that you believed in the potential of this collaboration, and that you defended my position in every occasion. Many thanks also to IMST's director, Prof. Peter Waldow, for agreeing to start the cooperation with TU Delft.

My cornerstone during all this time was my colleague and friend Dr. Simona Bruni. Simona, I hope I will somehow be able to thank you for the immense support that you have given me during this time. Your support has covered all the layers in this hard period: technical, logistic, emotional. I have always looked up to you for the passion that you put in everything, for your courage and for your brightness. You have taught me that it is never late to pursue my dreams, to turn life upside down and go chase happiness, fulfilment. I just cannot imagine working without you, and I hope we retire together some day in the remote future.

Another key contributor to this thesis, and to the preservation of my mental health, was Dr. Giorgio Carluccio. Giorgio, I would like to thank you for your unconditional help, which continued after you left Delft, until today. Your dedication and knowledge in electromagnetics are extraordinary. I am deeply grateful for all the time that you have spent with me discussing about the thesis, helping me understand all the details, and being always such a patient and kind teacher. Your ability to find tiny typos is stunning; I hope someday you will lend me your secret glasses. I hope our professional ways cross again in the near future.

This thesis would barely contain measurement results if it was not for the support of TU Delft Electronics Research Laboratory team. I would like to thank specially Carmine de Martino and Dr. Marco Spirito, for the many times they have given me a hand in the lab, always so kindly.

Many thanks also to Bert, Leon and Humphrey from DEMO, for their effort and accuracy in the prototype fabrication, and for the nice and positive discussions. You were always available, even for short notice adjustments, and I appreciate it greatly.

I owe the successful realization of one whole chapter of this thesis to the great Fraunhofer IAF team. Dr. Arnulf Leuther, Dr. Katarzina Holc, and Rainer Weber, thank you so much for the innumerable interactions within Hypatia project, for your always valuable input and for providing your wonderful technological capacities for our design. I really learnt a lot during this time working with you, and I am grateful for that.

I would also like to thank Rohde & Schwarz team, especially Dr. Benoit Derat and Sebastian Schmitz, for the fruitful collaboration activity and for agreeing to include the results in this thesis.

Although I could not be present in TU Delft's office so much time, every time I visited it just felt as if I was part of it. This was thanks to such awesome colleagues that I was lucky to find, and who I already miss. Sven, we shared the office almost until the end, and it was so much fun! I was always happy to find you there when I came rushing from the station. You were always available to help me, and I really appreciate that. Alejandro, I am still thinking... what is the chance to find someone from León in the far-off Delft? I could talk to you about everything since the beginning. I wish you and Ángela would live near us, because I always enjoy so much the time with you! Shahab, I love your sense of humor, I enjoyed so much those crazy conversations. You just surprised me every time with your weird, funny thoughts! I thank you as well for helping me with your amazing Matlab tools. Cristina, you were always there for me as well when I needed it, you filled

the office with joy. And for some reason, a conference in San Diego always comes to my mind when I think about you… Harshitha, it was so nice to have you beside me in the office for some time. You are such a natural, cheerful person. Alessandro, thank you for being always so kind, I have only good memories from you. Huasheng, it was great to share the office with you as well, always with a smile on your face! Paolo, I laughed so much with you, I will miss that too. Thanks for having only kind words and for speaking so frankly with me. Darwin, I thank you too for the time that we worked together, and I hope you are happy with your new life. Arturo, Ralph, Sjoerd, we had a great time in Dubrovnik, and you were always so nice to me, thank you. Thanks also to all the rest of people who I had the pleasure to interact with these years: María, Daniele, Erio, Juan, Jochem, Angelo. Big thanks also to Everdine always willing to help and reacting so fast to any inquiry.

I would like to specially thank Sjoerd for the translation of the summary to Dutch. You were in such short notice available and responded so fast!

I am very grateful to all the colleagues in IMST who expressed their support for my decision, and who were always interested in the status of my work. I would like to especially thank Dr. Andreas Lauer, for pulling some strings which gave me the chance to work in Hypatia project, and being always ready for interesting discussions; Dr. Silja Ehrich, for being open as project leader to welcome me in Hypatia team; Dr. Peter Uhlig and Alexandra Serwa, for the fruitful discussions, for having the door of the technology facilities always open for me, and for the implementation of Hypatia's lens matching layer; Martin Böttcher for helping me with the first material characterizations; Ilona Willimovski for helping me understand the complex tax arrangements between Germany and the Netherlands. I would also like to mention my colleagues Roman Gieron, Dr. Simon Otto, Winfried Simon, Markus Krengel, Anke Wolter, who showed interest and encouraged me in this path.

I cannot do other than thank IMST south-European gang, for making working days in IMST so much fun, for the hilarious lunch and coffee conversations, for being open to talk about anything… yes, anything. Itziar, Jon, Marta, Lila, Enrico, Vasilis, Jordi, Ismael: thank you for spicing up working time, for blowing away the clouds when needed. Enrico, thank you for sharing this kamikaze initiative with me. It was always a relief to know there is someone sharing this (pain) with me.

For making life in Germany feel like home, I am so grateful to Erika, Cristina, Jon, Maya, Juan Fernández, Sina, Daniel, Juan Ramírez, Lucy. You were and are always there in bad and good times. My collection of good memories is full with your faces, and I am just so glad that I have or had you here.

To my old friends Nuria, Javi, Helena, Maria Navarrete. It is such a long time that our paths went apart, and yet I can still feel you so near me. I have always missed you so much, and I hope from now on I can find again more time to spend quality time with you.

I also have to mention the thousands of Airbnb houses, hotels, hostels which hosted me during this time; the Deutsche Bahn and NS trains with which I travelled from Duisburg to Delft (summing up to what feels like millions of kilometers). So many (terrifying) stories to tell. Now that I stopped travelling, I guess they are all fearing that I suddenly got lost somewhere.

It would have been impossible to finish this work without having my husband, Sebastian, always on my side. You are so patient with me; you listen so carefully, you always know what I need and find a way to calm me down, to cheer me up. Thank you for going through all this mess with me, and for always believing that I could do it. Life is so much easier with you. I love you, and I look forward to our long life together.

Thanks so much also to Sebastian's family, *meine Familie in Deutschland. Ela, Wilfried, Kristin, Patrick und Anja: Danke dafür, dass ihr mir immer zugehört und mich ermuntert habt, wenn ich mich durch die schlechten Zeiten gekämpft habe. Ich bin so glücklich so eine tolle Familie gefunden zu haben, mit der ich mich immer wie zu Hause fühle.*

To my amazing family. *A mis padres, Diego y Merche, por habérnoslo dado todo, por haber posibilitado todos los caminos que he querido seguir para llegar hasta aquí: os lo debo todo a vosotros. Gracias por todos los sacrificios que habéis hecho por nosotras, por habernos educado con tanto cuidado y cariño, y por habernos hecho las personas que somos hoy. A mi hermana Ángela, por haber compartido toda una vida, de juegos y risas, por haberme enseñado tantas cosas, por haberme ayudado a espabilar y perder muchos miedos. A mis abuelos y tíos, también a los que ya no están, por cuidar de nosotras en innumerables ocasiones y por tantísimos buenos momentos que guardo conmigo. Os quiero a todos muchísimo, y os echo de menos.*